Exploring plasma stability and confinement with high resolution density measurements on the ZaP-HD Flow Z-Pinch

Michael Patrick Ross

A dissertation
submitted in partial fulfillment of the
requirements for the degree of

Doctor of Philosophy

University of Washington

2016

Reading Committee:

Uri Shumlak, Chair

Brian A. Nelson

Setthivoine You

Program Authorized to Offer Degree:
William E. Boeing Department of Aeronautics & Astronautics

University of Washington

Abstract

Exploring plasma stability and confinement
with high resolution density measurements
on the ZaP-HD Flow Z-Pinch

Michael Patrick Ross

Chair of the Supervisory Committee:
Professor Uri Shumlak
Aeronautics & Astronautics

The ZaP-HD Flow Z-Pinch project provides a platform to explore how shear flow stabilized Z-pinches could scale to high-energy-density plasma (plasma with pressures exceeding 1 Mbar) and fusion reactor conditions. The Z-pinch is a linear plasma confinement geometry in which the plasma carries axial electric current and is confined by its self-induced magnetic field. ZaP-HD generates shear stabilized, axisymmetric Z-pinches with stable lifetimes approaching 60 μs. The goal of the project is to increase the plasma density and temperature compared to the previous ZaP project by compressing the plasma to smaller radii ($\approx$ 1 mm).

Radial and axial plasma electron density structure is measured using digital holographic interferometry (DHI), which provides the necessary fine spatial resolution. ZaP-HD's DHI system uses a 2 ns Nd:YAG laser pulse with a second harmonic generator ($\lambda = 532$ nm) to produce holograms recorded by a Nikon D3200 digital camera. The holograms are numerically reconstructed with the Fresnel transform reconstruction method to obtain the phase shift caused by the interaction of the laser beam with the plasma. This provides a two-dimensional map of line-integrated electron density, which can be Abel inverted to determine the local number density. The DHI resolves line-integrated densities down to 3×10^{20} m^{-2} with spatial resolution near 10 μm.

This dissertation presents the first application of Fresnel transform reconstruction as an

analysis technique for a plasma diagnostic, and it analyzes the method's accuracy through study of synthetic data. It then presents an Abel inversion procedure that utilizes data on both sides of a Z-pinch local number density profile to maximize profile symmetry. Density measurements from DHI reveal the quality of ZaP-HD's confinement, specifically its scaling properties. DHI measurements also enable an evaluation of Z-pinch stability metrics.

TABLE OF CONTENTS

LIST OF FIGURES

ACKNOWLEDGMENTS

I could not have completed this dissertation without the support of others. First and foremost, I thank my adviser, Professor Uri Shumlak, for supporting me throughout my doctoral work. His inspiring encouragement, technical expertise, and thoughtful advice were critical to my success. I will miss working with him. I also owe many thanks to Professor Brian Nelson, Professor Raymond Golingo, and Dr. Sean Knecht for training me and generously offering their assistance and expertise in day-to-day lab operations.

My fellow students have meant the world to me. I have learned so much from them, and their companionship inspired me to complete my research. Special gratitude is due to Dr. Michal Hughes, with whom I worked throughout all six years of graduate school. The two of us cooperated as the graduate students in charge of designing, building, and running ZaP-HD, and I am proud of our mutual success. I would also like to thank my friends and co-workers Clayton Chu, Gerard Finnegan, Dr. Eder Sousa, Jonathan Weed, Shawn Doty, Eleanor Forbes, Mark Kaufman, Elliot Claveau, and Dr. Tobin Weber among many others for their invaluable contributions to my success and happiness as a graduate student.

Last but not least, I thank my parents and extended family, especially those in Grand Junction, Colorado, for everything they have done for me.

Chapter 1

INTRODUCTION

Mankind's boldest aspirations hinge on the development of plasma physics. Harnessing the power plasmas promise would supply humanity with fusion reactors generating clean electricity from limitless fuel. Applying fusion technology to space propulsion would enable manned colonization of distant planets. Ultimately, mastery of plasmas may give us the opportunity to leave our solar system, explore our galaxy, and perhaps even allow our species, in some form, to outlive our sun.

The reasons to study plasmas are compelling, but what gives plasmas such captivating potential? Plasmas are ionized gases composed of charge particles, which can be moved and contained by magnetic fields. The ability to act on plasmas at a distance allows for compression without physical wall contact, which opens the possibility of confining extremely hot, high energy matter. Most concepts for terrestrial energy sources or highly efficient space thrusters rely on confining a plasma at high density and temperature for long periods of time.

The ZaP-HD Flow Z-Pinch Experiment tests the efficacy of the flow shear stabilized Z-pinch concept of plasma confinement. The project aims to extend Z-pinch lifetimes while learning how density and temperature scale. This research described in this dissertation applies a laser diagnostic called digital holographic interferometry (DHI) to investigate the scalability of ZaP-HD's plasma confinement and stability.

1.1 General plasma and Z-pinch theory

1.1.1 Z-Pinch plasma equilibrium

Among the simplest confinement geometries is the Z-pinch: a linear column of plasma with electric current flow along its length. The magnetic field induced by the current compresses

the plasma on its axis. The magnetic force balances the confined plasma pressure, P, as in

$$\nabla P = \vec{j} \times \vec{B} \tag{1.1}$$

where $\vec{j}$ is the current density and $\vec{B}$ is the magnetic field. Expressing Eq. (1.1) in cylindrical vector components yields

$$\frac{d}{dr}\left(P + \frac{B_\theta^2}{2\mu_0}\right) = \frac{B_\theta^2}{\mu_0 r} \tag{1.2}$$

where $B_\theta^2/2\mu_0$ is magnetic pressure, and $B_\theta^2/\mu_0 r$ is magnetic field tension. Within the plasma radius, the magnetic tension and pressure both balance the plasma pressure. Outside the plasma radius, the magnetic tension balances the magnetic and plasma pressures.

A figure of merit for plasma confinement, $\beta = 2\mu_0 P/B^2$, indicates how effectively a plasma can be contained with a given magnetic field. Most plasma confinement concepts have β values of a small fraction of unity, but Z-pinches have unity average β as defined by

$$\beta = \frac{\langle P \rangle}{B_a^2/2\mu_0} = 1 \tag{1.3}$$

where $\langle P \rangle$ is the average pressure and B_a is the field at the edge of the plasma. High β confinement makes the Z-pinch an attractive concept as long as it can be sustained.

1.1.2 Z-Pinch stability

Generally, Z-pinches are difficult to sustain because they are highly susceptible to sausage ($m = 0$) and kink ($m = 1$) mode instabilities, which reduce plasma lifetimes by ending confinement. Figure 1.1 illustrates the two instability modes. When a Z-pinch constricts as in the sausage mode, the local current density increases, which increases the magnetic compression at the constriction. Unmitigated, a sausage mode will constrict until it cuts the plasma apart. When a Z-pinch bends off axis as in a kink mode, the magnetic field concentrates on the concave side and diminishes on the convex side. The imbalance in
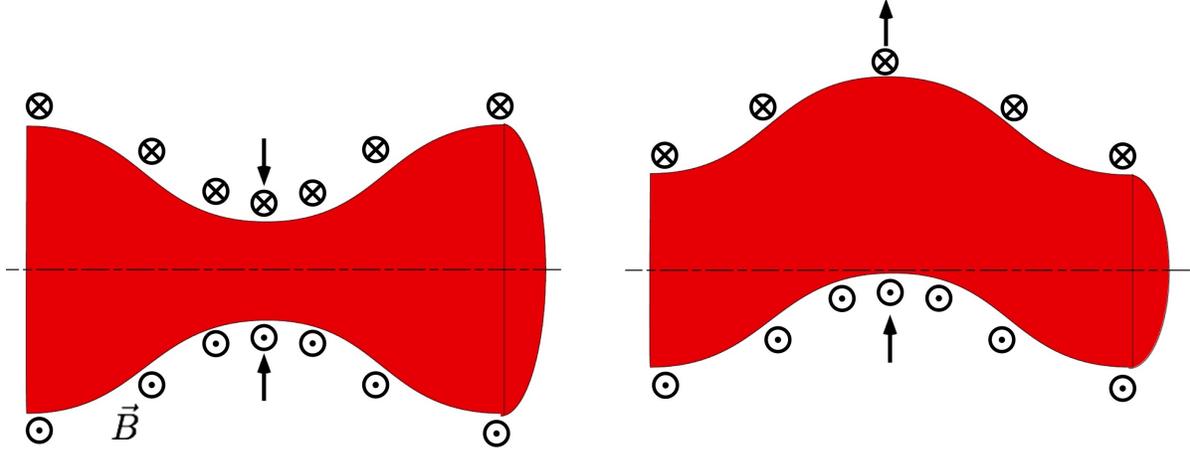
Figure 1.1: Sausage and kink mode instabilities are shown at left and right respectively. The magnetic fields induced by current flow from right to left are shown. The sausage mode results in azimuthally symmetric $\vec{B}$ concentration that causes the pinch to further constrict. The kink mode causes an asymmetric $\vec{B}$ concentration that drives the pinch further off axis.

magnetic pressure bends the Z-pinch further until it rips apart.

These instabilities can be neutralized by several methods. Some are proven, but come with severe drawbacks. Close-fitting conducting walls induce image currents, which oppose and mitigate plasma perturbations [1]. This works for relatively cool plasmas, but they cannot be used to stabilize high temperature, high energy plasma as their proximity to the plasma exposes them to extreme heat loads. Another stabilization concept relies applying an axial field component to the Z-pinch, turning it into a screw pinch. This introduces magnetic shear, which stabilizes the plasma. However, the axial field provides a pathway along which charged particles can exit the equilibrium, which causes significant energy losses and exposes metal electrodes to high heat loads. Additionally, the axial field component can only stabilize pinches with axial currents up to a maximum set by the Kruskal-Shafranov limit [2, 3].

Methods do exist to mitigate the instabilities without the negative repercussions of the aforementioned methods. Z-pinches with sufficiently gradual pressure profiles are stable against sausage modes. Kadomtsev showed the stability criterion to be

$$\frac{d\ln P}{d\ln r} \leq \frac{4\gamma}{2+\gamma\beta} \tag{1.4}$$

where $\gamma = C_p/C_v$, which must be satisfied everywhere in the plasma for stability against the sausage mode [4].

Sheared axial flows can stabilize kinks. The radial shear of the axial flow must meet the criterion

$$\frac{dV_z}{dr} \geq 0.1kV_A \tag{1.5}$$

where k is the wave number of the instability, and $V_A = B_a/\sqrt{\mu_0\rho_0}$ is the Alfvén speed defined by the maximum field and density. To ensure stability everywhere in the plasma, the shear must be maintained for at least the time it takes the plasma to flow along the Z-pinch's length. In other words, the plasma's viscous damping time must exceed a bulk flow through time to ensure the shear is not dissipated by viscosity [5].

Magneto-Rayleigh-Taylor (MRT) instabilities with $m = 0$ and $m = 1$ azimuthal mode numbers also occur in Z-pinch implosions. Related to the Rayleigh-Taylor (RT) fluid instability, MRTs may occur when the vacuum-plasma interface accelerates [6]. The RT instability occurs when a light fluid accelerates into a heavy one. Imagine a closed classroom filled with air at atmospheric pressure. An atmosphere of pressure is enough to hydro-statically support a sizable layer of water at the room's ceiling, yet the world is devoid of such fascinating classrooms. If such a room did exist, it would not take long for the gravitational acceleration imparted on the fluids to drive RT instabilities to interchange the relatively dense water with the relatively sparse air. Localized perturbations at the interface between the fluids grow into a pattern of bubbles and spikes. Oftentimes, the instability growth terminates in a global interchange where the fluids either mix or switch positions [7]. The MRT instability operates in analagous fashion with a magnetic field acting as the light fluid. MRT instabilities frequently limit dynamic Z-pinch performance [8], but steady state Z-pinches are stable against the MRT because the vacuum-plasma boundary remains stationary. In ZaP-HD,

MRTs are most likely to occur near the inner electrode nosecone where the plasma rapidly converges on axis.

Current-driven microinstabilities can also disturb the plasma and limit its current. When the plasma drift speed, $v_d = |v_e - v_i|$, exceeds the ion thermal velocity, $v_{t_i} = \sqrt{kT_i/m_i}$, kinetic effects cause disturbances such as two-stream and lower-hybrid drift instabilities, which are thought to cause anomalous resistivity and reduce v_d [9]. Sec. 1.1.3 describes how reducing a Z-pinch's linear density, N, leads to increased temperature and density. However, because T_i depends on linear density through Bennett's relation, decreasing the linear density too much reduces the ion thermal velocity to the point microinstabilities develop [10].

1.1.3 Ideal Z-pinch scaling

To explore how Z-pinch properties scale, consider the Bennett pinch relation,

$$8\pi NkT(Z+1) = \mu_0 I^2,\tag{1.6}$$

which applies to Z-pinches with arbitrary current profiles. Here, $T = T_e + T_i$, Z is the charge state, k is Boltzmann's constant, and the total current $I = \int_0^a 2\pi J_z r dr$. The relation is derived from applying Ampere's Law to radial pressure balance, treating the plasma as an ideal gas, and defining a linear density $N = \int_0^a 2\pi n r dr$ where a is the plasma radius [11].

Rearranging the Bennett relation expresses how Z-pinch temperature scales with plasma current and linear density as indicated in

$$\frac{T_2}{T_1} = \left(\frac{I_2}{I_1}\right)^2 \frac{N_1}{N_2}\tag{1.7}$$

where the subscripts 1 and 2 indicate initial and final states respectively. Theoretical scalings for number density, $n = Zn_i = n_e$ when $Z = 1$, and pinch radius, a, can be found by assuming adiabatic compression. An adiabatic process occurs without heat transfer from the system, i.e. it happens so fast that no energy flow is possible, which means the quantity $P/n^\gamma = (1+Z)kT/n^{\gamma-1}$ remains constant. This relates density to temperature, and radius
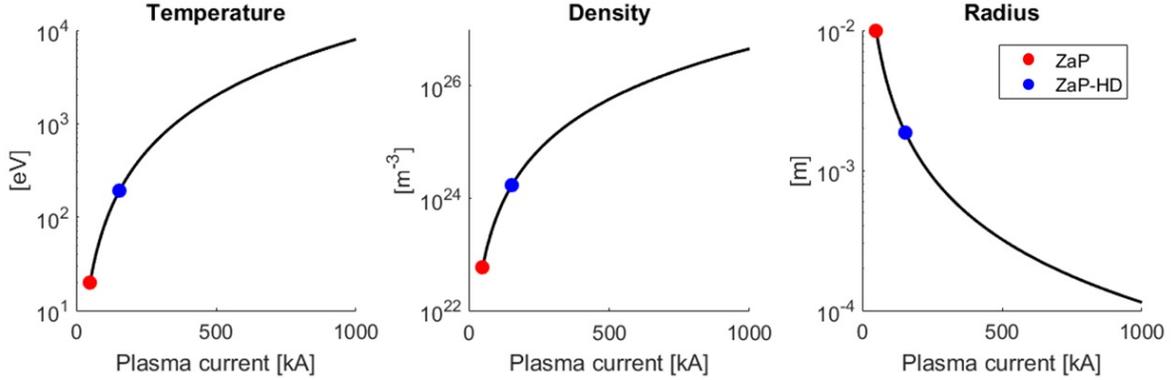
Figure 1.2: The ideal scaling of temperature, density, and radius with plasma current for an adiabatically compressed Z-pinch with constant linear density. The red and blue dots indicate the nominal run conditions for ZaP and ZaP-HD respectively.

relates to density as in $n = N/\pi a^2$. This gives everything necessary to obtain scaling relations for density and pinch radius given by

$$\frac{n_2}{n_1} = \left(\frac{I_2}{I_1}\right)^{\frac{2}{\gamma-1}} \left(\frac{N_1}{N_2}\right)^{\frac{1}{\gamma-1}} \tag{1.8}$$

$$\frac{a_2}{a_1} = \left(\frac{I_1}{I_2}\right)^{\frac{1}{\gamma-1}} \left(\frac{N_2}{N_1}\right)^{\frac{\gamma}{2(\gamma-1)}}. \tag{1.9}$$

The temperature and density both scale directly with increased current but inversely with linear density. Optimal scaling results from increasing plasma current independent of linear density, which has been plotted in Fig. 1.2. These plots use the original ZaP experiment ($n_1 = 6 \times 10^{22}$ m^{-3}, $T_1 = 20$ eV, $I_1 = 50$ kA, and $a = 1$ cm) as the initial state and trace out a series of final states for a range of elevated currents [12]. As current increases, pinch radius shrinks, which means high resolution diagnostics are required to view hot, dense Z-pinches. These ideal scalings help predict how much current, and therefore power, is required to sustain certain temperatures and densities. The ZaP-HD experiment explores how the flow Z-pinch scales in reality.

1.1.4   Historical context of Z-pinches, X-pinches, and Dense Plasma Foci

Research into Z-pinches as potential magnetic confinement fusion (MCF) reactors began in the 1950s [13], but MHD instabilities plagued these static, μs-timescale discharges [14]. Moving forward, fast (10-100 ns) Z-pinches were explored as a means to compress the plasma faster than the instabilities could grow, which led to improved compression and X-ray emission [15]. Fast Z-pinches employ various loads including wire arrays, gas-puffs, and cylindrical liners [16]. Today's experimental concepts include Magnetic Liner Inertial Fusion (MagLIF) [17] and the staged Z-pinch [18].

Delivering more than 10 percent conversion efficiency from capacitor bank energy to radiation, Z-pinch X-ray sources could be relatively efficient drivers for implosions of spherical fuel pellets in inertial confinement fusion (ICF) schemes [19]. Presently, at experiments like the National Ignition Facility (NIF) such implosions are driven by costly, inefficient high power lasers striking a hohlraum. A hohlraum is a cylindrical gold shell that surrounds a spherical fuel pellet. At NIF, 192 of the world's most powerful ultraviolet lasers simultaneously strike the hohlraum, which then emits X-rays that drive the fuel implosion [20].

Bursts of X-ray emission from Z-pinches emanate from small micropinches caused by sausage mode instabilities, and the locations of these micropinches are unpredictable in both space and time. X-ray bursts are generated with greater predictability by a similar category of devices called X-pinches, which drive loads consisting of metal wires that contact each other at a cross point [21]. The pre-pulse load of a two-wire X-pinch literally looks like the letter X. X-ray emission consistently occurs at the cross point in X-pinches, which enables their use as point sources of X-rays for radiography, a diagnostic useful in imaging dense Z-pinch and X-pinch plasma implosions [22].

Another related class of devices, the dense plasma focus (DPF), is being explored as a source of X-rays, particle beams, and fusion neutrons [23]. Two broad categories of DPF geometry exist: the Filippov and Mather designs. The Filippov design consists of concentric, circular, co-planar electrodes and is rather similar to plasma guns used to study magnetic

reconnection and astrophysical plasma jets [24, 25]. The Mather design ostensibly resembles the geometry of the ZaP-HD accelerator, but it lacks the downstream assembly region provided by ZaP-HD's outer electrode. Also, DPFs are typically driven with power supplies with much faster rise times (< 1 μs) than ZaP-HD ($\approx$ 50 μs). DPFs employ gas puff loads and generate Z-pinches, which quickly break up due to instabilities. These instabilities accelerate ion and electron beams, which enables beam target fusion to generate neutrons [23]. Unlike thermonuclear fusion, which relies on heating a plasma to such a high temperature that random particle motions are sufficiently energetic to cause fusion reactions, beam target fusion relies on the directed kinetic energy of a particle beam to overcome the electrostatic repulsion of similarly-charged ions [26]. The resulting fusion neutrons can be used to test the robustness of materials for potential use in future fusion power plants. A high energy neutron source could also aid remote nuclear weapon detection. Exposure to high energy neutrons causes fissile material to undergo fission reactions, which can be detected via the neutrons and gamma rays they produce at a distance around 10 m [27].

1.2 Motivating the flow shear stabilized Z-pinch

1.2.1 Space propulsion

A flow Z-pinch could provide a plasma thruster for interplanetary and interstellar space travel. Plasma propulsion concepts offer far greater fuel efficiency than chemical rockets because they allow greater control of exhaust velocity, c_e. Their development could open realistic opportunities for manned exploration and colonization on other planets.

A chemical rocket releases energy from fuel through combustion and turns it into a directed flow to produce thrust. Combustion releases thermal energy, which is converted to directed kinetic energy when the rocket's working fluid expands through a converging-diverging nozzle. The heat of combustion and the nozzle geometry fix c_e.

Alternatively, plamsa thrusters accelerate propellant by applying electromagnetic forces. Varying the applied power enables control over the rocket's c_e. Much higher c_e are possible
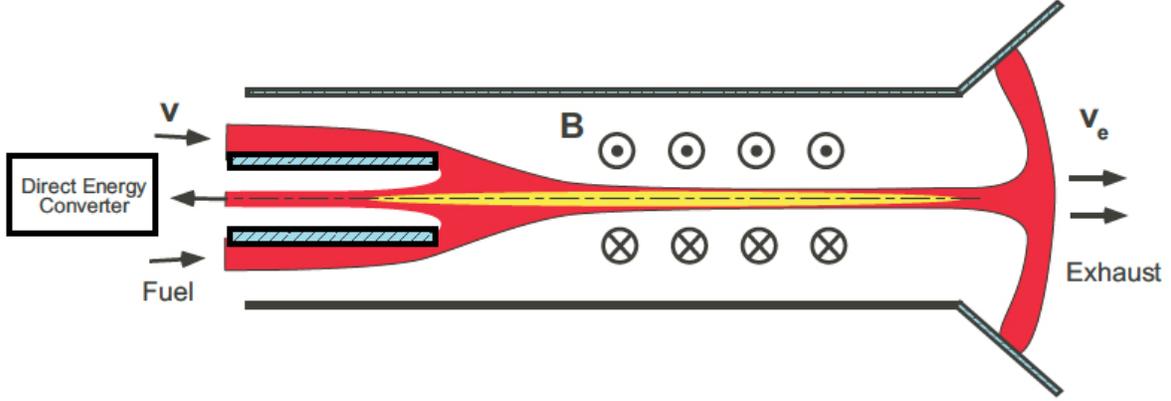
Figure 1.3: A proposed concept for a flow Z-pinch thruster with propellant exhausting to the right. Points of plasma contact with the electrodes would be distributed over large areas to minimize heat loading. Some of the fusion power could be extracted via direct energy converter to power spacecraft systems. This concept has favorable mass requirements as it requires no external field coils and could generate plasmas hot and dense enough to employ aneutronic fusion reactions [28].

with plasma propulsion because the applied power has no theoretical limit although increasing c_e requires a more massive power supply. Increasing c_e can improve fuel efficiency, but practically there exists a c_e above which further fuel savings no longer justify a larger power supply.

To understand why exhaust velocity plays a key role in rocket efficiency, consider the force balance for a rocket losing propellant mass exhausted at velocity c_e as in

$$m\frac{d\vec{v}}{dt} = \frac{dm}{dt}\vec{c}_e + \vec{F}_g, \tag{1.10}$$

where m is the rocket's mass, $\vec{v}$ is the rocket's velocity, and $\vec{F}_g$ is the force of gravity. Ignoring gravity and solving Eq. (1.10) assuming a constant c_e yields the rocket equation,

$$\frac{m_0}{m_f} = \exp\left(\frac{\Delta V}{c_e}\right). \tag{1.11}$$

Here, m_0 and m_f are the initial and final masses respectively, and $\Delta V = |v_f - v_0|$, the

difference of the final and initial velocities of a straight trajectory. More generally, ΔV quantifies the energy required to conduct a spacecraft maneuver.

For simplicity, consider a mission that starts at rest, $v_0 = 0$, and accelerates along a straight path to v_f. If c_e is constant, the fuel mass, $m_0 - m_f$, required to accelerate to higher v_f increases exponentially. Achieving long distance missions over a reasonable time period demands high v_f, which can require impractical, or even impossible, amounts of fuel.

If c_e can vary, much greater fuel efficiency is possible. Consider a spacecraft that starts at a small initial velocity, ϵ, but accelerates while incrementally increasing its exhaust velocity to match its own. Solving Eq. (1.10) with $c_e = v + \epsilon$ where v is the spacecraft's velocity yields

$$\frac{m_0}{m_f} = \left(\frac{v_f}{\epsilon} + 1 \right). \tag{1.12}$$

In this variable-c_e case, the fuel mass increases linearly with v_f, which is far more efficient than the exponential scaling of the fixed-c_e case.

The flow Z-pinch presents many features advantageous to space propulsion. Fig. 1.3 illustrates a theoretical concept, in which accelerated plasma flows out of the confinement chamber to the right where the released propellant would cool and recombine into neutral particles. The concept could operate in steady state to generate exhaust velocities in excess of 1×10^6 m/s and thrusts on the order of 1×10^5 N. Fusion reactions would provide power to sustain the plasma and run spacecraft systems.

Compared to other plasma rockets, flow Z-pinches offer significant mass savings. The plasma self stabilizes and uses its own magentic field for confinement, so it does not demand heavy external field coils. The high β confinement enables higher temperatures and densities, allowing aneutronic fusion reactions like proton-boron fusion, $p + B^{11} \longrightarrow 3\,He^4$. Generating power with aneutronic fusion means a spacecraft would not need to carry heavy neutron shielding to protect the payload.

As with terrestrial fusion reactors, the keys to developing a fusion thruster are figuring out how to sustain the plasma at high temperatures and densities.

1.2.2   Thermonuclear fusion reactor

A stable Z-pinch could be used as a fusion reactor to generate clean electricity with practically limitless Deuterium fuel extracted from sea water. Much plasma physics research focuses on attaining MCF, which utilizes magnetic fields to confine and stabilize a plasma hot enough to generate fusion reactions. Working MCF reactors could provide humanity with an extraordinarily fuel efficient source of electricity while posing no risk of catastrophic failure and generating relatively benign waste.

Fusion reactors can be highly efficient because each fusion reaction releases a tremendous amount of extractable energy. Atomic nuclei electrostatically repel each other, but they will fuse if they move close enough together that the strong nuclear force overcomes their coloumb repulsion. Light atomic nuclei heated to 10 keV or hotter have sufficient kinetic energy to overcome their repulsion, collide, and fuse. The binding energy of a resulting fused nucleus is much less than the energy in the fusing nuclei, and the energy remaining after fusing is released.

The lightest elements fuse most easily because their nuclei have the fewest protons and therefore the least electrostatic charge. Therefore, Hydrogen-based reactions are those most considered for use in reactors. The fusion reaction with its peak rate at the lowest temperature is the fusion of deuterium (D) and tritium (T), two isotopes of hydrogen. D-T fusion is expressed by the chemical formula: $D + T \longrightarrow He^4(_3 \cdot 5\,\text{MeV}) + n(_{14} \cdot 1\,\text{MeV})$. The He^4 alpha particles produced are charged and therefore confined to the plasma, so their energy can help sustain fusion conditions. The chargeless high energy neutrons escape.

In a D-T fusion reactor, energy could be extracted from the energetic neutrons colliding with a flowing liquid Pb-Li blanket surrounding the core. The neutrons would heat the Pb-Li, which could transfer that energy to a steam generator. The neutrons would also react with the Li to form more tritium. As tritium has a 12-year half life, this breeding would be key to the sustained success of a D-T reactor. Conversely, a practically limitless supply of Deuterium can be extracted from ocean water. The tritium required to start a D-T reactor

could be supplied from the world's reserves generated during H-bomb testing or from D-D fusion.

To obtain ignition (a self-sustaining reactor with net power output), a plasma of at least 10 keV must be generated at sufficient density for a sufficient time duration. We can obtain a required product of density and confinement time required for ignition through analysis by first observing the power generated, P_r, must exceed the power required to confine the plasma, P_c. The power required to maintain the equilibrium is the energy confined divided by the energy confinement time

$$P_c = \frac{\frac{3}{2}nk(T_e + T_i)}{\tau_c}.$$
(1.13)

The energy the reactor retains by confining produced alpha particles is given by

$$P_r = n_D n_T \langle \sigma v \rangle E_\alpha = \frac{1}{4} n^2 \langle \sigma v \rangle E_\alpha.$$
(1.14)

Here, the equation is reduced assuming D-T fusion with equal reactant number densities $(n_D = n_T = n)$, E_α is the energy of the alpha particle ejected by each reaction, and $\langle \sigma v \rangle$ is the reaction rate averaged over the velocity distribution.

Plugging Eq. (1.13) and Eq. (1.14) into the requirement for ignition, $P_r > P_c$, gives

$$n\tau_c > \frac{12T}{E_\alpha \langle \sigma v \rangle}$$
(1.15)

as a requirement on the plasma density and confinement time to obtain ignition. This product is commonly known as the Lawson Criterion. ZaP-HD's aim to increase the plasma density and confinement time of the shear flow stabilized Z-pinch takes the concept closer to ignition.

1.3 The ZaP Flow Z-Pinch Experiment

The ZaP Flow Z-Pinch investigates velocity shear stabilization and Z-pinch scaling. The experiment consists of a coaxial electrode gun, which ejects plasma into a cylindrical flux
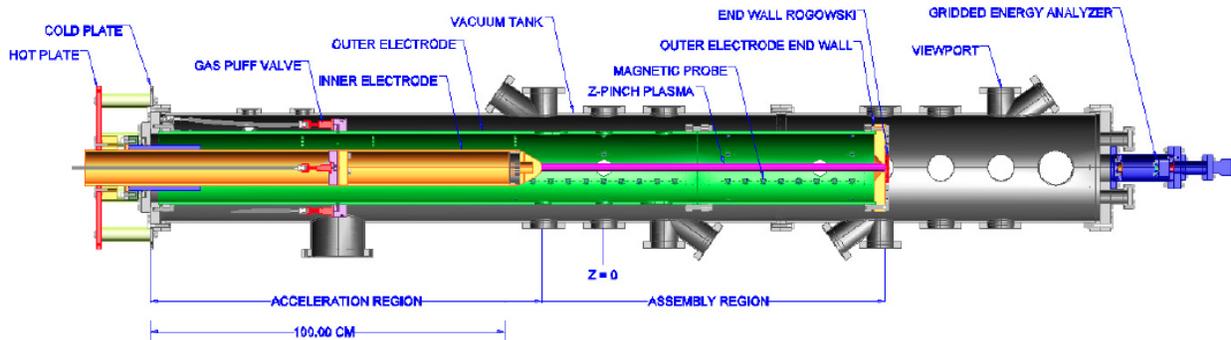
Figure 1.4: A cross-section of the ZaP experiment shows its internal design. The inner and outer electrodes are colored yellow and green respectively, the vacuum chamber is shown in gray, and the Z-pinch is in pink. The coaxial accelerator ionizes plasma and pushes it into the assembly region. The z = 0 location for ZaP's axial coordinate system is shown. The z-coordinate increases to the right in units of cm; locations left of z = 0 are negative.

conserver called the assembly region where a Z-pinch forms on machine axis. Fig. 1.4 illustrates the experiment's geometry.

Prior to each plasma pulse, a power supply charges a capacitor bank (composed by as many as 16 170 μF capacitors) to up to 10 kV, roughly 150 kJ of energy. The capacitors store this energy while neutral gas is puffed between the electrodes and given time to expand within the accelerator. Then, ignitron switches apply the capacitors' potential to the electrodes, which breaks down the neutral gas into a conducting plasma. The capacitors discharge, and currents flowing in the plasma and through the electrode walls induce magnetic fields, which push the plasma from the accelerator to the assembly region where the plasma convenes on axis into a Z-pinch.

1.3.1 Shear flow stabilization of ZaP

ZaP sustains Z-pinches for several flow through times and thousands of instability growth times with flow shear stabilization [29]. The extended period of plasma stability, called the quiescent period, is identified by examining data from arrays of azimuthally spaced magnetic field probes. The Fourier decomposition of these data detailed in Sec. 2.1.3 allows estimation

of the plasma current centroid in the plane of a probe array. ZaP identifies a quiescent period as when the current centroid is steadily centered within 1 cm of machine axis at z = 0 [30].

Strong correlation exists between the quiescent period and the presence of velocity shear. Radial profiles of plasma velocity are measured by observing Doppler shifts of impurity line radiation. ZaP measures such shifts with a 0.5 m spectrometer with an attached intensified charge-coupled device (ICCD), which records one 100 ns exposure per plasma pulse and is discussed in more detail in Sec. 2.1.4. A bundle of 20 fibers views the z = 0 location at an oblique angle to observe axial velocity. Imaging optics allow the 20 chords to view roughly 24 mm across the plasma with spatial resolution of 1.2 mm. If repeatable Z-pinches are generated, the time evolution of the velocity profiles can be obtained by varying the timing of ICCD. Fig. 1.5 shows such an evolution as a contour plot in space and normalized time. The time normalization is applied such that $\tau = 0$ and $\tau = 1$ correspond to the start and end of the quiescent period respectively; this normalization makes for a better comparison between similar plasma pulses with small differences in quiescent period. A sheared flow profile exists throughout the quiescent period except for a shear reversal that occurs roughly halfway through. Oftentimes fluctuations in the current centroid are measured at the time of the shear reversal as the plasma's flow profile is briefly uniform [29].

The end of the quiescent period correlates with depletion of density in the accelerator [31] [32]. When the accelerator runs out of neutral gas, it no longer has fuel to sustain the Z-pinch's shear with a flow of newly ionized plasma. A large fraction of the neutral gas puff can be ionized and accelerated early on during a pulse leaving less in the accelerator to supply sustained shear later. Increasing the total amount of injected neutral gas lengthens quiescent periods to some degree by giving the machine more fuel, but it does not prevent excessive early fuel consumption [31]. An insulator installed between the inner and outer electrodes extends from the farthest upstream point in the machine (z = -120 cm) to z = -70 cm, 5 cm downstream from the gas injection plane. This modification prevents the initial ionization front from moving upstream in the accelerator, which limits the neutral gas it ionizes and accelerates before Z-pinch formation. Operating with the insulator extension
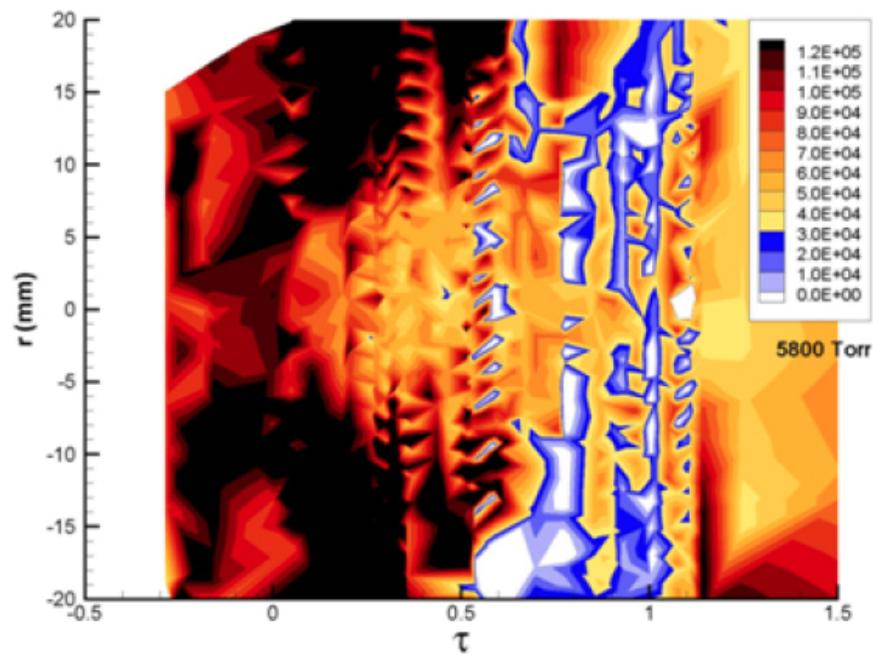
Figure 1.5: The contour plot of axial plasma velocity in space and normalized quiescent time shows the presence of sheared flow for the duration of the quiescent period. The shear typically reverses halfway though the quiescent period probably due to flow stagnation at the outer electrode endwall [29].

z = -75   z = -25   z = 0   z = 25   z = 109

(a) 10 cm inner electrode

Perforated
extension

(b) 16 cm inner electrode
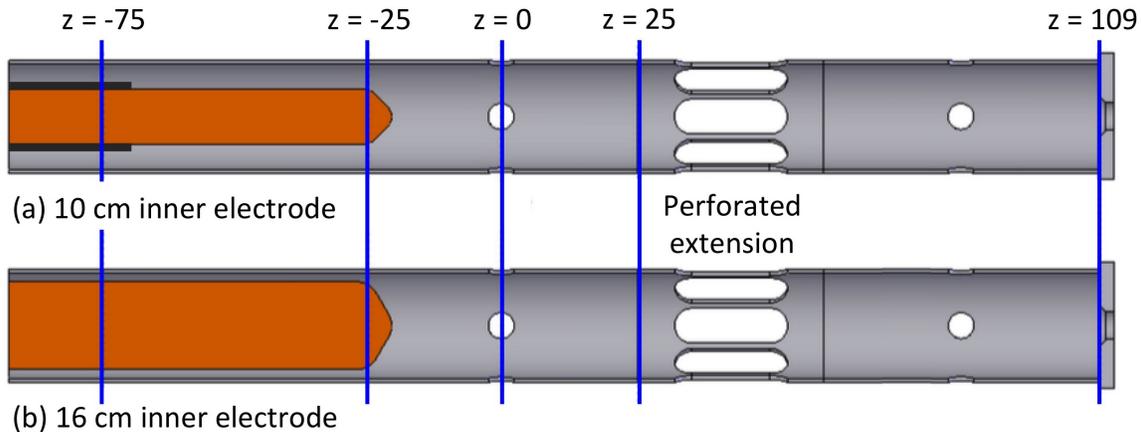
Figure 1.6: The 10 cm and 16 cm inner electrode configurations of the ZaP experiment are shown along with the outer electrode with the perforated section installed. Axial locations are referenced in units of cm. Gas injection from outer and inner vales occurs at z = -75 cm. The insulator extension shown in black extends downstream from these valves by 5 cm.

prevented premature gas depletion leading to longer quiescent times, which were only limited by the duration of the current pulse supplied by the capacitors [33].

To isolate the flow shear stabilization mechanism from the potentially stabilizing effect of a conducting wall, the outer electrode was extended with a perforated section. Illustrated in Fig. 1.6, roughly 70 percent of the perforated section is removed to prevent stabilizing azimuthal current flow. Plasma pulses with and without the performated section with otherwise identical settings exhibit similar quiescent times, and data from optical images and interferometry corroborate pinch stability through the perforated section [1]. These observations agree with theoretical predictions that the outer electrode is too far away from the plasma to provide stabilization [5].

1.3.2 Investigating Z-Pinch scaling on ZaP

Changing the diameter of ZaP's inner electrode allows for investigation of Z-pinch scaling with modified linear density for constant plasma current. Consider a model for Z-pinch formation as the compression of an annular plasma (contained in the geometry of the ac-

celerator) to a cylindrical pinch. Assume that the length of the annular plasma and the pinch are equal. For a given plasma current and accelerator conditions ($n = n_i = n_e$ and $T = T_i = T_e$ in the accelerator), a larger diameter inner electrode decreases the linear density by reducing the total amount of gas required to match accelerator conditions. If the plasma compresses adiabatically, reduced linear density should increase pinch density and temperature while shrinking its radius as in Eqs. (1.7 - 1.9).

Comparing Z-pinches generated with 10 cm and 16 cm diameter inner electrodes exposes difficulties in reducing linear density and suggests the presence of non-adiabatic processes. For given accelerator conditions and plasma current, the 16 cm electrode should compress the plasma to three times the density and twice the temperature as the pinches generated by the 10 cm electrode. In reality, the 16 cm electrode produces plasmas larger, colder, and less dense than those of the 10 cm electrode. Non-adiabatic effects like shock heating, ohmic heating, and radiation explain some of the disagreement with the anticipated scaling. The major culprit in the poor compression of the 16 cm configuration is that a repeatable run condition cannot be established at low enough gas injection pressure to match the accelerator conditions of the 10 cm electrode configuration [32].

Chapter 2

THE ZAP-HD FLOW Z-PINCH EXPERIMENT

ZaP-HD provides a more versatile platform to study Z-pinch scaling than ZaP because it allows more effective, independent control over linear density and plasma current. Shown in Fig. 2.1, the experiment utilizes three co-axial electrodes to form shear flow stabilized Z-pinches.

ZaP-HD's operation consists of two main processes: plasma acceleration and compression. Separate control over the two processes is exerted by two capacitor bank power supplies connected to the three electrodes. The acceleration bank (680 μF connected as a pulse forming network (PFN) with 90 μs half period) drives current between the inner and middle electrodes. Neutral hydrogen is puffed between the electrodes before high voltage is applied across the gap to ionize the gas. The Lorentz force induced by the resulting currents pushes the plasma downstream to the assembly region. Once the plasma enters the assembly region, the compression bank (680 μF connected as a PFN with 90 μs half period) drives current between the outer and inner electrodes, which compresses the plasma on axis as its momentum carries it down the length of the machine. After the pinch compresses, a steady stream of flow from the accelerator provides the shear necessary for plasma stability.

Decoupling plasma acceleration and compression such that each process is primarily controlled by an independent power supply allows for effective temperature and density scaling. The current flow in the accelerator dictates the linear density, N, in the assembled pinch, while the current flow in the assembly region is the plasma current, I, in scaling Eqs. (1.7 - 1.9). ZaP-HD aims to scale up density and temperature by minimizing linear density and maximizing plasma current.
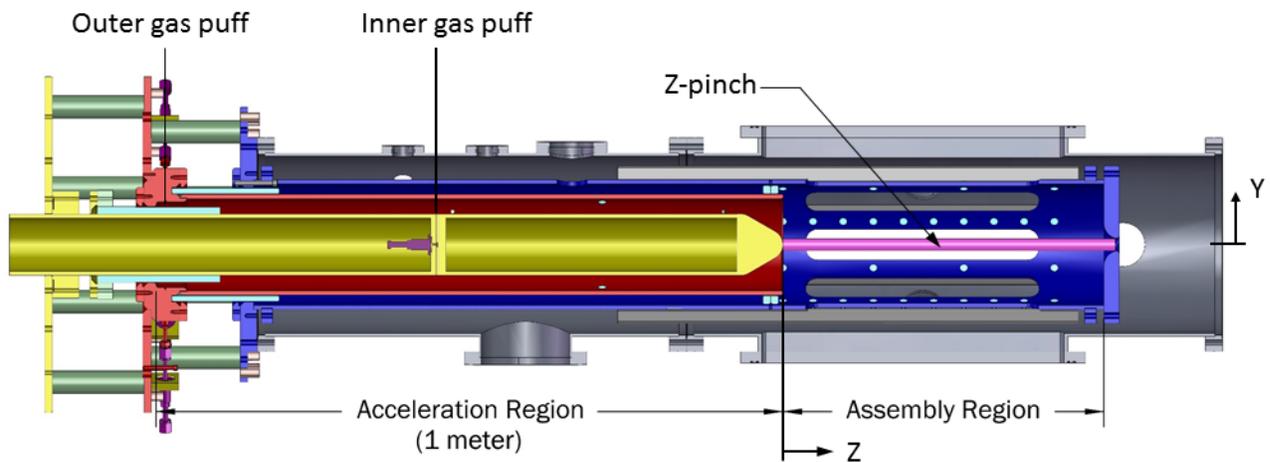
Figure 2.1: A cross section of the ZaP-HD experiment reveals its triaxial electrode design. A coaxial accelerator ionizes and accelerates plasma into the assembly region where the plasma is compressed on axis as a Z-pinch. The inner, middle, and outer electrodes are colored yellow, red, and blue respectively. The vacuum chamber is shown in gray, and the Z-pinch is in pink. The ZaP-HD coordinate system is also shown; unlike in ZaP, $z = 0$ is located at the inner electrode nosecone. Neutral gas injection into the accelerator between the middle and inner electrodes occurs at the two labeled axial locations. The inner gas injection puffs from a single valve through a manifold with eight outlets spaced evenly on the circumference of the inner electrode. The outer gas injection puffs inward from the exterior of the middle electrode through eight valves at the farthest upstream location in the accelerator.

2.1 Diagnostics

A versatile suite of instruments diagnoses the ZaP-HD Z-pinch. Augmenting standard current and voltage measurements, magnetic field probes embedded in the outer and middle electrodes measure the field topology in space and time. Axially-spaced probes measure the radial current distribution in the machine, while azimuthally-spaced probes allow for determination of pinch position based on its current centroid.

Four large rectangular windows and matching cutouts in the outer electrode provide extensive viewing access in the assembly region for optical diagnostics. Passive spectroscopy looks for Doppler broadening and Doppler shifts to measure spatially-resolved ion temperature and plasma velocity profiles respectively. High speed optical camera imaging reveals insights about the Z-pinch's structure and dynamics. A heterodyne quadrature interferometer measures time-resolved electron density at movable discrete locations within the assembly region, and digital holographic interferometry (DHI) measures line-integrated electron density with fine spatial resolution at one time instant at movable locations in the assembly region The DHI's resolution allows for Abel inversion of line-integrated density to obtain number density.

2.1.1 Current Measurements

Rogowski coils provide measurements of the total plasma current, I_P, and the compression current, I_C. These coils are positioned as shown in Fig. 2.2 and each measures the net current passing through the area enclosed by each coil. The acceleration current, I_A, can be computed by subtracting the compression current from the total plasma current,

$$I_A = I_P - I_C. \tag{2.1}$$

Fig. 2.7 (a) shows I_A and I_C traces for a typical plasma pulse.

Rogowski coils operate based on Faraday's law. A current passing through the area

enclosed by a Rogowski coil generates a magnetic field, which penetrates the poloidal loops wrapped around the coil's toroidal core. This changing magnetic flux, Φ, induces a voltage at the Rogowski coil terminals

$$V_{rogo} = -\frac{d\Phi}{dt} = -\mu_0 n A \frac{dI}{dt},$$ (2.2)

which can be integrated to give the current, I, passing through the area enclosed by the coil. For proper operation, the turn density and cross-sectional area must remain constant along the length of the coil, and the coil ends must be carefully matched to make a closed loop.

ZaP-HD's Rogowski coils are constructed by stripping the outer black insulator off of co-axial cable and winding 32 gauge, enamel-coated copper wire around the exposed white insulator. The 32 gauge wire is soldered to the inner conductor of the co-axial cable at one end and to the outer braid at the other end. A BNC plug is attached to the co-axial cable to allow for easy digitization.

2.1.2   Voltage Measurements

Voltages between the ZaP-HD electrodes are measured by observing the currents through high power non-inductive carborundum resistors connected between each pair of electrodes. The resistances (≈ 500 Ω) are selected to divert a small fraction (< 1 percent) of the power supply current from the plasma while still providing a large enough signal for the Pearson current probes to obtain ample current signals. Knowing the resistances and the current passing through the resistors is sufficient to determine the electrode voltage with Ohm's law, $V = IR$.

ZaP-HD employs two voltage measurements: one between the inner and middle electrodes gives the acceleration voltage, V_A, and the other between the inner and outer electrodes gives the compression voltage, V_C. A circuit diagram of the voltage measurements is shown in Fig. 2.2. V_C effectively is the voltage of the inner electrode. The middle electrode voltage
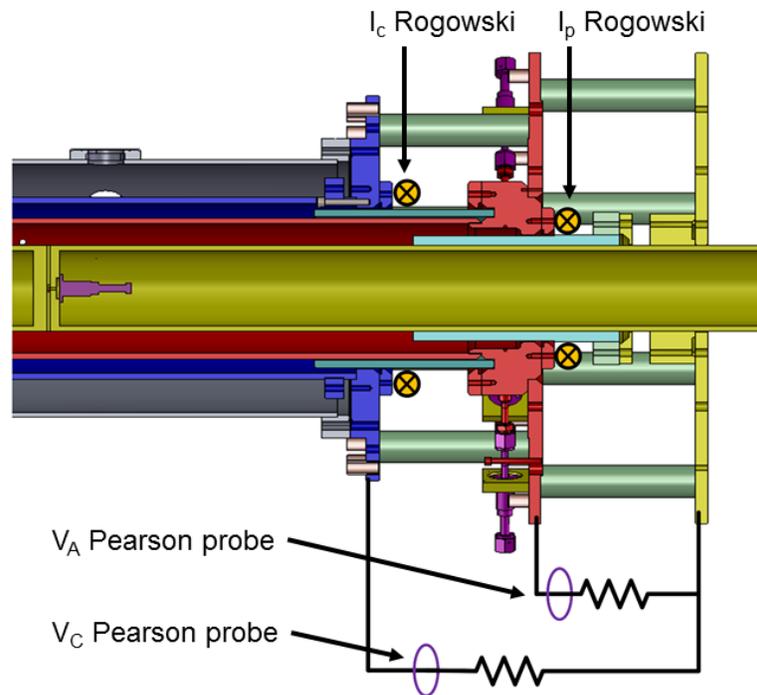
Figure 2.2: A view of the upstream portion of the ZaP-HD electrodes shows the location of the experiment's current and voltage measurements. The orange dots with black crosses indicate the positions of the I_c and I_p Rogowski coils, and the circuit diagram at the bottom illustrates the design of the voltage measurement, which uses Pearson probes to measure the current across high power, non-inductive resistors.

can be computed by subtracting the acceleration voltage from the compression voltage,

$$V_M = V_C - V_A. \tag{2.3}$$

The measurements of V_M and V_C are referenced to the potential of the outer electrode cold plate, which can conceivably float relative to the data acquisition ground during a pulse. Fig. 2.7 (b) shows V_M, V_A, and V_C for a typical plasma pulse.

2.1.3 Magnetic Probes

ZaP-HD's magnetic field probe array provides extensive insight into its plasma dynamics and stability. As shown in Fig. 2.3, probes are embedded in the outer and middle electrodes at many axial and azimuthal locations. All probes measure the azimuthal component of the magnetic field. The assembly probes are digitized at 40 MHz by Joerger TR1612 12-bit digitizers, and the accelerator probes are digitized at 20 MHz by 8-bit T2008 digitizers. The time resolution of this digitization paired with the spatial resolution and large number of probes makes the array a powerful diagnostic tool. Four eight-probe azimuthal arrays (with 45 degrees spacing between probes) and six four-probe azimuthal arrays (with 90 degrees spacing between probes) exist in the assembly region. One eight-probe azimuthal array and one fifteen-probe linear array exist in the accelerator. In total, the assembly region has 56 probes and the accelerator has 22.

The probes convert changing magnetic flux to a voltage, V_ϕ, as in Faraday's Law,

$$V_\phi = -\frac{d\Phi}{dt} = -nA\frac{dB}{dt}, \tag{2.4}$$

where n is the number of windings of area A. This voltage is integrated by active analog integrating circuits to provide a signal proportional to B, which is then digitized. The same 32 gauge wire used for ZaP-HD's Rogowskii coils is wound 10 times around in a machined groove in a Kel-F plastic form. The form and coil are glued with Torr-Seal into machined
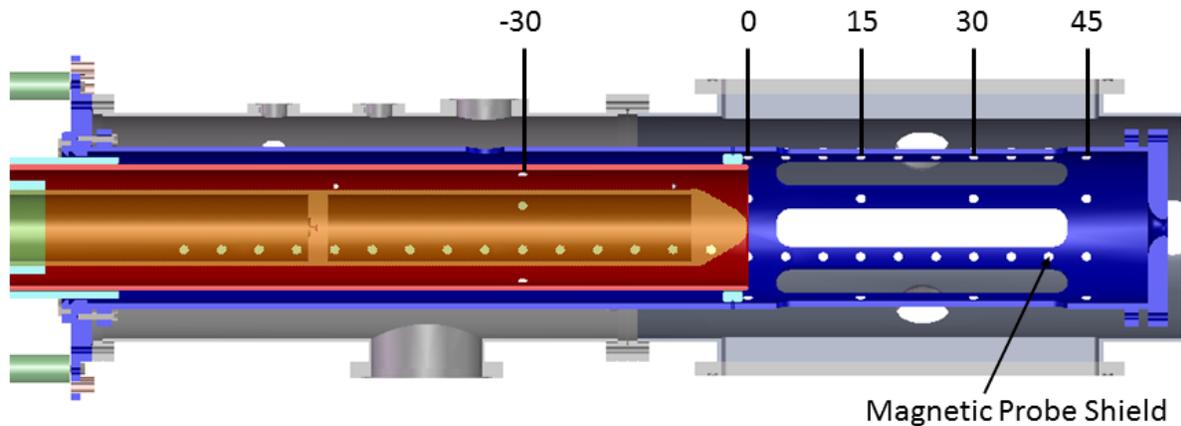
Figure 2.3: A cross-section of the ZaP-HD experiment with transparent inner electrode shows the magnetic probe locations. The white circles visible on the outer and middle electrodes are machined boron nitride probe shields, in which copper windings around a Kel-F form are protected from plasma contact. The labels indicate the locations of the eight-probe azimuthal arrays in units of cm from the end of the accelerator.

boron nitride shields. The shields insert into holes in the electrodes and are secured in place with silver-plated, vented bolts. These shields protect the windings from plasma contact, and they also allow magnetic flux to penetrate to the windings because the material is electrically non-conductive.

The metal surrounding probes, however, is conductive, and it affects the field measurement because image currents in the metal oppose magnetic field from pushing into the probe windings. Proper calibration enables compensation of the image currents. Calibration is performed by installing, in place of the inner electrode, a copper rod, which connects to the outer electrode endwall and the inner electrode hot plate. A pulsed power supply drives a known current through the outer electrode and the copper rod, which enables computation of a calibration coefficient for each probe. This calibration method works for the assembly probes, but it provides an incomplete calibration for the accelerator probes. The calibration of the assembly probes is accurate because the set up directs currents through the paths expected during an actual plasma pulse as shown in Fig. 2.4 (b). The set up provides an incomplete calibration for the accelerator probes because it does not account for the current
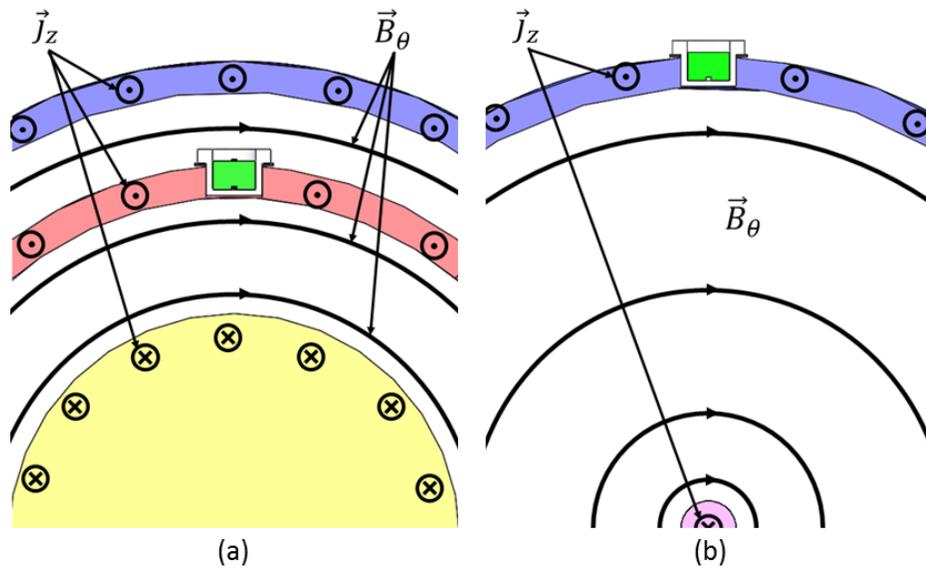
Figure 2.4: Axial cross-sections show the magnetic fields near wall-embedded magnetic field probes for (a) an accelerator probe and (b) an assembly region probe. The inner, middle, and outer electrodes are shown in yellow, red, and blue respectively in (a). In (b), the outer electrode is blue and the Z-pinch plasma is pink. Directions of current flow are shown by vectors into and out of the page, and magnetic field lines are also drawn. Boron nitride probe shields are shown in white, and Kel-F plastic forms are green.

flow in the middle electrode shown in Fig. 2.4 (a), which would be expected during a plasma pulse. In the future, new calibration hardware will be constructed to drive known currents through the middle electrode and a central copper rod to obtain a second calibration coefficient for each accelerator probe. Using coefficients from the original and new calibrations will allow accurate computation of the field measured at the middle electrode wall.

Because the accelerator probe calibration is incomplete, this disseration shows accelerator probe data in arbitrary units. The accelerator's linear array still reveals much about the current distribution in that region, which is useful in understanding how the initial plasma formation and rundown operate and how the gun continues to fuel the assembly region later in time. Because no current connection exists between the outer and middle electrodes upstream of $z = 0$ cm, using the incomplete calibration gives an accurate measure of the relative magnitudes of fields in the accelerator. Fig. 2.8 (b) shows data from the accelerator linear array during a typical plasma pulse. As the initial current front flows downstream, the probe signals rise one by one. Determining the time differences between the signals' initial rises allows for computation of the speed of the front. The radial component of Ampere's law in cylindrical coordinates,

$$\mu_0 j_r = -\frac{\partial B_\theta}{\partial z}, \tag{2.5}$$

states that axial gradients in the magnetic field necessarily coincide with radial current flow. Therefore, the relatively uniform field gradient during the quiescent period in Fig. 2.8 (b) indicates an axially uniform radial current. The presence of radial current in the accelerator is a positive sign that plasma is being accelerated by the Lorentz force downstream to sustain stabilizing flow shear in the assembly region.

The assembly probes provide important information about the Z-pinch's stability and structure. The axial current and current centroid position in the plane of each azimuthal array can be determined by computing Fourier modes of the raw azimuthal field data. Current centroids provide an objective determination of the Z-pinch's stability: at a given axial location, a quiescent period of plasma stability can be defined as the time when the centroid

resides within some threshold distance from the machine's axis. A stable Z-pinch of long length will have quiescent times along its length that overlap in time.

Determination of the current centroid relies on a Fourier decomposition of azimuthal magnetic probe data, which is written in discrete form as

$$B_\theta(\theta_i) = \sum_{j=0,m} a_j \cos(j\theta_i) + \sum_{j=1,m} b_j \sin(j\theta_i). \tag{2.6}$$

For a single axial location, this equation expresses the discrete Fourier series as a function of θ_i, the azimuthal position of each probe.

Solving for the coefficients, a_j and b_j, in the Fourier series allows the determination of azimuthal mode amplitudes, m_j, and phase, ϕ_i, as in

$$m_j = \sqrt{a_j^2 + b_j^2} \tag{2.7}$$

$$\phi_j = \tan^{-1}\left(\frac{b_j}{a_j}\right). \tag{2.8}$$

This can be done by posing the series expansion as a linear algebra problem. The measured fields and unknown coefficients are written as vectors, while the sine and cosine terms are arranged as a matrix. Taking a pseudo-inverse of the matrix solves for the coefficients a_j and b_j [30].

Each mode amplitude, m_j, indicates the contribution of a different modal shape to the total current distribution. For instance, as the zeroth-order mode of the Fourier series, m_0, is the mean magnetic field, which is proportional to the mean current. Like with the accelerator probes, observing axial gradients in the mean fields in the assembly region as in Fig. 2.8 (a) reveals where and when radial and axial currents exist in the Z-pinch.

The m_1 amplitude relates to the radial displacement of current from the geometric center

of the probe array. The radial displacement can be written as

$$\Delta r = \frac{1}{2}\frac{m_1}{m_0}r_{wall} \tag{2.9}$$

by assuming axially uniform current perturbations and $\Delta r/r_{wall} < 0.5$ [30]. A value of normalize mode data, m_1/m_0, below 0.2 means the current is displaced within a centimeter of the geometric center. On ZaP, if $m_1/m_0 < 0.2$ for an extended time while the $m_0 > 0$, the plasma was defined to be stable. The duration the stability lasts is called a quiescent period. Note that the condition for $m_0 > 0$ ensures axial current is actually flowing to provide plasma confinement during the quiescent period. Fig. 2.9 shows m_1/m_0 data for a typical ZaP-HD pulse. At high bank charge voltages on ZaP-HD, the m_1/m_0 takes higher values than ZaP during the quiescent period, but as described more in Sec. 2.2, the plasma moves gradually as a coherent, stable structure during this time. Note that obtaining the radial displacement Δr and phase ϕ_1 allows computation of the current centroid location in the x and y coordinates of the plane of the azimuthal probe array.

2.1.4 Spectroscopy

ZaP-HD employs two spectrometers. The ICCD Czerny-Turner spectrometer, a 0.5 m Acton Research SpectraPro 500i with intensified CCD (ICCD) Roper Scientific PI-MAX camera, allows for impurity identification and measures ion temperature and bulk velocity profiles. The CCD spectrometer, a 0.5 m Jarrell Ash model 82-020 spectrometer with Santa Barbara Research Group ST-6 CCD camera, pairs with a photo-multiplier tube (PMT) to give time-resolved intensity of a single selectable spectral line.

The ICCD's measurements rely on the Doppler effect, which dictates how the wavelength of an observed wave changes as a function of the relative velocity between an observer and the wave source. Waves moving toward an observer appear to shift to shorter wavelengths, while those moving away shift to longer wavelengths. The Doppler shift is commonly discussed in astronomy: light is a wave phenomenon, so stars moving towards Earth appear blue-shifted

and stars moving away appear red-shifted.

The ICCD spectrometer views the plasma through oblique and transverse telescopes, which mount to a rail system on the rectangular viewports for easy movement of the axial measurement locations. The telescopes use telecentric irises to image 20 parallel lines of sight in the plasma onto 20 fibers, which convey the light to the spectrometer [34]. The 20 chords view roughly 24 mm across the plasma with spatial resolution of 1.2 mm. The ICCD has adjustable gain and gate (to a duration as short as 200 ns) and records one spectrum per plasma pulse. Oriented at a 45 degree angle relative to the ZaP-HD centerline, the oblique telescope observes blue shifts in impurity line radiation to detect bulk plasma velocity profiles. Velocity measurements usually observe the C III line at 229.687 nm because its brightness eases the identification of the Doppler shift. The transverse telescope observes Doppler broadening of line radiation to detect ion temperature. The ions in a plasma in thermodynamic equilibrium follow a Maxwellian distribution in velocity space, which leads to a broadening in the observed impurity line radiation. In an average sense, particles move towards and away from the telescope in equal quantities and at equal speeds, so the integrated Doppler shift of the entire population appears as a broadening of line radiation. The width of the ion's Maxwellian distribution and therefore the magnitude of Doppler broadening depend on the ion temperature. Various lines are observed to determine temperature because different impurities are present in different temperature ranges; for ZaP-HD's usual operating conditions, the O V triplet at 278.101 nm, 278.699 nm, and 278.985 nm is most often used.

The CCD spectrometer employs a CCD and a PMT to resolve the time-evolution of impurity lines. The input to the CCD spectrometer comes from a single fiber viewing the plasma. The dispersed light from the spectrometer's diffraction grating passes through a beam splitter, which sends half the light to a CCD sensor and half to a PMT. The CCD collects a single time-integrated spectrum for each plasma pulse. The diffraction grating in the spectrometer can be tilted to change the wavelength of the spectrum recorded by the CCD. A certain pixel on the CCD corresponds to alignment with the PMT. The PMT converts incident photons to an electric signal, which can be digitized, so matching an impurity line

to the proper CCD pixel allows for measurement of the time-evolution of that impurity line.

2.1.5 High-speed optical imaging

A high-speed Kirana-05M camera provides optical images with great spatio-temporal resolution. The camera employs a 10 bit monochrome sensor of 924 x 768 pixels with 30 μm pixel size. Its frame rate is adjustable between 1,000 and 5,000,000 frames per second, and it stores 180 frames even at the fastest rates. The camera views light in the visible spectrum. Fig. 2.5 shows images from the camera immediately before, during, and after the quiescent period of plasma pulse 160310013. Taken from the positive x side of the experiment, these images show from 5 cm to 20 cm in the assembly region. A stable plasma exists in this region during a quiescent period from 38 μs to 46 μs.

Due to the plasma's high energy, much of its light emission is UV. Even so, useful insight can be obtained from the visible light emission. Much of the visible light emitted by hydrogen plasmas is Hα line radiation at 656.28 nm. Bound electrons falling between specific energy states emit this light (for more about the quantum theory of light, see Sec. A.1). Operating the camera without a filter allows viewing of Hα and other line radiation from impurities. Observation of Hα radiation is an indication of neutral hydrogen because bound electrons emit at this wavelength. Alternatively, free electrons unbound from any nucleus emit broadband light called bremsstrahlung (German for "braking radiation"). Free electrons pushed by local electric fields emit photons to conserve energy. Using a band pass filter, which cuts out line radiation such as Hα, allows observation of bremsstrahlung. ZaP-HD employs Wratten #18 and #12 filters together as a bandpass filter in the 500-600 nm range [35]. Generally, the presence of bremsstrahlung correlates to hotter, well-ionized plasma, while Hα appears at cooler regions. The images in Fig. 2.5 were taken with the bremsstrahlung bandpass filter in place.
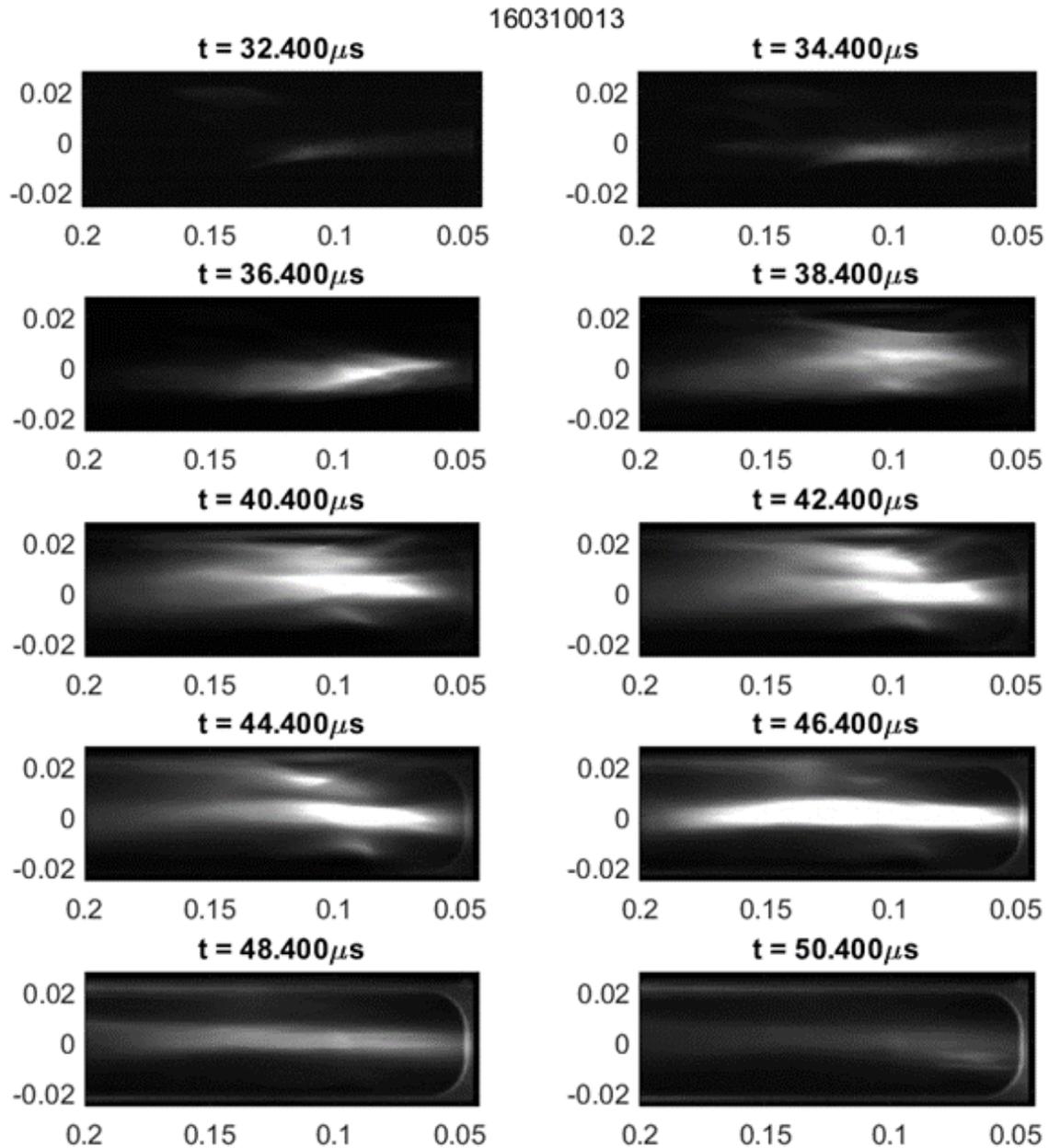
Figure 2.5: Images taken 2 μs apart with the bremsstrahlung bandpass filter installed on the camera lens show a shear flow stabilized Z-pinch between 5 and 20 cm throughout this pulse's quiescent period from 36 μs to 48 μs. The axes are labeled in units of meters relative to the coordinate system of Fig. 2.1.

2.1.6 Heterodyne Quadrature Interferometery

Interferometry measures line-integrated electron density by passing a laser beam through plasma and observing the phase shift imparted on the beam. Such measurements involve splitting a single laser into scene and reference beams, passing the scene beam through the plasma, and recombining the beams onto single sensor as in Figs. 2.6 and 3.1.

Because light's phase velocity in plasma is faster than in air, the scene beam's phase angle leads that of the reference beam at the sensor. The interference of the beams at the sensor captures the phase shift of the scene beam, ϕ_{n_e}, which is related to line-integrated electron density by

$$\phi_{n_e} = -\frac{e^2}{4\pi c^2 m_e \epsilon_o} \lambda N_e, \tag{2.10}$$

where the line-integrated density, N_e is given as the integral

$$N_e = \int n_e \mathrm{d}l, \tag{2.11}$$

along the laser's path, e is the electron charge, c is the speed of light, m_e is the electron mass, λ is the laser wavelength, and ϵ_0 is the permittivity of free space.

Heterodyne quadrature interferometery measures time-resolved line-integrated density at discrete spatial locations. ZaP-HD's heterodyne quadrature interferometer employs a 10 mW continuous wave (CW) Helium-Neon (HeNe) laser with wavelength $\lambda = 633$ nm. The system applies heterodyning in the sense it interferes visible light beams (frequency ≈ 100 THz) of slightly different frequencies to create a much lower frequency light amplitude beat (40 Mhz), which can be resolved by a photodiode. This gives the system its time resolution. The phase shift between the beams is measured as phase modulations to the resulting 40 MHz light intensity beat. In practice, an acousto-optic modulator (AOM, or Bragg Cell) splits the laser into two beams while shifting the reference beam to 40 MHz higher frequency than the scene beam. Recombining the two beams of differing frequencies on a photodiode creates to a detectable beat frequency of 40 MHz in the light amplitude. The heterodyne quadrature
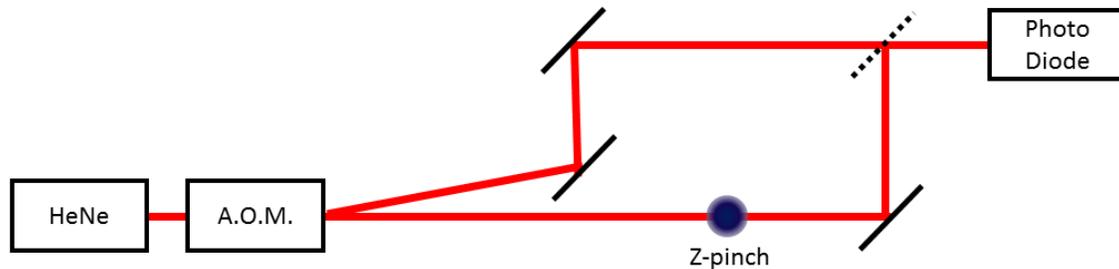
Figure 2.6: The heterodyne quadrature interferometer splits a laser beam into two beams of similar intensity with the reference beam shifted 40 MHz higher in frequency. The scene beam passes through the plasma while the reference beam bypasses the experiment. The beams are recombined with a beamsplitter and directed to a photodiode. Co-linear alignment of the beams after the beamsplitter generates spatially uniform illumination on the photodiode. The phase shift between the beams is measured as phase modulations to the resulting 40 MHz light intensity beat measured by the photodiode.

interferometer relies on co-linear alignment of the recombined beams to generate a spot of illumination with more or less uniform intensity across the photodiode.

The system employs quadrature with analog circuitry and low-pass filtering to obtain voltage signals proportional to $\sin(\phi_{n_e})$ and $\cos(\phi_{n_e})$, which are digitized by Joerger TR 3412 12-bit digitizers at 25 MHz. By identifying both the sine and cosine, applying quadrature allows for unambiguous determination of the phase shift ϕ_{n_e}, which is ambiguous if only sine or cosine is known.

The heterodyne quadrature interferometer works well when ZaP-HD operates at low compression bank voltages, but increasing the compression bank voltage beyond 7 kV leads to massive disturbances to the line-integrated density signals. This limits the utility of the data to identifying the time of plasma arrival and observing the density evolution before the compression bank trigger. The cause of these disturbances has been traced to plasma phenomena. An interferometry chord directed over the experiment so that both the scene and reference beams bypass the plasma does not encounter disturbances even at high compression bank voltages. This suggests the erroneous signal behavior does not result from

electrostatic noise pickup from discharging the compression bank. The disturbances in each chord directed through the plasma correlate with a loss of signal from the photodiode similar to that when the chord's scene beam is blocked. This suggests that something in the plasma either prevents the scene beams from reaching the photodiode or disturbs the co-linear alignment of the scene and reference beams incident on the photodiode. Plasma density gradients caused by the compression bank discharge could cause refraction to redirect the scene beams enough to disturb their signals. Because of such disturbances in the heterodyne quadrature interferometer data during the ZaP-HD quiescent period, limited comparisons can be drawn between these measurements and those of DHI.

2.2   Chronology of a ZaP-HD plasma pulse

This section explains the events in a plasma pulse representative of the behaviors observed in great generality on ZaP-HD. This exhibition aims to simultaneously familiarize the reader with ZaP-HD's performance and illustrate the experiment's diagnostics. The pulse considered is a pure Hydrogen discharge conducted with acceleration and compression bank charges of 9 kV and 8 kV respectively. Respectively, the inner and outer gas injection puffs trigger at 1.6 ms and 1.5 ms prior to the accelerator bank discharge, and the inner and outer gas feed pressures are 5500 Torr and 3500 Torr. These settings generate plasma pulses with consistent quiescent periods visible in high speed camera images and that provide sufficiently dense, centered line-integrated density distributions for successful DHI measurement and analysis.

The pulse begins with the acceleration bank discharge, which ionizes the plasma, drives acceleration current, and accelerates plasma downstream. The acceleration bank discharge coincides with the initial I_A rise in Fig. 2.7 (a) as well as the discrete steps in V_A and V_M in Fig. 2.7 (b). Next, the accelerator magnetic probe signals rise one after another in Fig. 2.8 (b) as the initial plasma front moves downstream. The time delay between the initial rise of I_A and of the accelerator probe signals indicates the initial plasma breakdown takes place upstream of the linear probe array. The successive rises of the accelerator probes indicate the plasma reaches the end of the accelerator around $t = 20$ μs when the conductive plasma
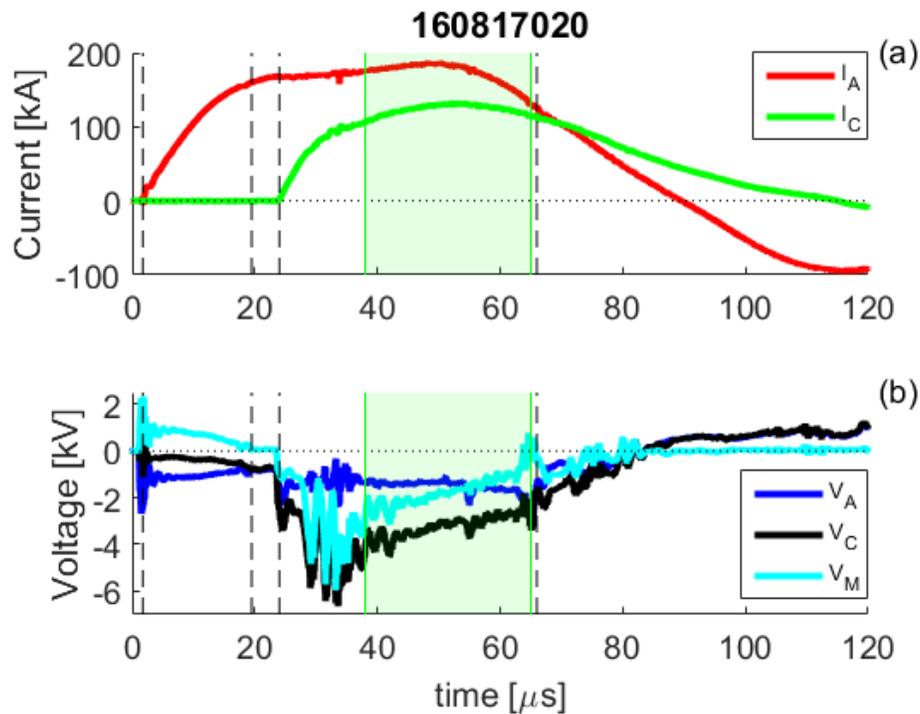
Figure 2.7: In a typical ZaP-HD plasma pulse, (a) the acceleration current, I_A, begins rising when the acceleration bank discharges, and the compression current, I_C, rises when the compression bank discharges. (b) The accelerator voltage, V_A, and middle electrode voltage, V_M, step when the acceleration bank discharge applies voltage. V_M goes to zero when conductive plasma exits the accelerator and grounds the middle electrode to the outer electrode. The compression voltage, V_C, as well as V_M and V_A all step when the compression bank discharges. Plasma dynamics during Z-pinch formation cause voltage spikes after the compression bank discharge, and once the Z-pinch forms on axis, V_A stabilizes to a constant value during a quiescent period denoted by the shaded green region. The quiescent period concludes with voltage spikes, after which V_M usually proceeds to zero while V_A approaches V_C. The first, second, third, and fourth dashed vertical lines correspond to the acceleration bank discharge, plasma exiting the accelerator, the compression bank discharge, and the high peak in the assembly magnetic field respectively.
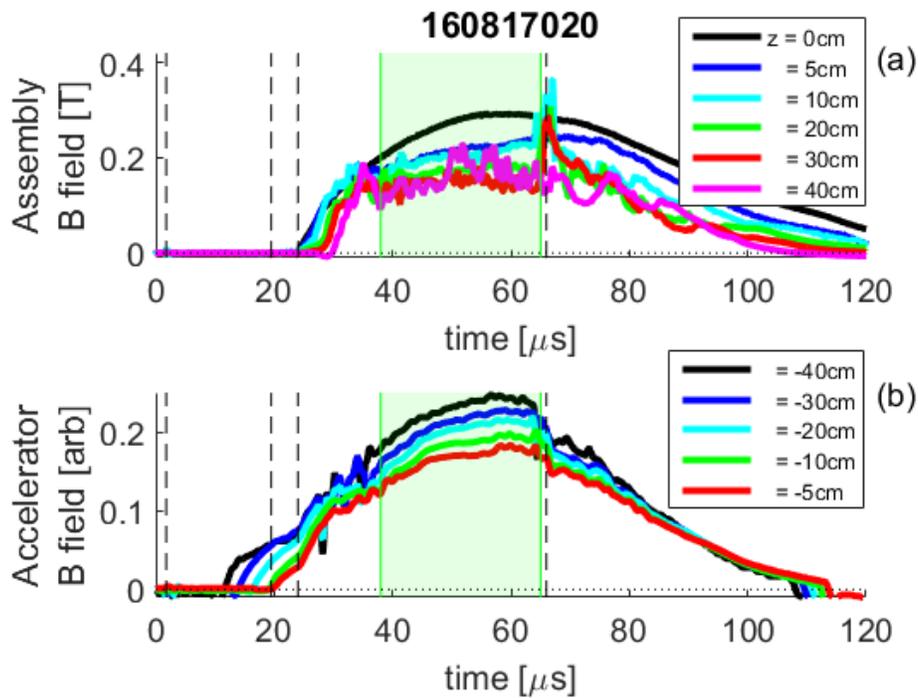
Figure 2.8: In a typical ZaP-HD plasma pulse, (a) the average magnetic fields from assembly azimuthal probe arrays rise one after another starting with the $z = 0$ array at the time of the compression bank discharge. During the quiescent period denoted by shaded green, the radial current distribution in the assembly region remains more or less constant in time. Radial currents exist between $z = 0$ cm and 20 cm, although current further downstream is more purely axial. (b) The relative magnitudes of the magnetic fields in the accelerator linear probe array initially rise one after another as the initial plasma front moves down the gun. The time this plasma front exits the accelerator matches the time V_M goes to zero in Fig. 2.7. During the quiescent period, radial current exists in the accelerator, while an abrupt decrease in the radial current marks the end of the quiescent period. The first, second, third, and fourth dashed vertical lines correspond to the acceleration bank discharge, plasma exiting the accelerator, the compression bank discharge, and the high peak in the assembly magnetic field respectively.

grounds the middle electrode to the outer electrode, causing V_M to move to zero.

Then, the compression bank discharges, which drives compression current. The compression bank discharge coincides with the initial rise in I_C Fig. 2.7 (a) and with abrupt steps in the voltages in Fig. 2.7 (b). The current propagation downstream is seen by the assembly probes in Fig. 2.8 (a). As the plasma current proceeds down the assembly region, the plasma's geometry changes rapidly and chaotically, affecting its inductance and causing rapid spikes in V_A, V_M, and V_C between 28 μs and 38 μs.

After the plasma arranges itself on machine axis, it stabilizes for a quiescent period of roughly 25 μs shown by the green boxes in Figs. 2.7, 2.8, and 2.9. During this quiescent period, a constant V_A drives a steady radial current in the accelerator. The presence of this radial current suggests a steady flow of plasma out of the gun, which should supply stabilizing flow shear. Also during this period, radial currents exist in the assembly region between $z = 0$ cm -15 cm although further downstream most current is axial. The normalized mode data, $\frac{m_1}{m_0}$, during the quiescent period is low and slowly-varying relative to other times in the plasma evolution as seen in Fig. 2.9. This indicates the current centroid remains near machine axis without chaotic deviations. Optical images such as those in Fig. 2.5 corroborate that the plasma moves slowly as a coherent structure during the quiescent period.

The quiescent period concludes abruptly as the accelerator runs out of the fuel necessary to sustain the flow for shear stabilization. The behavior observed at the end of the ZaP-HD quiescent period resembles the high peak magnetic field operational mode of ZaP in which a peak in the assembly region magnetic field coincided with the end of the quiescent period and with a drop in accelerator region line-integrated density. These phenomena were thought to indicate the accelerator running out of fuel causing the quiescent period to end as the supply of flow shear from the gun ceased [32]. Similar to ZaP, ZaP-HD observes a magnetic field peak coincident with the end of the quiescent period. At the time of the field peak, voltage spikes occur that drive V_M to zero and make V_A approach V_C. The radial current in the accelerator disappears at this time, and optical images show irregular blobs of plasma expelled from the accelerator at times after the field peak. ZaP-HD's accelerator interferometry ports are
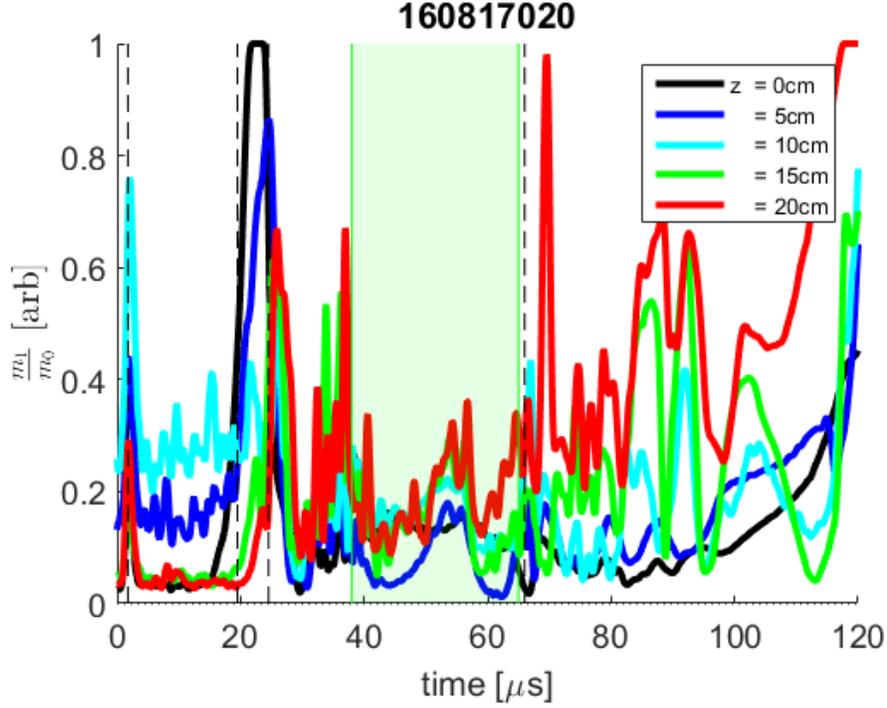
Figure 2.9: In a typical ZaP-HD plasma pulse, a quiescent period of relatively low mode activity occurs, which corresponds to optical camera images showing stable, slowly varying plasma behavior. The normalized mode data, $\frac{m_1}{m_0}$, remains relatively low during this period denoted in shaded green. On ZaP, $\frac{m_1}{m_0}$ would remain below 0.2 for the quiescent period. On ZaP-HD, $\frac{m_1}{m_0}$ often takes higher values than 0.2 during the quiescent period, but $\frac{m_1}{m_0}$ between $z = 0$ cm and 20 cm changes slowly during this time, which indicates the current centroid moves gradually. Optical images corroborate than the plasma moves slowly as a coherent structure during the quiescent period. The $\frac{m_1}{m_0}$ further downstream in the assembly region exhibits more rapid oscillations that the data from $z = 0$ cm to 20 cm. Optical images also suggest less coherent plasma structure and less stable dynamics further downstream. The first, second, third, and fourth dashed vertical lines correspond to the acceleration bank discharge, plasma exiting the accelerator, the compression bank discharge, and the high peak in the assembly magnetic field respectively.

covered by insulating material to prevent arcing in the region between the middle and outer electrodes upstream of $z = 0$ cm, and this prohibits measurements of the ZaP-HD accelerator density. However, as the timing of the field peak can be moved by changing gas puff timing, this behavior on ZaP-HD also likely relates to gas starvation.

2.3 Accelerator operation

The operation settings exhibited in the previous section lead to plasma behavior optimal for capturing DHI holograms, which means ZaP-HD creates dense, on-axis Z-pinches. Optimization of these settings resulted from a wide exploration of the available machine settings. The coarsest means of changing the plasma behavior comes from adjusting the capacitor bank settings, which is discussed further in Sec. 2.4. Finer adjustment of plasma behavior is exercised by tuning the gas injection settings. The gas settings play a major role in the accelerator's operation, which affects the behavior of the Z-pinch in the assembly region. This section discusses the design and operation of the ZaP-HD accelerator and demonstrates what practical control regulating the gas injection affords.

ZaP-HD's accelerator design originates from ZaP's, which was designed to match the aspect ratio of the Marshall Gun [36]. The addition of ZaP-HD's middle electrode has changed the accelerator's aspect ratio, and its gas injection system has evolved as well. The Marshall gun started with gas injection solely from the inner electrode. ZaP added gas injection from eight equidistant azimuthally-spaced valves in the outer electrode halfway down the length of the accelerator at the same axial location of the inner gas injection. Based on results from a gas supply study on ZaP [37], ZaP-HD moved the outer gas injection upstream to the breech of the gun to provide a neutral gas plenum to supply the gun with fuel for a longer time.

Coaxial plasma accelerators operate in two modes: snowplow (detonation) and deflagration [38, 39]. A snowplow occurs in accelerators with uniform gas fill so that the initial plasma accelerates downstream into neutral particles. This accelerated ionization sheet forms a shock, which entrains and ionizes neutrals, compressing the plasma to high temperature

as it moves down the accelerator. A deflagration happens in low pressure accelerators where gas is supplied from a transient gas puff. In this case, when the initial plasma accelerates downstream, it does not encounter neutral gas. Instead it can expand into the vacuum while simultaneously accelerating due to the Lorentz force. Lacking compression and the obstruction caused by neutral gas fill, deflagrations more efficiently convert the electrical discharge into kinetic energy, yielding a cooler plasma at a higher velocity. In a deflagration into a pure vacuum, the ionization front will remain stationary.

Changing the gas injection timing relative to the accelerator bank discharge provides significant control over the accelerator's behavior. Timing gas injection to allow more gas dissipation before the voltage discharge promotes snowplow behavior, while giving the gas puff less time to expand favors deflagration. Past work observed an abrupt bifurcation between the operation modes in a coaxial accelerator [40]. Tests of the ZaP-HD outer gas injection system reveal similar behavior. Fig. 2.10 (a) and (b) show data from pulses triggering the outer gas at -1.0 ms and -0.8 ms relative to the acceleration bank trigger respectively. Adjusting the outer gas trigger by 0.2 is enough to move the accelerator operation from a snowplow to a deflagration operational mode. The -1.0 ms timing gives the gas more time to fill the gun, which leads to a initial current front that moves relatively slowly according to magnetic data from the acceleration and assembly regions. A chord of heterodyne quadrature interferometry in the assembly region at $z = 7$ cm and $y = 0$ cm reveals the abrupt arrival of a slab of plasma accumulated by the snowplow. The -0.8 ms timing causes a faster current front with a more gradual density arrival consistent with deflagration operation.

Conceptually, ZaP-HD seeks to operate in a combination of the two modes. Ideally, an initial snowplow ionizes and accelerates any neutrals that have expanded downstream of the location of the original discharge. This establishes an initial plasma in the assembly region ready to accept the compression current and also clears out neutrals in the gun so a deflagration can operate. Then, the deflagration efficiently accelerates the plasma to high velocity for a sustained time. The snowplow helps form the Z-pinch and the deflagration supplies sustained flow shear to stabilize it. It is unclear what actually happens as diagnostic
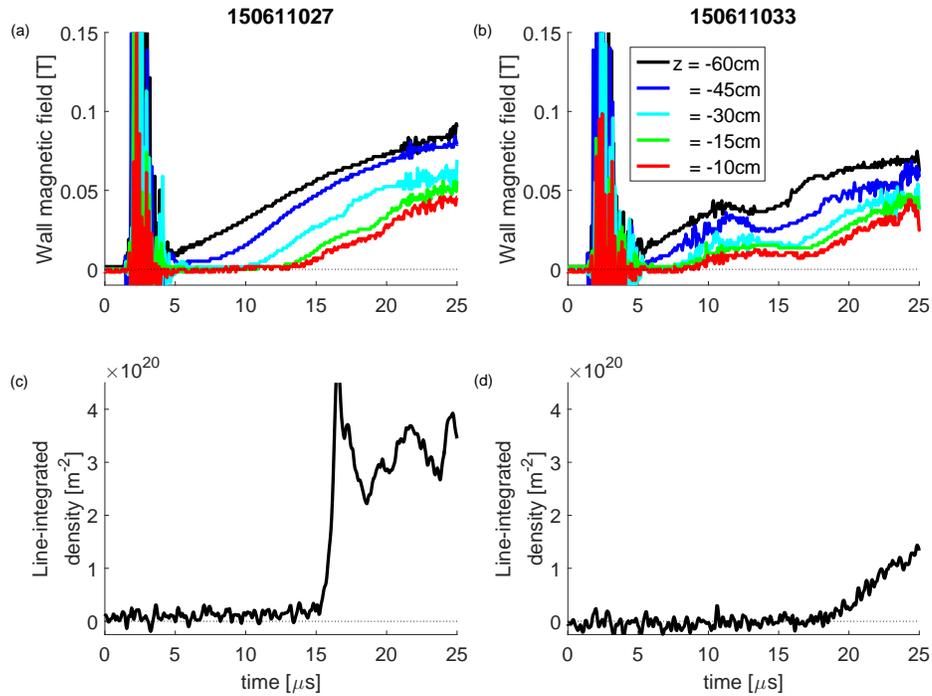
Figure 2.10: (a) Accelerator probe data shows a slower-moving current front when the outer gas is given more time to expand. (c) An interferometry chords at z = 7 cm and y = 0 cm shows an abrupt arrival of density in the assembly region. These characteristics are indicative of snowplow operation where plasma is entrained by the current front and pushed downstream. Pulse 150611027 had inner/outer gas timings of -0.6/-1.0 ms. (b) Accelerator probe data shows a faster-moving current front when the outer gas is given less time to expand. (d) Interferometry shows a more gradual density arrival. Both these characteristics are indicative of a deflagration mode of operation. Pulse 150611033 had inner/outer gas timings of -0.6/-0.8 ms.

access to the accelerator is limited. The relatively early inner/outer gas timings presented in Sec. 2.2 of -1.6 ms/-1.5 ms ostensibly promote snowplow behavior, but these settings create stable Z-pinches, which suggest a deflagration may also exist that supplies requisite flow shear. More study will be possible once the acceleration probe calibration is complete and when optical viewports to the accelerator can be sufficiently insulated to allow interferometry access without allowing arcing between the middle and outer electrodes.

The acclerator's operation most strongly depends on the outer gas injection timings although the inner gas injection time also plays a significant role in determining its mode of operation. Varying the gas feed pressures on the inner and outer puff independently at settings of 3500, 4500, and 5500 Torr did not significantly alter the accelerator's behavior.

2.4 Interface between acclerator and assembly regions

Complicated plasma dynamics occur at the end of the accelerator as the plasma exits into the assembly region. These behaviors correlate to coupling between ZaP-HD's acceleration and compression phases, which leads to inefficient compression and non-optimal scaling. An exploration of the plasma behavior at the gun exit led to changes in the ZaP-HD design to improve performance.

Although the initial ZaP-HD design assumed any current contact between the outermost electrodes would be swept away by magnetic flux exiting the accelerator, initial results indicated sustained, significant plasma current flow between these electrodes upstream of z = 0 cm. An early design to stop this current includes a machined ring of alumina as shown in Fig. 2.11(a) to block plasma from moving into the volume between the middle and outer electrodes upstream of z = 0 cm. This insulator is held in place by four set screws and overlaps with a Teflon sheet, which provides additional necessary insulation. This arrangement stops currents between the outer and middle electrodes upstream of z = 0 cm, but measurements of the magnetic field at the outer electrode wall in the assembly region still indicate significant radial current flow just downstream of the gun exit. The large difference between the average field at z = 0 cm and 5 cm between 35 μs and 55 μs in Fig. 2.12(a) indicates

a large radial current in that axial region. This amounts to a substantial inefficiency in the compression process as a sizable fraction of the applied compression current flows radially driving acceleration instead of flowing axially to drive compression.

Optical high-speed camera images captured surface arcing across the alumina ring insulator, revealing a possible mechanism allowing radial current flow. Fig. 2.14 shows an arc between the middle and outer electrode across the ring insulator. The position of such arcs observed in camera images corroborates with magnetic field measurements from the azimuthal probe array at z = 0 cm. The azimuthal location of the arc observed in optical images corresponds to the location of the probes measuring the highest fields.
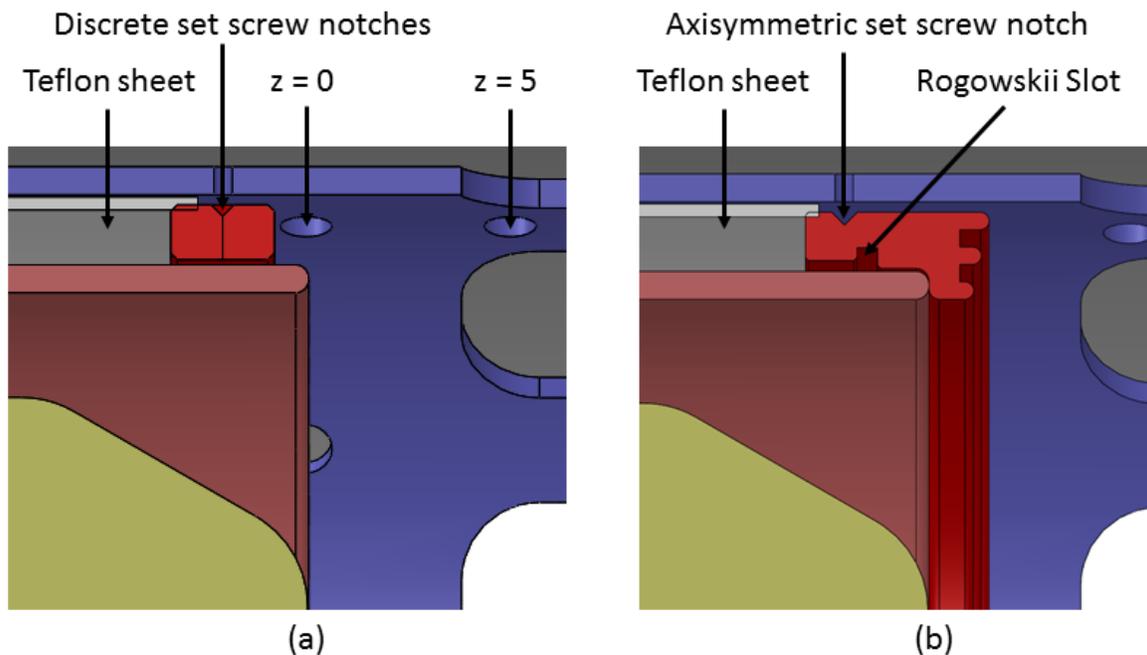
Figure 2.11: (a) In ZaP-HD's original design, a simple ring of electrically insulating alumina was intended to block plasma flow into the gap between the middle and outer electrodes upstream of the accelerator exit. Plasma arcing across the insulator surface may have contributed to large radial currents just downstream of the accelerator. (b) A modified ring insulator extends further downstream with machined grooves meant to baffle surface tracking arcs.
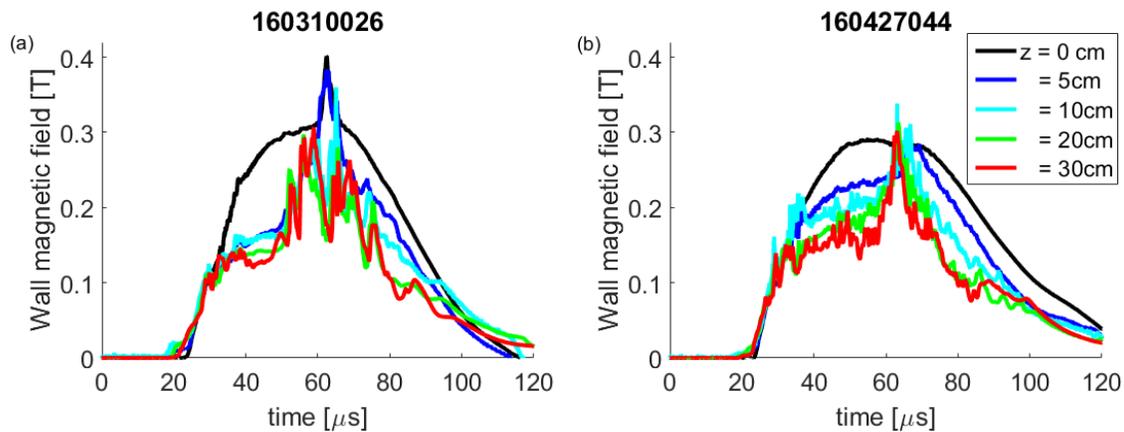
Figure 2.12: For pulses with the same run settings, (a) the average wall magnetic field at each axial location plotted versus time for the first ring insulator design of Fig. 2.11(a). The large gradient in magnetic field versus axial position indicates large radial currents, which causes inefficiency. (b) The same average fields plotted for the modified ring insulator design of Fig. 2.11(b). The new design inhibits the radial current flow allowing for sustained axial currents far downstream.

A new ring insulator design, shown in Fig. 2.11(b), strives to block these radial currents. The new design extends further downstream and includes three ridges to increase the tracking length arcs must follow to bridge the electrodes. The new ring extends axially as far as possible while retaining ease of installation. Limiting the axial extent of the ring allows for it to be inserted through the rectangular openings in the outer electrode, turned ninety degrees, and then pushed into place. Installing a wider insulator would require removing the outer electrode endwall, a labor-intensive process. The new insulator includes a slot for a Rogowskii coil, which may be used in the future as a measurement of plasma current with fast time response to check the time delay on the relatively slow magnetic field probes.

With the new insulator in place, magnetic data and optical imaging still observe radial current at the gun exit, but the effects are reduced. Optical images suggest that arcs still occur across the insulator as Fig. 2.15 shows an arc jumping between the insulator's three ridges to bridge the middle and outer electrodes. Comparing pulses before and after insulator installation with otherwise identical run settings, Fig. 2.12 shows significantly higher average
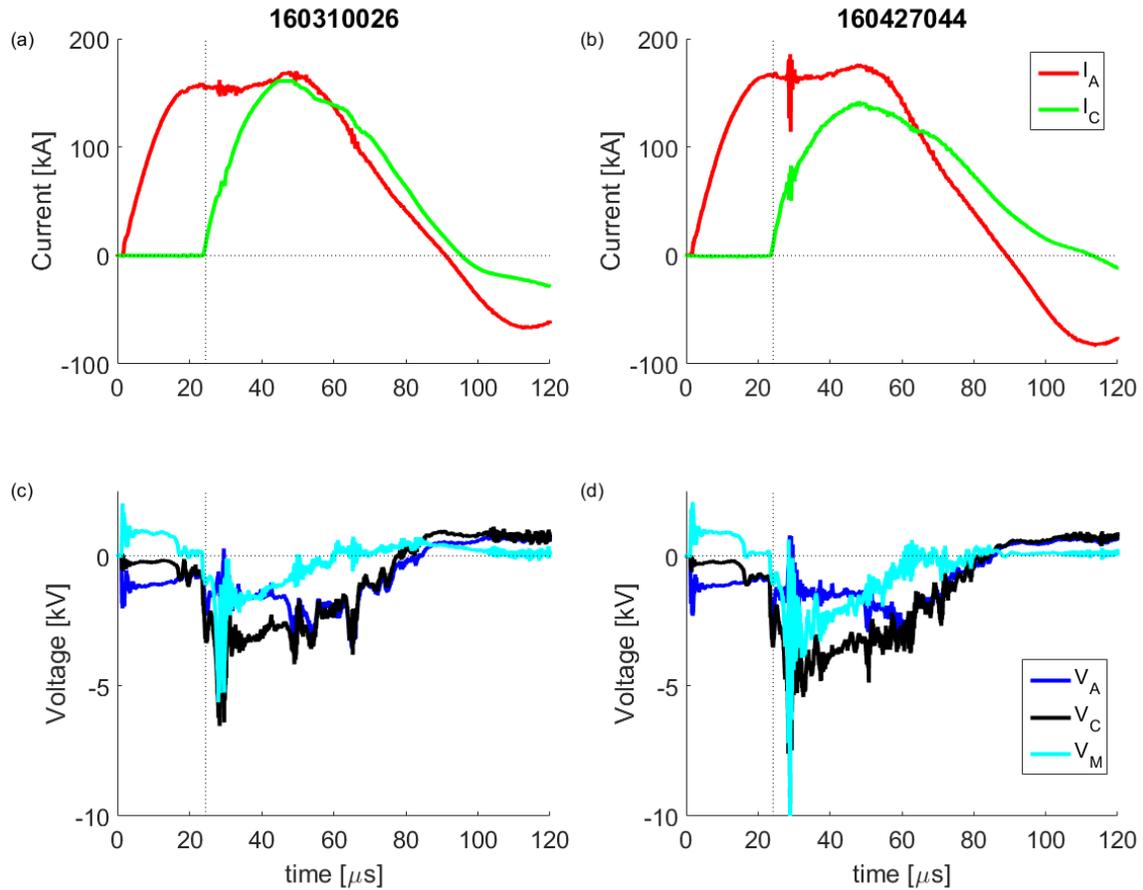
Figure 2.13: For pulses with the same run settings, (a) the current and (c) voltage time series for a pulse with the first ring insulator. (b) The current and (d) voltage time series for a pulse with the modified ring insulator. The insulator modification increases the impedance between the middle and outer electrodes, leading to lesser compression current and higher middle electrode voltage. The vertical dashed lines indicate the timing of the compression bank trigger.
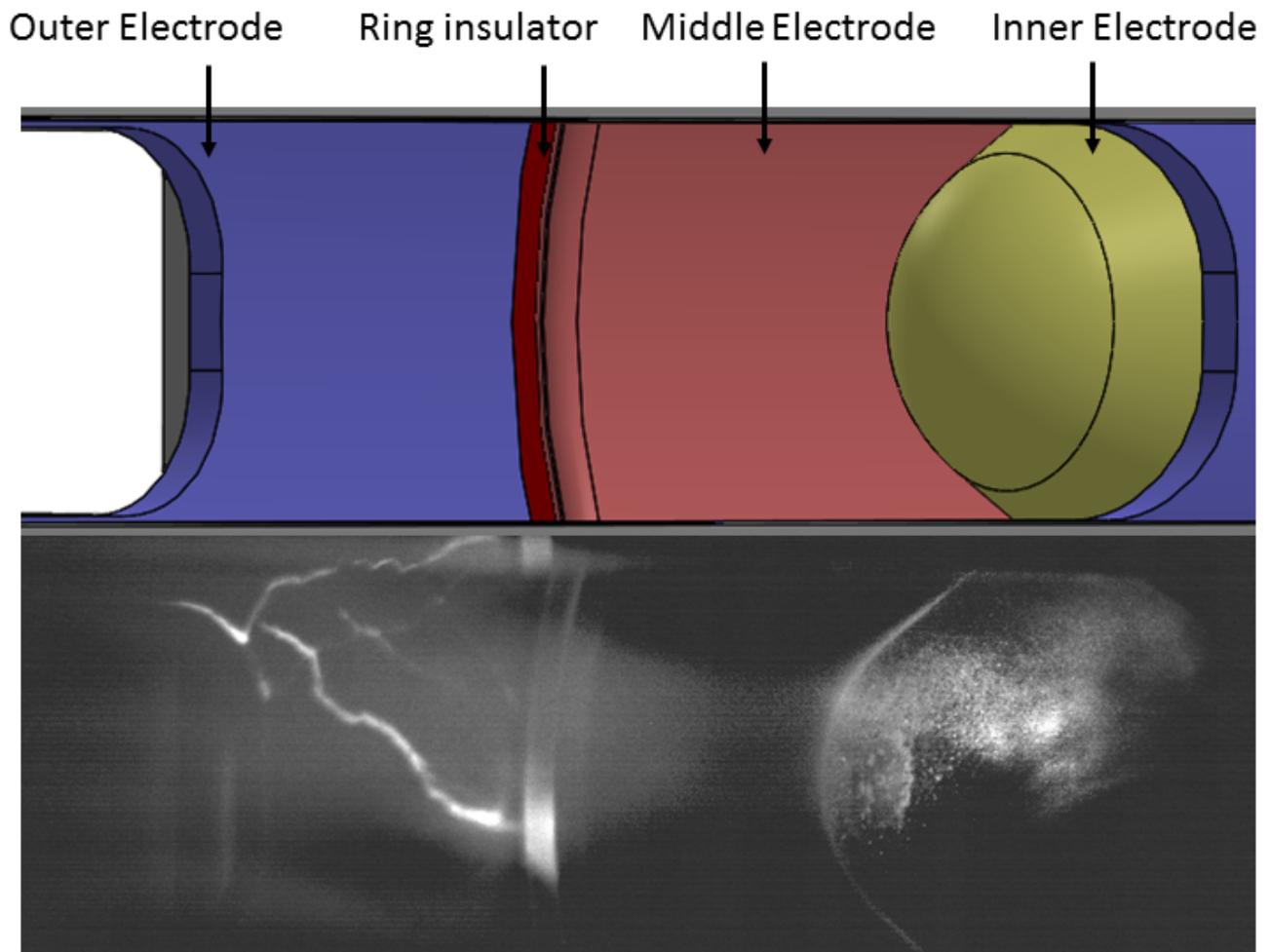
Figure 2.14: (top) A CAD image indicates the positions of the electrodes and ring insulator. (bottom) An optical camera image taken with a bremsstrahlung filter, f stop of 5.6, and exposure time of 200 ns (pulse 160224046). Localized plasma contact between the middle and outer electrodes across the ring insulator correlates with current centroid position data at z = 0 and suggests current flow directly between the outer and middle electrodes.

magnetic fields extend further down the assembly region. Instead of the radial current existing entirely within 5 cm downstream of the gun, it now spreads over at least 30 cm downstream. This increases the effectiveness of compression in the upstream portions of the plasma. This redirection of current correlates with an increased inductance between the middle and outer electrodes. Comparing the current and voltage in the pulses in Fig. 2.13 reveals the modified insulator geometry decreases the compression current while increasing the middle electrode voltage, which is the voltage between the middle and outer electrodes.

The interaction between the assembly and acceleration regions also depends on the relative charge voltages of the compression and acceleration capacitor banks. Evidence suggests the current paths in ZaP-HD are topologically different for different charge settings. Fig. 2.16 shows voltage and assembly magnetic field data for three different charge settings. In the three cases shown, the accelerator bank is charged to 9 kV, and the compression bank is charged to (a) 0 kV, (b) 2 kV, and (c) 8 kV respectively.

Running with only the accelerator, V_M floats positive for the majority of the pulse except for a brief moment when the plasma first exits the gun and creates a low impedance short to the outer electrode. The outer electrode is the reference ground for the voltage measurements, so a positive V_M implies current flow from the middle electrode to the outer electrode. Fig. 2.17 (a) illustrates what the paths of the acceleration and compression currents look like in this case. Note that when running with only acceleration bank charge, no compression current exists. Fig. 2.16 (a) shows reduced magnetic field magnitudes at z = 0, 5, and 10 cm, which corroborate this current flow topology. The probe calibration assumes that all current flow in the positive z-direction, which is called return current here, goes through the outer electrode. Here, some of the return current flows through plasma instead, which reduces the magnetic field apparent to the probes.

Charging the compression bank to 2 kV, V_M still floats positive, but to a lesser magnitude. Therefore, the current flow topology remains the same as in Fig. 2.17 (a) although less return current flows through the plasma. The addition of compression current may help move plasma out of the region where the return current flows readily during accelerator-
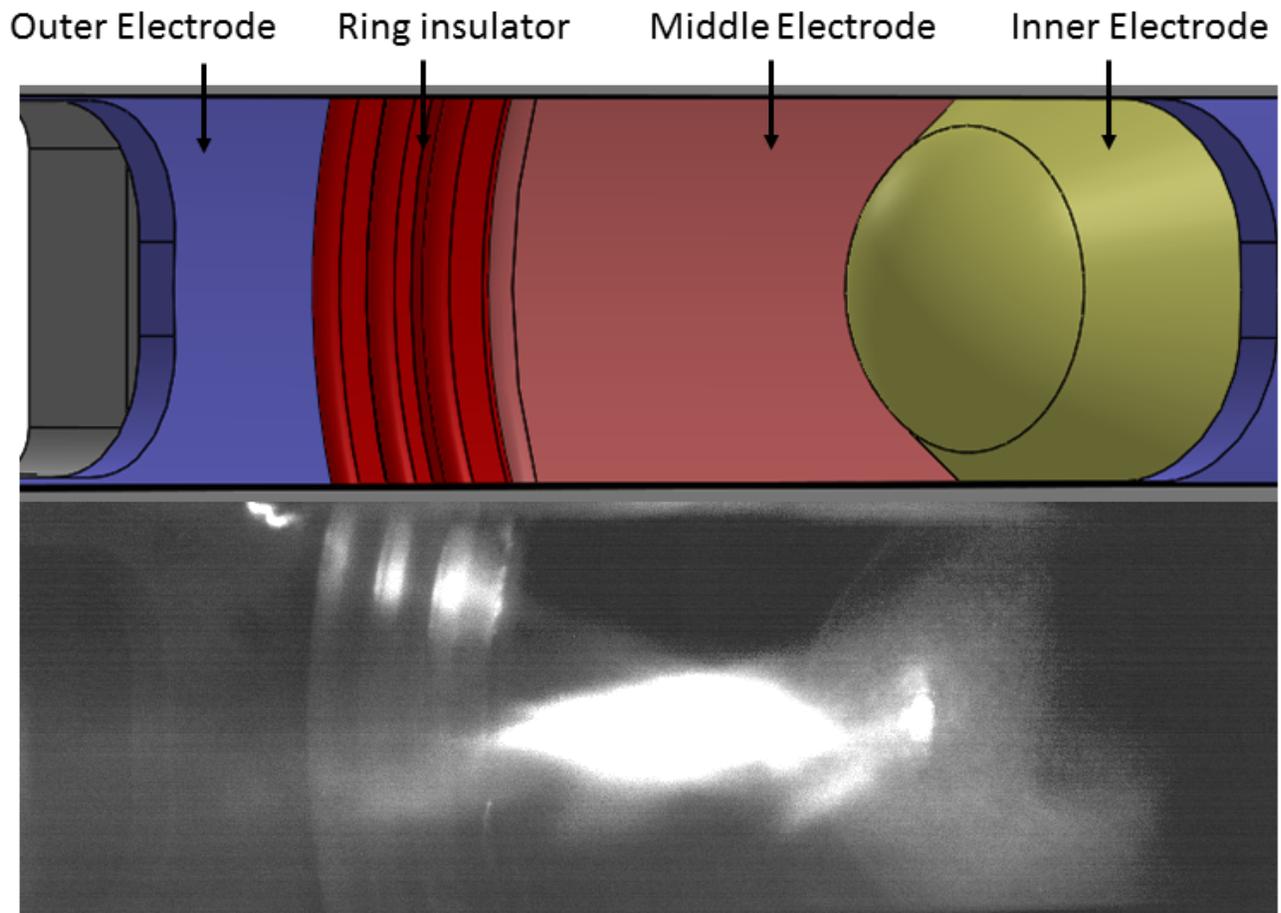
Figure 2.15: (top) A CAD image indicates the positions of the electrodes and ring insulator. (bottom) An optical camera image taken with a bremsstrahlung filter, f stop of 5.6, and exposure time of 200 ns (pulse 160427024). Localized plasma contact between the middle and outer electrodes across the ring insulator correlates with current centroid position data at z = 0 and suggests current flow directly between the outer and middle electrodes. The plasma appears to jump across each of the three ridges in the ring insulator.
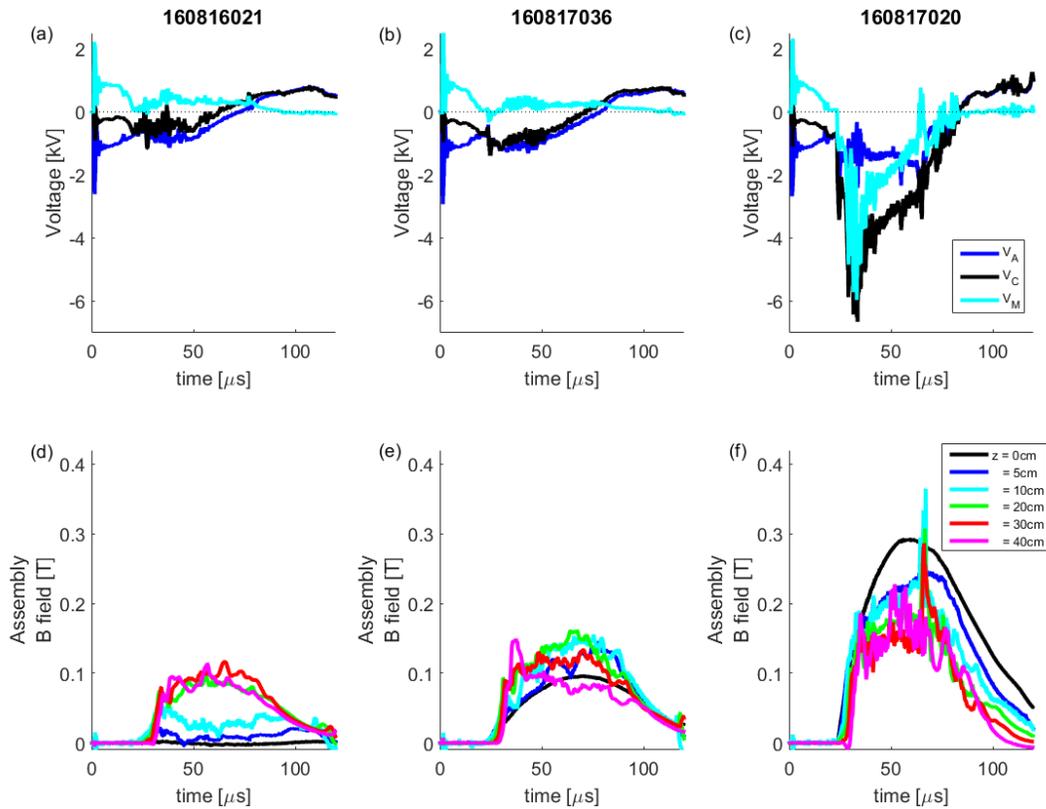
Figure 2.16: Comparison of the voltage and assembly probe data at different compression bank charge voltages, (a) and (d) 0 kV, (b) and (e) 2 kV, and (c) and (f) 8 kV, suggests different current flow topologies exist depending on the relative magnitude of the acceleration and compression bank charge voltages. The polarity of V_M indicates direction of current flow between the middle and outer electrodes. Probe data suggests some return current flows in the plasma.

only operation. Compared to running with only the acceleration bank, the magnetic field measurements at z = 0 and 5 cm are reduced to a lesser degree.

Employing an 8 kV compression bank charge, the current flow appears topologically different as shown in Fig. 2.17 (b). Here, after the compression bank discharge, V_M goes negative, which implies current flow from the outer electrode to the middle electrode. The assembly region field data suggests substantial radial current flow between z = 0 and 5 cm, some of which, as suggested by optical camera images earlier in this section, likely proceeds from the outer electrode to the middle electrode.

The compression current that flows to the middle electrode must eventually proceed to the inner electrode, which means the compression bank can drive radial current in the accelerator. This represents an inefficiency in the plasma confinement as energy that could go to compression is instead expended in accelerating plasma. Detailing how and where the compression current proceeds to the inner electrode is difficult, especially as the accelerator probe calibration is presently incomplete and prohibits the identification of the radial current flow between z = -5 and 0 cm. Regardless of exactly how the compression current distributes in the accelerator, applying the compression bank discharge does drive more plasma acceleration as the magnetic field peak indicating fuel exhaustion only occurs at higher compression charge voltages. Exhaustion at high compression bank charge may occur simply because the compression current must flow through the inner electrode, which increases the field strength in the accelerator. Increasing the total current in this manner is unavoidable, but exhaustion could also relate to the compression bank driving more radial current in the accelerator, which may be addressable by further design modifications.

The interplay between the acceleration and compression banks adds a great deal of complexity to the ZaP Flow Z-Pinch concept, and the coupling between the acceleration and assembly regions deserves more investigation.
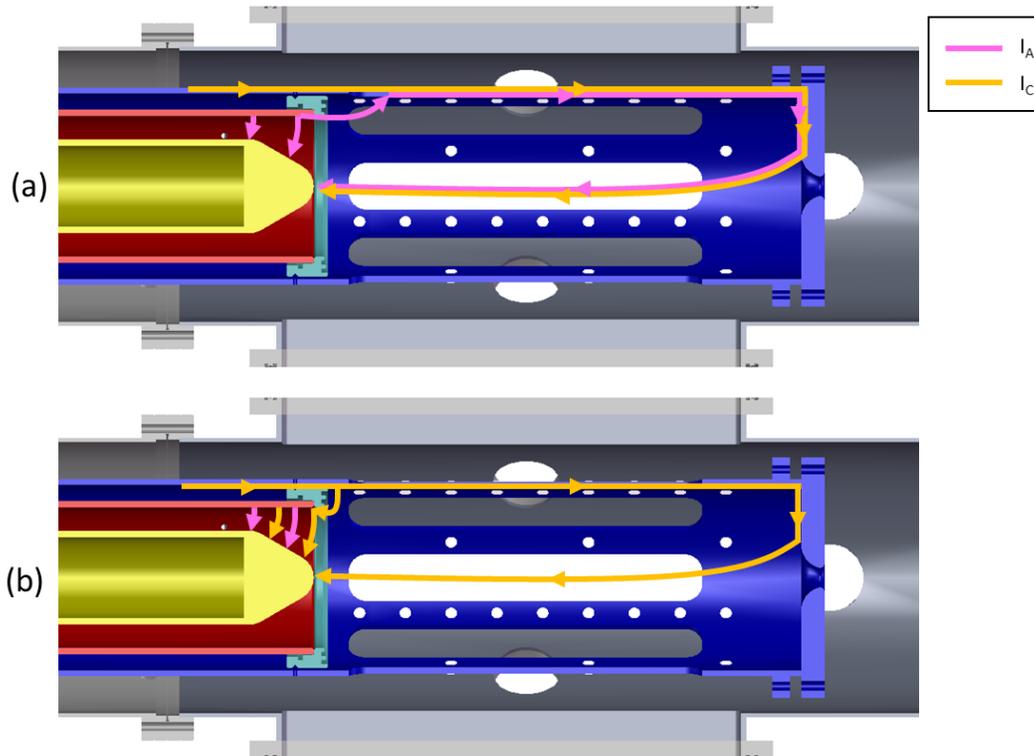
Figure 2.17: Illustration of the flow of I_A and I_C in ZaP-HD for (a) the case of low compression bank charge voltage relative to acceleration bank charge voltage. Acceleration current flows from the middle electrode to the outer electrode. This topology applies for 0 kV compression bank charge except in that case $I_C = 0$. (b) The case of high compression bank charge voltage relative to acceleration bank charge voltage. Compression current flows from the outer electrode to the middle and inner electrodes.

Chapter 3

DIGITAL HOLOGRAPHIC INTERFEROMETRY

ZaP-HD can generate smaller, denser Z-pinches that ZaP. The small size (radius of 2-5 mm) of ZaP-HD's plasmas motivates the development and use of digital holographic interferometry (DHI). The diagnostic's spatial resolution approaching 10 microns allows it to resolve line-integrated electron density profiles of pinches less than a millimeter across at one instant per plasma pulse. This spatial resolution allows for Abel inversion of line-integrated density to number density. Identification of the actual number density is crucial to understanding the scaling properties of ZaP-HD and useful in computing other plasma parameters such as temperature and magnetic field. This chapter discusses the theory of DHI and demonstrates the diagnostic by applying holographic reconstruction and error analysis to measured holograms.

3.1 Historical context

Holography originated as a means to improve the resolution of transmitting electron microscopes (TEM) [41]. Unavoidable aberrations in TEM degrade image clarity by mixing electron beam amplitude and phase information. Measuring both amplitude and phase simultaneously with holography allows for deconvolution of the two for improved imaging [42]. The demonstration of the laser in 1960 opened up holography to more applications including nondestructive stress testing [43], data encryption [44–46], and fluid dynamics diagnostics [47]. Before the advent of high-resolution digital sensors, laser-based holography required holographic plates, optical reconstruction, and multi-exposure techniques like phase-shifting [48] and spatial heterodyning [49, 50] to measure phase information because optical reconstructions can only explicitly recover amplitude. Explicit simultaneous recovery of amplitude and

phase is possible with numerical reconstruction, which simulates the diffraction process of optical reconstruction. Today's digital sensors record holograms with sufficient resolution to allow seamless integration of holograms and reconstruction algorithms to efficiently provide phase data.

Several methods have been developed to conduct numerical reconstruction, and some have been applied to plasma physics research. Research in electron holography led to a reconstruction algorithm [51] now used to observe neutral gas injection on the Lithium Tokamak Experiment (LTX [52,53] and proposed to observe plasma facing component erosion [54]. A similar, independently developed method originating in laser-based holography research [55] is used to measure electron density on Z-pinch experiments [56]. Both of these methods Fourier transform the hologram, filter the data in the Fourier domain, and then apply an inverse Fourier transform to obtain the phase. Such Fourier transform methods are similar to Fast Fourier Transform (FFT) methods used in two-dimensional inteferometry analysis discussed in the next paragraph [57]. The method presented in this dissertation uses a single modified Fourier transform called a Fresnel transform [58–60]. This dissertation presents the first application of the Fresnel transform reconstruction method as part of a plasma diagnostic as well as novel analysis of the method's accuracy.

Interferometric techniques resembling, yet distinct from DHI have been applied to measure Z-pinch electron densities. Although interferometric and holographic methods both rely on interfering scene and reference beams, interferometric methods generally employ co-linear interfering beams to generate interferograms with relatively large fringes, while holography interferes the beams at an angle to generate holograms with comparatively small fringes, which enable holographic reconstruction [53]. A method known as digital interferometry subtracts the amplitudes of plasma and vacuum interferograms to obtain an intensity pattern from which a computer algorithm can count fringes to compute the spatially resolved phase [61,62]. Another method uses well-aligned scene and reference beams to generate large-scale fringes, which are modulated by phase shifts. This method employs an algorithm to trace fringes and computes their shift between plasma and vacuum interferograms [63]. Inter-
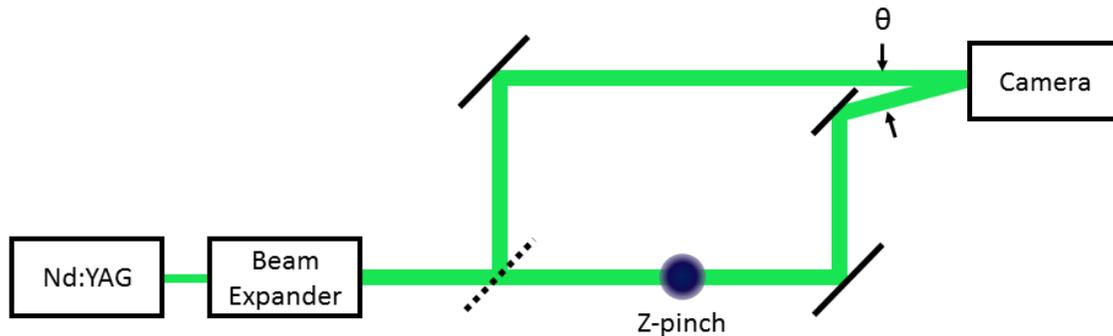
Figure 3.1: A Mach-Zehnder interferometer splits a laser beam into two identical beams. One beam passes through the plasma while the other bypasses the experiment. Then, the beams are recombined with a beamsplitter and recorded on a camera or other sensor. The phase shift between the two beams is proportional to the plasma's line-integrated electron density.

ferogram analysis employing FFTs enables phase computation without fringe counting [57], and such methods are also applicable to holographic reconstruction [64].

3.2 Theory of holographic reconstruction

ZaP-HD employs an Ekspla NL-121 Nd:YAG laser with a second harmonic generator and 2 ns pulse length (see Sec. A.3 for more details about the laser) as well as a Nikon D3200 digital single-lens reflex (DSLR) camera with Thorlabs absorptive neutral density filters. The camera shutter is left open through the plasma pulse, so the laser pulse defines the hologram exposure time.

DHI obtains fine spatial resolution by employing a two-dimensional sensor with sufficient resolution to measure the interference pattern of the interferometry beams. A recording of this pattern is called a hologram. The interfering beams in a holographic system are more misaligned than those in a 2D interferometer, which leads to fringes of higher spatial frequency and enables holographic reconstruction. Previously, only special holographic films and plates could resolve holograms, but modern consumer CMOS and CCD cameras provide the resolution (the Nikon D3200 pixels are 3.85 μm wide) necessary as long as scene and

reference beams are misaligned by no more than a few degrees when directed to the camera. Interferometric fringe spacing δ decreases as misalignment angle θ increases as in $\delta = \frac{\lambda}{\sin\theta}$. A misalignment less than 4 degrees is required to ensure a fringe spacing greater than two pixel widths at $\lambda = 532$ nm to meet the Nyquist sampling criterion and avoid fringe aliasing.

A hologram implicitly contains the amplitude and phase of the scene beam, which can be reconstructed through optical or numerical means. Optical reconstruction involves shining the reference beam through the hologram and allowing diffraction of that beam to recreate the original scene beam amplitude. Reconstruction can be performed numerically by simulating this optical diffraction process.

The result of numerical reconstruction is the electric field strength, E, of the scene beam. In this dissertation, light waves are described by their electric field strength. The field strength is a complex number at each point in space, from which the light intensity, I, and wave phase, ϕ, can be computed at any location. These quantities are defined by

$$I(\xi, \eta) = |E(\xi, \eta)|^2 \tag{3.1}$$

$$\phi(\xi, \eta) = \tan^{-1}\left(\frac{\operatorname{Im} E(\xi, \eta)}{\operatorname{Re} E(\xi, \eta)}\right) \tag{3.2}$$

in a user-defined reconstruction plane with coordinates (ξ, η), downstream from the hologram plane with coordinates (x, y) (see Fig. 3.2).

Modeling the scene and reference beams as complex exponentials mathematically reveals how passing the reference beam through a recorded hologram reconstructs the scene beam. This section illustrates the theoretical foundation for reconstruction by assuming a linear model for the camera's light response where

$$T(x, y) = \alpha - \beta\tau I(x, y) \tag{3.3}$$

describes the transmittance $T(x, y)$ of a recorded hologram, which is the sensor's measured exposure to amplitude $I(x, y)$ for a duration τ. Constant α accounts for uniform background
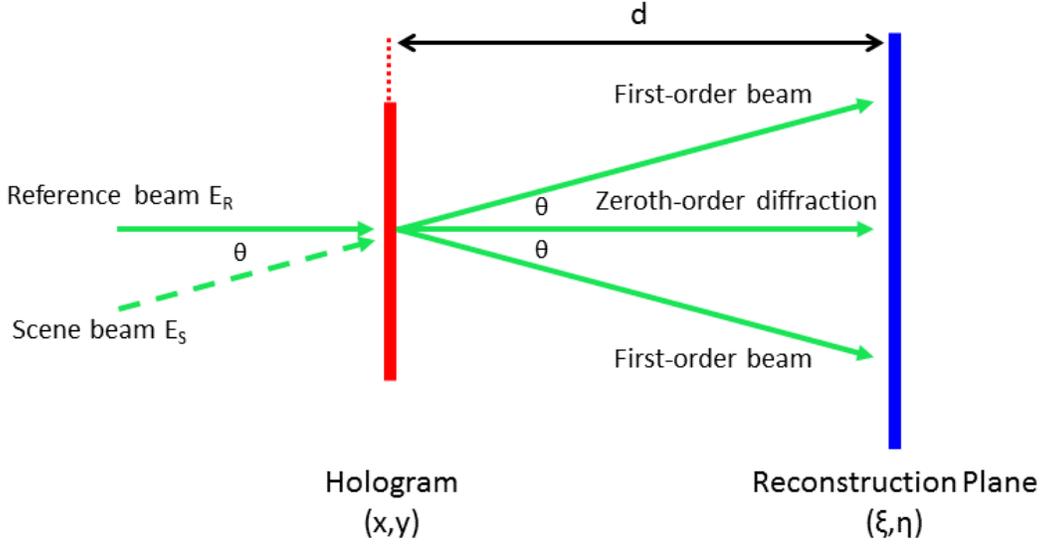
Figure 3.2: If the reference beam is incident normal to the hologram, both first-order beams propagate at the incident angle of the original scene beam, θ. Reconstruction distance, d, spans from the hologram to the reconstruction plane. In the case of a planar reference beam, the phase distributions of the two first-order diffraction beams are identical except for being 180-degrees shifted. Therefore, the reconstructed phase maps resulting from the first-order diffraction beams are commonly called twin images. Zeroth-order diffraction is the portion of the reference beam that does not diffract; it contains no useful information.

illumination, and β is the sensor's light sensitivity.

$I(x, y)$ is the amplitude of the sum of the incident reference and scene beams, which are expressed as spherical waves in

$$E_R = \frac{E_{0R}}{d_R} e^{i(kd_R + \phi)} \tag{3.4}$$

$$E_S = \frac{E_{0S}}{d_S} e^{i(kd_S + \psi)}. \tag{3.5}$$

These waves describe the spatial distribution of the electric field strength of each beam. For the reference and scene beams respectively, E_{0R} and E_{0S} are the beams' amplitudes, d_R and d_S are the distances from the beams' point sources, $k = 2\pi/\lambda$, and ϕ and ψ are arbitrary phases. Note that treating these beams as spherical waves gives the most general results

from this analysis.

Computing the amplitude of the combined beams from Eq. (3.1) yields

$$I(x,y) = E_S E_S^* + E_S E_R^* + E_R E_S^* + E_R E_R^* \tag{3.6}$$

where $*$ indicates the complex conjugate.

Passing the reference beam through the recorded hologram is done mathematically by multiplying the transmittance and the reference beam

$$E_{rec} = T E_R, \tag{3.7}$$

which gives E_{rec} as the reconstructed field. Substituting Eqs. (3.3) and (3.6) into Eq. (3.7) yields

$$E_{rec} = -\beta\tau |E_R|^2 E_S \cdots$$
$$-\beta\tau E_R^2 E_S^* \cdots$$
$$+(\alpha - \beta\tau(|E_R|^2 + |E_S|^2))E_R. \tag{3.8}$$

Eq. (3.8) shows that the reconstructed field contains the original scene beam, illustrating the theoretical basis for why the scene can be reconstructed [60]. E_{rec} consists of three images, each corresponding to a different term in Eq. (3.8). The scene is contained in the first term ($\propto E_S$), which is the product of the original scene field and a scalar that does not affect its phase. The second term ($\propto E_R^2 E_S^*$) is a conjugate image of the scene. The third term ($\propto E_R$) corresponds to light passing through the hologram without diffracting (e.g., zeroth-order diffraction), while the first and second terms represent first-order diffraction. In practice, E_R can be treated as a plane wave, and the phase maps of the first-order terms are 180-degrees out of phase but otherwise identical. The first-order waves propagate at the incident angle of the scene beam, θ, if the reference beam is normal to the hologram as in Fig. 3.2 [60]. The reconstructed phase maps resulting from the first-order diffraction

beams are commonly called twin images due to their similarity. The reconstructed phase shown in Fig. 3.6 exhibits a zeroth-order diffraction image as well as two pairs of twin images containing the reconstructed phase from a synthetic hologram. The nomenclature used in this dissertation comes from laser-based holography; in electron holography, the zeroth-order diffraction image is called the autocorrelation and the twin images are called sidebands [52].

This section's analysis assumed a sensor with a linear response, but testing revealed the Nikon D3200 CMOS to be non-linear. The above analysis still applies to DHI with a non-linear sensor because the non-linearity does not affect the phase of the first-order images. It does distort the reconstructed amplitude and adds harmonics to the reconstructed phase, but these effects do not change the diagnostic's operation. The harmonics sometimes show up as apparent additional twin image pairs with greater sensitivity to phase shift than the first-order images [58] .

3.3 *Fresnel transform reconstruction*

The analysis of the previous section shows that reconstruction of the original scene is theoretically possible by passing the reference beam through the hologram. This section presents a tractable means to compute the reconstruction in practice. Numerical reconstruction computes the phase of the original scene beam by modeling the reference beam's propagation downstream of the hologram as scalar diffraction.

While light propagation really involves a coupled evolution of electric and magnetic field vectors, scalar diffraction theory models light as a scalar amplitude of a single transverse (transverse to the propagation direction) component of either field. This treatment is accurate in cases where the diffraction aperture is large compared to the wavelength and the diffracted wave field is observed far from the aperture. In this treatment, the linear Helmholtz equation is the appropriate model for monochromatic light propagation [58].

The Huygens-Fresnel principle provides the most common heuristic explanation of diffraction. It posits that each point on an electromagnetic wavefront is a source of secondary spherical wavelets. The interference between these secondary wavelets manifests itself in the

alternating light and dark regions of diffraction patterns. This statement's mathematical analog is written in its general form as

$$E_{rec}(\xi, \eta) = \int_{-\infty}^{\infty} \int_{-\infty}^{\infty} h(\xi, \eta; x, y) T(x, y) dx dy, \tag{3.9}$$

where $E_{rec}(\xi, \eta)$ is the reconstructed electric field strength, $T(x, y)$ is the transmittance of the hologram, and $h(\xi, \eta; x, y)$ is the mathematical representation of a secondary wavelet. Here, $E_{rec}(\xi, \eta)$ is obtained by convolving the hologram transmittance with a secondary wavelet impulse response. This two-dimensional convolution integrates the contributions of wavelets from all transparent points on the hologram at downstream locations on the (ξ, η) plane.

The secondary wavelets can be modeled most generally as spherical waves emanating from point sources. Spherical waves are mathematically represented as

$$h(\xi, \eta; x, y) = \frac{1}{i\lambda} \frac{\exp(ik\rho)}{\rho} \tag{3.10}$$

in which ρ is the distance from the source [58] . To obtain $E_{rec}(\xi, \eta)$ numerically from Eq. (3.9) using a spherical wavelet would require a Fourier transform and an inverse Fourier transform. The convolution theorem states the convolution of two functions, f and g, can be expressed as

$$f * g = \mathcal{F}^{-1} \left\{ \mathcal{F} \left\{ f \right\} \mathcal{F} \left\{ g \right\} \right\} \tag{3.11}$$

where $\mathcal{F}$ and $\mathcal{F}^{-1}$ represent the Fourier and inverse Fourier transforms respectively. When applying Eq. (3.11) to Eq. (3.9), the Fourier transform of the spherical wavelet, $H = \mathcal{F} \left\{ h(\xi, \eta; x, y) \right\}$, does not have to be computed for each hologram, but a transform of the transmittance as well as an inverse transform are required for each hologram as in

$$E_{rec}(\xi, \eta) = \mathcal{F}^{-1} \left\{ H \mathcal{F} \left\{ T(x, y) \right\} \right\}. \tag{3.12}$$

Choosing a parabolic wave as a model for the secondary wavelets simplifies Eq. (3.9) such

that computing $E_{rec}(\xi, \eta)$ requires one Fourier transform. Using parabolic waves (the Fresnel approximation) provides accuracy as long as the reconstruction distance d (see Fig. 3.2) is large compared to the lateral size of the aperture. To arrive at the equation for a parabolic wave,

$$h(\xi, \eta; x, y) =$$
$$\frac{\exp(ikd)}{i\lambda d} \exp\left(i\frac{k}{2d}[(x - \xi)^2 + (y - \eta)^2]\right), \tag{3.13}$$

Eq. (3.10) is modified by approximating $\rho \approx d$ in the denominator and using a binomial expansion to approximate $\rho \approx d\left[1 + \frac{1}{2}\left(\frac{x-\xi}{d}\right)^2 + \frac{1}{2}\left(\frac{y-\eta}{d}\right)^2\right]$ in the exponential [58].

Substituting Eq. (3.13) into Eq. (3.9) and applying a change of variables

$$\nu = \frac{\xi}{d\lambda} \tag{3.14}$$

$$\mu = \frac{\eta}{d\lambda}, \tag{3.15}$$

the two-dimensional convolution reduces to a form involving one Fourier transform as in

$$E_{rec}(\nu, \mu) = A\mathcal{F}\{T(x, y)C(x, y)\}, \tag{3.16}$$

where A is a real-valued coefficient that does not effect the phase of the reconstructed field, and

$$C(x, y) = \exp\left(\frac{i\pi}{d\lambda}(x^2 + y^2)\right) \tag{3.17}$$

does not have to be computed for each hologram. The change of variables can be reversed after conducting the Fourier transform to revert to spatial coordinates, and $E_{rec}(\xi, \eta)$ can be computed numerically with a single FFT allowing expedient reconstruction of the scene phase [58]. Eq. (3.16) is called the Fresnel transform [60]. While software packages exist that conduct Fresnel transform reconstruction [65, 66], here the reconstruction is conducted

in MATLAB to facilitate data analysis and storage immediately after each plasma pulse with minimal user input.

Note that the change of variables reduces the resolution of the reconstruction. The pixel sizes in the reconstruction plane, $\Delta \xi$ and $\Delta \eta$, relate to the hologram pixel sizes, Δx and Δy, as in

$$\Delta \xi = \frac{d\lambda}{M \Delta x} \tag{3.18}$$

$$\Delta \eta = \frac{d\lambda}{N \Delta y} \tag{3.19}$$

where M and N are the total number of pixels along the x and y axes of the hologram respectively [60]. ZaP-HD's DHI's reconstructed phase resolution is near 10 μm even though its CMOS sensor has a pixel size of 3.85 μm. As the reconstruction distance increases, the reconstruction plane expands leading to lower resolution since the same number of pixels is available to resolve the larger area. In holographic reconstruction of a scene beam scattered off of a solid object, the choice of reconstruction distance selects what portion of the solid object appears in focus in the reconstructed image. Because a laser beam passing through a transparent plasma retains a planar wave front, the choice of reconstruction distance only affects the reconstructed phase's resolution and not its value. Even so, the reconstruction distance cannot be set to arbitrarily small values because the three images contained in E_{rec} of Eq. (3.8) have finite size, and the twin images can be obscured if the reconstruction distance is too short for the twin images to diverge outside the bounds of the zeroth-order diffraction image. Fig. 3.8 illustrates a reconstruction performed with a reconstruction distance just long enough to prevent the zeroth-order term from obscuring the first-order terms. The misalignment of the scene and reference beams should be maximized without inducing aliasing to allow for use of a minimal reconstruction distance.

3.4 Unwrapping the phase information of the hologram

The reconstructed phase information in one of the twin images is analyzed to extract the measured N_e given by Eq. (2.11); the rest of the reconstruction plane is discarded as it contains no additional data. The numerically reconstructed phase difference is computed as the difference

$$\Delta\phi = \phi_p(\xi, \eta) - \phi_v(\xi, \eta) \tag{3.20}$$

where ϕ_p and ϕ_v are the plasma and vacuum phases respectively, each computed using a two-argument arctangent to avoid divisions by zero, so the phase difference is confined in the interval $(-\pi, \pi]$. Phase shifts greater than 2π may still be reconstructed, but discontinuous fringe jumps occur wherever the phase crosses $\pm\pi$. A map of the actual phase shift can be recreated by unwrapping the fringe jumps.

Unwrapping algorithms typically follow an arbitrary path through the wrapped phase map and look for the fringe jumps by examining the first derivative of the phase. Where the derivative exceeds a critical value, a fringe is identified and $\pm 2\pi$ is added to all points on the remaining path. The sign of the addition depends on the sign of the derivative of the phase at the fringe jump.

Noise in the reconstructed phase can encumber unwrapping methods, but smoothing the phase map prior to unwrapping can help. Any method that smooths the phase must leave the sharp, discontinuous fringes unaffected; otherwise the derivative-based unwrapping algorithm can no longer detect the fringes. Smoothing the sine and cosine of the phase independently and then taking the arctangent of their ratio as in

$$\Delta\phi_{\text{smoothed}} = \tan^{-1}\left(\frac{(\sin\Delta\phi)_{\text{smoothed}}}{(\cos\Delta\phi)_{\text{smoothed}}}\right) \tag{3.21}$$

smooths the data while retaining the sharp fringes [60].
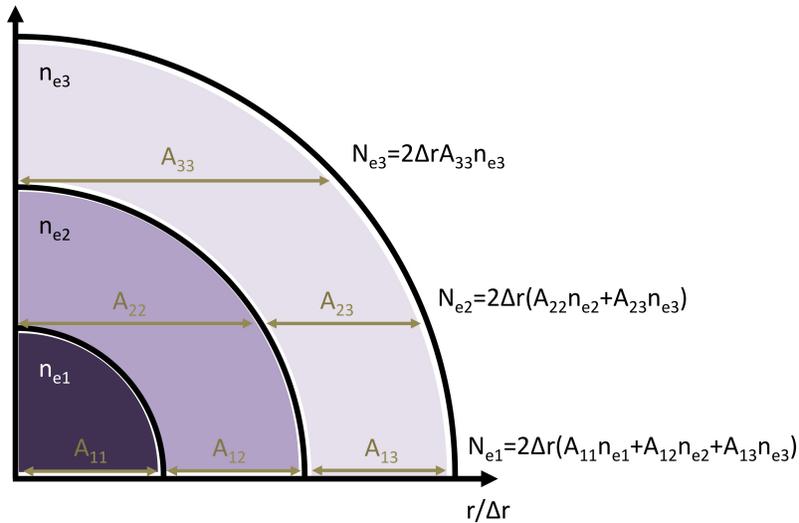
Figure 3.3: The Abel transform breaks up an axisymmetric plasma into concentric annular areas. Assuming uniform n_e in each annulus makes computation of N_e a matter of multiplying the discrete n_e by a matrix $\mathbf{A}$ containing the relative lengths of chord lengths in the geometry. The elements of $\mathbf{A}$ for a coarse discretization are shown here. $\mathbf{A}$ can be expanded to arbitrary size to transform arbitrarily large n_e profiles.

3.5 Abel transform and inversion

Assuming an axisymmetric Z-pinch allows for conversion of N_e density measured by DHI to n_e. Expressed as

$$N_e(y) = 2 \int_y^\infty \frac{n_e(r)r\,dr}{\sqrt{r^2 - y^2}}, \tag{3.22}$$

the analytic Abel transform expresses N_e as a function of impact parameter, y, in terms of n_e as a function of the radial coordinate, r. For each impact parameter, the transform integrates n_e along a chord at height y from the pinch center to infinity. Note that this transform holds if n_e is a function of r alone (ie: if n_e is axisymmetric).

The analytic transform can be discretized as in

$$\vec{N_e} = 2\Delta r \mathbf{A} \vec{n_e} \tag{3.23}$$

in terms of a matrix, $\mathbf{A}$. Figure 3.3 shows the employed discretization, which splits the plasma into concentric annular areas of uniform n_e. The thicknesses of the areas equal the resolution of the n_e profile, Δr. To compute N_e for each impact parameter, the contributions to that N_e of all the annuli are summed. The contribution of each annulus is the product of the chord length through the annulus times its n_e. The relative lengths of these chords are expressed as elements in $\mathbf{A}$, so multiplying $\mathbf{A}$ by Δr gives the actual chord lengths. Eq. (3.23) is multiplied by 2 because the matrix multiplication only integrates through half the plasma.

This discrete treatment of the Abel transform makes computing the inversion as easy as inverting $\mathbf{A}$ as in

$$\vec{n_e} = \frac{1}{2\Delta r} \mathbf{A}^{-1} \vec{N_e}. \tag{3.24}$$

The discrete Abel transform and inversion are used to convert both densities and refractive indices between line-integrated and local quantities [67].

3.6 Identifying sign of twin image phase

As discussed in Sec. 3.2, the phase shifts in the twin images are 180-degrees out of phase relative to each other. Keeping track of the coordinate system to identify which twin image corresponds to the scene beam is possible, but imaging a candle flame to perform a calibration is an easy way to verify the correct phase shift sign. The hot interior of a flame is less dense than the surrounding atmosphere, so placing a flame in the scene beam and observing the reconstructed phase provides a known reference for the phase shift sign. The flame is assumed to be neutral gas, which is significant because neutral density causes phase shifts opposite the shift caused by electron density [68].

3.7   Exploring Digital Holography's Accuracy

3.7.1   Uncertainty quantification using synthetic holograms

Synthetic holograms provide controlled inputs to test the Fresnel transform reconstruction algorithm and evaluate its accuracy. Holograms generally contain a superposition of many fringe patterns of varying length scales caused by interference between scene and reference beams, interference of reflected beams, and diffraction due to imperfections in the DHI optics (see Fig. 3.7). To match this characteristic, the synthetic holograms are constructed as sums of cosine functions as

$$T_v(x,y) = \sum_{i=1}^{N} \left\{ C_i \cos\left(\frac{2\pi}{\delta_{x,i}} x + \frac{2\pi}{\delta_{y,i}} y \right) \right\} + \zeta_h \tag{3.25}$$

$$T_p(x,y) = \sum_{i=1}^{N} \left\{ C_i \cos\left(\phi_{n_e}(x) + \frac{2\pi}{\delta_{x,i}} x + \frac{2\pi}{\delta_{y,i}} y \right) \right\} + \zeta_h \tag{3.26}$$

where the vacuum transmittance, $T_v(x,y)$, and plasma transmittance, $T_p(x,y)$, are expressed in terms of the phase shift caused by the plasma at one axial location, $\phi_{n_e}(x)$. Quantities $\delta_{x,i}$ and $\delta_{y,i}$ are the components of the ith fringe pattern's spacing, and constants C_i set the patterns' relative magnitudes. Uniform random pixel noise, ζ_h, is also added to the holograms to investigate its effects on the reconstruction.

The transmittances are scaled as 8-bit amplitude values ranging from 0 to 255 to match the bit depth of experimental JPEG holograms, and the resolution (3.85 μm) and fringe sizes of the synthetic holograms are picked to mimic experimentally observed values. Fig. 3.4 shows holograms containing two superposed fringe patterns: a purely horizontal pattern with spacing $\delta_{x,1} = 0$ μm and $\delta_{y,1} = 30$ μm and a diagonal fringe pattern with $\delta_{x,2} = 20$ μm and $\delta_{y,2} = 20$ μm.

Selection of an $n_e(r)$ profile sets $\phi_{n_e}(x)$, which appears in the plasma hologram as a
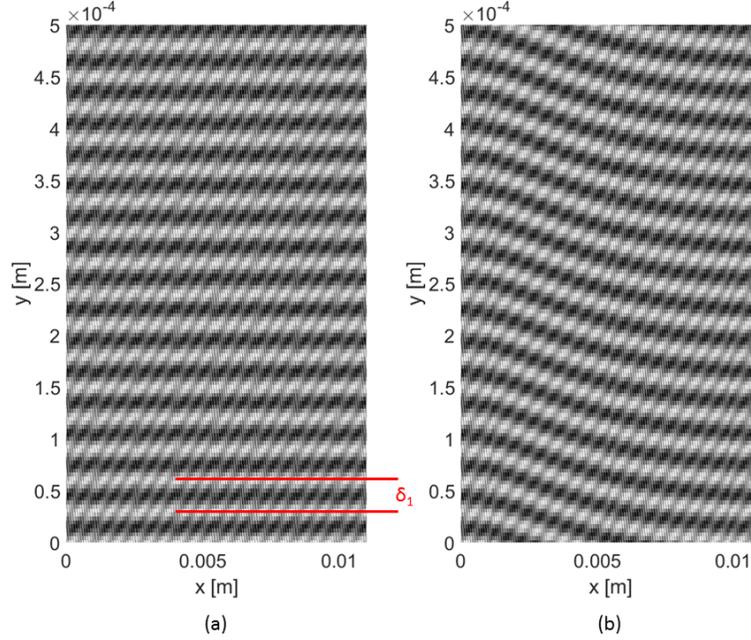
Figure 3.4: Synthetic (a) vacuum and (b) plasma holograms for the Lorentzian n_e profile of Eq. (3.29) demonstrating the phase change caused by the plasma. The vertical scales have been expanded to reveal the horizontal fringes (horizontal fringe spacing δ_1 with $\delta_{x,1} = 0$ μm and $\delta_{y,1} = 30$ μm, which causes the red-outlined twin images in Fig. 3.6). The disparity between the horizontal and vertical scales does not fully resolve the diagonal fringes (diagonal fringe spacing δ_2 with $\delta_{x,2} = 20$ μm and $\delta_{y,2} = 20$ μm), which cause the green-outlined twin images in Fig. 3.6. The phase shift $\phi_{n_e}(x)$ appears as a modulation to the plasma hologram.

modulation to both fringe patterns. Profiles considered here include

$$n_e(r) = n_{e_0} \left\{ \frac{a^2}{r^2 + a^2} \right\} \tag{3.27}$$

$$n_e(r) = n_{e_0} \left\{ \exp\left(-\frac{(r-a)^2}{(a/2)^2} \right) \right\} \tag{3.28}$$

$$n_e(r) = \frac{n_{e_0}}{2} \left\{ 1 - \tanh\left(\frac{k(r-a)}{a} \right) \right\} \tag{3.29}$$

where a is the characteristic radius of the plasma and n_{e_0} is the maximum electron density. Fig. 3.5 shows the prescribed profiles in blue. The Lorentzian profile, Eq. (3.27), has a gradual gradient. The hollow profile, Eq. (3.28), is composed of a Gaussian distribution

offset from $r = 0$. The hyperbolic tangent profile, Eq. (3.29), is internally uniform, and its edge gradient can be tuned via parameter k. A discrete Abel transform converts the selected $n_e(r)$ profile to line-integrated density, $N_e(x)$, which is related to $\phi_{n_e}(x)$ by Eq. (2.10).

The Fresnel transform reconstruction method described in Section 3.3 reconstructs the phase difference of Eq. (3.20) between the vacuum and plasma holograms at a user-defined reconstruction distance, d. The transmittances of Eqs. (3.25) and (3.26) are used in Eq. (3.16) to compute the E_{rec} for the plasma and vacuum holograms, and the phase of each hologram is computed with Eq. (3.2). The phase difference with $d = 0.6$ m is shown in Fig. 3.6. Each pair of twin images corresponds to a different cosine term, and the displacement of the twin image centers (h_{i_x}, h_{i_y}), are predictable based on the fringe spacing and reconstruction distance as in

$$h = d \tan \left(\sin^{-1} \frac{\lambda}{\delta_f} \right). \tag{3.30}$$

Recall from Section 3.2 that the twin images propagate at the incident angle of the scene beam, θ, which was prescribed by choosing fringe spacing, δ_f. Changing the reconstruction distance, d, controls the distance of the twin images from the center of the reconstruction plane, but the orientation at which the twin images are displaced from the center is controlled by the fringe orientation (e.g. the purely horizontal fringe pattern δ_1 generates the vertically displaced red twin images in Fig. 3.6 while the diagonal fringe pattern δ_2 leads to the diagonally displaced green twin images), which is physically set by the optical alignment.

Each of the twin images contains the same phase information, so any of them can be chosen for unwrapping and conversion to the reconstructed density, n_e. The synthetic holograms are uniform in y, so a single cross-section of the twin image reveals all usable information about the phase $\phi_{n_e}(x)$, which gives N_e from Eq. (2.10) and n_e from an Abel inversion. Fig. 3.5 shows the reconstructed profiles in red.

Uncertainty in the reconstructed n_e, $\sigma_{n_e}(r)$, comes from two sources: the finite resolution of the Frenel transform's FFT and hologram pixel noise, ζ_h. As described in Section 3.3, finite FFT resolution leads to resolution loss in the reconstructed twin images, which ultimately
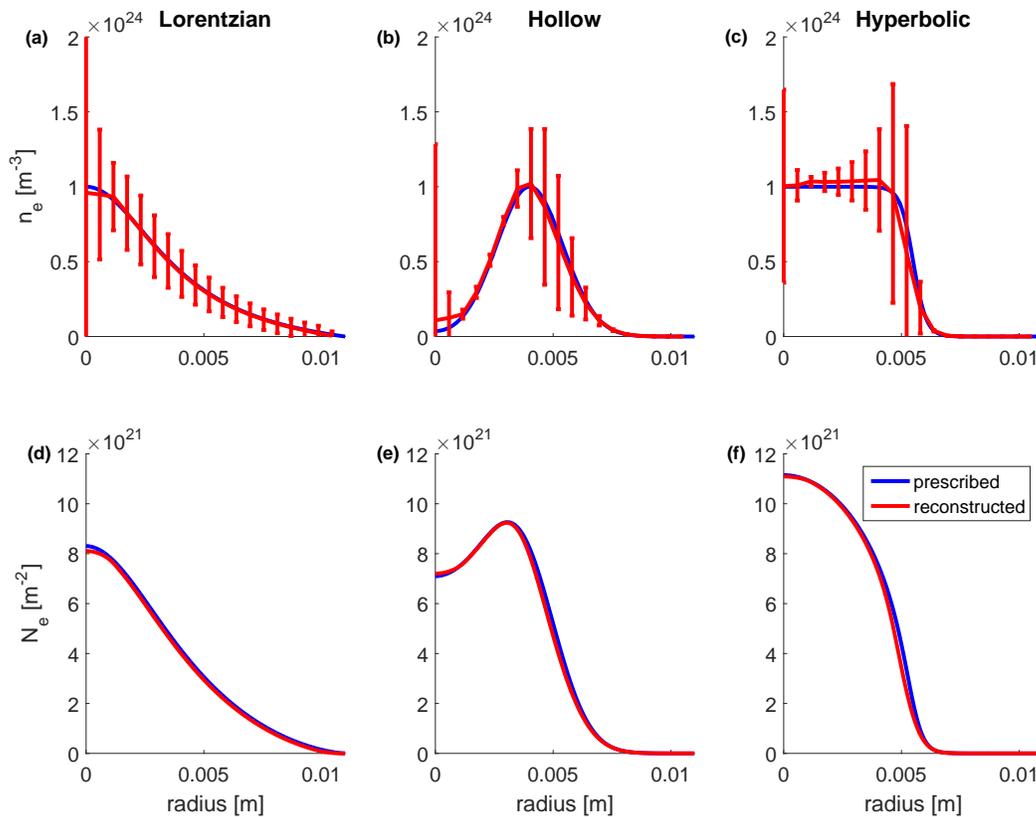
Figure 3.5: Prescribed number density profiles and their corresponding line-integrated profiles are shown in blue in (a) and (d) for the the Lorentzian profile of Eq. (3.27), (b) and (e) for the hollow profile of Eq. (3.28), and (c) and (f) for the hyperbolic tangent profile of Eq. (3.29). The red curves are the profiles reconstructed from synthetic holograms. The differences between the assumed and reconstructed line-integrated density profiles are propagated through an Abel inversion to compute the uncertainties in the number densities, which are plotted as red error bars.
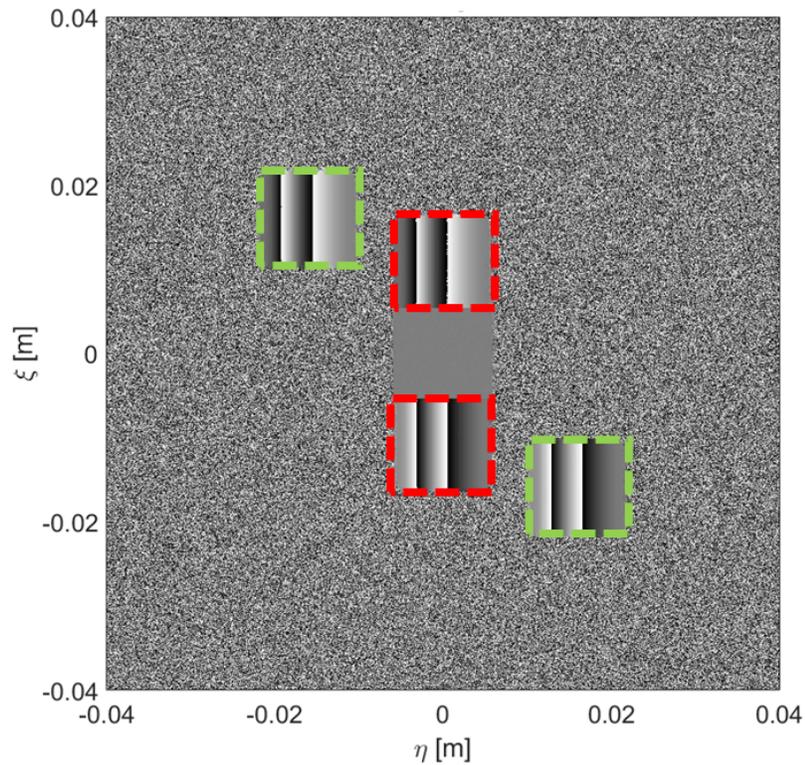
Figure 3.6: The reconstructed phase difference of the synthetic holograms of Fig. 3.4 at reconstruction distance $d = 0.6$ m. The zeroth-order diffraction image is visible at the center of the image. The twin images indicated in red come from the fringe pattern δ_1 with $\delta_{x,1} = 0$ μm and $\delta_{y,1} = 30$ μm, and the images in green come from the pattern δ_2 with $\delta_{x,2} = 20$ μm and $\delta_{y,2} = 20$ μm. Fringe jumps are visible within the twin images because unwrapping has not yet been applied.

contributes to the difference between the prescribed and reconstructed line-integrated density profiles in Fig. 3.5,

$$\sigma_{N_e}(r) = N_{e_{pre}}(r) - N_{e_{rec}}(r). \tag{3.31}$$

This difference is propagated through an Abel inversion to obtain $\sigma_{n_e}(r)$ [67]. The uncertainty caused by resolution error is isolated by conducting reconstructions with $\zeta_h = 0$, and the resulting $\sigma_{n_e}(r)$ is shown by the red error bars in Fig. 3.5. Hologram pixel noise causes additional uncertainty, which is analyzed by a Monte Carlo approach. For each profile, this analysis conducts twenty reconstructions, each with a unique set of uniform random pixel noise with a max value of 2 percent of the dynamic range of the hologram. This noise level was estimated from observing blank camera exposures. Averaging the uncertainties of the twenty reconstructions reveals the $\sigma_{n_e}(r)$ from pixel noise is insignificant compared to that from resolution error.

Reduction of $\sigma_{N_e}(r)$ is possible by increasing sensor resolution, which allows measurement of finer fringe patterns. Generating finer fringes requires greater misalignment of scene and reference beams, and increased misalignment allows for unobstructed twin images with a shorter reconstruction distance. This leads to larger twin images with better resolution. Note that the resolution error observed in Fig. 3.5 depends on the shape of the prescribed n_e profile. For reasonably smooth and continuous profiles, Fresnel transform reconstruction provides accurate density data.

3.7.2   Experimental data

Analyzing experimental data is more challenging since there is no prescribed profile structure. Unlike with the synthetic data where the plasma's density centroid is specified to reside on the edge of the hologram, the centroid of an empirical measurement could reside outside the bounds of the image. Because the Abel inversion employed is sensitive to centroid location [50], accurate inversion demands the centroid reside somewhere within the hologram where it can be unambiguously located.
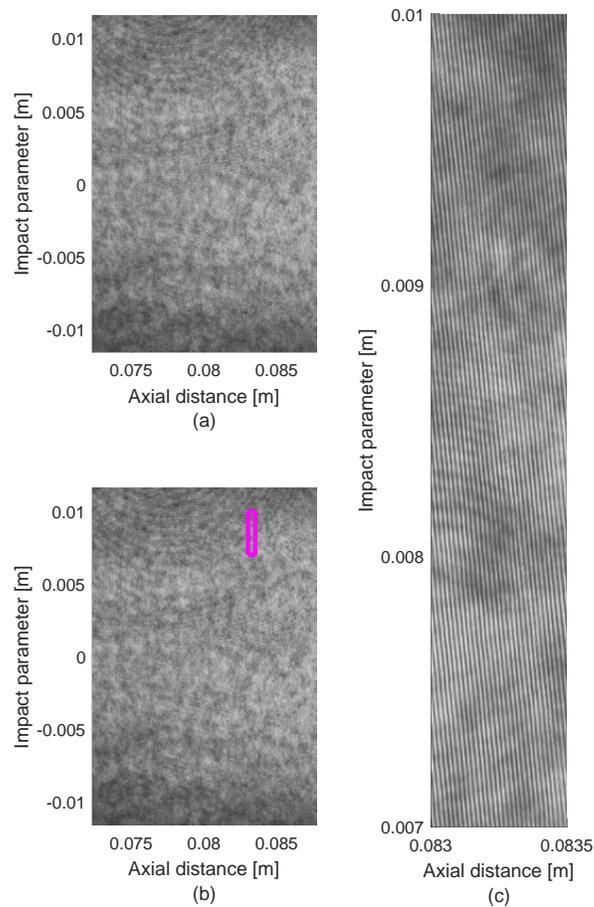
Figure 3.7: Raw experimental (a) vacuum (pulse 160524020) and (b) plasma (pulse 160524021) holograms. The horizontal axes measure the distance downstream from the ZaP-HD nose cone, and the vertical axes indicate the impact parameter relative to the geometric axis of the outer electrode. The full holograms exhibit aliasing at this size, so the subsection of the plasma hologram identified by the magenta box has been magnified in (c) to resolve the approximately vertical $d_f \approx 20$ μm fringes. The small fringe size and gradual density gradient make it difficult to see the phase shift in the raw data, but Fresnel transform reconstruction reveals shifts of approximately one fringe.

For each axial cross-section, an iterative analysis searches for a centroid location and edge density value to make the n_e profiles on either side of the centroid as similar as possible, thereby enforcing the axisymmetry condition implicit in the Abel inversion. The centroid search is centered about the peak in N_e, and an Abel inversion is applied to the N_e profiles on either side of each centroid. The number density at the edge of one of the profiles is also varied to maximize profile similarity. If the lengths of the two sides are equal, the edge with the lower phase value is set at zero density, and the other edge value is iteratively increased starting from zero. If the lengths differ, the edge of the longer profile is taken to be zero density, and the edge of the shorter profile is varied through values centered on the density of the longer profile at the same radial distance. Profile similarity is maximized by minimizing

$$\Psi = \frac{\sqrt{\sum_{i=1}^{K} |n_{e_{\text{left}}}(r) - n_{e_{\text{right}}}(r)|^2}}{K}, \tag{3.32}$$

the l^2-norm of the difference between the resulting n_e profiles to the left and right of the centroid normalized by K, the number of pixels common to both sides of the cross-section.

All the Abel inversions done in this analysis assume zero N_e at the edge, which is not always true and therefore requires correction. Prior to each inversion, the edge value of N_e is subtracted from the profile, and then the resulting n_e profile is corrected by adding a constant number density. For a given cross-section, the first such correction takes place when different edge densities are added to one of the profiles to optimize profile similarity. After identifying the best centroid and edge density, the analysis accounts for axial variations in N_e. Axial variation in N_e means the edge N_e will generally be non-zero and require a correction applied to the profiles on both sides of the centroid. These corrections are computed by dividing the N_e at the edge by the path length through ZaP-HD's outer electrode at the edge's impact parameter.

The analysis is shown here for a plasma pulse with 9 kV acceleration bank charge and 8 kV compression bank charge, which drove approximately 90 kA through the plasma at the time and location imaged. Raw holograms are shown in Fig. 3.7, and although the full holograms
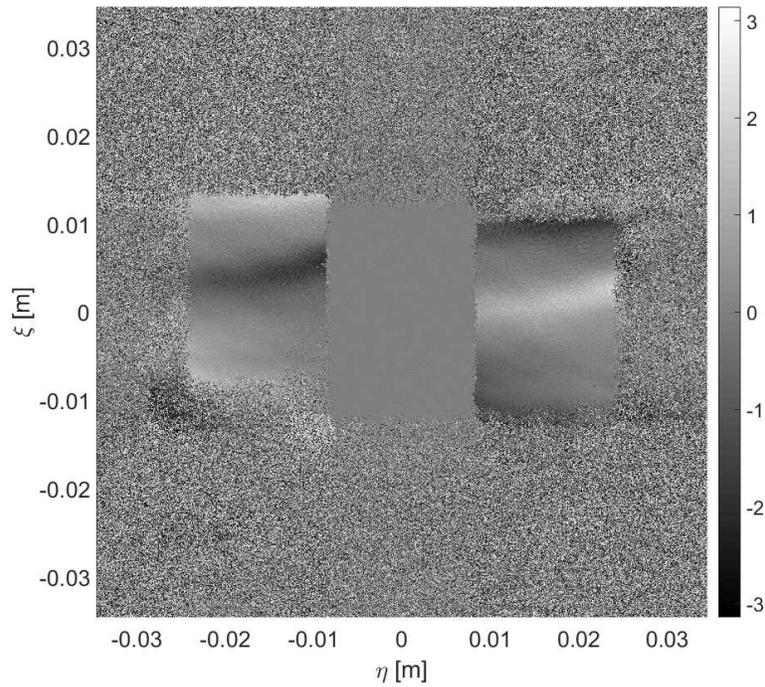
Figure 3.8: The reconstructed phase difference (between pulses 160524021 and 160524020) at a reconstruction distance $d = 0.5$ m. This figure shows the equivalent of the reconstructed phase difference shown in Fig. 3.6 for experimental plasma data. The choice of reconstruction distance here maximizes the size of the twin images and therefore the resolution obtained for the reconstruction. A smaller reconstruction distance would lead to the zeroth-order image obscuring the twin images.
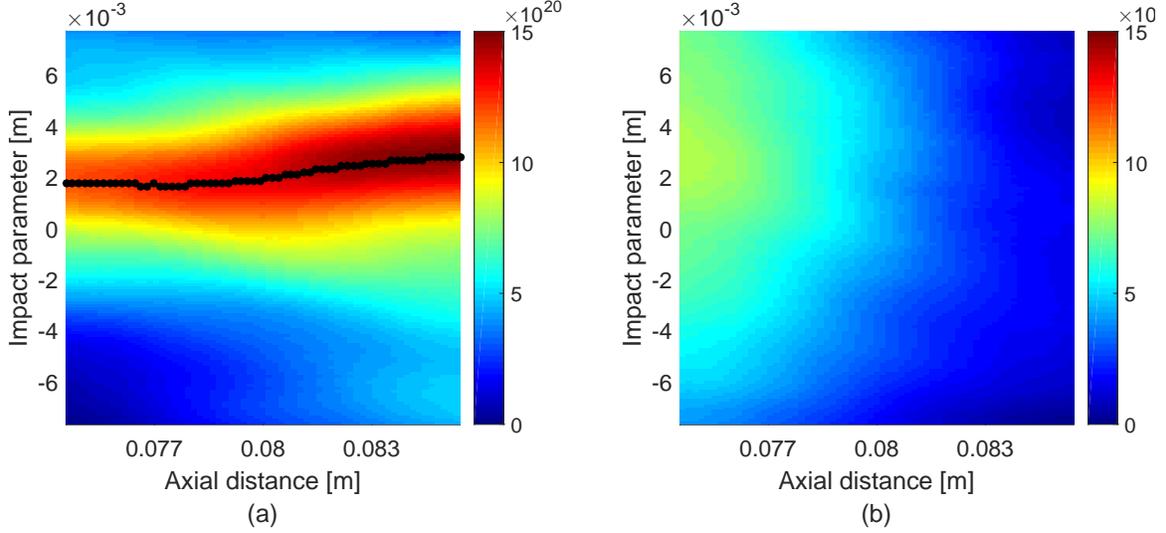
Figure 3.9: (a) A subsection of one of the twin images of Fig. 3.8 smoothed and converted to N_e. The horizontal axis measures the distance downstream from the ZaP-HD nose cone, and the vertical axis indicates the impact parameter relative to the geometric axis of the outer electrode. The black dots indicate centroid locations identified by the Abel inversion process. (b) A twin image of N_e obtained from computing the phase difference between two vacuum holograms (pulses 160524020 and 160524017), one of which was used to find the phase difference with the plasma hologram leading to Fig. 3.9(a). The N_e variation of 1.5×10^{21} m^{-2} observed across axial cross-sections of (a) is much larger than the 3×10^{20} m^{-2} variation seen across (b).

printed at this size exhibit aliasing, a subsection of the plasma hologram is magnified to resolve the $\delta_f \approx 20$ μm interference fringes. Fig. 3.8 shows the reconstructed phase difference prior to smoothing and further processing. To maximize the spatial resolution of the phase difference, the reconstruction distance is selected such that the twin images just border the zeroth-order image. Smoothing one of the twin images from Fig. 3.8 and converting it to line-integrated density yields the contour plot of N_e in Fig. 3.9(a), which shows a profile peaked within the image.

Several vacuum holograms are collected during each experimental run day by triggering DHI prior to gas injection, which provides a measurement of background variations between

plasma pulses. Computing the phase difference between two vacuum holograms ideally results in a perfectly flat map of N_e, but in practice some non-uniformity exists. Installation of beam guide tubes along the laser path is necessary to reduce variations between vacuum holograms caused by air currents. Fig. 3.9(b) is the phase difference of two vacuum holograms converted to N_e. One of these two vacuum holograms was used to compute the phase difference of Fig. 3.8 and N_e of Fig. 3.9(a). The N_e in Fig. 3.9(b) varies as much as 3×10^{20} m^{-2} across an axial cross-section, which is much smaller than the 1.5×10^{21} m^{-2} variation observed across Fig. 3.9(a).

Performing the Abel inversion and adding the edge densities that maximize symmetry and account for axial variation leads to Fig. 3.10, a contour plot of n_e. The DHI resolves radial and axial structures, with density peaking around 2.5×10^{23} m^{-3} at the center of a pinch with radius $a \approx 2.5$ mm, which is reasonable for a Z-pinch in equilibrium with $T_e = 1000$ eV and a peak magnetic field around 9 T computed with the uniform drift velocity model of Ch. 4. The axial variation along the bottom of Fig. 3.10 of around 1×10^{21} m^{-3} is insignificant compared to the peak density. The similarity of the sides of the n_e cross-sections is evident in Fig. 3.11, which shows n_e profiles corresponding to the vertical lines in Fig. 3.10.

The peak density and pinch radius from ZaP-HD compare favorably with profiles measured on the original ZaP experiment with a heterodyne quadrature interferometer. Although that interferometer does not have the spatial resolution necessary to measure ZaP-HD's profiles, it is sufficient to measure ZaP's pinches ($a \approx 6-10$ mm). It resolves profiles with peak densities around $2-6 \times 10^{22}$ m^{-3} at $40-60$ kA pinch currents [69]. Using measurements of ZaP as an initial plasma condition, Eqs. (1.9) are applied to scale to the current and linear density seen on ZaP-HD. The resulting density and pinch size are consistent with the DHI measurements of ZaP-HD.

As described in Section 3.7.1, $\sigma_{n_e}(r)$ depends on density profile shape, so each profile requires its own uncertainty analysis. For each measured n_e profile, a test hologram is generated by the same means as the synthetic holograms of Section 3.7.1 except now the measured profile is used in place of a prescribed profile. Each test hologram is reconstructed,
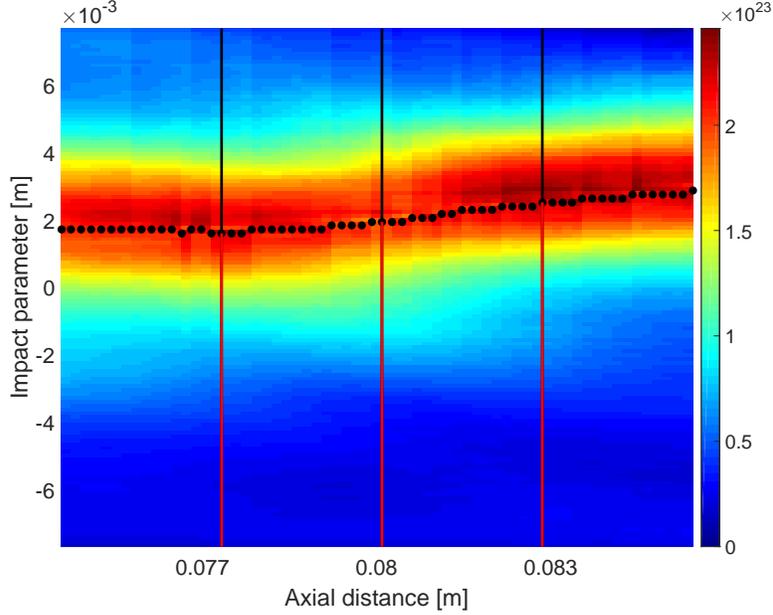
Figure 3.10: The n_e from Abel inversion of the N_e in Fig. 3.9(a) using the centroids plotted as black dots. The vertical lines correspond to the profiles plotted in Fig. 3.11.

and the N_e profiles before and after the reconstruction are subtracted to give $\sigma_{N_e}(r)$ of Eq. (3.31), which is then propagated to obtain $\sigma_{n_e}(r)$. Each test hologram is created with a single fringe pattern of $\delta_x = 20$ μm and $\delta_y = 0$ μm and spatial resolution of 3.85 μm to mimic experimental holograms. Fig. 3.11 shows the uncertainty in n_e as errorbars with the experimental profiles. Note that these errorbars do not include the uncertainty implied by the phase shifts seen between vacuum holograms.

Details about the set up and operation of the DHI system can be found in the appendices. Appendix B describes how to align the interferometer and how to run the system with ZaP-HD to collect data. Appendix C explains how to run the basic hologram analysis codes.
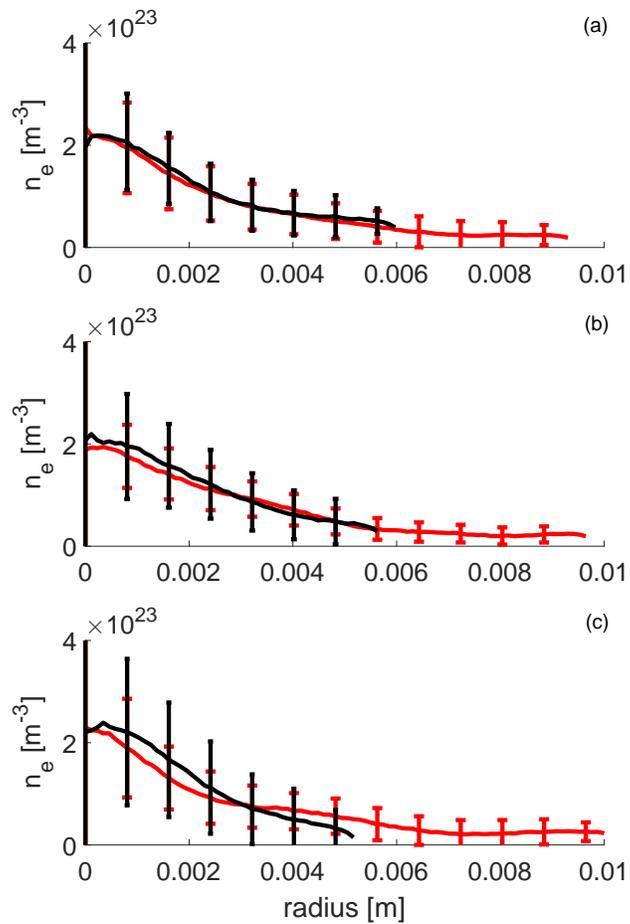
Figure 3.11: The two sides of the n_e cross-sections are shown for axial locations (a) $z = 0.077$ m, (b) $z = 0.080$ m, and (c) $z = 0.083$ m corresponding to the vertical lines in Fig. 3.10. For each cross-section, the red profile shows the side with impact parameters less than the centroid, while the black is the side with impact parameters greater than the centroid. The search for centroid and edge density maximizes the similarity between the sides of each cross-section. The errorbars shown correspond to the uncertainty σ_{n_e}, which includes error from Abel inversion.

Chapter 4

EVALUATING ZAP-HD'S CONFINEMENT WITH DENSITY MEASUREMENTS AND Z-PINCH EQUILIBRIUM MODELS

Measuring density profiles from many plasma shots allows empirical analysis of ZaP-HD's confinement and scaling. This chapter describes equilibrium modeling that allows computation of other plasma properties from the DHI-measured density profiles. These computed plasma properties characterize ZaP-HD's confinement, and analyzing data from many plasma pulses enables comparison of empirical Z-pinch scaling to the theoretical scaling described in Sec. 1.1.3.

4.1 Modeling the Z-pinch equilibrium

Although Ch. 2 describes the ZaP-HD lifetime as a pulsed, dynamic process, a force balance equilibrium does not require steady state behavior in which all plasma properties are constant in time. A time dependent equilibrium maintains force balance while the internal energy changes with time [70]. This section presents one means of applying force balance to n_e profiles measured on ZaP-HD to compute profiles of B and T_e.

Assuming a spatially uniform plasma drift velocity,

$$v_d = v_e - v_i, \tag{4.1}$$

greatly simplifies the equilibrium analysis. Then, the current density becomes proportional to the electron density, i.e. the current becomes proportional to the number of charge carriers, as in

$$j_z(r) = -v_d e n_e(r). \tag{4.2}$$

The drift velocity is computed by numerically integrating $n_e(r)$ as in

$$v_d = -\frac{I}{2\pi e \int_0^a n_e(r) r \, dr},$$

(4.3)

where the total current $I = 2\pi B_{\theta_0} R_0 / \mu_0$ is computed from B_{θ_0}, the azimuthal magnetic field measured by magnetic field probes embedded in the outer electrode, at radius R_0. All the plasma current is assumed to flow within radius a.

Integrating Ampere's law

$$\mu_0 \vec{j} = \nabla \times \vec{B}$$

(4.4)

gives

$$B_\theta(r) = \begin{cases} \frac{\mu_0 e v_d}{r} \int_0^r n_e(\imath) \imath \, d\imath & r < a \\ \frac{\mu_0 I}{2\pi r} & r \geq a \end{cases}$$

(4.5)

where $\imath$ is a dummy variable for integration.

Integrating force balance

$$\nabla P = \nabla(2 n_e k T_e) = \vec{j} \times \vec{B}$$

(4.6)

gives

$$T_e(r) = \begin{cases} \frac{e v_d}{2 n_e(r) k} \int_a^r n_e(\imath) B_\theta(\imath) \, d\imath & r < a \\ 0 & r \geq a \end{cases}$$

(4.7)

where k is Boltzmann's constant. The pressure is $P = 2 n_e k T_e$ assuming the ideal gas law, $n_e \approx n_i$, and $T_e \approx T_i$, which are conditions observed on ZaP [69]. The integration in Eq. (4.7) assumes as a boundary condition that the plasma pressure is zero at and beyond a. Force balance in the radial direction is

$$\frac{d}{d\imath}(2 n_e T_e) = -j_z B_\theta = e v_d n_e B_\theta.$$

(4.8)

Integrating both sides

$$\int_a^r \frac{d}{d\imath} \left(2 n_e T_e\right) d\imath = e v_d \int_a^r n_e B_\theta d\imath \tag{4.9}$$

$$2 \left(\left. n_e T_e \right|_{\imath=r} - \left. n_e T_e \right|_{\imath=a} \right) = e v_d \int_a^r n_e B_\theta d\imath \tag{4.10}$$

reduces to the form in Eq. (4.7) since $\left. n_e T_e \right|_{\imath=a} = 0$.

Although ZaP-HD relies on bulk flow shear for stabilization of MHD modes, this does not universally invalidate the application of a uniform drift velocity model because the drift velocity and bulk plasma velocity are independent. Commonly known as viscosity, momentum transfer across adjacent layers of flow plays an integral role in shaping velocity profiles. Assuming $n_i \approx n_e$ in MHD, the bulk flow velocity, v, reduces to $v \approx v_i$ because ions carry the vast majority of the flow inertia. Therefore, ion viscosity mediates the bulk flow shear. Conversely, the drift velocity profile is controlled by both the ion and electron viscosities. Differences in the viscosities and species flow velocities can expand the applicability of the uniform v_d model.

Understanding where the model best applies requires some comprehension of the difference between ion and electron viscosities. The following provides a cursory explanation of plasma viscosity relevant to the present discussion, and a more detailed treatment applicable to ZaP-HD exists [35]. In a ZaP-HD-relevant Cartesian coordinate system with magnetic field in the z-direction, axial flow in the x-direction, and flow shear in the y-direction, the non-zero viscous components of Maxwell's stress tensor in an unmagnetized plasma ($\omega_i \tau_{ii} << 1$, where ω_i is the ion cyclotron frequency and τ_{ii} is the ion-ion collision time) are $\pi_{xy} = \pi_{yx} = -\eta_0^\sigma \frac{\partial v_x}{\partial y}$ where σ represents species. The viscosities for the ions and electrons are

$$\eta_0^i = 0.96 n_i T_i \tau_{ii} \tag{4.11}$$

$$\eta_0^e = 0.73 n_e T_e \tau_{ee}, \tag{4.12}$$

where τ_{ee} is the electron-electron collision time.

In a magnetized plasma ($\omega_i \tau_{ii} >> 1$), the stress tensor components are $\pi_{xy} = \pi_{yx} = -\eta_1^\sigma \frac{\partial v_x}{\partial y}$ where the ion and electron viscosities are

$$\eta_1^i = 0.3 \frac{n_i T_i}{\omega_i^2 \tau_{ii}} \tag{4.13}$$

$$\eta_1^e = 0.51 \frac{n_e T_e}{\omega_e^2 \tau_{ee}} \tag{4.14}$$

and ω_e is the electron cyclotron frequency [71].

In the unmagnetized region, the viscosity is directly proportional to the collision times. More time between collisions means that particles uninfluenced by a magnetic field travel longer distances between collisions thereby transfering their momentum across a larger distance. In the magnetized region, the viscosity varies inversely with the collision time. The magnetic field confines the moving particles, so more time between collisions does not lead to more effective transfer of momentum. When the particles are bound close to a field line, the more effective means of transferring momentum is through a larger number of collisions. In a heuristic sense, more frequent collisions serve to transfer momentum from particles surrounding one field line to the particles surrounding adjacent field lines. For equal species temperatures, $T_i = T_e$, the ratio of the collision times is

$$\tau_{ee} : \tau_{ii} : \tau_{ei} = 1 : \sqrt{\frac{m_i}{m_e}} : \frac{m_i}{m_e}. \tag{4.15}$$

In magnetized plasmas, the electron viscosity is larger than the ion viscosity by a factor of m_i/m_e. In unmagnetized plasmas, the ion viscosity exceeds the electron viscosity by the same m_i/m_e factor. The bulk plasma flow shear exists at the plasma edge, where the magnetic field is highest and ion viscosity is low. In this magnetized region, electron viscosity is far higher than the ion viscosity, which should lead to a relatively flat electron velocity profile. The ion viscosity is highest at the unmagnetized plasma center and compels a uniform bulk plasma velocity in the core plasma. It is more difficult to predict the electron viscosity at

the plasma center without separate measurements of n_e and T_e.

Because the uniform v_d model has limitations, understanding those limits is important when applying the model to analyze equilibria. When $v_d \gg v_i$ and the electron viscosity is sufficient to flatten the v_e profile, v_d becomes uniform as the amount of bulk shear is insignificant compared to the magnitude of v_d. If the electron viscosity is low in the core, the uniform drift velocity model may not be as accurate in the center of the plasma as shear in v_e could exist with little damping. As v_d approaches v_i, the uniform v_d model becomes less accurate as bulk shear becomes more of an influence on the v_d profile.

The radius a in Eqs. (4.3-4.7) is chosen as the radius at which the density drops to half its peak value to match a previous investigation on ZaP [69]. Although meant to facilitate comparison with previous analysis, this choice is somewhat arbitrary. Figure 4.1 shows the sensitivity of several parameters to the plasma radius for the red Lorentzian profile of Fig. 4.2 defined by Eq. (4.16) with peak density of 10^{23} m^{-3}, $a_l = 0.004$ m, and plasma current $I = 100$ kA. Note that a_l defines the profile in Eq. (4.16) and, unlike a, does not necessarily correspond to the radius where n_e drops to half its maximum. The drift velocity decreases with increased radius, and the region at small radii where the drift velocity exceeds the thermal velocity is not physical as microinstabilities described in Sec. 1.1.2 act to decrease v_d to v_{th_i} when $v_d > v_{th_i}$. The magnetic field at the edge $B_\theta(a)$ is less sensitive at larger radii where $v_d < v_{th_i}$ as is the maximum T_e.

The shape of a measured density profile also affects the equilibrium analysis. In Ch. 3, error analysis quantifies the uncertainty in the measured density profiles, and this uncertainty propagates to the computed fields and temperatures. Figures 4.2 and 4.3 illustrate the error propagation for various Lorentzian-like profiles. The red profiles in each figure are prescribed the same as the Lorentzian shown in Fig. 3.5 except the peak densities of 10^{23} m^{-3} are chosen to more closely match measured values. The red error bars are obtained through the process described in Sec. 3.7.1. Modifying the shape of the Lorentzian profile of Eq. (3.27) to include a changable parameter, h, as in

$$f(r) = \frac{a_l}{hr^2 + a_l^2},$$
(4.16)
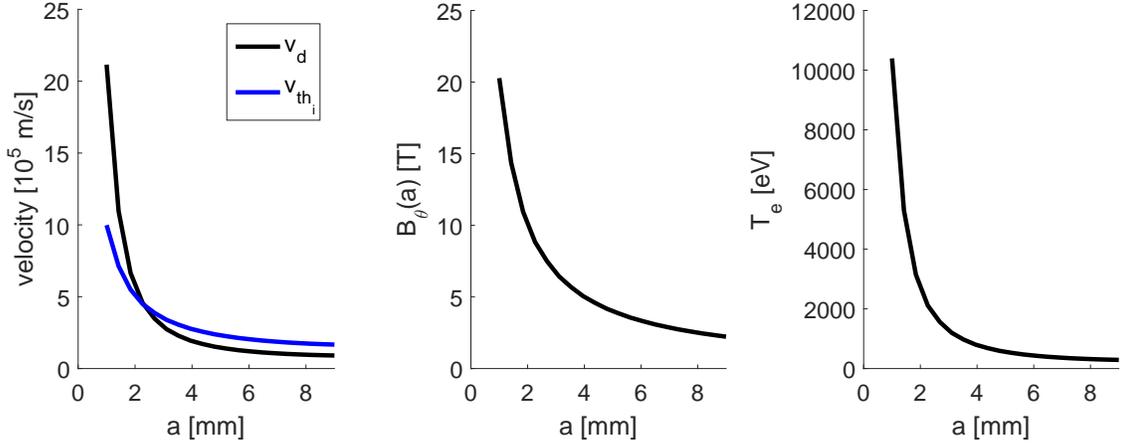
Figure 4.1: The sensitivity of plasma parameters to chosen plasma radius a. Conditions where $v_d > v_{th_i}$ are non physical. The magnetic field at the plasma radius $B_\theta(a)$ is less sensitive at larger radii as is the maximum T_e.

allows tuning of the profile shape. Here, a_l is the characteristic radius selected to define the profile. Enforcing the profile to go to zero at radius R_{max} and normalizing to allow easy selection of peak density, n_0, yields

$$n_e(r) = n_0 \frac{f(r) - f(R_{max})}{f(0) - f(R_{max})} \tag{4.17}$$

as an adjustable, Lorentzian-like profile valid for $r = [0, R_{max}]$.

Computing the equilibrium analysis for various Lorentzian-like profiles within the error bars of the red prescribed Lorenztian profile provides insight into the uncertainty of the field and temperature. The three tested profiles in Fig. 4.2 are the same shape (i.e. they all have $h = 1$) but have different peak densities. Changing the peak density does not change the magnetic field profiles while it does affect the temperature profiles. Fig. 4.3 shows three Lorentzian-like profiles with the same peak density but with different shapes. Varying the shape has a more pronounced effect on temperature and affects the field because such changes affect the plasma radius a.
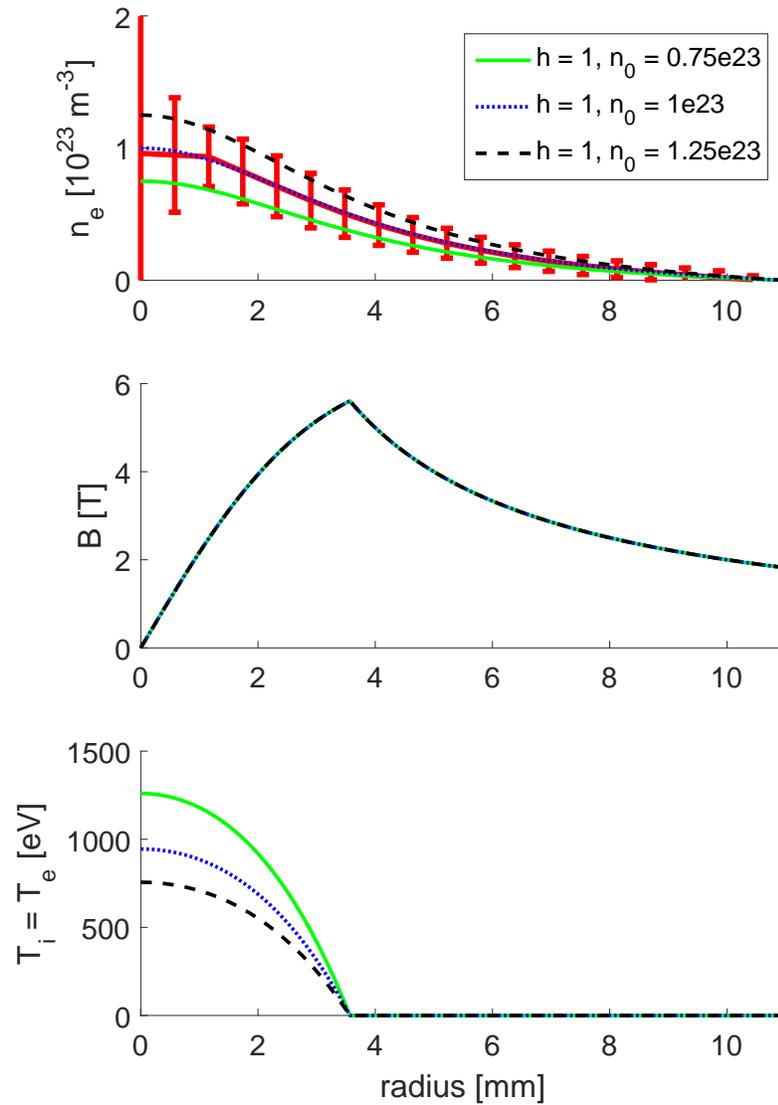
Figure 4.2: Results of equilibrium analysis of three Lorentzian density profiles with different peak densities and identical shape parameter, $h = 1$. Changing the peak density does not affect the magnetic field, but it does change the temperature profile. Changing only the peak density does not affect the radius a.
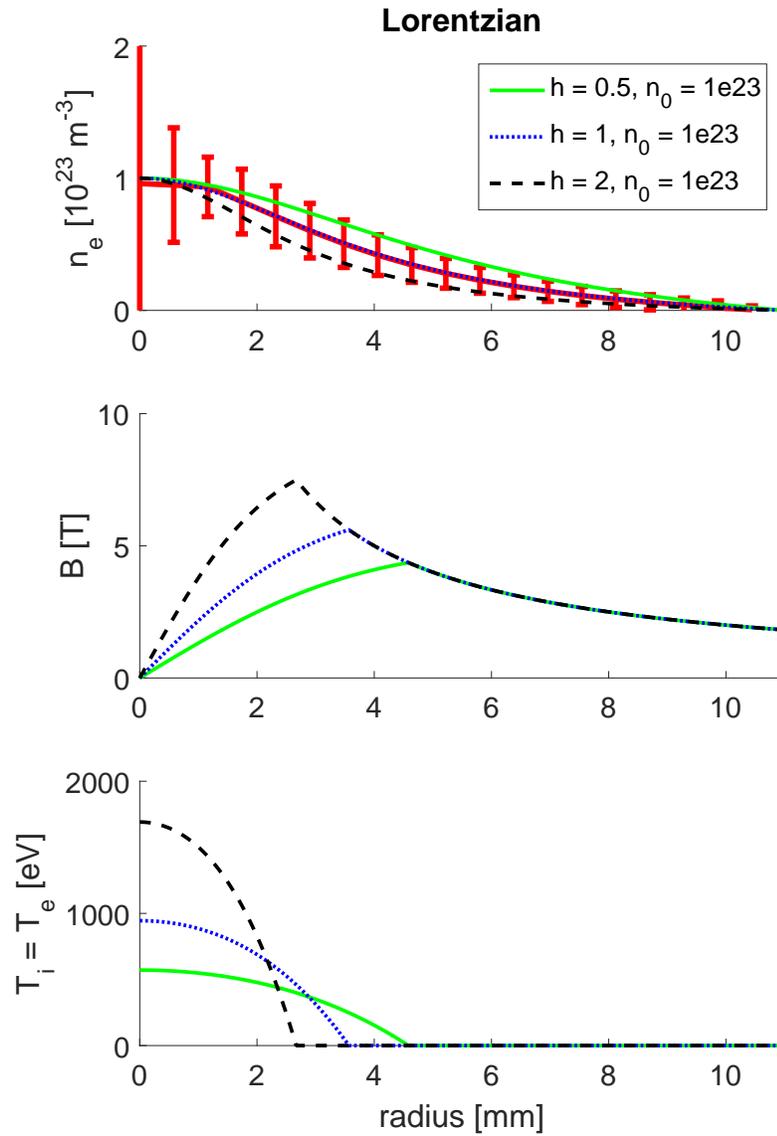
Figure 4.3: Results of equilibrium analysis of three Lorentzian-like density profiles with identical peak densities and different shape parameters. Changing the density profile shape affects both the field and the temperature. Note that changing the profile shape affects radius a.

Conducting a similar analysis for the hyperbolic tangent profile from Sec. 3.7.1,

$$n_e(r) = \frac{n_{e0}}{2}\left\{1 - \tanh\left(\frac{k(r - a_h)}{a_h}\right)\right\}, \tag{4.18}$$

provides additional insight. Here, k allows tuning of the profile steepness, and the radius of the specified profile, a_h, is also tunable. Fig. 4.4 shows the field and temperature are insensitive to the steepness of this profile type. The size of the pinch has a much greater effect, with smaller pinches exhibiting higher fields and temperatures.

In general, changes in the plasma radius, a, can significantly affect the field and temperature profiles. Observing how the field and temperature profiles change in response to changes in density suggests computed peak temperatures and edge field magnitudes likely lie within a factor of two of their nominal values.

4.2 Applying equilibrium analysis to individual ZaP-HD pulses

Applying the equilibrium analysis of the previous section to measured density data reveals the shape of plasma parameters in experimental plasma pulses. The DHI's axial resolution allows for identification of non-adiabatic heating mechanisms for individual plasma pulses.

As seen in the synthetic data of Sec. 4.1, computed magnetic field and temperature profiles are sensitive to the specific shape of the density profile. Figs. 4.5 and 4.6 show the computed Z-pinch equilibria for different experimentally-measured plasma density profiles. Fig. 4.5 exhibits a relatively narrow density profile from pulse 160524021 with high fields and temperatures, while Fig. 4.6 shows a wider density profile from pulse 160628009 with correspondingly reduced fields and temperatures. These figures identify the peak density, peak temperature, and magnetic field at the radius a as characteristic equilibrium parameters. Reducing the profiles down to these characteristic values enables the comparison across many plasma pulses performed in Sec. 4.3.

Applying the equilibrium analysis to all density profiles from a hologram reveals two-dimensional field and temperature structure. Computed field and temperature contour plots
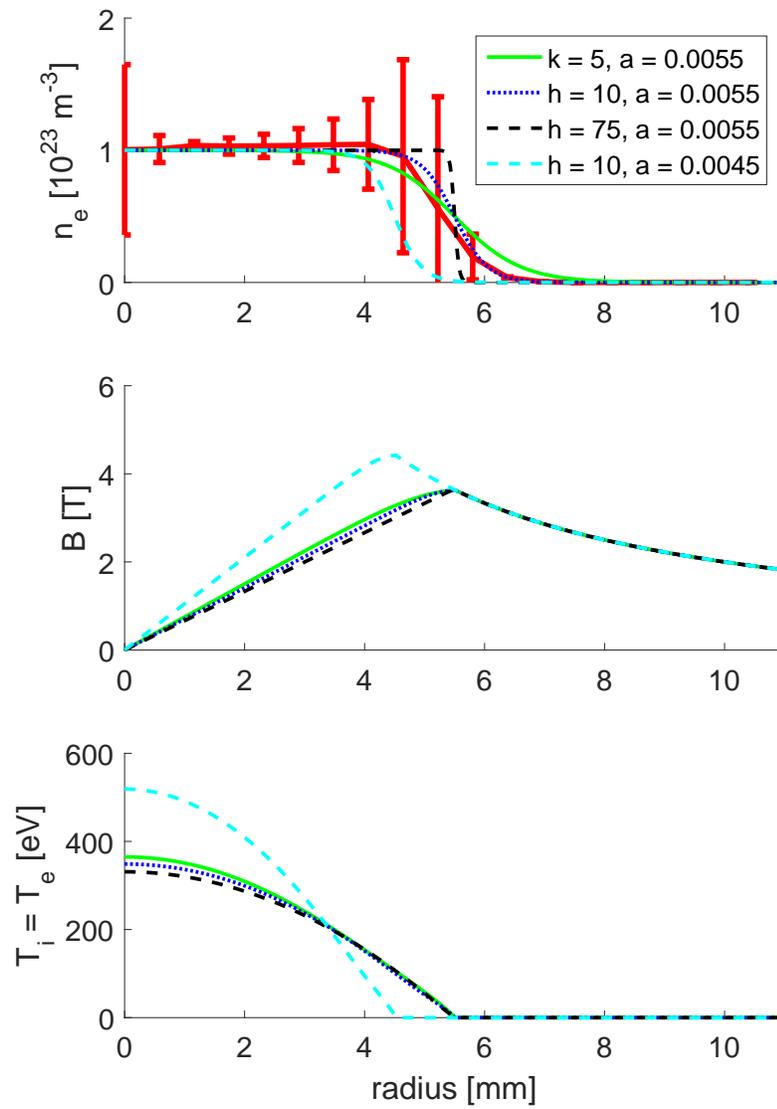
Figure 4.4: Results of equilibrium analysis of four hyperbolic tangent profiles with varying steepness and size. The field and temperature are insensitive to profile steepness, while changing the specified radius makes a greater difference in the analysis.
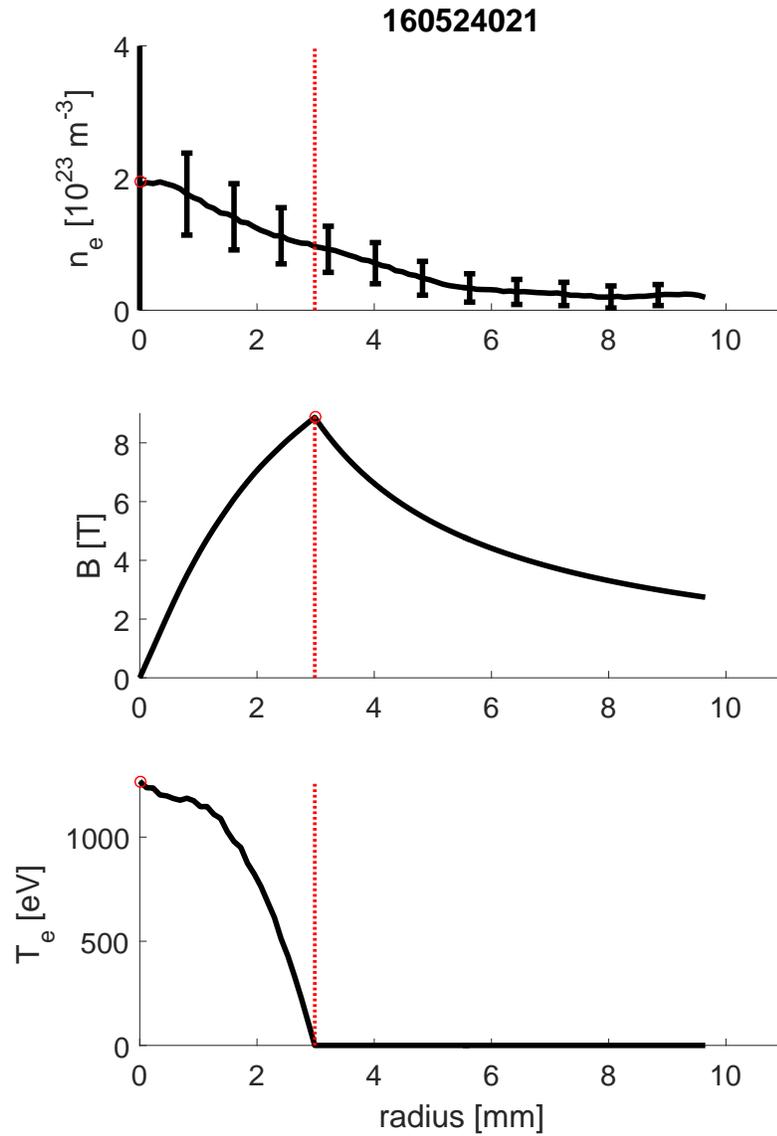
Figure 4.5: Cross-sections of measured density and computed field and temperature from the uniform drift velocity equilibrium model for pulse 160524021. This pulse exhibits relatively narrow profiles. The vertical red lines indicate the pinch radius, a, and the red circles indicate the peak density, edge field, and peak temperature values taken as characteristic property values.
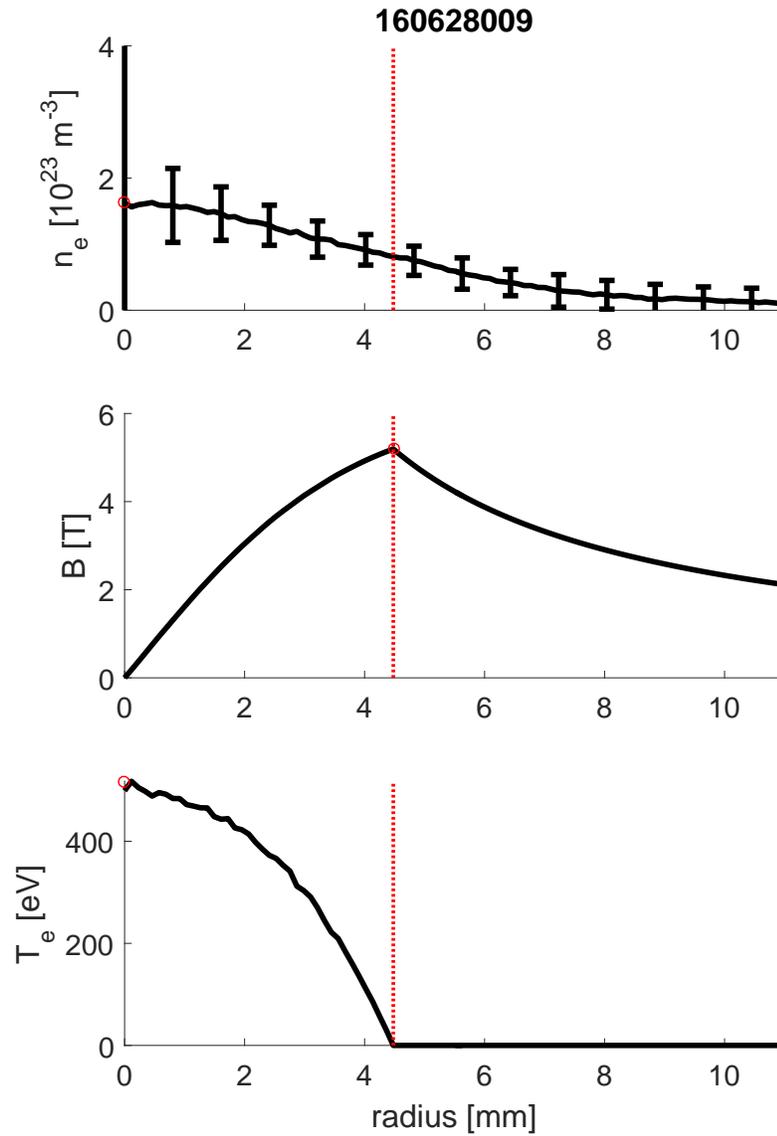
Figure 4.6: Cross-sections of measured density and computed field and temperature from the uniform drift velocity equilibrium model for pulse 160628009. This pulse exhibits relatively wide profiles. The vertical red lines indicate the pinch radius, a, and the red circles indicate the peak density, edge field, and peak temperature values taken as characteristic property values.
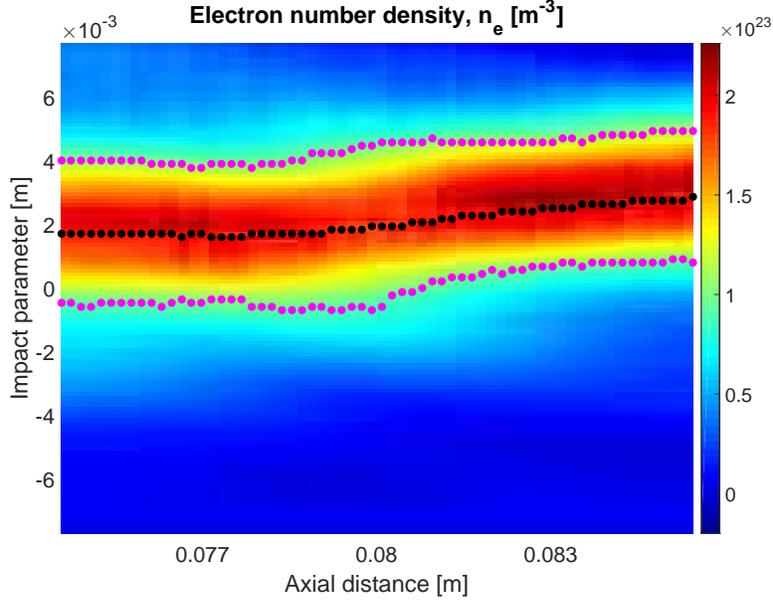
Figure 4.7: Contour plot of electron density measured on pulse 160524021 with markers indicating density centroid and pinch size. The black markers indicate the density centroids identified during Abel inversion, and the magenta markers show the radius a for each profile defined as the location where the density drops to half the max value in the cross-section. The plasma radius bulges slightly near 0.081 m but otherwise remains largely uniform axially.

corresponding to the density contour of Fig. 4.7 are shown in Figs. 4.8 and 4.9 respectively. The field and temperature show mild axial variation due to the plasma radius bulge at $z = 0.081$ m.

Observing how pinch properties relate for individual pulses indicates the mechanisms of Z-pinch heating in ZaP-HD. Specifically, data from equilibrium modeling can distinguish between adiabatic and non-adiabatic processes. For an adiabatic process, the number density scales as

$$
\begin{aligned}
\frac{n_2}{n_1} &= \left(\frac{T_2}{T_1}\right)^{\frac{1}{-\gamma-1}} \\
&= \left(\frac{I_2}{I_1}\right)^{\frac{2}{\gamma-1}} \left(\frac{N_2}{N_1}\right)^{\frac{1}{\gamma-1}} .
\end{aligned}
\tag{4.19}
$$
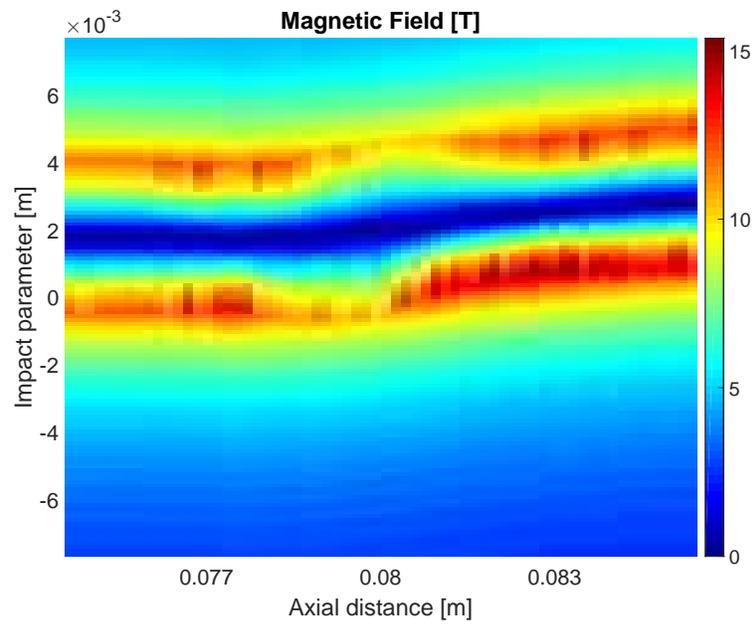
Figure 4.8: Contour plot of magnetic field strength computed from uniform drift velocity equilibrium analysis for pulse 160524021. The density contour for this relatively axially uniform pulse is Fig. 4.7.
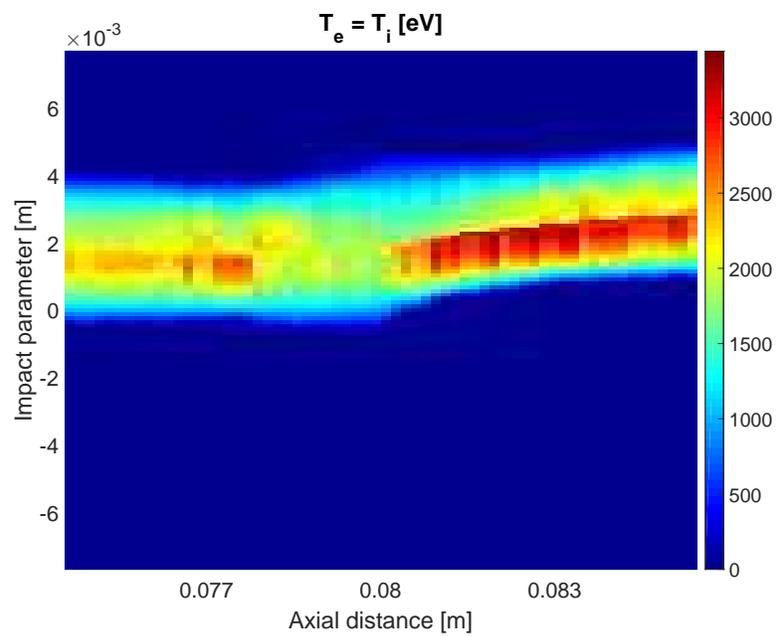
Figure 4.9: Contour plot of temperature, $T_e = T_i$, computed from uniform drift velocity equilibrium analysis for pulse 160524021. The density contour for this relatively axially uniform pulse is Fig. 4.7.

Combining Eq. 4.19 with $n = N/\pi a^2$ and Ampere's law, $B = \mu_0 I/2\pi a$, leads to

$$\frac{T_2}{T_1} = \left(\frac{a_2}{a_1}\right)^{-2(\gamma-1)} \left(\frac{N_2}{N_1}\right)^{\gamma-1} \tag{4.20}$$

$$\frac{B_2}{B_1} = \left(\frac{a_2}{a_1}\right)^{-\gamma} \left(\frac{N_2}{N_1}\right)^{\frac{\gamma}{2}}, \tag{4.21}$$

which relate magnetic field and temperature to pinch radius. The density relates to pinch radius as in

$$\frac{n_2}{n_1} = \left(\frac{a_2}{a_1}\right)^{-2} \left(\frac{N_2}{N_1}\right), \tag{4.22}$$

although this relation only depends on the definition of the linear density and does not require assumption of an adiabatic process.

Using equilibrium analysis data to plot the left-hand-side normalized to the right-hand-side of each Eq. (4.20, 4.21) elucidates how closely a plasma pulse conforms to adiabatic conditions. In comparing a secondary plasma state $(n_2, T_2, B_2, N_2, a_2)$ reached from an initial plasma state $(n_1, T_1, B_1, N_1, a_1)$ through an adiabatic process, the fractions

$$\frac{\frac{B_2}{B_1}}{\left(\frac{a_2}{a_1}\right)^{-\gamma} \left(\frac{N_2}{N_1}\right)^{\frac{\gamma}{2}}}, \tag{4.23}$$

$$\frac{\frac{T_2}{T_1}}{\left(\frac{a_2}{a_1}\right)^{-2(\gamma-1)} \left(\frac{N_2}{N_1}\right)^{\gamma-1}} \tag{4.24}$$

should each be 1. Comparing the plasma state measured by DHI at different axial cross-sections reveals the presence of non-adiabatic processes. This analysis assumes that the profiles at all axial locations share the farthest upstream profile as a common initial state. All the profiles from one side of a hologram, i.e. either above or below the density centroids, are chosen for this analysis. The characteristic properties from the most upstream cross-section are taken as $(n_1, T_1, B_1, N_1, a_1)$, and the characteristic properties of each downstream profile are taken as $(n_2, T_2, B_2, N_2, a_2)$. Linear density is numerically integrated for each profile as $N = \int_0^a 2\pi n r dr$.
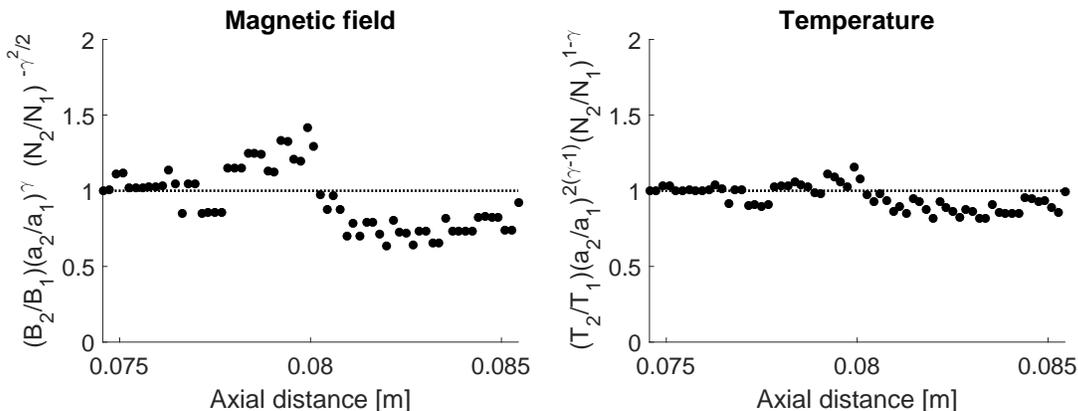
Figure 4.10: Examining relations between pinch size and density and field and temperature to determine if an axially uniform Z-pinch behaves adiabatically. The two plots compare the left and right-hand-sides of Eqs. (4.20, 4.21) for pulse 160524021. The profiles below the density centroids in Fig. 4.7 are used in this analysis, and each black marker corresponds to a profile at a different axial location. Upstream of 0.077 m, the markers near a value of 1 on the ordinate indicate states reached in agreement with the adiabatic scaling laws. Between 0.077 and 0.081 m, non-constant deviations of the markers from 1 suggest non-adiabatic processes are responsible for the difference of the plasma state in this region compared to the upstream region. The flat region in the markers downstream of 0.081 m indicates differences in the plasma state within this region are explained by adiabatic processes.

Figure 4.10 shows the ratio from each profile plotted as a single marker for plasma pulse 160524021, which exhibits fair axial uniformity in density. Upstream of 0.077 m, the markers near a value of 1 on the ordinate indicate states reached in agreement with the adiabatic scaling laws. Between 0.077 and 0.081 m, where the ratio Eq. (4.23) increases and then decreases with axial distance, non-adiabatic processes are at least partially responsible for the differences in the plasma state between adjacent cross-sections. This non-adiabatic behavior correlates with the bulge in the plasma radius seen in Fig. 4.7. The flat region downstream of 0.081 m suggests differences between cross-sections in this region are explained by adiabatic processes.

For a different pulse with more axial variation in density (pulse 160621026), Fig. 4.11 shows more pronounced deviation from adiabatic behavior. Figures 4.13-4.14 show contours

of density, field, and temperature for this pulse, and all show significant axial variation. Specifically, they show an expansion of the plasma downstream of 0.081 m. The observation of greater deviation from adiabatic behavior for axially-varying Z-pinch equilibria corroborates with data from ZaP, which indicated that pinches with large oscillations in pinch size exhibited non-adiabatic behavior [32]. The study performed on ZaP used density data measured at one axial location with the HeNe interferometer to compute the volume-averaged adiabatic function,

$$\left\langle \frac{P}{\rho^\gamma} \right\rangle = \frac{(Z+1)kn_aT_a}{(m_in_a)^\gamma},$$ (4.25)

as a function of time. Here, n_a and T_a are volume-averaged density, $n = n_i = n_e/Z$, and temperature, $T = T_e = T_i$, respectively. P/n^γ remains constant in adiabatic processes, and ZaP data showed changes in the adiabatic function during oscillations in plasma size. If the axially-varying structures (size $\approx$ 1 cm) observed with DHI on ZaP-HD translate at the bulk flow speed ($\approx$ 1 cm/μs), they could lead to oscillations in plasma radius apparent at one axial location comparable to those observed on ZaP over similar time scales.

4.3 Empirical observation of ZaP-HD's plasma property scalings

Extending the equilibrium analysis across many plasma pulses elucidates how ZaP-HD's confinement properties scale. Plotting the characteristic pulse properties n, T, B, N, and a in various parameter spaces reveals the empirical scaling.

Pulses examined in this analysis all have similar run settings. They all share identical charge voltages (9 kV acceleration bank voltage, 8 kV compression bank voltage) and gas injection pressures (5500 Torr inner gas pressure, 3500 Torr outer gas pressure), and they have similar gas injection timings (-1.6 to -1.5 ms inner gas timing, -1.6 to -1.4 ms outer gas timing) and compression bank trigger times (17 to 20 μs). All holograms are centered at $z = 8$ cm where optical images observe stable confinement (see Fig. 5.3). All profiles from 13 high quality hologram reconstructions are considered for this analysis, and a single marker represents each profile in Figs. 4.15-4.21. The profiles above and below the centroid of each
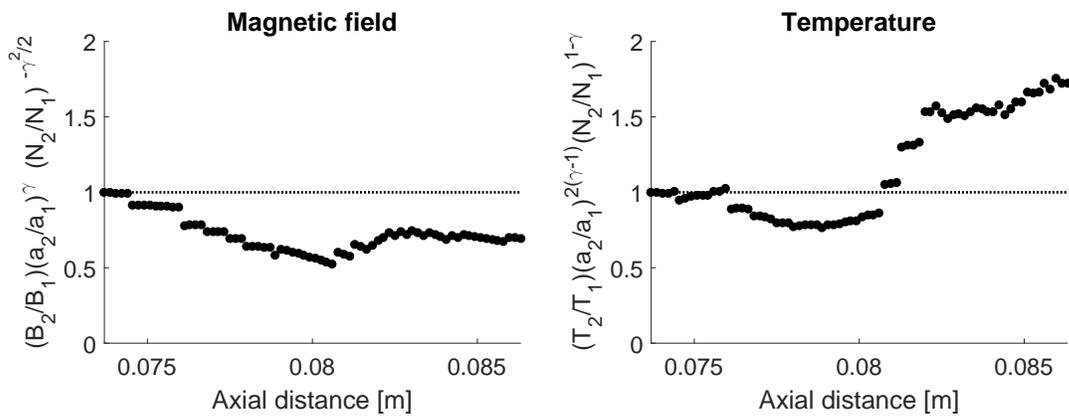
Figure 4.11: Examining relations between pinch size and field and temperature to determine if an axially non-uniform Z-pinch behaves adiabatically. The two plots compare the left and right-hand-sides of Eqs. (4.20, 4.21) for pulse 160621026. The profiles below the density centroids in Fig. 4.12 are used in this analysis, and each black marker corresponds to a profile at a different axial location. Upstream of 0.076 m, the markers near a value of 1 on the ordinate indicate states reached in agreement with the adiabatic scaling laws. Abrupt changes in the ratios of Eqs. (4.23, 4.24) at 0.076 m and 0.081 m suggest non-adiabatic processes dictate the difference between the plasma states at adjacent cross-sections in these locations. The more abrupt change at 0.081 m corresponds to the plasma radius change.
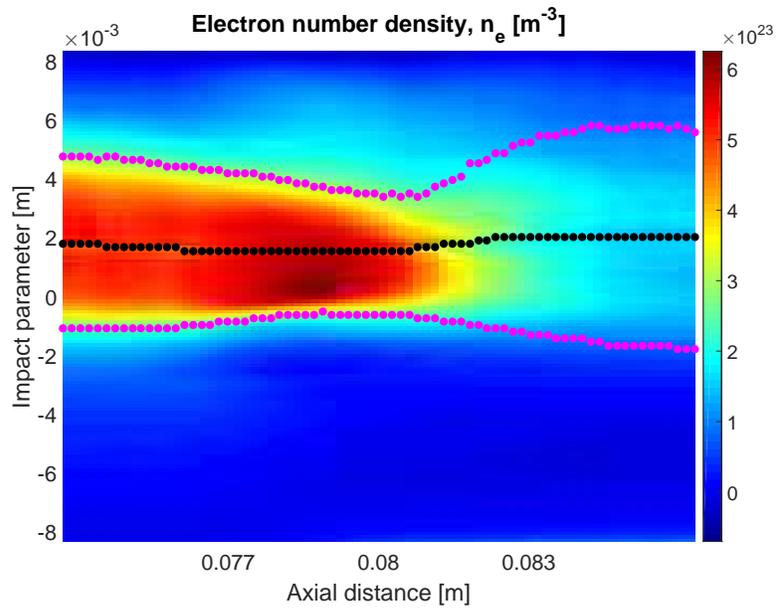
Figure 4.12: Contours of density for pulse 160621026 analyzed in Fig. 4.11. The black dots indicate the centroids used in Abel inversion, and the magenta dots indicate the radius a for each profile where the density drops to half its peak value. This pulse exhibits significant axial variation in density.
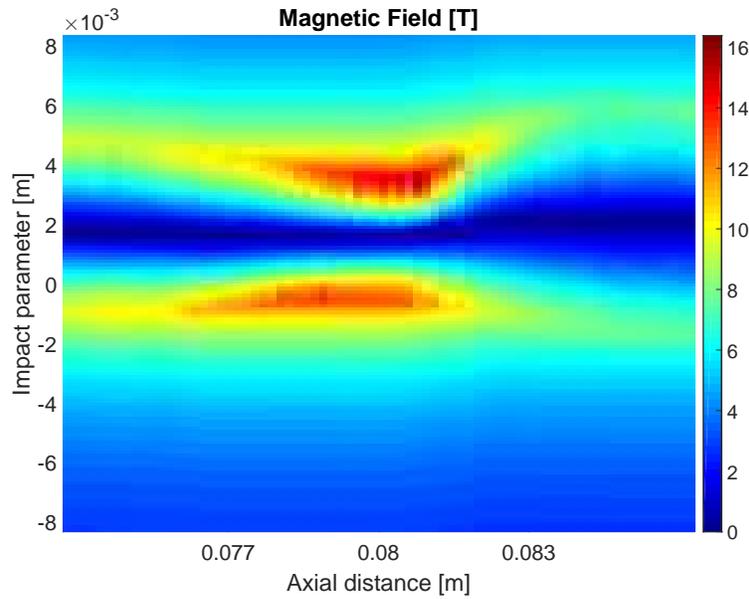
Figure 4.13: Contours of magnetic field for pulse 160621026 analyzed in Fig. 4.11. This pulse exhibits significant axial variation in field with the highest fields in cross-sections with the smallest pinch radii.
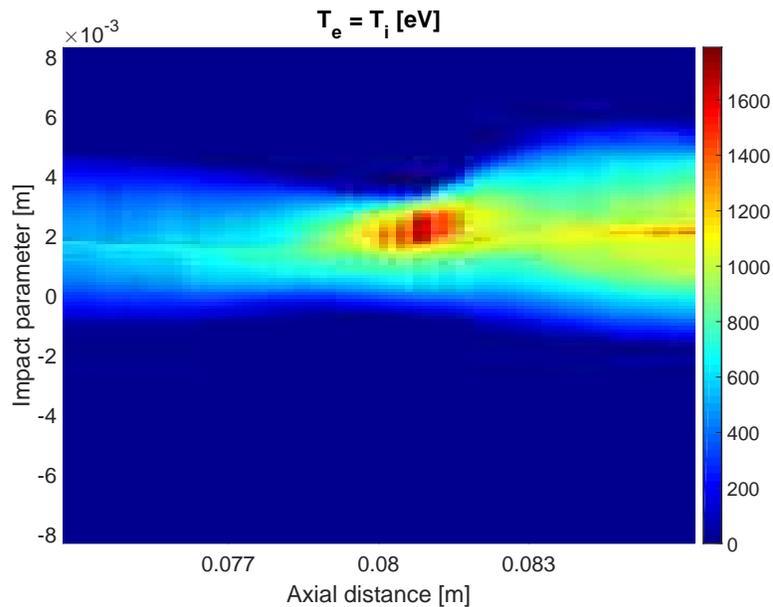
Figure 4.14: Contours of temperature for pulse 160621026 analyzed in Fig. 4.11. This pulse exhibits significant axial variation in temperature with the hottest temperatures in cross-sections with the smallest pinch radii.
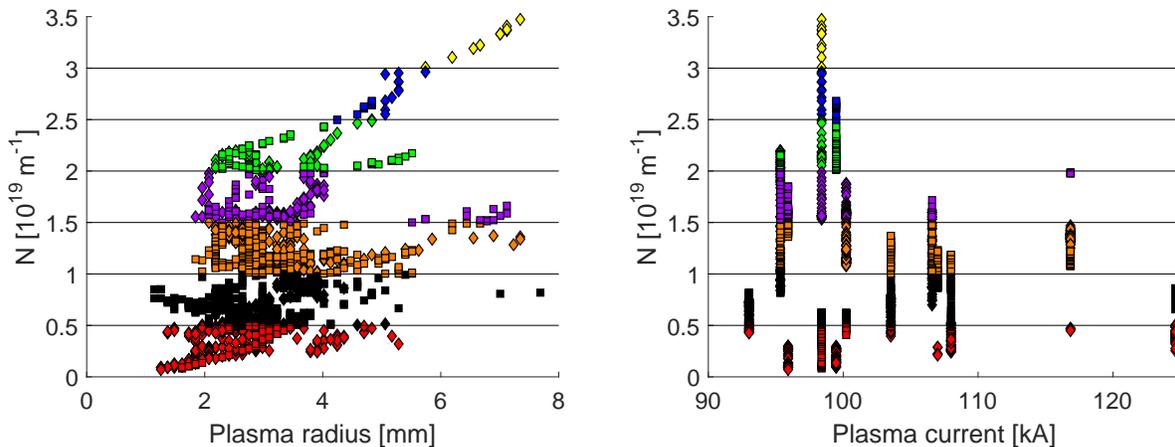
Figure 4.15: Linear density versus plasma radius and linear density versus plasma current. Each marker represents a profile from a reconstructed hologram, and all profiles from 13 high quality holograms taken at pulses with similar run settings are displayed. Profiles above and below the centroid of each cross-section are indicated by diamond and square markers respectively, and markers are assigned colors determined by ranges of linear density. The horizontal black lines show the boundaries of the linear density ranges, and the assigned colors are consistent throughout the remaining figures in this section. The profiles show no strong functional relationships exist between N and a or N and plasma current. The observed linear densities are lower than those measured on ZaP ($N_{ZaP} \approx 3$ - 5×10^{19} m^{-1}), and plasma currents seen exceed those on ZaP ($I_{ZaP} \approx 30$ - 60 kA) [69]. The lack of a strong relationship between N and plasma current suggests the acceleration and compression processes in ZaP-HD are effectively uncoupled in terms of these parameters.

cross-section are indicated by diamond and square markers respectively, and marker colors are determined by the linear density.

ZaP-HD has expanded upon the operating regime of ZaP by driving more compression current while reducing linear density. Figure 4.15 shows the linear density versus plasma radius and linear density versus plasma current with horizontal lines indicating the linear density ranges. The observed linear densities are lower than those seen on ZaP ($N_{ZaP} \approx 3$ - 5×10^{19} m^{-1}), and plasma currents exceed those on ZaP ($I_{ZaP} \approx 30$ - 60 kA) [69]. The plasma current discussed in this section is computed as the axial current at the magnetic probe array closest to the DHI measurement location. The current is computed from the average magnetic

field measured at that probe array. The combination of increased current and reduced linear density leads to smaller pinches with higher densities, fields, and temperatures. Unlike the ZaP experiment, which exhibited coupling between the plasma current and linear density, the plot of N versus plasma current in Fig. 4.15 shows the current does not significantly affect the linear density in ZaP-HD, which allows for improved compression. The scatter plot of $n(a)$ in Fig. 4.16 shows an expected trend that pinches compressed to smaller radii reach higher density. The profiles seen on ZaP-HD exceed the parameter space attained by ZaP illustrated by the transparent red box. Similarly, scatter plots of $B(a)$ and $T(a)$ in Figs. 4.17 and 4.18 show increased field and temperature for smaller pinches. Values of field and temperature computed with the uniform v_d model are sensitive to the plasma radius at smaller radii (see Fig. 4.1), which could lead to exaggeration of the fields and temperatures for small pinches. Even so, values computed at relatively large radii exceed values from the same equilibrium model applied on ZaP, which saw fields around 1 T and temperatures near 200 eV [31]. ZaP-HD compresses plasma more effectively than ZaP.

For a plasma that behaves adiabatically, the loci of markers in Figs. 4.16-4.18 would follow the scaling relations Eqs. (4.20-4.22). The colored curves in Figs. 4.16-4.18 show the adiabatic scaling for different values of N. A reference state, i.e. (n_1, a_1), (B_1, a_1), and (T_1, a_1), is required to plot Eqs. (4.20-4.22), and the reference state for each orange curve is chosen to maximize its proximity to the orange markers in each plot so that the orange curve represents the adiabatic scaling for the linear density bin $1 \times 10^{19} \text{ m}^{-1} < N < 1.5 \times 10^{19} \text{ m}^{-1}$. A linear density ratio $N_2/N_1 = 1$ is chosen to draw the orange curves. The green and red curves use $N_2/N_1 = 2$ and $N_2/N_1 = 1/2$ respectively, and these curves roughly represent where the adiabatic scaling should lie for the green and red linear density ranges. The empirical $n(a)$ scaling of Fig. 4.16 follows the qualitative trends of the adiabatic scaling. The density increases with decreased plasma radius, and the locus of markers for lower N are shifted towards the bottom-left of the plot. The empirical $B(a)$ scaling in Fig. 4.17 appears insensitive to N, which is inconsistent with adiabatic theory. While the general trend of increased field with decreased pinch size is consistent with adiabatic theory, the empirical

trend is less steep than predicted. In Fig. 4.18, the trend of increased $T(a)$ with smaller radius matches the adiabatic prediction, but the dependence on N appears inverted from the adiabatic scaling with markers for lower N shifted towards the upper-right of the plot. Deviations from the adiabatic scalings seen across multiple pulses are consistent with the non-adiabatic behavior shown in individual pulses in Sec. 4.2.

Understanding the scaling of n and T with respect to plasma current has major ramifications for applications like fusion energy power plants and space propulsion. The markers in Figs. 4.19-4.21 show the empirical relations for $n(I)$, $a(I)$, and $T(I)$. In these plots, the curves indicate the adiabatic scaling of Eqs. (1.7-1.9). The orange curves are again chosen to have $N_2/N_1 = 1$ and initial states so they conform to the majority of the orange markers. The red and green curves once again roughly correspond to the red and green linear density ranges. The empirical density does not scale up as effectively as adiabatic theory predicts. Both the adiabatic and empirical scalings indicate low sensitivity of a, and T to plasma current over this range of currents. In its present form, DHI only has success measuring density profiles at the highest capacitor bank charge voltage settings. As changing the charge voltage settings are the primary means of changing the plasma current, future studies discussed in Ch. 7 will need to open the operating space of DHI to enable data collection at lower plasma currents, lower densities, and larger pinch sizes. An investigation over an expanded range of currents would help appraise the utility of the flow stabilized Z-pinch to applications requiring high temperature and density.

DHI measurements reveal ZaP-HD provides more effective plasma compression than ZaP. Equilibrium modeling using the measured 2D density data allows investigation of the 2D structure of magnetic field and temperature. This structure reveals non-adiabatic processes associated with axial variation in the plasma, specifically with changes in the plasma radius. Such observations support previous work observing a relationship between Z-pinch radius oscillations and non-adiabatic behavior [69]. A study of data from many plasma pulses indicates non-adiabatic behavior commonly occurs in ZaP-HD leading to poorer than predicted density scaling. More research is necessary to provide a conclusive appraisal of the scalability
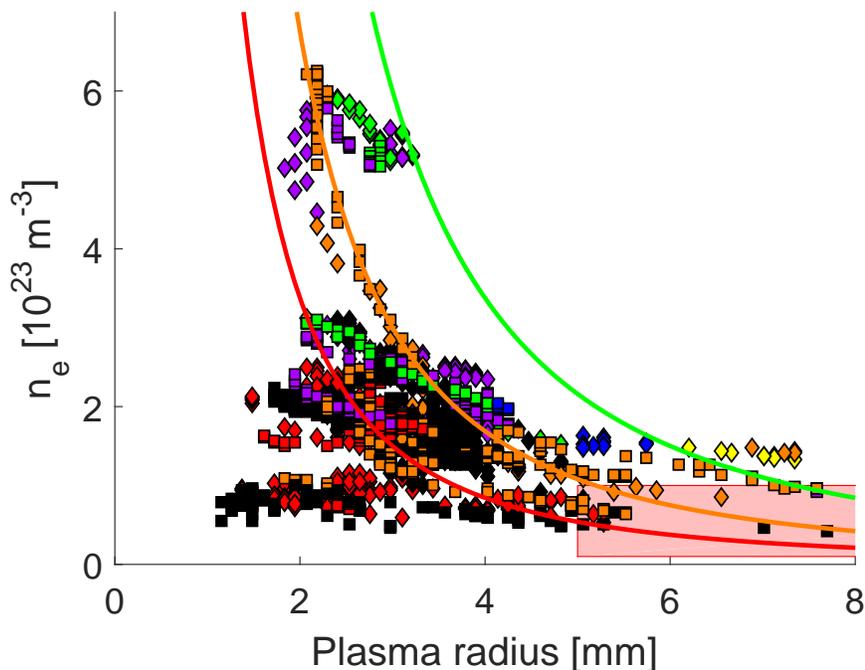
Figure 4.16: Peak density versus plasma radius for profiles from many plasma pulses with similar run settings. Markers are colored according to the linear density ranges in Fig. 4.15. The orange curve represents the adiabatic scaling of Eq. (4.22) for the orange linear density bin. The curve is drawn from Eq. (4.22) with $N_2/N_1 = 1$ and an initial state chosen to maximize the proximity of the curve to the orange markers. The green and red curves indicate the adiabatic scaling for values of N_2/N_1 of 2 and 1/2 respectively, which correspond to the green and red linear density ranges. The red-shaded box indicates the region of ZaP operations, and extends off the plot to radii of 0.015 m. The empirical data exhibits the same trends as the adiabatic predictions: density increases as pinch size decreases, and markers of higher linear density generally appear towards the upper-right of the plot. The empirical relation between density and radius is more gradual than the adiabatic prediction.
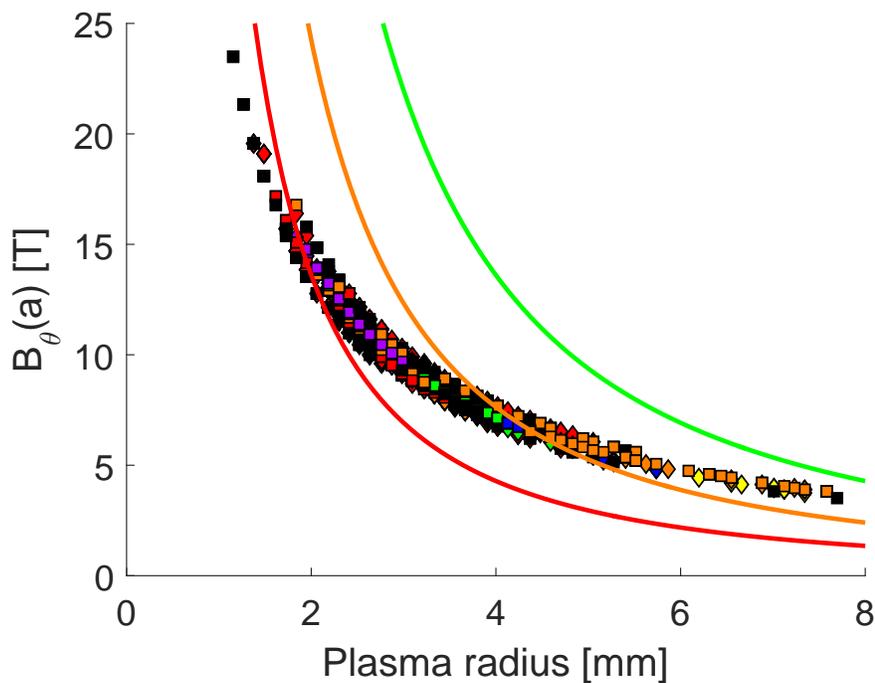
Figure 4.17: Magnetic field plotted versus plasma radius for profiles from many plasma pulses with similar run settings. Markers are colored according to the linear density ranges in Fig. 4.15. The orange curve represents the adiabatic scaling of Eq. (4.21) for the orange linear density bin. The curve is drawn from Eq. (4.21) with $N_2/N_1 = 1$ and an initial state chosen to maximize the proximity of the curve to the orange markers. The green and red curves indicate the adiabatic scaling for values of N_2/N_1 of 2 and 1/2 respectively, which correspond to the green and red linear density ranges. The empirical $B(a)$ relation appears insensitive to linear density, which does not match the adiabatic prediction. Also, the empirical trend is more gradual than the prediction.
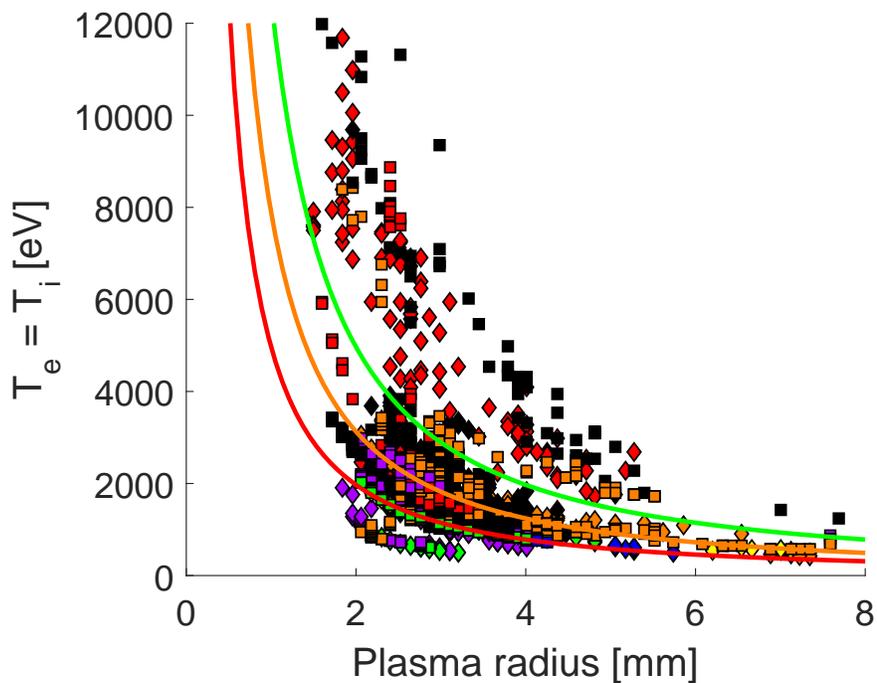
Figure 4.18: Temperature plotted versus plasma radius for profiles from many plasma pulses with similar run settings. Markers are colored according to the linear density ranges in Fig. 4.15. The orange curve represents the adiabatic scaling of Eq. (4.20) for the orange linear density bin. The curve is drawn from Eq. (4.20) with $N_2/N_1 = 1$ and an initial state chosen to maximize the proximity of the curve to the orange markers. The green and red curves indicate the adiabatic scaling for values of N_2/N_1 of 2 and 1/2 respectively, which correspond to the green and red linear density ranges. The observed temperature follows the predicted trend of increased temperature at smaller pinch sizes. The dependence of the empirical data on linear density appears inverted from the adiabatic predictions with markers of higher linear density generally shifted towards the lower-left corner of the plot.

of flow stabilized Z-pinches.
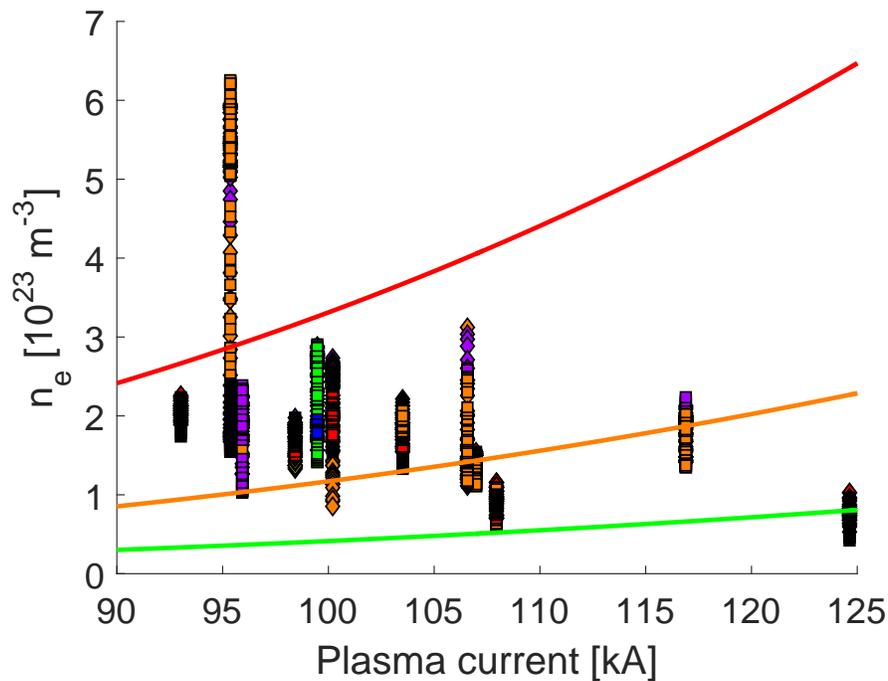
Figure 4.19: Electron density plotted versus plasma current for profiles from many plasma pulses with similar run settings. Markers are colored according to the linear density ranges in Fig. 4.15. The orange curve represents the adiabatic scaling of Eq. (4.19) for the orange linear density bin. The curve is drawn from Eq. (4.19) with $N_2/N_1 = 1$ and an initial state chosen to maximize the proximity of the curve to the orange markers. The green and red curves indicate the adiabatic scaling for values of N_2/N_1 of 2 and 1/2 respectively, which correspond to the green and red linear density ranges. The dependence of the measured density on the linear density does not appear to follow the adiabatic theory. The empirical density does not scale up as effectively as adiabatic theory predicts.
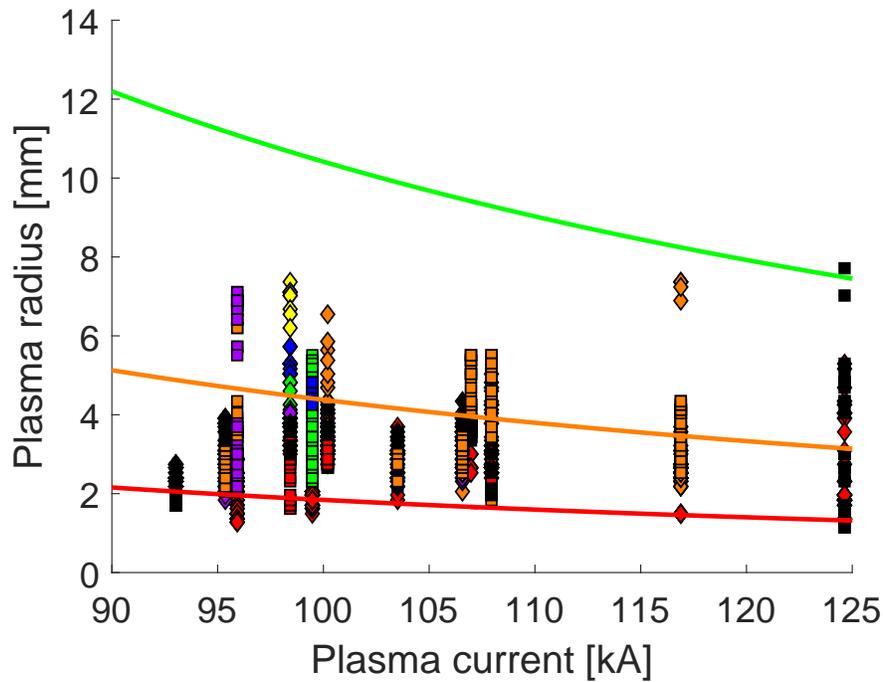
Figure 4.20: Plasma radius plotted versus plasma current for profiles from many plasma pulses with similar run settings. Markers are colored according to the linear density ranges in Fig. 4.15. The orange curve represents the adiabatic scaling of Eq. (1.9) for the orange linear density bin. The curve is drawn from Eq. (1.9) with $N_2/N_1 = 1$ and an initial state chosen to maximize the proximity of the curve to the orange markers. The green and red curves indicate the adiabatic scaling for values of N_2/N_1 of 2 and 1/2 respectively, which correspond to the green and red linear density ranges. The insensitivity of the observed plasma radius over this range of currents matches the adiabatic prediction. The dependence of the radius on the linear density appears to follow the trend of adiabatic theory with lower linear density markers generally located towards the bottom of the plot.
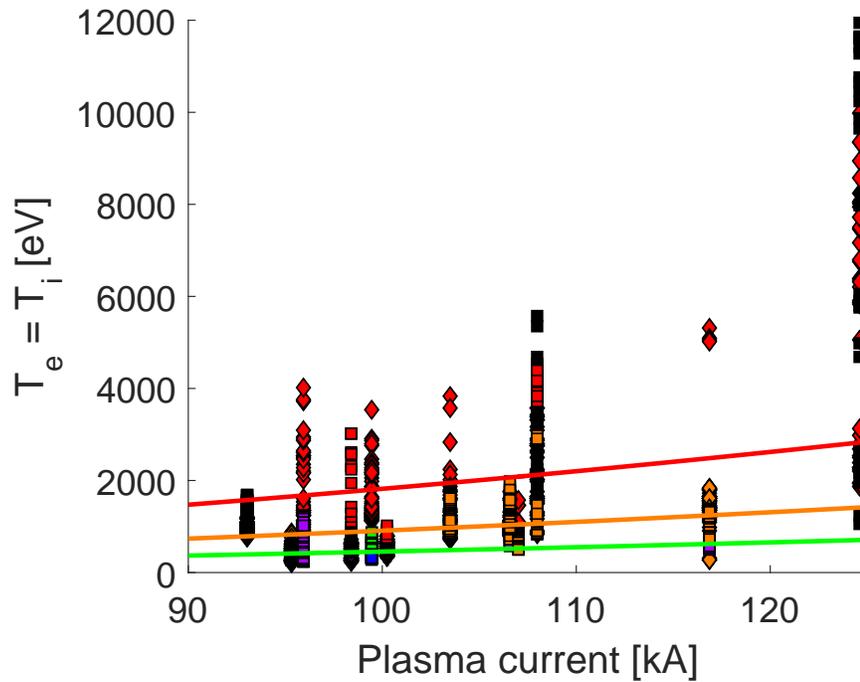
Figure 4.21: Temperature plotted versus plasma current for profiles from many plasma pulses with similar run settings. Markers are colored according to the linear density ranges in Fig. 4.15. The orange curve represents the adiabatic scaling of Eq. (1.7) for the orange linear density bin. The curve is drawn from Eq. (1.7) with $N_2/N_1 = 1$ and an initial state chosen to maximize the proximity of the curve to the orange markers. The green and red curves indicate the adiabatic scaling for values of N_2/N_1 of 2 and 1/2 respectively, which correspond to the green and red linear density ranges. The insensitivity of the observed temperature over this range of currents matches the adiabatic prediction. The dependence of the temperature on the linear density appears to follow the trend of adiabatic theory with lower linear density markers generally located towards the top of the plot.

Chapter 5

EVALUATING ZAP-HD'S STABILITY WITH MULTIPLE DIAGNOSTICS

ZaP-HD's behavior differs from ZaP's in significant ways that compel investigation of new metrics of plasma stability. On ZaP, the primary means of determining plasma stability is magnetic mode data. Defining the plasma's quiescent period as the time duration where the normalized mode data, m_1/m_0, remains less than 0.2 gives an objective measure of stability. As described in Sec. 2.1.3, m_1/m_0 corresponds to the Z-pinch current centroid displacement, and the condition $m_1/m_0 < 0.2$ means the current centroid resides within 1 cm of machine axis. Defined as such, quiescent periods on ZaP-HD are shorter than on ZaP and ZaP-HD's normalized mode data is typically, higher indicating more off-centered plamas. The vastly increased resolution of ZaP-HD's field probes further confounds the definition of stability as a plasma that appears well-centered at one axial location can move chaotically at another location. This chapter evaluates the normalized mode data as a stability metric by comparing it to density measurements from DHI and optical images from the high-speed camera.

5.1 Characterizing ZaP-HD's stability with mode data

Initial attempts to optimize ZaP-HD's behavior were based on observing the magnetic mode data and trying to extend the quiescent period based on ZaP's definition of plasma stability. These attempts encountered many difficulties. The large number of tunable settings on the ZaP-HD machine makes the optimization difficult. Experiments must span a multi-dimensional parameter space, and results are time-consuming to obtain and difficult to comprehend. Taguchi methods, design of experiments techniques, and analysis of variance (ANOVA) were employed to span this parameter space more efficiently and also look for

dependencies obscured from experimental runs varying only one parameter at a time [72,73].

Such methods show the most influential parameters by far affecting the quiescent period are the capacitor bank charge voltages. Increasing acceleration bank charge voltage lengthens the quiescent period, so optimal plasma conditions are achieved with the acceleration bank charged to its maximum value, 9 kV. Fig. 5.1 shows normalized mode data from pulses during testing of the accelerator. During accelerator testing, the middle electrode is grounded to the outer electrode, which eliminates the complicated effects described in Ch. 2 at the end of the gun caused by the middle electrode floating. Mode data from this testing shows stability improves monotonically with increased accelerator charge voltage. During operation with the compression bank, pulses with zero compression bank charge show high mode activity due to the interaction at the interface between the acceleration and assembly regions. As the compression bank charge voltage increases, chaotic fluctuations in the magnetic mode data initially decrease but eventually tend to increase at higher voltages. These fluctuations at high compression bank charge voltages reduce the ability of the Taguchi methods to determine finer correlations between the quiescent period and other run parameters like gas puff timing, gas pressure, and compression bank trigger timing.

Taguchi and design of experiments methods rely on reducing the results of each experiment in a dataset to a single number or metric. The methods reveal changes in that metric as a response to changes in experiment inputs or set up. These methods are commonly used to optimize chemical reactions where identifying the reaction yield as the metric for each experiment is easy. Here, the metric is the quiescent time based on the magnetic mode data. On high compression bank charge pulses, the quiescent period is at least as sensitive to the chaotic processes in the plasma as it is to any change in experiment set up, so other methods are needed to fine-tune ZaP-HD's performance.

Despite the inconclusive results of Taguchi methods, changes in run parameters besides charge voltages certainly affect the plasma behavior and stability. Camera images were used to identify a run conditions of optimal stability, which led to more invertible DHI density data than other run conditions. Note that invertible DHI data comes from relatively centered
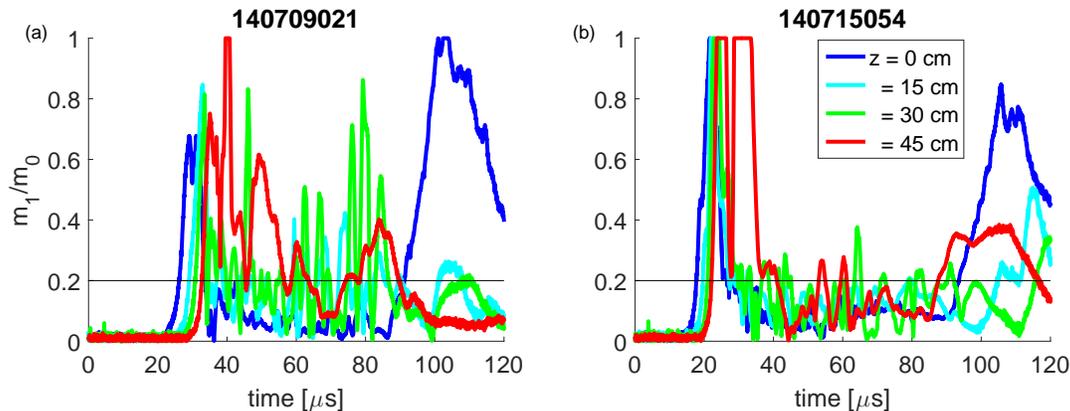
Figure 5.1: Normalized magnetic mode data, m_1/m_0, showing stability improves with increased acceleration bank voltage. The middle electrode was grounded to the outer electrode for the pulses shown during testing of the accelerator. Acceleration bank voltages of (a) 3.5 kV and (b) 6 kV are shown for pulses with otherwise identical run settings. Horizontal black lines indicate a current centroid displacement of 1 cm.
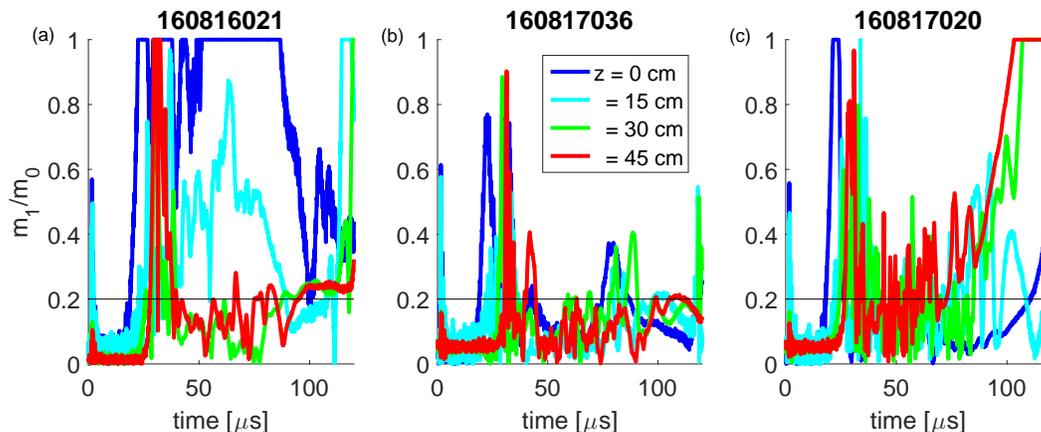
Figure 5.2: Normalized magnetic mode data, m_1/m_0, showing stability initially improves with increased compression bank voltage and then degrades at high voltages. Compression bank voltages of (a) 0 kV, (b) 2 kV, and (c) 8 kV are shown for pulses with otherwise identical run settings. Horizontal black lines indicate a current centroid displacement of 1 cm.

plasmas, so the prevalence of invertible DHI data at this condition corroborates with the well-centered pinches seen in the camera images. The prominent feature seen camera images of stable Z-pinches is the constriction seen at $z = 10 - 15$ cm in Fig. 5.3 in the frames at 41 and 46 μs. Plasma radially converges upstream of $z = 12$ cm and radially diverges downstream from that position. Downstream of $z = 20$ cm exhibits little light emission until later in the quiescent period when light appears from the farthest downstream location and works its way upstream, which may indicate flow stagnation at the end of the assembly region. Little light is ever seen between $z = 20$ and 30 cm.

5.2 Comparing the magnetic mode data to optical images

Error sources do exist that can affect the normalized mode data and may degrade its effectiveness as a stability metric. The increased instability implied by the mode data of ZaP-HD as well as instability observed in camera imaging prompted deeper investigation into possible shortcomings in the mode data. The most significant errors in current centroid position stem from two assumptions in the probe data analysis. First, the magnetic probes are assumed to react instantaneously to changes in plasma current. In reality the probes have limited frequency response because they are embedded in steel conducting walls. Therefore, it takes a finite time, related to the resistive diffusion time of the steel, for the field to buldge into the holes in the walls housing the probes. This means the probes are blind to quick changes in magnetic field, and relatively large non-uniform displacements flowing along very quickly or rapid time-varying oscillations can occur without detection. Second, the analysis assumes axially uniform displacements. As a result, the normalized mode data under-reports non-uniform displacements because the fraction of plasma moving closer to one side of a probe array is less for a localized displacement.

Examining saturated instabilities provides a great illustration of the magnetic mode data's limitations. Instabilities do appear in shear flow stabilized plasmas, but they do not grow to the point of destroying plasma confinement. The shear flow stabilization prevents the instabilities from growing beyond a point where their size saturates. After saturation, instabilities
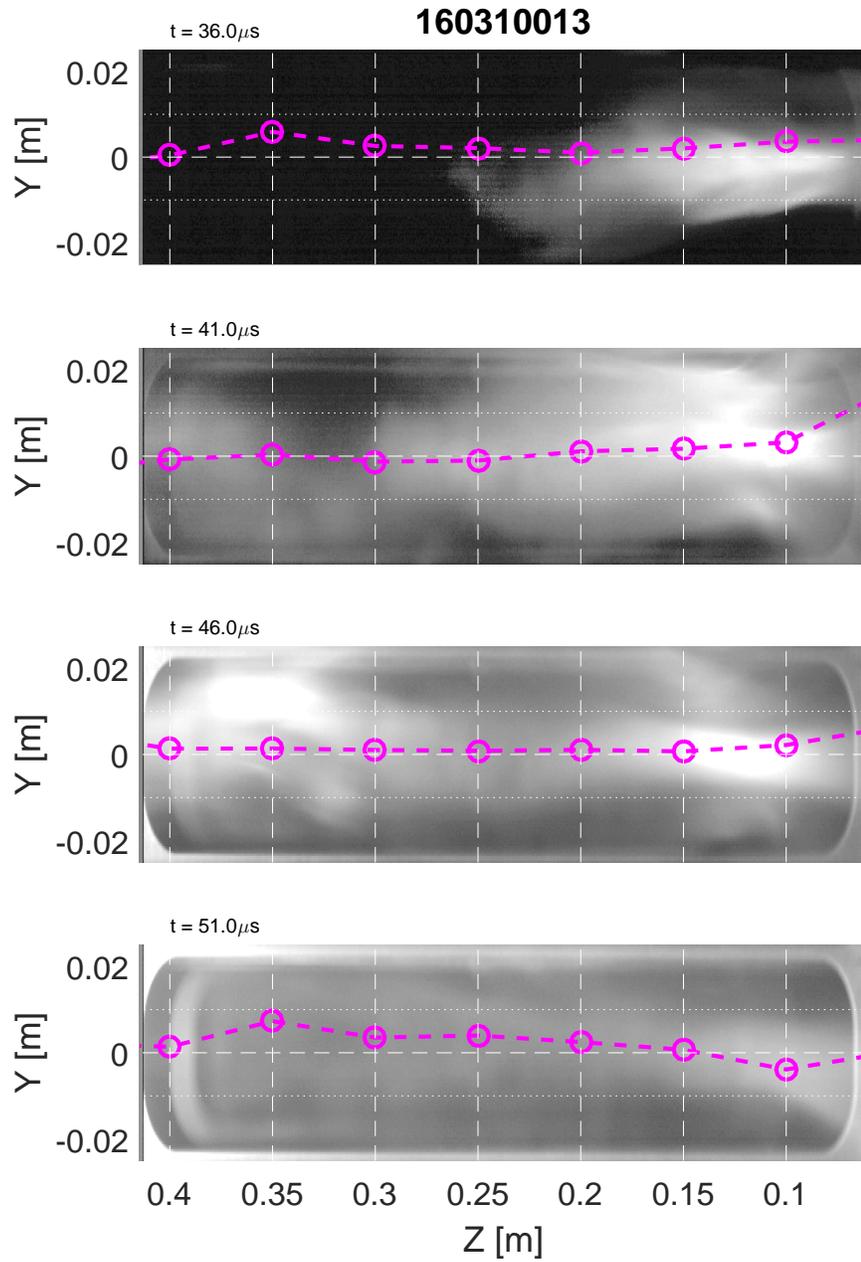
Figure 5.3: High speed camera images showing the typical appearance of a stable Z-pinch during a 14 μs quiescent period from 36 to 51 μs during pulse 160310013. The frame at 41 μs shows the distinct necking behavior localized at $z = 10 - 15$ cm typical of stable Z-pinches. The intensity is shown on a logarithmic scale.

are conveyed by the plasma flow to the end of the assembly region. Saturated instabilities may go unreported by the magnetic mode data. Fig. 5.4 shows four frames in which an apparent saturated kink instability propagates past the $z = 15$ cm probe array without affecting that location's current centroid. The size ($\lambda \approx 3$ cm) and velocity (≈ 5 cm/μs) of this kink instability match observations of saturated instabilities on ZaP [32]. The localized nature of the instability may make it invisible to the probes. Conversely, larger axial structures often corroborate well with optical images as seen in the four frames of Fig. 5.5. Correlation between optical images and mode data is not always consistent. Fig. 5.6 shows five frames where a large-sized (5-10 cm) structure starts far from the current centroid location before kinking and severing the plasma. The mode data remains unaware of this unstable behavior until 4 μs after the pinch severs.

Does such disagreement expose flaws in the magnetic mode data? The answer is complicated. The plasma emission in the visible spectrum integrated during the time of usual high speed camera operation is shown in Fig. 5.7 (top). Visible light emission is dominated by metal and Hα spectral lines, which are more likely found in the edge of the plasma than in its ionized core, so light emission generally does not correlate to plasma current or density. Better theoretical correlation exists between density and bremsstrahlung light emission, which comes from free electrons being deflected in the plasma. The radiation power output of bremsstrahlung radiation goes like

$$P_{br} \propto Z^2 n_e n_i T_e^{1/2}, \tag{5.1}$$

where Z is the effective charge state. In a hydrogen plasma, $P_{br} \propto n_e^2 T_e^{1/2}$, which is a strong function of density and a weak function of temperature. Because bremsstrahlung comes from electrons changing trajectory in response to electromagnetic fields, the emitted light is broadband as a continuum of trajectory changes are possible. Bremsstrahlung radiation intensity decreases with increased wavelength, but it will appear uniform over narrow wavelength ranges. Installing a Wratten No. 58 filter with a Wratten No. 12 on the camera lens
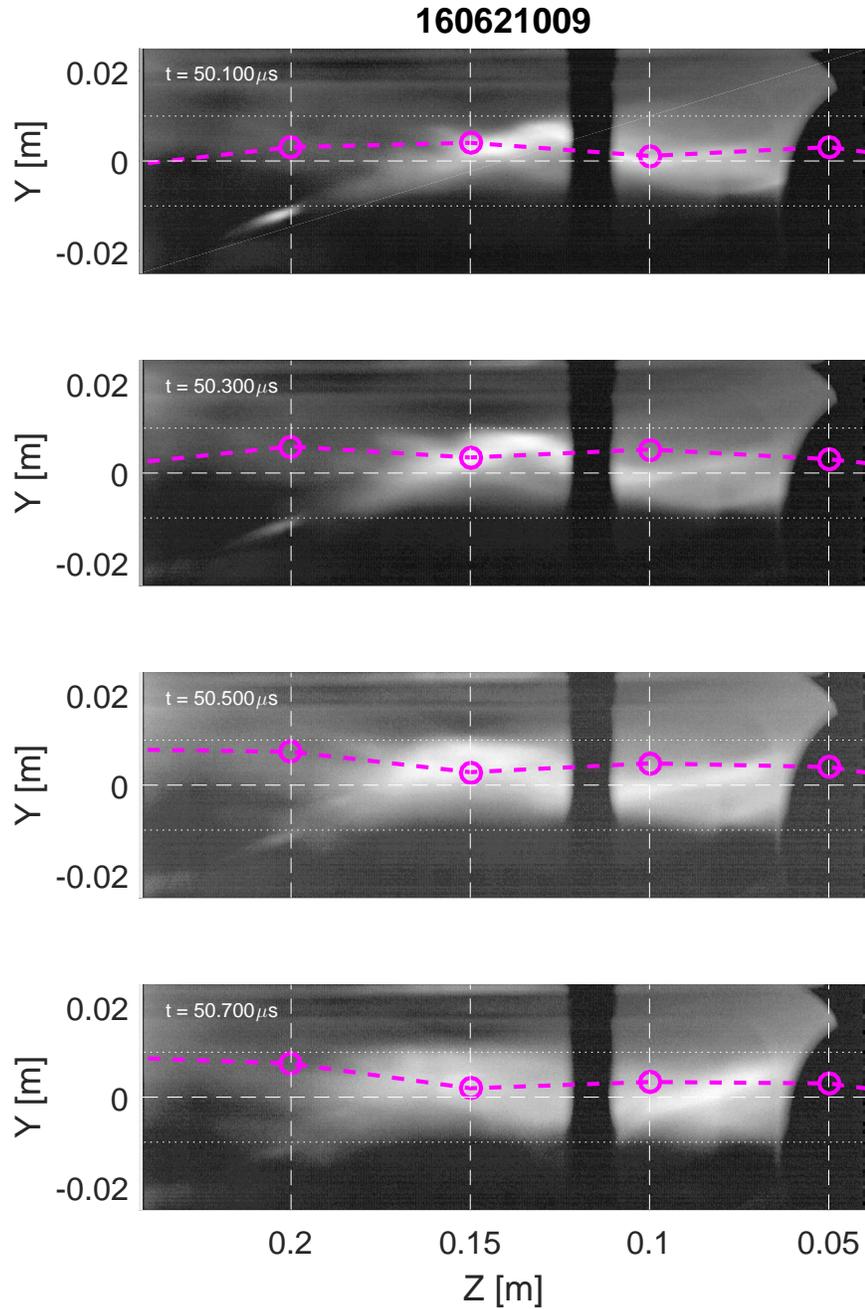
Figure 5.4: High speed camera images showing a saturated kink instability move past the $z = 15$ azimuthal probe array without affecting the current centroid. The intensity is shown on a logarithmic scale. The size ($\lambda \approx 3$ cm) and velocity (≈ 5 cm/μs) are consistent with instabilities seen on ZaP. The vertical shadow at 0.12 m is part of a 3D printed hanger holding a laser beam guide. The shadow of the beam guide is visible at the right edge of the image.
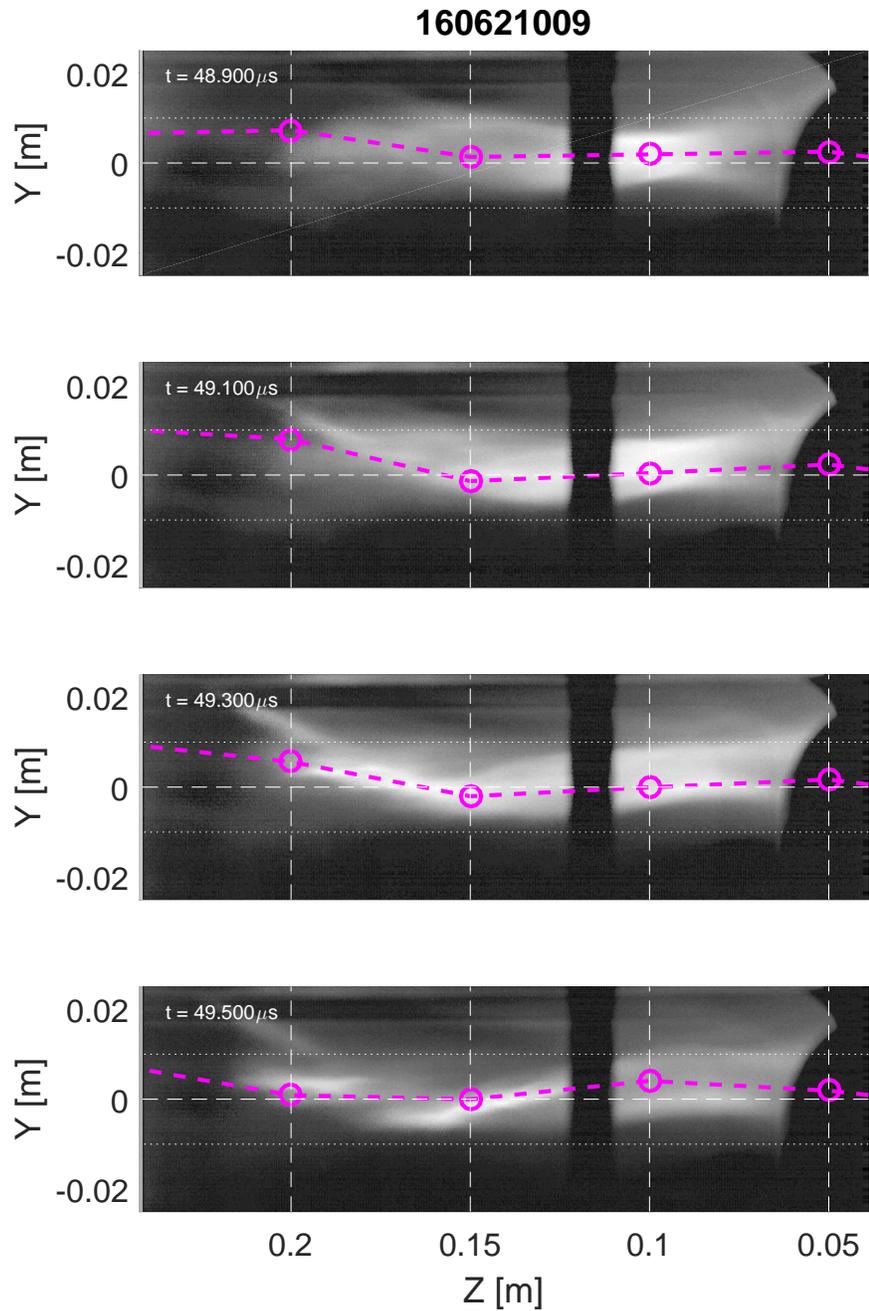
Figure 5.5: High speed camera images showing relatively large scale, slow moving structure correlates well with current centroid locations. The intensity is shown on a logarithmic scale. The vertical shadow at 0.12 m is part of a 3D printed hanger holding a laser beam guide. The shadow of the beam guide is visible at the right edge of the image.
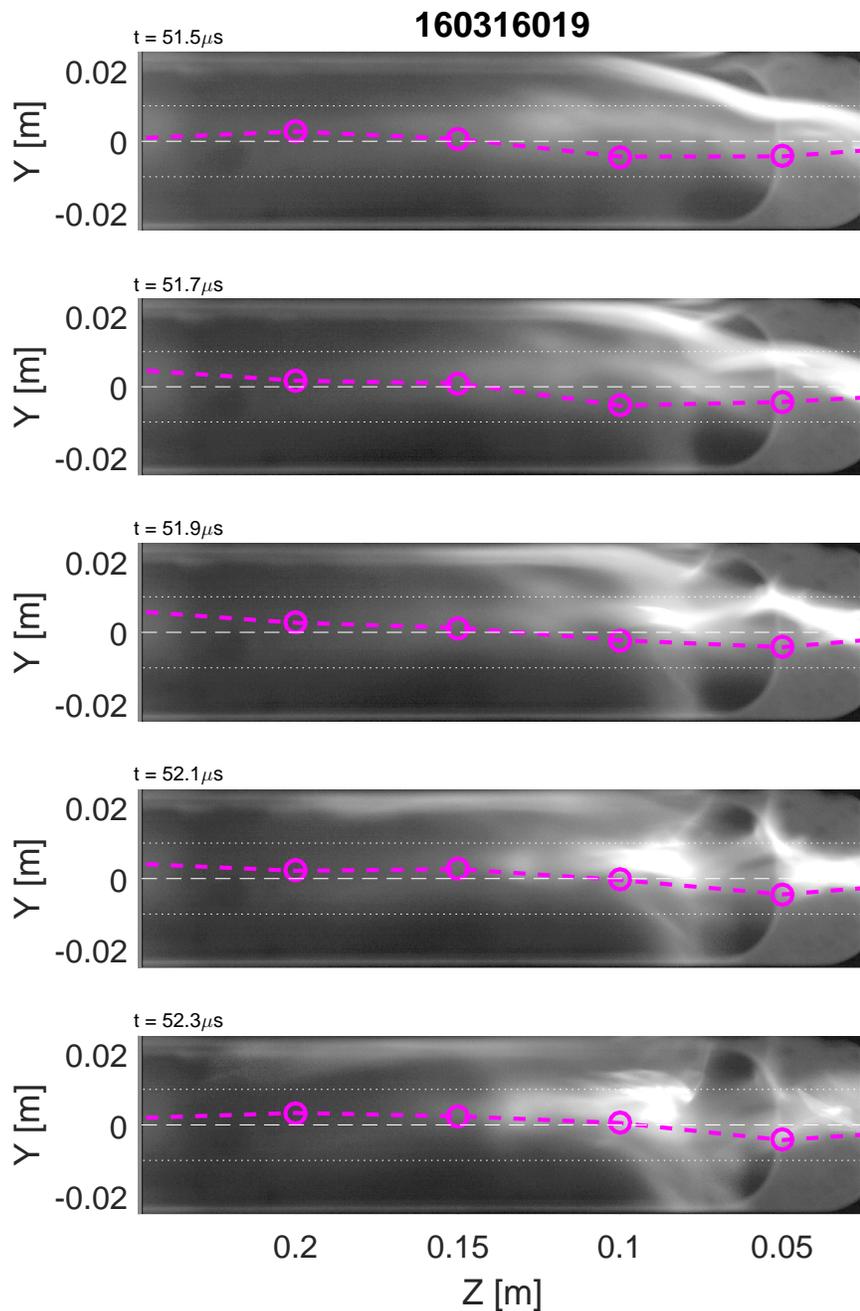
Figure 5.6: High speed camera images showing plasma translation and instability behavior not captured by magnetic mode data. In the first frame, a large structure has already deviated far from the current centroid. The subsequent frames show a kink instability grow and break apart. Throughout the instability breakup, the mode data remains well within the ZaP stability criterion. The mode data only register unstable conditions 4 μs after the final frame shown here.
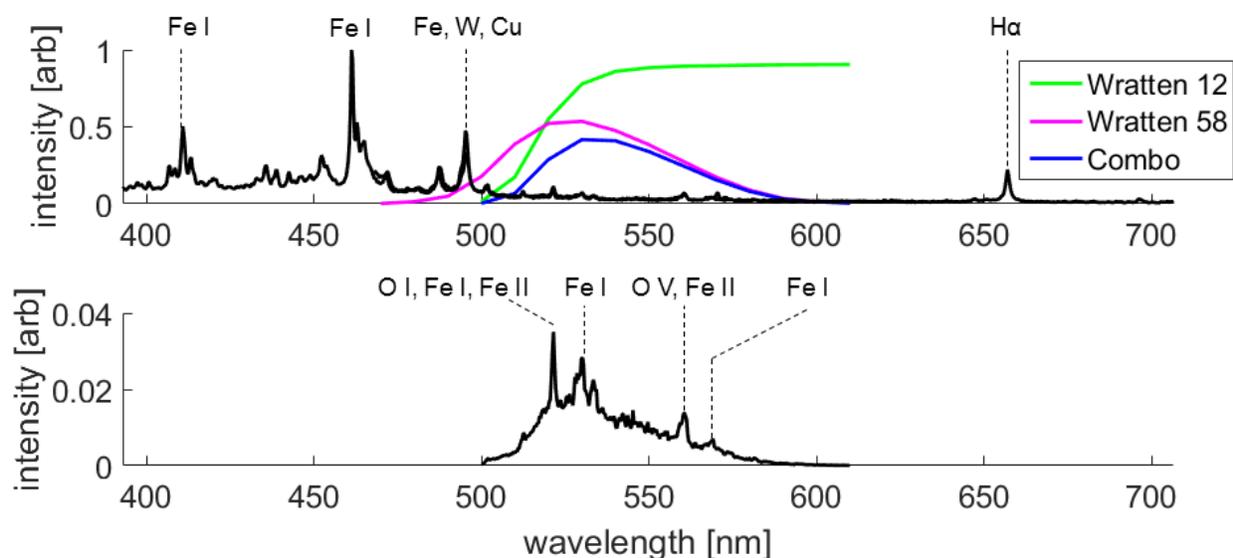
Figure 5.7: (top) Visible wavelength spectra collected by the ICCD spectrometer with a gate during the operation of the high speed camera. The intensities are normalized so the peak value equals 1. The green and magenta curves show the transmittances of the Wratten number 12 and 58 filters respectively. The blue curve is the transmittance of the combination of the two filters. (bottom) The filtered spectrum computed by multiplying the transmittance of the combined filter and the spectrum shown in (top).

is an attempt to reject line radiation and retain the uniform bremsstrahlung. The green and magenta curves in Fig. 5.7 (top) show the transmittances of the Wratten filters, and the blue curve shows their combined transmittance. Fig. 5.7 (bottom) shows the filtered spectrum. The integrated intensity of the line radiation in the filtered spectrum is small compared to the integrated intensity of the uniform regions, which suggests the filter does a good job of isolating bremsstrahlung. Unless otherwise noted, all camera images shown in this chapter are taken with the bremsstrahlung filter installed in an attempt to capture light with better correlation to plasma density.

Consistent correlation exists between unfiltered and filtered light. Placing the bremsstrahlung filter on ZaP-HD's rectangular viewport during imaging reveals structures seen in both filtered and unfiltered light. For instance, Fig. 5.8 shows plasma structures that begin upstream of a circular bremsstrahlung filter, remain visible while passing through the filtered region,

and then exit downstream. Throughout their journey, these structures retain consistent shapes. This could mean that the filter transmits enough line radiation for the camera to see the same structures through the filter as it does without it. It could also mean that the bremsstrahlung and line radiation are highly correlated in ZaP-HD.

5.3   Corroborating stability metrics with DHI

An unambiguous verification of plasma stability is provided by DHI as density profiles provide the plasma location unambiguously. Unfortunately, ZaP-HD's DHI provides only one image per plasma pulse in a relatively small area (2 cm × 1 cm). If bremsstrahlung light from camera images could be correlated to DHI measurements of density, the high speed camera could act as a surrogate for DHI to verify stability with great time resolution over a wider spatial extent of the Z-pinch.

Overlaying line-integrated density, number density, and the current centroid locations on optical images reveals how well the diagnostics correlate. As in Ch. 4, the DHI is aimed at z = 8 cm to image the apparent stable constriction of plasma seen in optical images like in Fig. 5.3. Figure 5.9 presents such data during a generally quiescent (except at z = 5 cm) time in a plasma pulse. The density centroid matches the current centroid within 1 cm, and the light emission matches the density centroid even more closely. Another pulse is shown in Fig. 5.10, which exhibits good agreement between all three diagnostics. Fig. 5.11 shows similar overlayed contours of magnetic field and temperature computed from the density shown in Fig. 5.10.

Agreement between the current centroid and density is common, but the light emission often deviates from the density. Axial variation is also common in the line-integrated density, which may obscure the diagnostic's ability to view kink instabilities as obvious kinks are never seen by DHI. Such axial variation does not significantly alter Abel-inverted number density, but the axisymmetry assumption inherent in the inversion ensures number density data can only capture axisymmetric sausage instabilities. Figs. 5.12 and 5.13 show DHI data with axial variation. Both figures show excellent correlation between the density and current

160817011
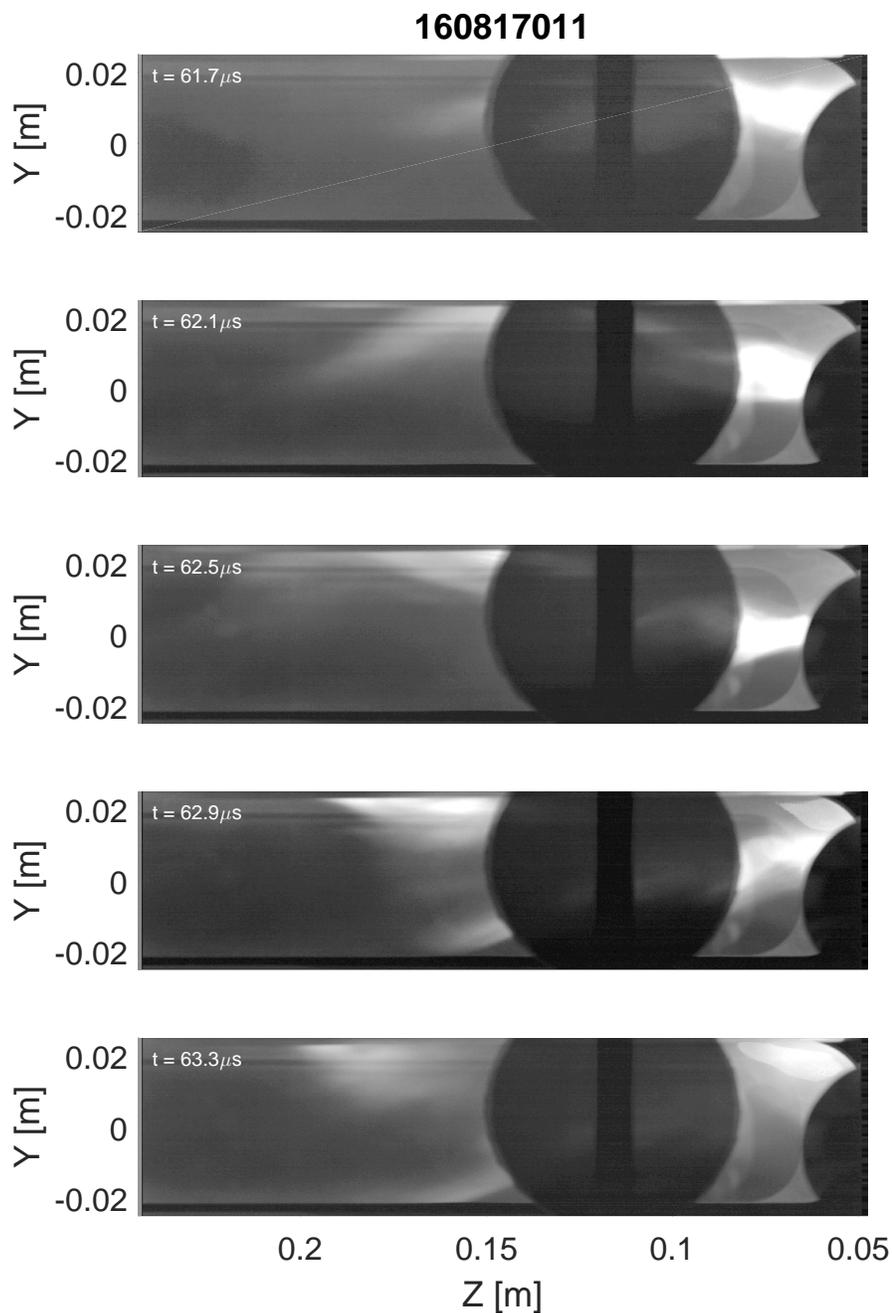
Figure 5.8: High speed camera images contrasting unfiltered and filtered plasma light emission. The circular bremsstrahlung filter is visible between $z = 10$ and 15 cm. Structures originating in the unfiltered region upstream are visible moving through the filtered region and then out into the unfiltered region downstream. Observations consistently see strong correlation between unfiltered and filtered structures. The vertical shadow at 0.12 m is part of a 3D printed hanger holding a laser beam guide. The shadow of the beam guide is visible at the right edge of the image.
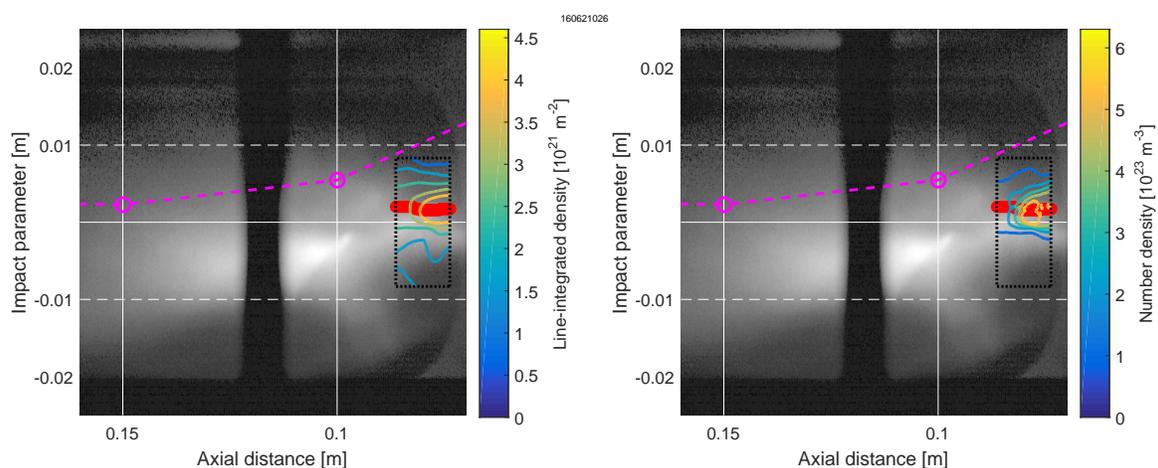
Figure 5.9: Contours of (left) line-integrated density and (right) number density are plotted over an optical image taken during pulse 160621026 at 50 μs, the time of the DHI pulse. The magenta circles are the current centroid locations projected into the plane of the image, and the red markers indicate the density centroids computed during Abel inversion. This image shows fair agreement between the image, density data, and centroid position. The vertical shadow at 0.12 m is part of a 3D printed hanger holding a laser beam guide. The shadow of the beam guide is visible at the right edge of the image.
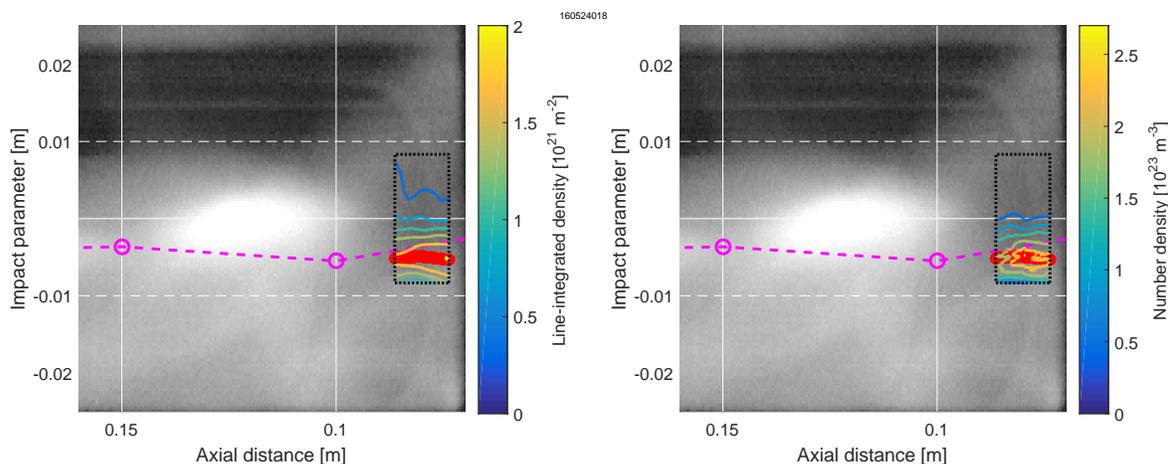
Figure 5.10: Contours of (left) line-integrated density and (right) number density are plotted over an optical image taken during pulse 160524018 at 50 μs, the time of the DHI pulse. The magenta circles are the current centroid locations projected into the plane of the image, and the red markers indicate the density centroid computed during Abel inversion. This image shows good agreement between the image, density data, and centroid position. The downstream scene beam guide was removed on this pulse, but testing showed this section of beam guide made little difference to the DHI's signal to noise.
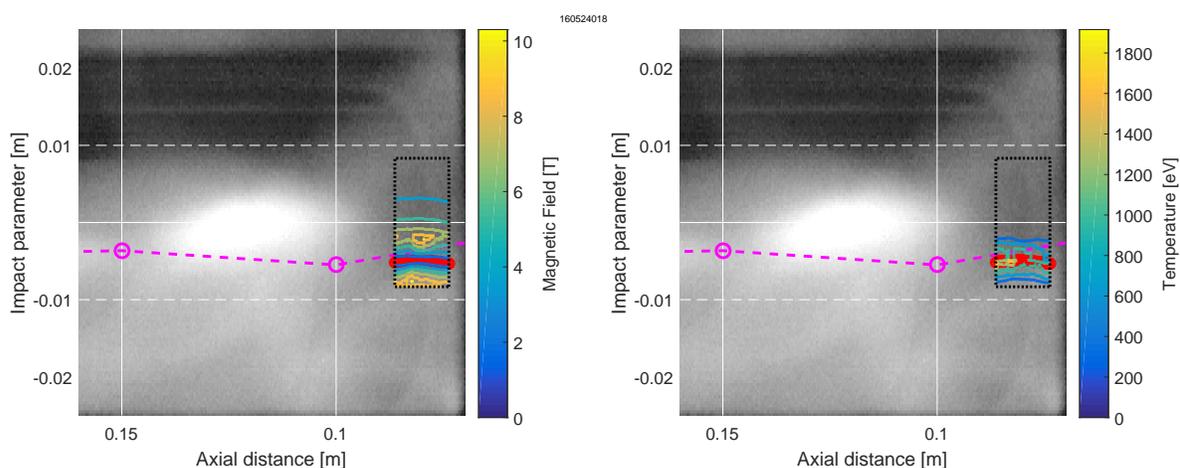
Figure 5.11: Contours of (left) magnetic field and (right) temperature are plotted over an optical image taken during pulse 160524018 at 50 μs, the time of the DHI pulse. The field and temperature are computed from the density in Fig. 5.10. The magenta circles are the current centroid locations projected into the plane of the image. Excellent correlation exists between the field, temperature, and current centroid.
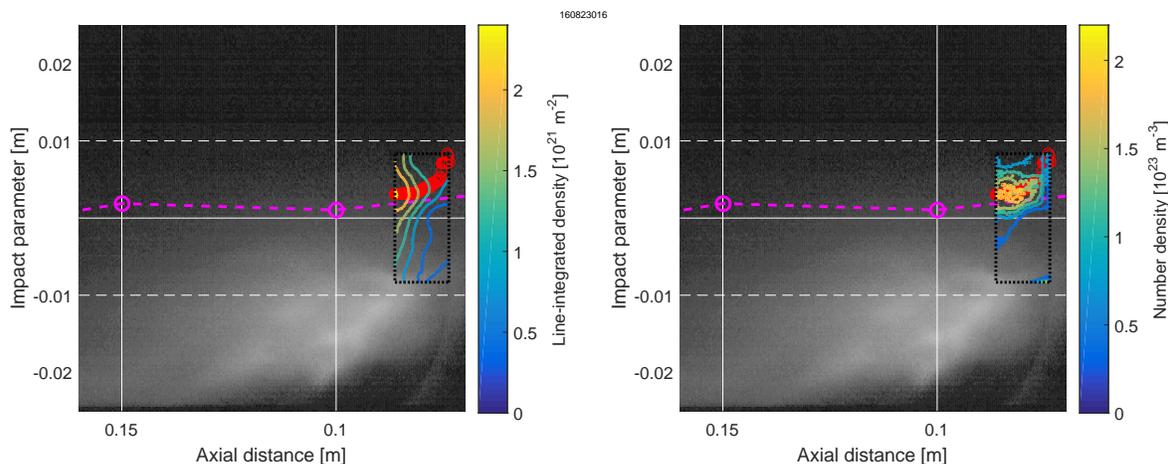
Figure 5.12: Contours of (left) line-integrated density and (right) number density are plotted over an optical image taken during pulse 160823016 at 60 μs, the time of the DHI pulse. The magenta circles are the current centroid locations projected into the plane of the image, and the red markers indicate the density centroid computed during Abel inversion. Here, excellent correlation exists between density and current centroid, but the light emission position is significantly different. In the upstream portion of the DHI data, the density centroid reaches the edge of the imaged area. At every cross-section where this happens, the number density is set to zero across the cross-section.

centroids. The light emission is displaced from the density in Fig. 5.12, and the light in Fig. 5.13 is too diffuse to make a meaningful comparison with the other diagnostics.

Possible sources of the axial line-integrated density variation include the plasma's radial features seen in optical images during the quiescent period (i.e. the plasma necking down near $z = 12$ cm and then expanding out). These radial features may be diffuse compared to the compressed on-axis plasma, but they extend over a wide area, and their effect would be weighted heavily in measurements of line-integrated density. Camera images also show irregular light structures emitting from the accelerator during the quiescent period, which pass through the DHI imaging area. These local perturbations as well as others invisible to the camera could cause the observed axial variations.

Comparison of the density with optical images and current centroids promote magnetic mode data as the better measure of plasma position and stability. At present, the high
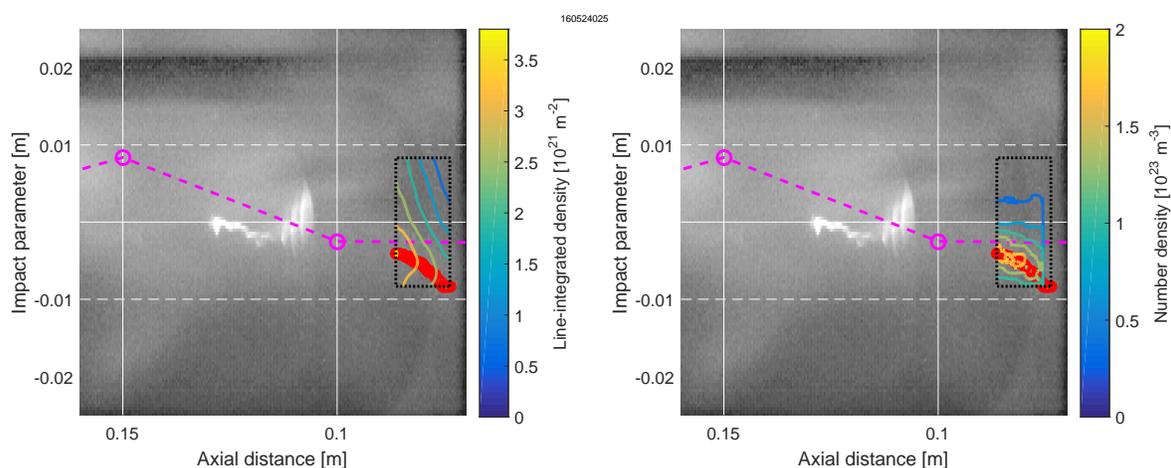
Figure 5.13: Contours of (left) line-integrated density and (right) number density are plotted over an optical image taken during pulse 160524025 at 50 μs, the time of the DHI pulse. The magenta circles are the current centroid locations projected into the plane of the image, and the red markers indicate the density centroid computed during Abel inversion. Excellent correlation exists between density and current centroid, but the light emission is too diffuse to make a meaningful comparison of its position to the other diagnostics. In the upstream portion of the DHI data, the density centroid reaches the edge of the imaged area. At every cross-section where this happens, the number density is set to zero across the cross-section.

speed camera cannot act as a reliable stability measure on its own. Different filters could be attempted in the future to cut out more line emission. As they are, the camera images are not so distinct from the mode data to not make them helpful in allowing the machine operator to more easily distinguish the general stability quality of different pulses.

5.4 Visualizing instability structure with DHI

As mentioned in Sec. 5.2, saturated instabilities appear in flow stabilized Z-pinches. ZaP-HD's DHI system has yet to capture kink instabilities, but it has observed sausage instabilities. While an instability does not appear in the optical images of Fig. 5.14, a sausage instability of size $\lambda \approx 1$ cm does appear in the number density for this pulse. The instability structure becomes more apparent when contours of density are plotted with magenta markers indicating the plasma radius in Fig. 5.15. Contours of magnetic field for this pulse in Fig. 5.16 are consistent with a sausage mode having increased field strength at the constriction. Temperature contours of Fig. 5.17 indicate a hotter plasma inside the instability. Despite extensive data collection, instabilities are not often seen with the DHI. This could mean their characteristic sizes typically exceed the DHI image size. Instabilities seen in camera images are typically around $\lambda \approx 3$ cm.

5.5 Searching for noise sources to improve DHI signals

Great care has been taken to maximize the quality of the DHI measurements. An initial lack of coherent structure consistently matching optical camera images compelled investigation of noise sources in the DHI system. Variations in vacuum holograms throughout the day can spoil the electron density measurements. Many baseline holograms (a more general term for vacuum hologram used here because some testing involved passing the entire DHI system through air) were collected consecutively from a variety of DHI set ups to look for correlation between the set up and the variation in the measured phase shifts. Vibrations mildly affected the measurements, and air currents significantly obscured them until installation of beam guides.
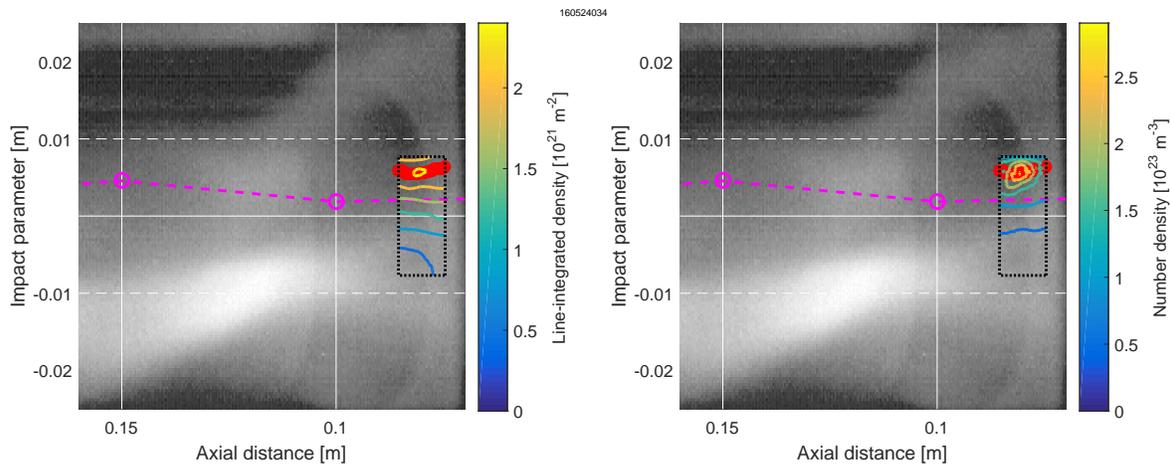
Figure 5.14: Contours of (left) line-integrated density and (right) number density are plotted over an optical image taken during pulse 160524034 at 50 μs, the time of the DHI pulse. The magenta circles are the current centroid locations projected into the plane of the image, and the red markers indicate the density centroid computed during Abel inversion. Excellent correlation exists between density and current centroid, but the light emission is too diffuse to make a meaningful comparison of its position to the other diagnostics.

Holographic reconstruction of a single hologram yields the phase front of the scene beam, which is difficult to analyze by itself. To ease the analysis of baseline hologram variability, the scene beam phase of each baseline under analysis is subtracted by the scene beam phase of the preceding baseline. The resulting phase difference is analogous to the reconstructed phase differences of Figs. 3.6 and 3.8. After smoothing and unwrapping the twin image phase difference as in Sec. 3.4, the maximum phase difference between any two points in the image for each baseline pair is identified. This investigation converts this maximum phase difference to an equivalent maximum variation in line-integrated density with Eq. 2.10 as the metric to monitor baseline variability. Fig. 5.18 compares the maximum variation in line-integrated density for many vacuum and plasma holograms at the start of the investigation. The noise affecting the vacuum holograms is of comparable magnitude to the measurements of the plasma holograms.

The DHI set up was systematically stabilized to search for the noise source. The can-
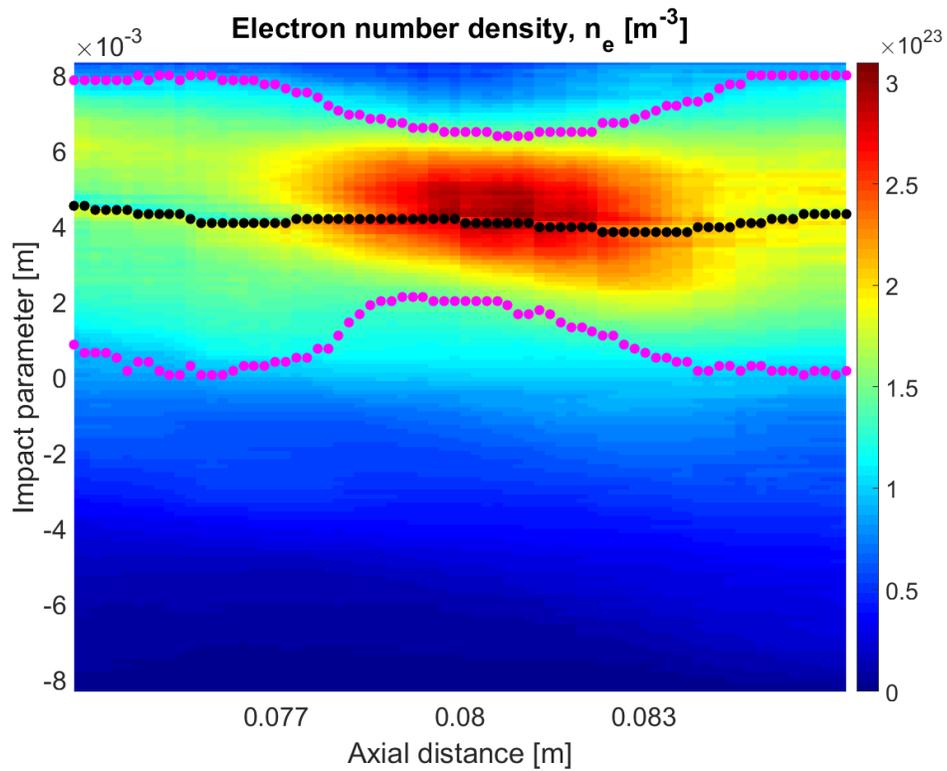
Figure 5.15: Electron number density contour plot showing a sausage mode instability. The DHI image was taken on pulse 160524034 at 50 μs. It shows a $\lambda \approx 1$ cm sausage mode instability where the plasma size constricts and density increases near $z = 8$ cm.
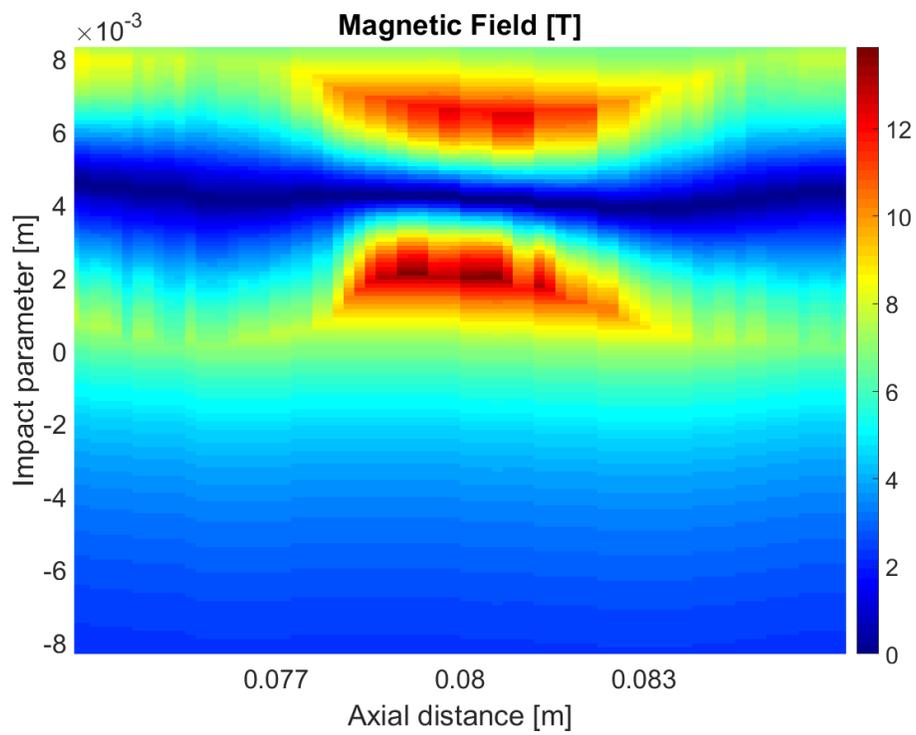
Figure 5.16: Magnetic field contour plot showing field concentration at the constriction of a sausage mode instability. Field values are computed with the analysis of Ch. 4 from the density in Fig. 5.15.
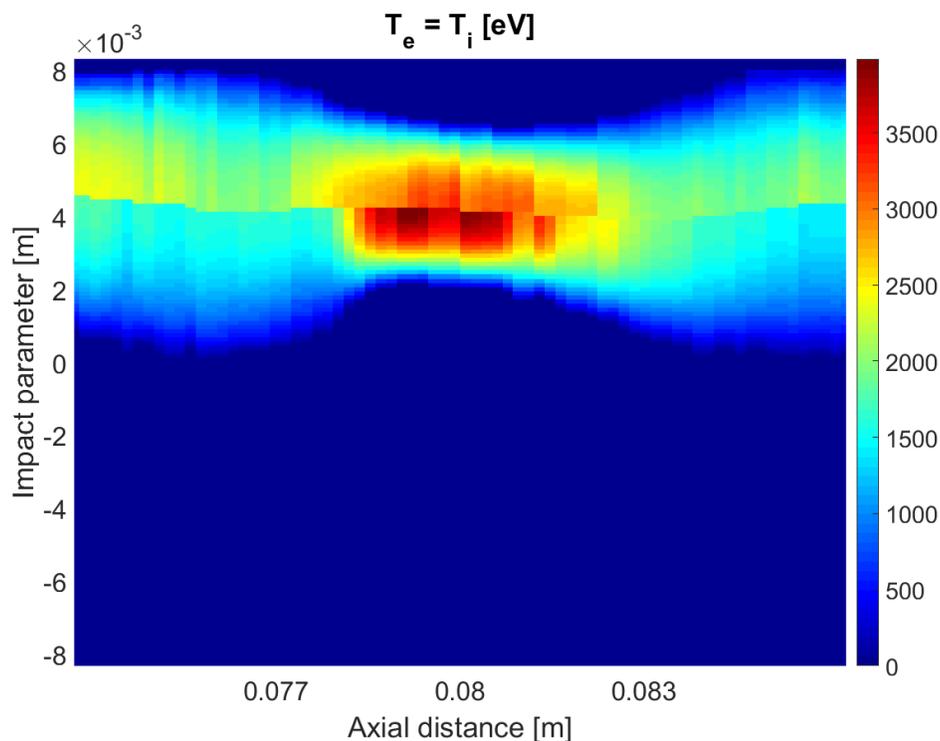
Figure 5.17: Temperature contour plot showing high temperature at the constriction of a sausage mode instability. Temperature values are computed with the analysis of Ch. 4 from the density in Fig. 5.15.
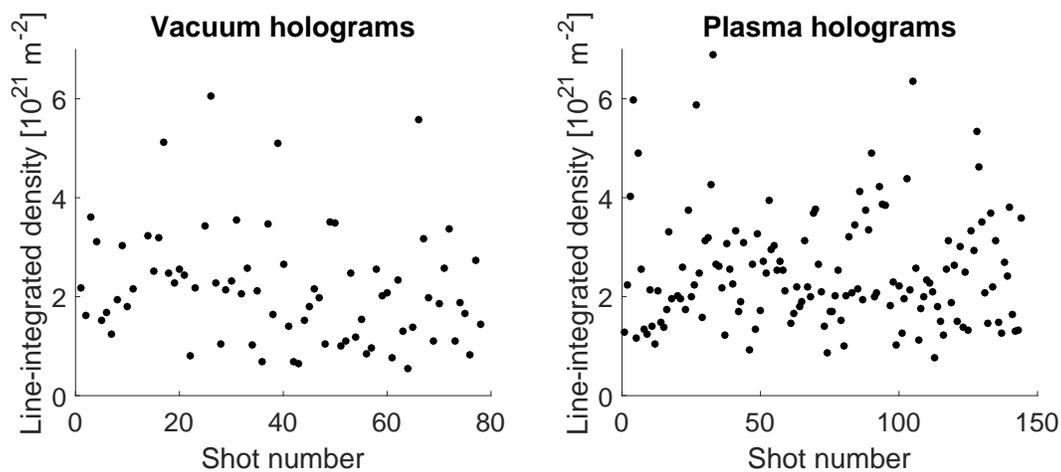
Figure 5.18: Line-integrated density from many vacuum and plasma holograms prior to DHI beam guide installation showing the noise level on baselines is similar to the line-integrated density seen on plasma pulses.
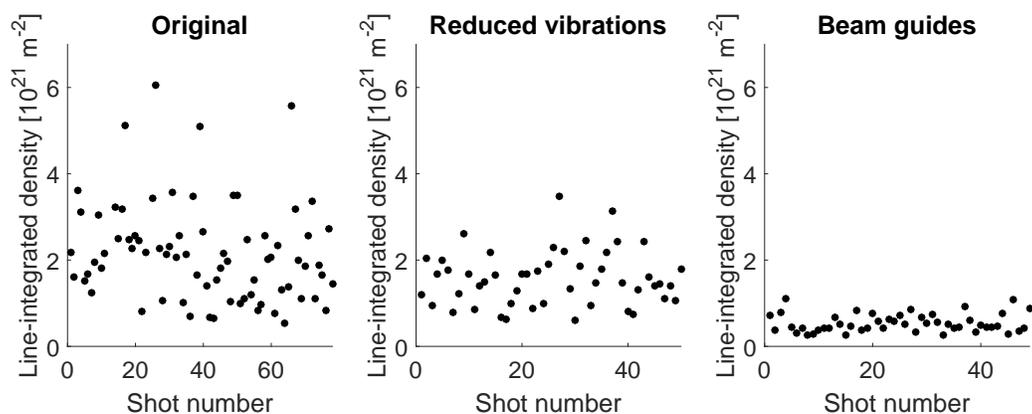
Figure 5.19: Comparison of the baseline variability during the original DHI set up, a reduced vibration set up, and the reduced vibration set up including beam guides. The beam guides significantly reduced baseline variability.

tilevered beam expander was supported, mirror mounts were tightened, reference beam mirrors were lowered, and the camera was moved from a tripod to a rigid stand on the downstream optics table. The vacuum system was turned off and the rectangular windows were removed to allow the scene beam to pass directly through the machine. The set up with reduced vibrations slightly reduces the observed noise. Installation of beam guides far more significantly reduced the noise. Fig. 5.19 compares noise levels between the original set up, the reduced vibration set up, and the reduced vibration set up with beam guides.

Subsequently collecting plasma data with the beam guides in place reduced the vacuum hologram variation to a level below the measured density. Fig. 5.20 compares baseline and plasma holograms from a run day after beam guide installation. All DHI data presented this thesis was collected after the beam guide installation unless otherwise noted.
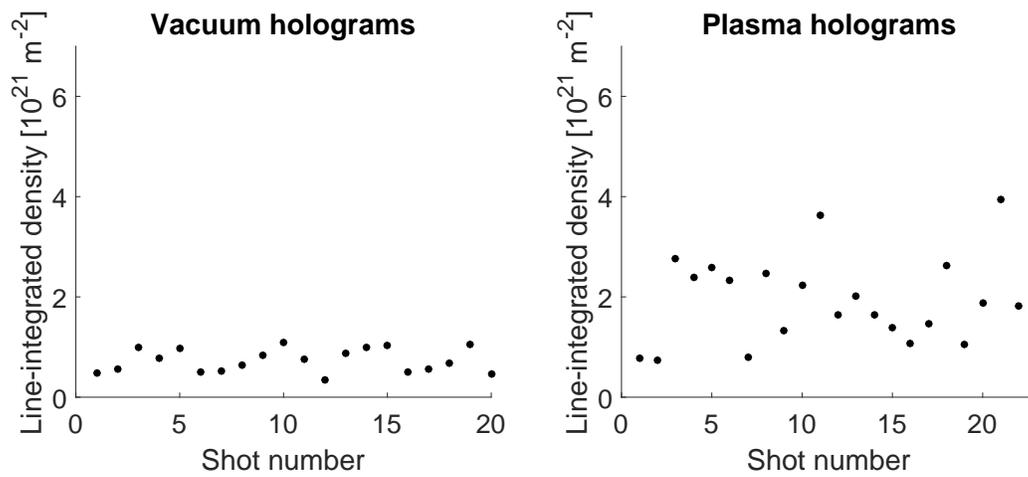
Figure 5.20: Line-integrated density from many vacuum and plasma holograms after DHI beam guide installation showing the noise level on baselines is below the line-integrated density seen on plasma pulses.

Chapter 6

CONCLUSIONS

The ZaP-HD Flow Z-Pinch experiment investigates how the shear stabilized Z-pinch concept scales to higher energy density. The experiment's three-electrode design allows for improved plasma compression over the previous ZaP experiment while still sustaining pinches with stable lifetimes of 15-60 μs. Electron density data from DHI demonstrates ZaP-HD's pinches have less linear density ($N_{ZaP-HD} \approx 0.5$ - 2×10^{19} m^{-1}) than ZaP's ($N_{ZaP} \approx 3$ - 5×10^{19} m^{-1}), and magnetic field measurements indicate larger compression currents in ZaP-HD (90 - 125 kA) than in ZaP (30 - 60 kA) [69]. The combination of greater current and reduced linear density allows ZaP-HD to more effectively compress plasma, leading to higher electron densities ($\approx 2.5 \times 10^{23}$ m^{-3}) and smaller pinch sizes (≈ 2.5 mm).

DHI provides an expedient means of measuring spatially-resolved electron density. Fresnel transform reconstruction allows the extraction of the phase shift from holograms measured with a Mach-Zehnder-like interferometer. The phase shift provides the line-integrated electron density, which is Abel-inverted to obtain electron number density.

ZaP-HD generates less stable plasmas than ZaP, and this instability proves a difficulty in collecting DHI data. The best confinement observed in ZaP-HD by both magnetic mode data and optical images is located around $z = 5$-15 cm, which is where most DHI data is obtained. Complex and dynamic interactions at the interface between the acceleration and assembly regions at $z = 0$ cm likely extend into the DHI view and affects the density measurements, causing apparent axial variation and making Abel-inversion more difficult. Unfortunately, the plasma stability farther downstream is too poor for reliable measurements removed from these dynamics.

The highest quality holographic reconstructions are selected for further study. An equi-

librium analysis, which computes magnetic field and temperature profiles from measured density, suggests portions of the Z-pinch compression process are non-adiabatic. Analysis of individual plasma pulses, especially those with significant axial variation, suggests deviations from adiabatic behavior because temperatures and fields predicted by adiabatic theory are not consistent with measured pinch sizes. Non-adiabatic behavior correlates strongly with axial variation in pinch size, which supports previous work observing a relationship between Z-pinch radius oscillations and non-adiabatic behavior [32].

The invertible DHI data supports the reliability of the magnetic mode data over optical imaging for determining plasma position and stability. DHI does not observe kink instabilities, which are sometimes seen in optical images, but it has captured sausage instabilities. The smallest observed instabilities are 1 cm in wavelength.

Over the range of plasma currents tested, the peak plasma density does not increase with current, which disagrees with the predicted adiabatic scaling. Invertible DHI measurements were only obtainable at the highest observed plasma currents, so a relatively small range of currents are considered. Further testing over an expanded range is required to draw more definite conclusions about the viability of the flow Z-pinch for fusion and high-energy-density plasma applications.

Chapter 7

FUTURE WORK

Expanding the capability of the DHI can enable a more conclusive study of the scalability of the flow shear stabilized Z-pinch. In its present form, much of the line-integrated density data collected by the DHI system is non-invertible, which means the DHI's view is not wide enough to see both sides of the density cross-sections. The lack of time resolution also makes data interpretation difficult.

Identifying if the sheared flow Z-pinch could scale to high-energy-density plasma conditions requires data collection with DHI over a wider range of plasma currents. This requires expanding the operating envelope of the DHI diagnostic to measure larger, less-dense plasmas. Widening the view of the DHI by expanding the scene beam through the experiment and then contracting it back down to the size of the camera sensor should increase the amount of invertible data by making both sides of the cross-sections visible. Presently, the scene and reference beams are expanded to roughly a 1 inch diameter, but the rectangular openings in the outer electrode are 2 inches across, which allows for significant beam expansion.

Employing 2D interferometry with the high speed camera could also allow for easier data interpretation and better understanding of noise sources. The Kirana camera does not have sufficient resolution to enable Fresnel transform reconstruction, but its 30 μm pixel size is sufficient to resolve the larger fringes used in 2D interferometry. Using a CW HeNe laser with the camera would provide 180 interferograms per plasma pulse. Using such a 2D interferometry system to study baseline variations and to observe the time evolution of the plasma density could reveal noise sources and density dynamics invisible to the single pulse Nd:YAG system. Using 2D interferometry requires a different method to convert the raw interferograms to line-integrated density, but software packages are available with such

capabilities [65, 66].

Perhaps the single biggest difficulty in collecting quality DHI data was the plasma's own dynamics. The DHI was consistently aimed in the region between $z = $ 5-10 cm where optical images and magnetic mode data identified stable, compressed plasma. Although this region exhibits relative quiescence, the plasma structures from the dynamics occurring near the end of the accelerator likely reach into this region. As the DHI measures line-integrated density, structures at large radii moving out of the accelerator can significantly affect the measurements. One example of such structure is the radial constriction often observed during stable plasmas as in Fig. 5.3. Visible irregular blobs of light also intermittently eject from the gun, and objects invisible to the camera also likely flow through the DHI view. The next iteration of the ZaP-HD experiment, FuZE, has plans to arrange the three electrodes differently to improve stability. The design will remove the middle electrode and instead use an endwall insulated from the outer electrode to act as the third electrode. This design aims to eliminate the troublesome interactions at the end of the accelerator, leading to improved stability while retaining scalability.

BIBLIOGRAPHY

[1] S. D. Knecht, W. Lowrie, and U. Shumlak. Effects of a conducting wall on Z-pinch stability. *Plasma Science, IEEE Transactions on*, 42(6):1531–1543, 2014.

[2] V. D. Shafranov. The stability of a cylindrical gaseous conductor in a magnetic field. *The Soviet Journal of Atomic Energy*, 1956.

[3] M. Kruskal and M. Schwarzschild. Some instabilities of a completely ionized plasma. 1954.

[4] B. B. Kadomtsev. Hydromagnetic stability of a plasma. *Reviews of Plasma Physics*, 1966.

[5] U. Shumlak and C. Hartman. Sheared flow stabilization of the m = 1 kink mode in Z pinches. *Physical Review Letters*, 75(18):3285–3288, October 1995.

[6] M. R. Weis, P. Zhang, Y. Y. Lau, P. F. Schmit, K. J. Peterson, M. Hess, and R. M. Gilgenbach. Coupling of sausage, kink, and magneto-rayleigh-taylor instabilities in a cylindrical liner. *Physics of Plasmas*, 22(3), 2015.

[7] D. Sharp. An overview of rayleigh-taylor instability. *Physica D: Nonlinear Phenomena*, 12(1):3 – 18, 1984.

[8] M. R. Douglas, J. S. De Groot, and R. B. Spielman. The magneto-Rayleigh-Taylor instability in dynamic z pinches. *Laser and Particle Beams*, 2001.

[9] R. Davidson and N. Krall. Anomalous transport in high-temperature plasmas with applications to solenoidal fusion systems. *Nuclear Fusion*, 17(6):1313, 1977.

[10] M. A. Liberman, J. S. D. Groot, A. Toor, and R. B. Spielman. *Physics of High-Density Z-Pinch Plasmas*. Springer, 1999.

[11] M. G. Haines. A review of the dense z-pinch. *Plasma Physics and Controlled Fusion*, 2011.

[12] U. Shumlak, J. Chadney, R. P. Golingo, D. J. Den Hartog, M. C. Hughes, S. D. Knecht, W. Lowrie, V. S. Lukin, B. A. Nelson, R. J. Oberto, J. L. Rohrbach, M. P. Ross, and G. V. Vogman. The sheared-flow stabilized Z-pinch. *Transactions of Fusion Science and Technology*, 61(1T):119–124, 2012.

[13] L. Artsimovich, A. Andrianov, O. Bazilevskaya, Y. Prokhorov, and N. Filippov. An investigation of high-current pulsed discharges. *Journal of Nuclear Energy (1954)*, 4(2):203 – 208, 1957.

[14] M. Rosenbluth. Stability of the pinch. Technical report, Los Alamos Scientific Lab., N. Mex., 1956.

[15] R. Spielman and J. De Groot. Z pinchesâĂŤa historical view. *Laser and Particle Beams*, 19(04):509–525, 2001.

[16] D. Ryutov, M. S. Derzon, and M. K. Matzen. The physics of fast z pinches. *Reviews of Modern Physics*, 72(1):167, 2000.

[17] M. R. Gomez, S. A. Slutz, A. B. Sefkow, D. B. Sinars, K. D. Hahn, S. B. Hansen, E. C. Harding, P. F. Knapp, P. F. Schmit, C. A. Jennings, T. J. Awe, M. Geissel, D. C. Rovang, G. A. Chandler, G. W. Cooper, M. E. Cuneo, A. J. Harvey-Thompson, M. C. Herrmann, M. H. Hess, O. Johns, D. C. Lamppa, M. R. Martin, R. D. McBride, K. J. Peterson, J. L. Porter, G. K. Robertson, G. A. Rochau, C. L. Ruiz, M. E. Savage, I. C. Smith, W. A. Stygar, and R. A. Vesey. Experimental demonstration of fusion-relevant conditions in magnetized liner inertial fusion. *Phys. Rev. Lett.*, 113:155003, Oct 2014.

[18] F. J. Wessel, H. U. Rahman, P. Ney, J. Valenzuela, F. Beg, E. McKee, and T. Darling. Fusion in a staged z-pinch. *AIP Conference Proceedings*, 1721(1), 2016.

[19] M. K. Matzen. Z pinches as intense x-ray sources for high-energy density physics applications. *Physics of Plasmas*, 4(5), 1997.

[20] E. Moses, J. Lindl, M. Spaeth, R. Patterson, R. Sawicki, L. Atherton, P. Baisden, L. Lagin, D. Larson, B. MacGowan, et al. Overview: Development of the national ignition facility and the transition to a user facility for the ignition campaign and high energy density scientific research. *Fusion Science and Technology*, 69(1):1–24, 2016.

[21] S. A. Pikuz, D. B. Sinars, T. A. Shelkovenko, K. M. Chandler, D. A. Hammer, G. V. Ivanenkov, W. Stepniewski, and I. Y. Skobelev. High energy density Z-pinch plasma conditions with picosecond time resolution. *Phys. Rev. Lett.*, 89:035003, Jun 2002.

[22] T. A. Shelkovenko, S. A. Pikuz, J. D. Douglass, R. D. Mcbride, J. B. Greenly, and D. A. Hammer. Multiwire x -pinches at 1-ma current on the cobra pulsed-power generator. *IEEE Transactions on Plasma Science*, 34(5):2336–2341, Oct 2006.

[23] A. Bernard, H. Bruzzone, P. Choi, H. Chuaqui, V. Gribkov, J. Herrera, K. Hirano, A. Krejci, S. Lee, C. Luo, et al. Scientific status of plasma focus research. *JOURNAL-MOSCOW PHYSICAL SOCIETY*, 8:93–170, 1998.

[24] A. L. Moser and P. M. Bellan. Magnetic reconnection from a multiscale instability cascade. *Nature*, 482(7385):379–381, 2012.

[25] P. M. Bellan, S. You, and S. C. Hsu. Simulating astrophysical jets in laboratory experiments. *Astrophysics and Space Science*, 298(1):203–209, 2005.

[26] J. G. Linhart. Beam-target fusion in a dense z-pinch. *Plasma physics and controlled fusion*, 30(12):1641, 1988.

[27] S. Fetter, V. A. Frolov, M. Miller, R. Mozley, O. F. Prilutsky, S. N. Rodionov, and R. Z. Sagdeev. Detecting nuclear warheads. *Science & Global Security*, 1:225–302, 1990.

[28] U. Shumlak, R. C. Lilly, C. S. Adams, R. P. Golingo, S. L. Jackson, S. D. Knecht, and B. A. Nelson. Advanced space propulsion based on the flow-stabilized Z-pinch fusion concept. In *42nd AIAA Joint Propulsion Conference*, Sacramento, California, July 2006.

[29] R. P. Golingo, U. Shumlak, and B. Nelson. Formation of a sheared flow Z-pinch. *Physics of Plasmas*, 12(6):062505, 2005.

[30] R. P. Golingo. *Formation of a Sheared Flow Z-Pinch*. PhD thesis, University of Washington, 2003.

[31] S. L. Jackson. *Density Characteristics of a Sheared-Flow Z-Pinch*. PhD thesis, University of Washington, 2006.

[32] S. D. Knecht. *Comparison of Electrode Configurations on ZaP: Investigation of Heating Mechanisms in a Flow Z-Pinch*. PhD thesis, University of Washington, 2012.

[33] M. C. Hughes, U. Shumlak, B. A. Nelson, R. P. Golingo, C. Bowers, S. Doty, S. D. Knecht, M. P. Ross, H. Stankey, and S. Swofford. Zap Flow Z-pinch extended source results and machine upgrade to ZaP-HD. APS-DPP, 2013.

[34] D. J. Den Hartog and R. P. Golingo. Telecentric viewing system for light collection from a z-pinch plasma. *Review of Scientific Instruments*, 72(4), 2001.

[35] J. Weed. Master's thesis to be completed march 2014.

[36] J. Marshall. Performance of a hydromagnetic plasma gun. *Physics of Fluids (US)*, 3, 1960.

[37] M. C. Hughes, U. Shumlak, R. P. Golingo, B. A. Nelson, and M. P. Ross. Quasi-steady accelerator operation on the zap flow z-pinch. *AIP Conference Proceedings*, 1639(1), 2014.

[38] D. Y. Cheng. Plasma deflagration and the properties of a coaxial plasma deflagration gun. *Nuclear Fusion*, 10(3):305, 1970.

[39] D. Y. Cheng. Application of a deflagration plasma gun as a space propulsion thruster. *AIAA Journal*, 9(9):1681–1685, 1971.

[40] D. M. Woodall and L. K. Len. Observation of current sheath transition from snowplow to deflagration. *Journal of Applied Physics*, 57(3), 1985.

[41] D. Gabor. Microscopy by reconstructed wave-fronts. *Proceedings of the Royal Society of London A: Mathematical, Physical and Engineering Sciences*, 197(1051):454–487, 1949.

[42] A. Orchowski, W. D. Rau, and H. Lichte. Electron holography surmounts resolution limit of electron microscopy. *Phys. Rev. Lett.*, 74:399–402, Jan 1995.

[43] F. Bruno, J. Laurent, C. Prada, B. Lamboul, B. Passilly, and M. Atlan. Non-destructive testing of composite plates by holographic vibrometry. *Journal of Applied Physics*, 115(15), 2014.

[44] M.-T. Shiu, Y.-K. Chew, H.-T. Chan, X.-Y. Wong, and C.-C. Chang. Three-dimensional information encryption and anticounterfeiting using digital holography. *Appl. Opt.*, 54(1):A84–A88, Jan 2015.

[45] L. Yu and L. Cai. Multidimensional data encryption with digital holography. *Optics Communications*, 215(4âĂŞ6):271 – 284, 2003.

[46] E. Tajahuerce and B. Javidi. Encrypting three-dimensional information with digital holography. *Appl. Opt.*, 39(35):6595–6601, Dec 2000.

[47] J. Desse, J. Soutade, P. Viguier, P. Picart, M. Ferrier, and L. Serre. Digital holographic interferometry at f4-onera hypersonic wind tunnel. *Visualization of Mechanical Processes: An International Online Journal*, 3(1):007554, 2013.

[48] I. Yamaguchi and T. Zhang. Phase-shifting digital holography. *Opt. Lett.*, 22(16):1268–1270, Aug 1997.

[49] F. C. Jahoda and R. E. Siemon. Holographic interferometry cookbook. Technical Report LA-5058-MS, Los Alamos Scientific Laboratory, 1972.

[50] S. L. Jackson and U. Shumlak. Abel inversion of a holographic interferogram for determination of the density profile of a sheared-flow Z-pinch. *Review of scientific instruments*, 77(8):083502, 2006.

[51] E. Völkl and M. Lehmann. The reconstruction of off-axis electron holograms. In *Introduction to Electron Holography*, pages 125–151. Kluwer Academic/Plenum, New York, 1999.

[52] C. E. Thomas, L. R. Baylor, S. K. Combs, S. J. Meitner, D. A. Rasmussen, E. M. Granstedt, R. P. Majeski, and R. Kaita. High speed digital holography for density and fluctuation measurements (invited). *Review of Scientific Instruments*, 81:10E527, 2010.

[53] E. M. Granstedt, C. E. Thomas, R. Kaita, R. Majeski, L. R. Baylor, S. J. Meitner, and S. K. Combs. High-speed digital holography for neutral gas and electron density imaging. *Review of Scientific Instruments*, 87(5), 2016.

[54] C. E. Thomas, E. M. Granstedt, T. M. Biewer, L. R. Baylor, S. K. Combs, S. J. Meitner, D. L. Hillis, R. Majeski, and R. Kaita. Digital holography for in situ real-time measurement of plasma-facing-component erosion. *Review of Scientific Instruments*, 85:11D810, 2014.

[55] T. Kreis. Digital holographic interference-phase measurement using the fourier-transform method. *J. Opt. Soc. Am. A*, 3(6):847–855, Jun 1986.

[56] C. Pavez, J. Pedreros, A. Tarifeño-Saldivia, and L. Soto. Observation of plasma jets in a table top plasma focus discharge. *Physics of Plasmas*, 22(4), 2015.

[57] M. Takeda, H. Ina, and S. Kobayashi. Fourier-transform method of fringe-pattern analysis for computer-based topography and interferometry. *J. Opt. Soc. Am.*, 72(1):156–160, Jan 1982.

[58] J. W. Goodman. *Introduction to Fourier Optics*. McGraw-Hill, New York, 1968.

[59] U. Schnars. Direct phase determination in hologram interferometry with use of digitally recorded holograms. *J. Opt. Soc. Am. A*, 11(7):2011–2015, Jul 1994.

[60] T. Kreis. *Handbook of Holographic Interferometry: Optical and Digital Methods*. Wiley, Germany, 2005.

[61] I. H. Lira and L. E. Moreno. Digital interferometry of phase objects. *Measurement Science and Technology*, 8(5):493, 1997.

[62] C. Pavez, J. Pedreros, C. Curin, G. Munoz C, and L. Soto. Digital interferometry applied to transient dense plasmas. *Plasma Science, IEEE Transactions on*, 40(12):3384–3389, Dec 2012.

[63] G. Swadling, S. Lebedev, N. Niasse, J. Chittenden, G. Hall, F. Suzuki-Vidal, G. Burdiak, A. Harvey-Thompson, S. Bland, P. De Grouchy, et al. Oblique shock structures formed during the ablation phase of aluminium wire array z-pinches. *Physics of Plasmas*, 20(2):022705, 2013.

[64] M. Takeda and Z. Tung. Subfringe holographic interferometry by computer-based spatial-carrier fringe-pattern analysis. *Journal of Optics*, 16(3):127, 1985.

[65] M. Hipp and P. Reiterer. *User Manual for IDEA 1.7*. Institut für Experimental Physik Technische Universität Graz, July 2003.

[66] Ø. Skotheim. *Holovision-A software package for reconstruction and analysis of digitally sampled holograms*. PhD thesis, Norwegian University of Science and Technology, 2001.

[67] S. L. Jackson. Holographic interferometry on the zap flow z-pinch. Master's thesis, University of Washington, 2003.

[68] B. V. Weber and S. F. Fulghum. A high sensitivity two-color interferometer for pulsed power plasmas. *Review of Scientific Instruments*, 68(2), 1997.

[69] S. D. Knecht, R. P. Golingo, B. A. Nelson, and U. Shumlak. Calculation of the equilibrium evolution of the ZaP Flow Z - Pinch using a four-chord interferometer. *Plasma Science, IEEE Transactions on*, 43(8):2469–2479, Aug 2015.

[70] M. Coppins, I. Culverwell, and M. Haines. Time dependent z-pinch equilibria. *Physics of Fluids (1958-1988)*, 31(9):2688–2694, 1988.

[71] S. Braginskii. Transport processes in a plasma. *Reviews of plasma physics*, 1:205, 1965.

[72] S. C. Pluntze. *Reynolds Number Trends in Computational Solutions of Two-Dimensional Airfoils with Taguchi Techniques and Grid Resolution*. PhD thesis, University of Washington, 1997.

[73] D. C. Montgomery. *Design and analysis of experiments*. John Wiley, 5th edition, 2001.

[74] Ekspla, Lithuania. *NL121 Series Laser Technical Description and User's Manual*, 2014.

[75] R. G. Budynas and J. K. Nisbett. *Shigley's Mechanical Engineering Design*. McGraw-Hill.

Appendix A

THEORY OF LASER OPERATION

Lasers are ubiquitous as light sources in research and industry because they generate amplified, coherent beams of light. In plasma physics, they allow for non-perturbing measurements of plasma parameters like density, temperature, and magnetic field. In this context, we will explore how lasers contribute to plasma diagnostics measuring electron density. Laser qualities of importance to this application include temporal and spatial coherence, pulse duration, and pulse energy.

A.1   Einstein's quantum theory of light

Einstein's 1916 quantum theory of light laid down the theoretical foundations that would later enable the development of the laser. His theory explained all of atomic spectral light emission with three processes: absorption, spontaneous emission, and stimulated emission (see Fig. A.1). Figuring out how to encite stimulated emission, which does not often occur in nature, was critical to the production of the first laser.

To understand these three processes, we first need to introduce quantum electronics. Bound electrons, which orbit atoms or molecules, can reside in many distinct orbits; the precise orbit each electron occupies at a given time depends on its energy. A finite number of orbits are possible, which means the electrons can only occupy discrete energy states. When gaining or losing energy, an electron must instantly jump from one energy to another. When an electron undergoes such a transistion, energy must either be absorbed or released; this energy is usually transferred as a photon. The frequency of that photon depends on the magnitude of the energy change as in
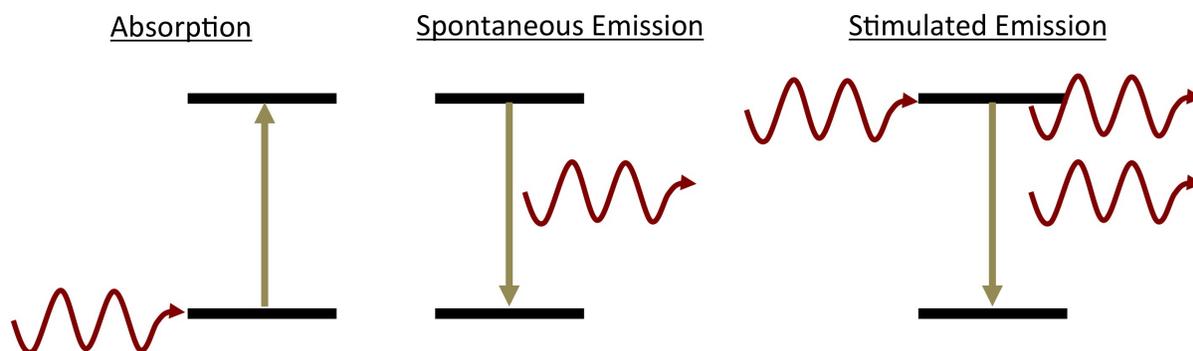
Figure A.1: At left, absorption of an incident photon raises an electron's energy level. At center, spontaneous emission of a photon at a random phase results from the random drop of an electron's energy. At right, stimulated emission caused by an incident photon with energy equal to that of the stimulated transition results in emission of an additional photon with identical energy and phase.

$$E = h\nu \tag{A.1}$$

where h is Planck's constant, E is the energy change, and ν is the photon's frequency in Hertz. Certain energy transitions are more probable than others, which helps lasers achieve monochromaticity.

Absorption occurs when a photon's energy raises the energy state of a bound electron in an atomic orbit. Spontaneous emission is the release of a photon when a bound electron drops to a lower energy state randomly at a random phase. Stimulated emission is the release of a photon when another photon causes an electron to drop energy levels. A stimulating photon must carry the same energy as the energy drop it stimulates, and each photon released by stimulated emission will carry the same frequency and phase as its stimulating photon, which allows lasers to attain coherence and monochromaticity. Because the stimulating photon is not destroyed in this process, stimulated emission can amplify radiation. Stimulated emission is not common in nature because the process requires electrons in an energetic state to fall to a lower energy state, and the steady equilibria observed in nature already contain minimal

energy.

A.2   General laser theory

To build a laser, we need to compel stimulated emission. Lasers commonly employ optical pumping to excite electrons in a gain medium to achieve a population inversion. A gain medium can be gaseous, liquid, or solid matter, which exhibits a probable electron transition of some utility. A population inversion occurs when the number of electrons in that transition's excited state exceeds the number in the lower state. This means a light beam of photons of this transition energy will be amplified each time the beam traverses the gain medium because more photons will stimulate emission rather than be absorbed.

Energy transitions involved in laser operation are mapped in Fig. A.2. Early lasers (i.e. ruby lasers) utilized three levels: an upper energy state, upper laser state, and a ground state, which effectively acts as the lower laser state. Optical pumping raises electrons to the upper energy state from which they spontaneously drop to the upper laser state via non-radiative decay. Pumping can maintain a population inversion between the upper laser state and the ground state because the rate of spontaneous emmission across the laser transition is much slower than the non-radiative decay that resupplies the upper laser state. Most present-day lasers, including Nd:YAG lasers, employ four levels because they can maintain the population inversion more efficiently. While three level lasers can only attain a population inversion by resupplying the upper laser state, four level lasers can also deplete the lower laser state.

To allow amplification, the gain medium is located between two mirrors, so that initially spontaneous emission will reflect back into the gain medium, stimulating emission, which will then oscillate in the cavity and amplify with each pass. Note that only radiation directed down the length of the cavity will be amplified, which gives the laser its collimation. The stimulated emission will resonate within the cavity at several different longitudinal modes, each of which is really a different wavelength of light. Having a single longitudinal mode (SLM) (ie: a very monochromatic beam), maximizes temporal coherence, and several techniques are employed to ensure SLM operation. All such techniques ultimately ensure one
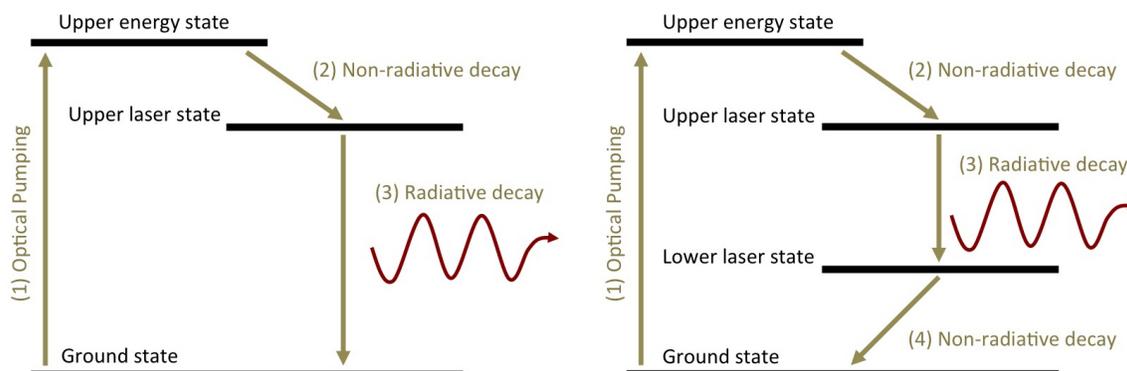
Figure A.2: At left, energy transistions of a three level laser are shown. Absorption of photons from optical pumping elevates electrons to the upper energy state. The electrons quickly drop to the upper laser state via a non-radiative decay. A population inversion is maintained between the upper laser state and the ground state. At right, energy transitions of a four level laser are shown. Four level lasers employ a separate lower laser state, which allows for easier sustainment of the population inversion. In the case of both designs, the goal is maintaining a population inversion across the laser transition to allow amplification of stimulated emission.

mode experiences more amplification from the gain medium than the other modes. The longitudinal modes compete for the finite energy of the gain medium, and if one mode grows larger than the rest, it will draw energy at the expense of the other modes. A Fabry-Pérot etalon is commonly employed within the laser cavity to give one mode preference over the others. An etalon itself is an optical cavity, which only transmits light wavelengths that resonate within it. By choosing its thickness and refractive index carefully, a narrow bandwidth can be selected to resonate in the laser cavity.

High energy pulsed lasers rely on an optical switching mechanism called a Q-switch to forestall the resonant mode growth until a large population inversion has been established. The switch resides within the cavity and is closed while the population inversion builds during pumping of the gain medium. When sufficient inversion is present, the switch is opened to allow mode growth. This leads to a short pulse of much higher power than that possible in continuous wave (CW) operation. Typical components of a pulsed laser are shown in
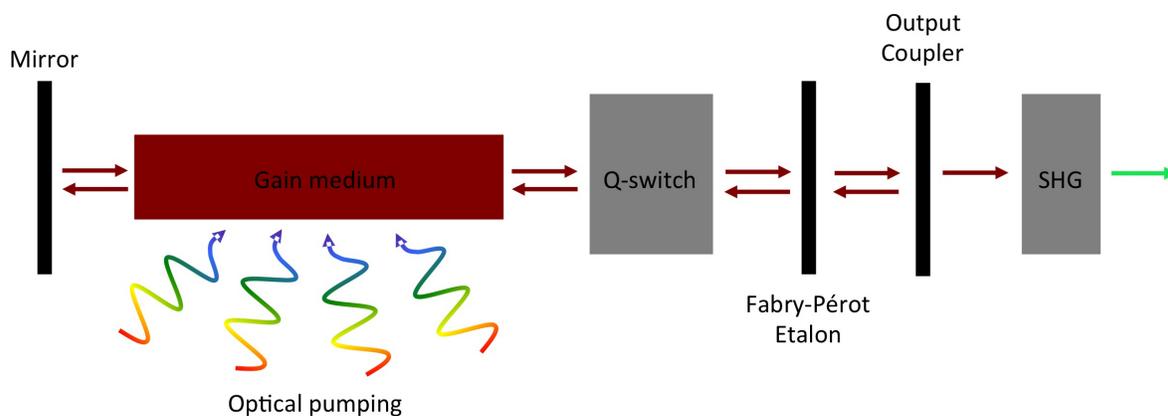
Figure A.3: A high energy pulsed laser cavity consists of a fully-reflective rear mirror, a partially transmitting output coupler, an optically pumped gain medium, and a Q-switch. Other intra-cavity optics like etalons are often employed to improve temporal coherence. SHG downstream of the cavity can frequency double the fundamental beam to produce additional useful wavelengths.

Fig. A.3.

A.3   ZaP-HD's pulsed Nd:YAG laser

ZaP-HD utilizes an Ekspla NL-121-G Nd:YAG laser, which uses a second harmonic generator (SHG) to emit 532 nm light. At the second harmonic, it delivers pulses of 20 mJ energy lasting 2 ns. The laser is designed to operate in single shot mode with external triggering, but it can also repeatedly pulse at 1 Hz, which helps in alignment. The laser's diode-pumped master oscillator generates an SLM pulse, which proceeds through a flashlamp-pumped amplification stage and then through a SHG before exiting the laser head. Many optical components in this section will be referenced with labels in parentheses, which point to the labels in the optical layout shown in Fig. A.4 [74].

The master oscillator employs self-seeding along with an etalon (6) to achieve SLM operation. Self-seeding relies on biasing the intra-cavity Pockels cell to open the intra-cavity Q-switch (8) slightly prior to the laser pulse. This allows a period of pre-lasing during which the etalon selects one longitudinal mode to grow. When the Q-switch is triggered to open
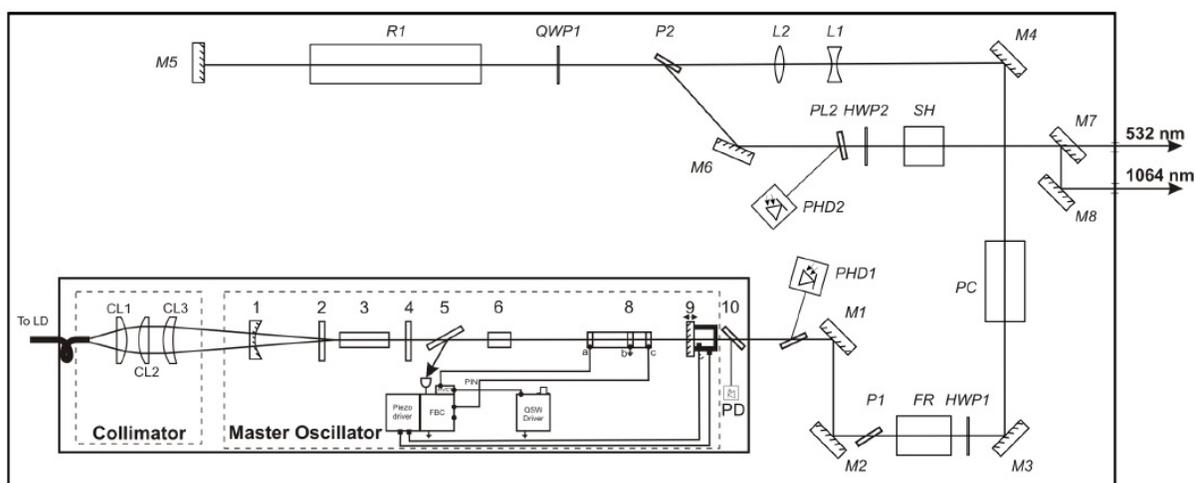
Figure A.4: The NL-125-G ND:YAG laser optical layout. Many of the component labels are referenced in this section. For a complete list of all optical components, see the NL-125-G manual [74].

completely, the mode growth competition is finished with only a single mode surviving in the cavity. The surviving mode is then amplified by the oscillator and proceeds towards the downstream amplification stage. An extra-cavity Pockels cell (PC) acts as a Q-switch to truncate the pre-lasing light from the pulse before it reaches the amplifier.

The quarter wave plates (2 and 4) on either side of the oscillator's Nd:YAG rod (3) also contribute to SLM operation by preventing spatial hole burning. Spatial hole burning is gain saturation in an amplification medium caused by the interference pattern of standing waves. Such gain saturation can make SLM operation more difficult to achieve because it limits the gain for the desired mode, which could allow competing modes to grow and survive to the end of pre-lasing. The quarter wave plates ensure that the polarization of counter-propogating waves are orthogonal in the Nd:YAG crystal, which prevents interference.

The laser has been configured to optimize spatial coherence and output a single transverse mode (ie: a Gaussian beam profile or TEM_{00}). The laser's optics have been adjusted at the factory to utilize a smaller cross-section of the amplifier crystal (R1). This outputs a beam with better spatial coherence at the expense of beam energy.

The gain applied by the amplification stage can be tuned by changing the relative timing between oscillator Q-switching and the amplifier flashlamp. The flashlamp sets up a time-dependent population inversion in the amplifier rod, and there exists an optimal time at which the pulse from the oscillator should travel through the amplifier to achieve maximum gain. Setting the amplification to the minimum value is convenient for alignment purposes because diffuse reflections of the second harmonic green beam can be viewed with the naked eye without danger. Glasses should be worn at all times when directing the IR beam outside the laser head.

The amplified fundamental beam passes through a Potassium Titanyl Phosphate (KTP) crystal, which acts as a SHG (SH) and outputs 532 nm light. For maximum conversion efficiency, the crystal needs to be adjusted to ensure phase matching of the fundamental and frequency doubled light at the output plane. Two knobs allow the crystal to tilt to change its apparent thickness along the laser's opitcal axis. The SHG's operation is polarization dependent, and a half-waveplate (HWP2) needs to be adjusted to match the crystal's orientation to maximize either 532 nm or 1064 nm light emission.

Important Notes on NL-121-G Adjustment and Maintenance

1. **Piezo Voltage:** the user can change a parameter called the piezo voltage, which affects the length of the laser cavity by actuating the output coupler. Adjusting the cavity length allows for optimal SLM operation. Changing the laser cavity length allows the user to shift the longitudinal modes in wavelength space until one can optimally transmit through the etalon. The single mode autotracker LabVIEW sub VI automatically sweeps the piezo voltage and measures the resulting oscillator amplitude as measured by photodiode 1 (PHD1). After conducting a sweep, this sub VI will suggest an optimal piezo voltage value that maximizes the oscillator output amplitude. The user can then apply this piezo voltage in the main FNL.vi GUI.

2. **Faraday Rotator:** install protective rubber caps on FR when working near this

component. Its large magnetic field can literally attract damage.

3. **SHG Crystal:** the KTP is mounted in a temperature-controlled heater, which is kept on at all times even when the key in the laser head is turned off. This protects the crystal against atmospheric humidity. KTP is very hygrophilic and water-soluble, so never clean it with water or liquids.

   When adjusting the SHG orientation note that the transmitted amplitude versus phase angle has multiple local maxima, but only one global maximum. This means that if the SHG is too far displaced from its optimal orientation, it may appear to be at an optimal position.

4. **Flashlamp Simmering:** to extend flashlamp lifetime, minimize simmering the flashlamp. Simmering maintains low-current plasma in the flashlamp to reduce the power requirements and wear of initial ionization. The flashlamp electrodes are composed of a Barium core coated in Tungsten; they are designed such that at the Temperature of a flash, the Barium will act as the electron source for the ionization. Simmering occurs at a much lower temperature, such that the Tungsten plays more of a role in the ionization, which leads to damage to the Tungsten layer. Over time, the tungsten coating can be redeposited on the glass walls of the lamp. The flashlamp driver simmers the flashlamp whenever the driver is turned on while the laser is not in run mode. The laser typically runs in single pulse mode, so some amount of simmering during the downtime between plasma pulses is unavoidable. But, when breaking for lunch or at the end of the day, the flashlamp driver should be turned off to stop the simmering.

Appendix B

ALIGNMENT AND OPERATION OF THE DHI

This section details how to initially align the DHI, how to perform routine alignment checks, and how to run the system during a usual run day.

B.1 Running the Nd:YAG laser manually from inside the lab

Enumerated below are steps for users to follow when operating the laser manually from inside the lab during alignment. For the Nd:YAG laser to operate, all interlock conditions except the grounding rod condition must be satisfied. This allows users to run the laser inside the lab while keeping the capacitor banks safely grounded. If a personnel switch is flipped or a door opens, laser operation will cease. The Nd:YAG laser is connected to ZaP-HD's interlock panel as in Fig. B.1. A manual light switch to toggle ZaP-HD's high voltage warning lights is positioned on the table next to the laser. During alignment, the warning lights should be turned on and a danger sign should be hung above the main entrance door knob to discourage unauthorized lab entry.

1. Turn on the laser. Turn the key in the laser head to on, and ensure the power on the cooling unit is on. Wait for 5 minutes before running the laser to allow the cooling system to achieve proper temperatures. Note that if the laser has just been connected to mains power, you should wait longer before running (see the laser manual). Until you are ready to fire the laser, leave the amplifier power supply off.

2. Check that the safety interlocks described above are met, that proper safety signage is placed on the main lab door, and that the high voltage warning lights are turned on. Ensure the lab windows are blocked.
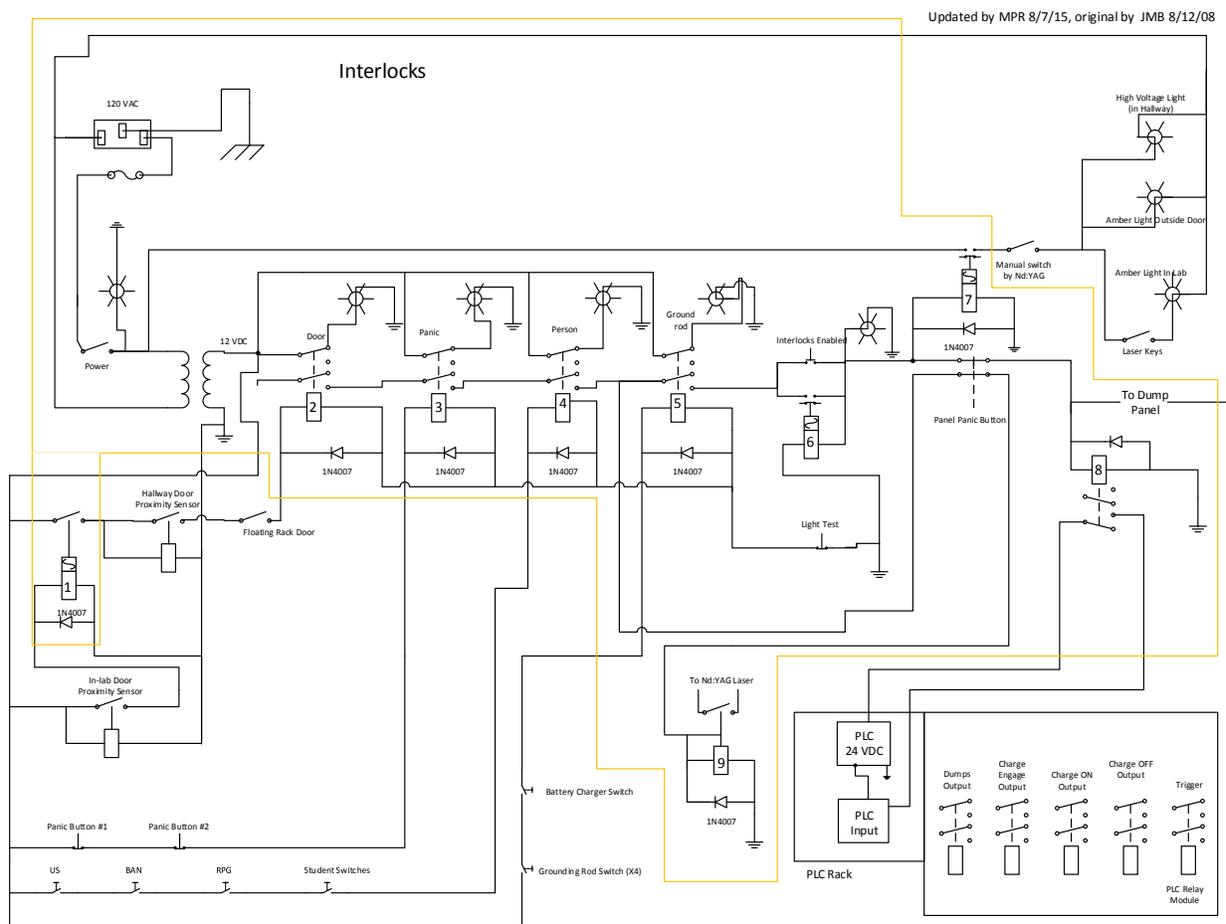
Figure B.1: Electronic schematic of the ZaP-HD interlocks system. Items within the orange box are inside the 19 inch rack mount panel while all other items are external. The Nd:YAG laser needs to see a short circuit connection to allow itself to enter run mode. Relay number 9 inside the panel will short the laser interlock circuit provided all interlock conditions are met except the grounding rod condition. A manual switch in the lab next to the laser allows the user to toggle the high voltage warning lights even when no interlocks are met. This allows users to discourage unauthorized lab entry during DHI alignment.

3. Ensure the laser shutter is closed.

4. Use the laser control pad to change the synchronization mode to internal. Push the "Menu" button on the control pad, use the arrows to scroll down to "Synchronization," and push the "OK" button. Then, scroll to "Synchroniz. mode" and push the "OK" button. Finally, use the arrows to toggle from "External sync. mode" to "Internal sync. mode" and push "OK." Internal synchronization is used for firing at 1 Hz for alignment, while external mode allows externally triggered single pulses during plasma pulses.

5. Connect the control laptop to the CAN-to-USB adapter. Open the FNL.exe control GUI and ensure the AMP is set to 1 and turned off. Most of the DHI alignment requires only the lowest amplification setting.

6. Turn on the amplifier power supply.

7. Put the laser into run mode by pushing the "Run" button either in the FNL.exe GUI or on the control pad. It should take 5 seconds for the laser to begin firing at 1 Hz. The laser status can be read on the upper left corner of the control pad. Fig. B.3 lists laser status symbols and their definitions. Normally, the hollow arrow will appear for the first 5 seconds before normal laser operation begins and the dark arrow appears.

8. Put on Nd:YAG laser goggles.

9. Hold a piece of orange laser paper in front of the laser output and open the shutter. Verify that the laser is operating at a low amplification by observing the intensity of the florescence of the laser paper, which is safely visible through the Nd:YAG laser goggles.

10. Proceed with alignment of downstream optics. The lowest possible amplification setting should be used at all times to maximize safety. Sometimes carbon buildup on the
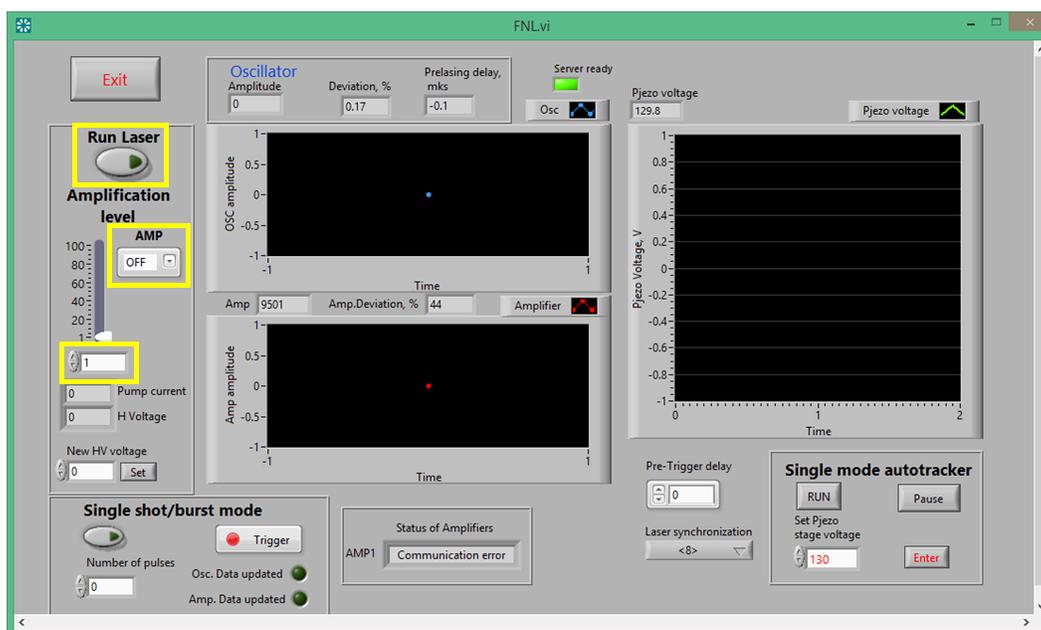
Figure B.2: The FNL.exe GUI controls the laser amplification and displays the amplitude of light detected by photodiodes in the oscillator (PHD1 in Fig. A.4) and downstream of the amplification stage (PHD2 in Fig. A.4). The amplification level is set in the numeric control in the lowest yellow box. The amplifier can be toggled on and off with the "AMP" button in the middle yellow box. The "Run Laser" button in the top yellow box toggles the laser in and out of run mode. The top center graph plots the oscillator amplitude as a function of pulse, and the bottom center graph plots the amplifier amplitude as a function of pulse.

☐	Laser operation is stopped and it is not ready for operation. It must to wait.
▨	Laser operation is stopped but it is ready for operation.
▷	Laser is operating but something is switched off, *e.c.* QSW.
▶	Laser is operating.
⊠	An error. See list of errors in Chapter 9.

Figure B.3: The meanings of status symbols displayed by the laser control pad. Most often, displayed errors correspond to the safety interlocks not being met. See Chapter 9 of the laser manual for error codes, which are also displayed on the control pad next to the error status symbol.

ZaP-HD vacuum tank windows attenuates the scene beam to the point increasing the amplification above 1 is necessary to see the beam downstream of the tank. Diffusive reflections of the Nd:YAG laser at the lowest amplification setting can be safely viewed without safety goggles although care should be taken before looking for such reflections to understand the beam path sufficiently to avoid specular reflections, which may be harmful. This can be helpful in some instances especially when directing the beam across long distances. Large black poster board makes an excellent background target for viewing such diffusive reflections.

B.2 DHI alignment

Aligning the downstream optics can be performed in many ways. This section describes a proven procedure. Before starting this procedure, the operator should sketch out the desired optical set up. Oftentimes, knowledge of the DHI's complete geometry is required to proceed through these steps efficiently. Figs. B.4-B.6 show the set up used to collect most of the data in this dissertation.

1. The first task in the DHI alignment is to direct the laser beam to the proper height to pass through the mid-plane of the vacuum tank. On ZaP-HD, the output of the Nd:YAG laser is lower than the mid-plane, but three turning mirrors (two prior to the beam expander and one after) raise the beam to the proper height. Start by

positioning and adjusting these three mirrors without the beam expander in place to raise the unexpanded beam to the height of the mid-plane (an approximate height is sufficient for now since adding the beam expander will affect the direction of the beam). In positioning these mirrors, be sure to leave room for the beam expander.

2. Place the beam expander in the system. The beam expander has a magnification of 6 and is composed of two lenses in a 68 cm long, 2" diameter beam tube. The expander is held by two 3D-printed clamps, which are attached to 1.5" diameter posts. Two linear translators attached to each post give the user independent control of the center position of each lens in the expander. For precise adjustment and minimal vibrations, the clamps should hold the expander on each end, but in practice the optics table can be crowded with other optics and require alternative positioning such as in Fig. B.4.

An easy way to align the expander is to first install it without lenses and adjust the tube to be co-linear with the unexpanded laser beam. The lenses can be removed from the beam expander by unscrewing the farthest upstream and downstream sections. Then, a 3D-printed cross-hair can be positioned on the open ends of the tube. Orange-red color PLA 3D-printing filament from justpla.com fluoresces just like orange laser paper, so the user can observe the laser beam impact the cross-hair while wearing laser goggles. Using the cross-hair, each side of the tube can be positioned with the laser beam at its center.

To avoid back reflections into the laser, the beam expander should be slightly misaligned prior to installing the lenses. This misalignment is normally applied by adjusting the horizontal position of one end of the beam expander slightly. The proper amount of misalignment can be computed considering the distance from the laser output to the expander.

After misalignment, install the lenses, fire the laser, and observe the beam downstream of the expander. The output beam of the beam expander should remain columnar far
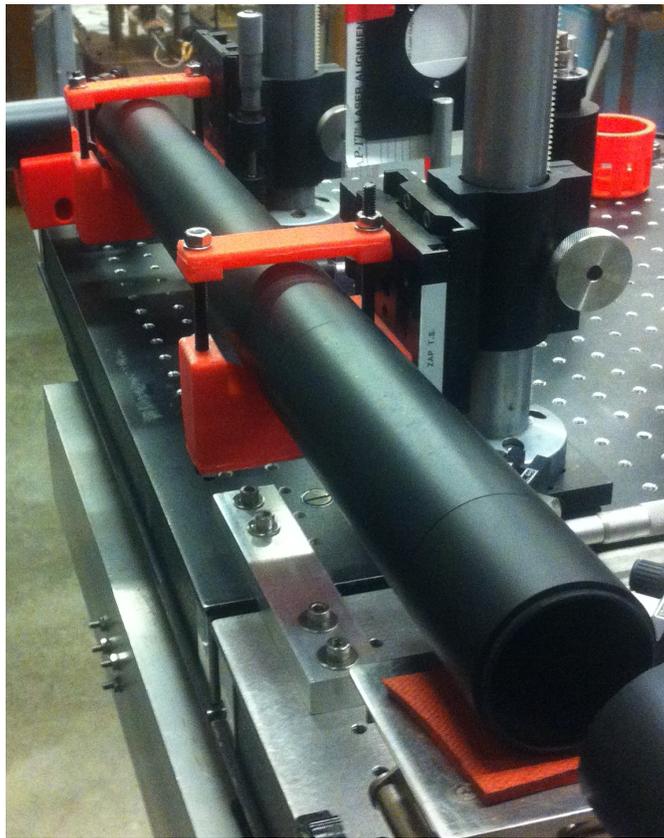
Figure B.4: The DHI beam expander is held by orange 3D-printed clamps. The clamps mount to 1.5" vertical posts and linear translators, which give the user independent control of the position of the two lenses in the expander.

downstream. If beam divergence is observed downstream of the expander, the distance between the lenses may be incorrect. The expander employs CVI optics lens numbers PLCX-50.8-386.3-C-1064/532 and PLCC-25.4-51.5-C-1064/532. The intentional misalignment of the expander will redirect the expanded beam off of its original path, so the position of the third turning mirror may require adjustment.

3. Direct the laser beam through the desired location in the experiment using the third turning mirror. This sets the measurement location as well as the locations of the other optics in the system. Positioning a cross-hair made of thin metal wire just downstream
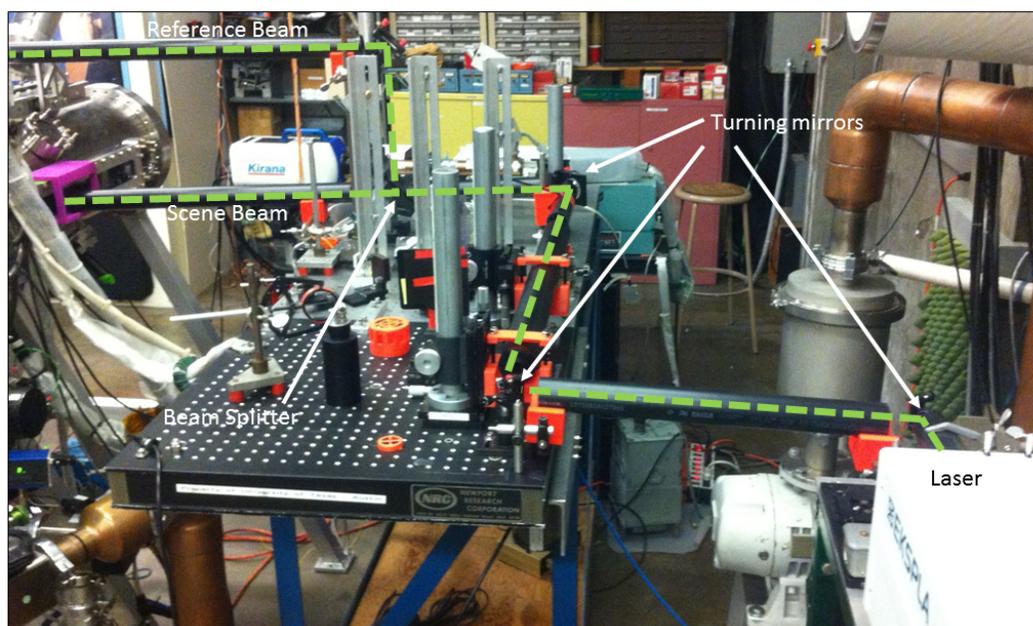
Figure B.5: The DHI's optical set up on the upstream optics table. The dashed green line shows the laser's path through black beam guides meant to block air currents. Three turning mirrors raise the Nd:YAG laser beam to the height of the ZaP-HD mid-plane.

of the beam expander is helpful for precisely determining the beam position relative to the experiment. This cross-hair should be centered in the middle of the beam exiting the expander. Note that the expander misalignment dictates that the center of the beam will not be at the center of the downstream lens tube, so the cross-hair will need to be positioned off the expander's axis. Observing the shadow of the cross-hair at the upstream and downstream rectangular windows allows for precise scene beam positioning.

Position a 1.5" diameter post with mirror on the downstream optics table to turn the scene beam vertically. Ensure the mirror is near a 45 degree angle by attempting to make the deflected beam as vertical as possible.

4. Direct the reference beam over the machine, to the final turning mirror, and finally to the camera. Install the 3" diameter visible wavelength beam splitter on a 1.5" diameter

post just downstream of the third turning mirror. Ensure the beam splitter is near a 45 degree angle by attempting to make the deflected beam as vertical as possible. On the same 1.5" post, install a turning mirror to direct the reference beam over the machine.

On the downstream optics table, install the final turning mirror on a 1.5" post at the same height as the reference beam turning mirror. The final turning mirror is a rectangular mirror large enough to allow it to turn both the scene and reference beams.

Install the digital camera on the downstream optics table at the same height as the final turning mirror. The horizontal side of the camera sensor is longer than its vertical side, so mounting the camera turned 90 degrees on a 1.5" post allows the camera to capture more of the density profiles across the Z-pinch axis.

For now, direct the reference beam to impact the camera's lens cover.

5. Direct the scene beam to the camera. To turn the scene beam horizontal, install a mirror towards the top of the same 1.5" post used for the initial scene beam turning mirror on the downstream optics table. Position this mirror at the same height as the final turning mirror and digital camera.

   For now, direct the scene beam to impact the camera's lens cover.

   Keeping the scene and reference beams in the same horizontal plane as they enter the camera, makes fine adjustments to the fringe pattern easier. Without moving posts or changing the orientation of the fringes, the size of the fringes can be changed.

6. Fine tune the alignment of the reference beam to the camera. Connect a push button to the bulb trigger input on the camera, install a 2.5-3.0 optical density neutral density filter on the camera, and set the camera's exposure time to 1.3 s. Block the scene beam and run the laser. Use the bulb trigger push button to take pictures. Alternate taking images and adjusting the final turning mirror until the cross-hair shadow appears at
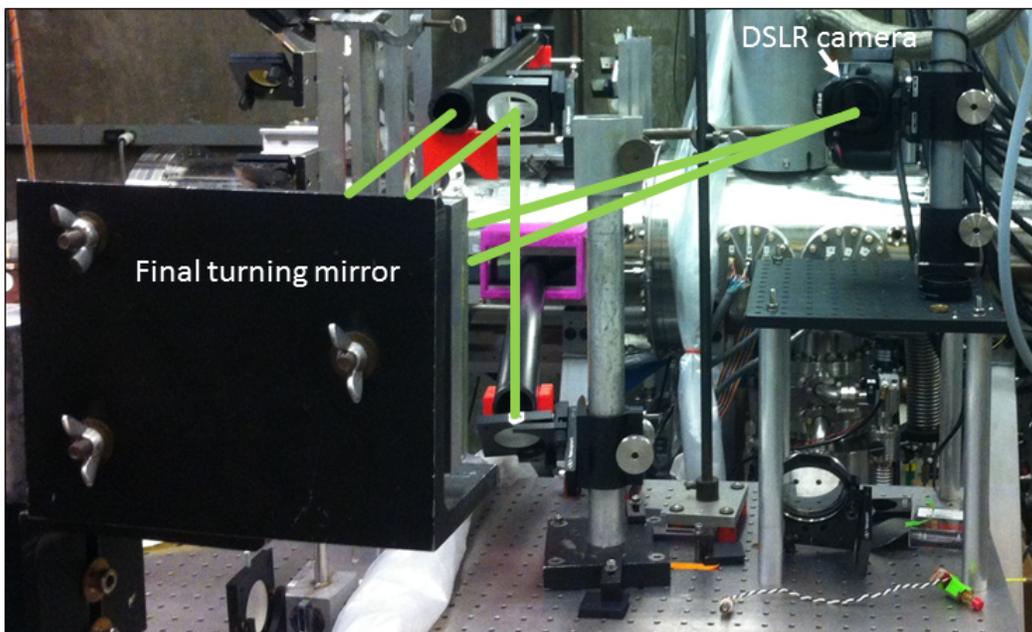
Figure B.6: The DHI's optical set up on the downstream optics table. The solid green lines show the laser paths incident on the final turning mirror and to the DSLR camera. Keeping the scene and reference beams in the same horizontal plane entering the camera makes it easier to change the fringe size.

the center of the image.

7. Fine tune the alignment of the scene beam to the camera. Unblock the scene beam and block the reference beam. Again, use the bulb trigger to take pictures while adjusting the two scene beam turning mirrors on the downstream optics table. Adjust the scene beam until the cross-hair shadow matches the position of the reference beam. Matching the cross-hair positions can be made easier by marking the position of the reference beam cross-hair on the camera screen with a dry erase marker or by viewing the camera output on a computer monitor using the camera's HDMI output.

8. Cover the beam path with beam guide tubes to block air currents, which can corrupt the quality of the holograms. 3D-printed v-blocks and window hangers along with 0.5" diameter posts provide a flexible means to support 2.5" diameter PVC tubes.

B.3   Running DHI on ZaP-HD

The following steps describe how to operate the laser during a normal run day.

1. Turn on the laser. Turn the key in the laser head to on, and ensure the power on the cooling unit is on. Wait for 5 minutes before running the laser to allow the cooling system to achieve proper temperatures. Until you are ready to fire the laser, leave the amplifier power supply off.

2. Turn on the two trigger boxes on top of the laser. The laser requires two signals to trigger externally. The trigger box with transistor-transistor logic (TTL) output plugged into the "GATE IN" plug on the laser head should be triggered at the desired laser pulse time. The trigger box with TTL output plugged into "SYNC IN" should be triggered 987.8 μs prior to the "GATE IN" trigger. The laser manual specifies this delay time in the Testing Data section.

3. Use the laser control pad to change the synchronization mode to external. Push the "Menu" button on the control pad, use the arrows to scroll down to "Synchronization,"

and push the "OK" button. Then, scroll to "Synchroniz. mode" and push the "OK" button. Finally, use the arrows to toggle from "Internal sync. mode" to "External sync. mode" and push "OK."

4. Ensure the CAN-to-USB adapter is connected to the fiber optic cable connected to the screen room computer. This enables the screen room computer to control the laser.

5. Turn on the DHI camera, and ensure the bulb trigger is connected to the push button by the charging rack. Operators employ this button to trigger the camera during each plasma pulse. Set the camera exposure time to 1.3 s and install the neutral density filter with optical density 4.0.

6. Turn on the laser amplifier.

7. Open the laser shutter.

8. Meet all safety interlocks and exit the laboratory.

9. Open the FNL.exe GUI on the screen room computer and turn the laser amplification on to a value of 6-12 depending on the attenuation caused by the rectangular windows. Note that when significant scene beam attenuation occurs requiring increased amplification, neutral density filters can be positioned to attenuate the reference beam to keep the scene and reference amplitudes similar.

10. Put the laser into run mode.

11. Prepare for a normal plasma pulse and charge the capacitor banks. When ready to trigger the pulse, press the push button connected to the DHI camera one second prior to triggering the experiment.

Anytime the safety interlocks are broken and reestablished, the operator should use the FNL.exe GUI to take the laser out of and back into run mode because the laser will not

automatically return to run mode once the interlocks are reestablished. Also if the amplifier power supply is turned off and then back on while the FNL.exe GUI is running, AMP must turned off and back on with the FNL.exe GUI to reset the software to communicate with the amplifier.

Recording DHI images of the cross-hair shadow for the scene and reference beams during the first two pulses of each run day provides a daily check of the system's alignment. Start the day by positioning the metal wire cross-hair downstream of the beam expander. Block the reference beam before the first shot of the day. Before the second shot, unblock the reference beam and block the scene beam. Compare the images from these two pulses to verify the cross-hair shadows are coincident. If the beams are not coincident, perform steps 6 and 7 in the alignment procedure above to fine tune the beam positions. Usually, such adjustment is required every 1 to 2 weeks.

Multiple baselines are collected throughout the day to account for drift in the optics. Each baseline is collected during a plasma pulse by setting the laser trigger time to 5 ms prior to shot trigger, which is long before gas injection. Operators should take a baseline between every 2 to 3 plasma holograms.

Appendix C

HOW TO RUN THE ANALYSIS CODES FOR HOLOGRAPHIC RECONSTRUCTION

This section provides instructions on how to run the DHI reconstruction and analysis codes. The procedure for daily hologram reconstruction is enumerated below. File locations referenced in the manual can be changed for future convenience. This section also includes flow charts as documentation intended to improve the transparency of code conducting the error analysis of the Abel inverted electron number density.

1. At the end of each run day, upload new holograms to the holography shared network drive using the Nikon Transfer software. When Nikon Transfer opens, select the "Primary Destination" tab (see Fig. C.1) and ensure the primary destination folder is set to `H:\Raw Holograms`. Select "Create subfolder for each transfer" and use the "Edit" button to instruct the program to name each new folder based on a `yyyy_mm_dd` formatted date (see Fig. C.2 (a)). Check "Rename photos during transfer" and use the "Edit" button to instruct the program to name the files according to a `yyyy_mm_dd_XXX` format where `XXX` is a three digit shot number (see Fig. C.2 (b)). Once these settings are in place, click the "Start Transfer" button to download the images to the computer.

2. Run `DHI_basicRecon.m` (script included below) to identify an appropriate reconstruction distance and mask filter for the day's shots. This requires changing variable `shotnum_def_it` to the shot number of the first plasma hologram of the day and `shotnum_base_vec` to the shot number of the vacuum hologram immediately preceding the first plasma hologram. Run the code and observe the plotted figure like the one in Fig. C.3. Ensure the twin images are positioned as close to the zeroth order images
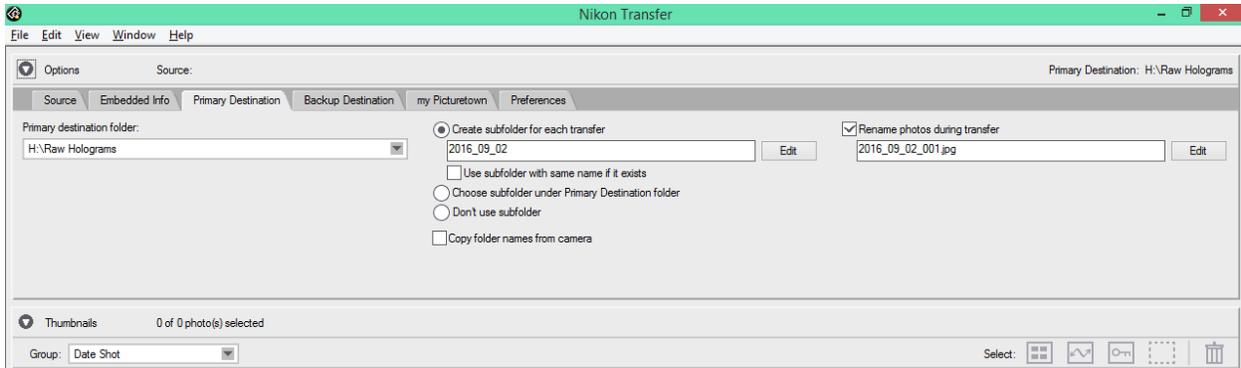
Figure C.1: These are the settings selected in the "Primary Destination" tab in the Nikon Transfer software.
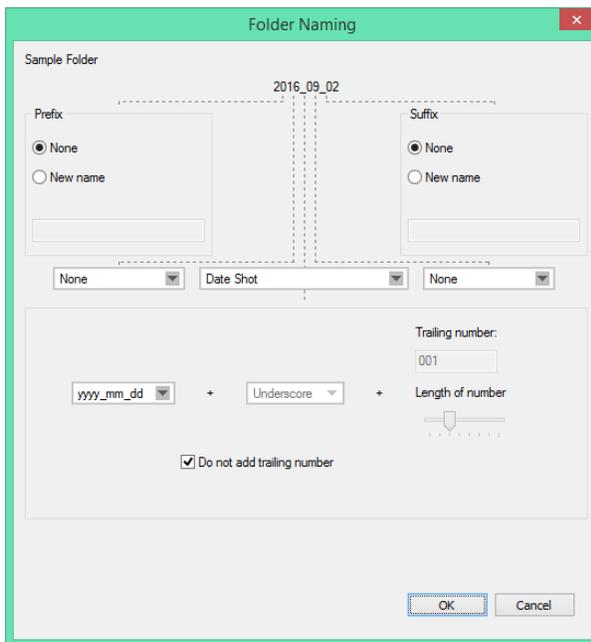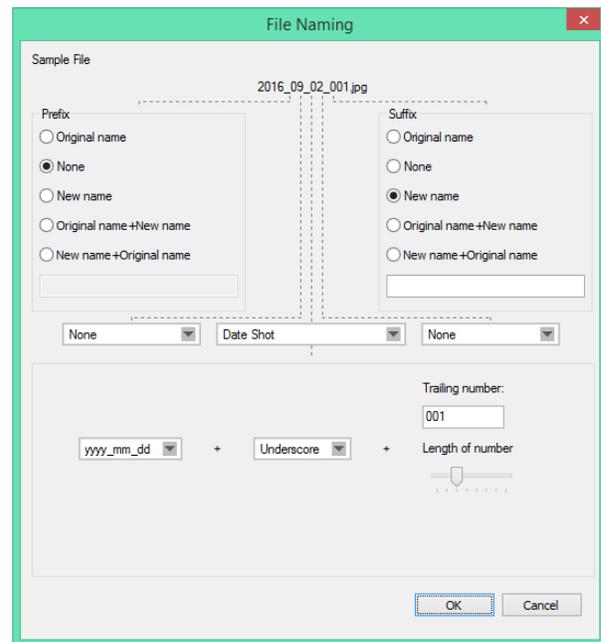
Figure C.2: The folder naming settings employed in the Nikon Transfer software. These settings are accessed through the "Edit" buttons in the "Primary Destination" tab shown in Fig. C.1.
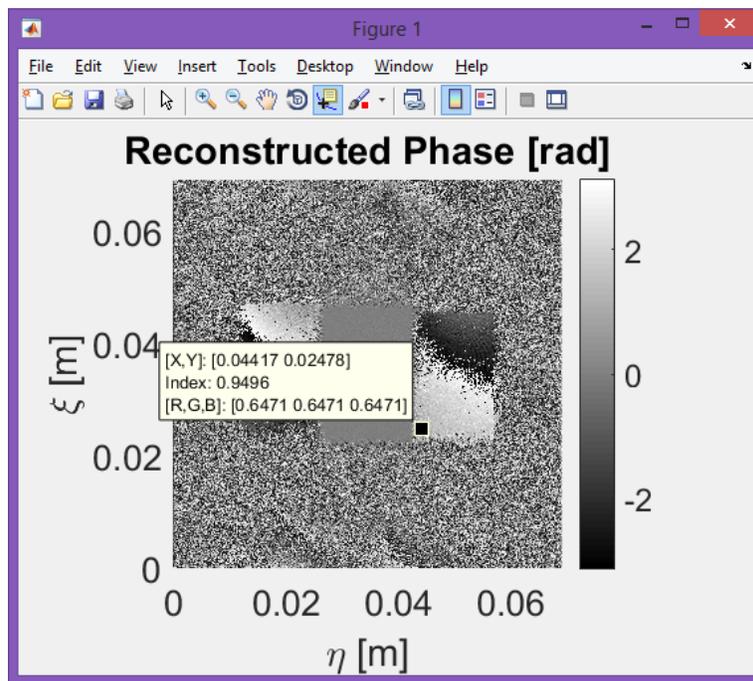
Figure C.3: The image of the reconstruction plane used to identify the proper reconstruction distance and twin image boundary coordinates. The data cursor allows the user to identify the corners of the twin image to the right of the zeroth-order image.

as possible by adjusting the reconstruction distance, `d`, on line 59 and rerunning the code. This takes some trial and error, but the positioning of the twin images does not need to be perfect. Once the twin image position is satisfactory, use MATLAB's "data cursor" to select the lower left and upper right corners of the twin image positioned on the right, and note the coordinates of the corners. The reconstruction distance and positioning of the twin images should only change if the interferometer alignment has been modified.

3. Open `shotnumber_inputs.m` (script included below) and modify the shotnumber and reconstruction settings. Change the vector `shotnum` to include all the hologram pulses from the day. Specify the identified reconstruction distance as variable `d` and input the coordinates of the corners of the twin image as variables `xmin`, `xmax`, `ymin`, and `ymax`.

The function `shotnumber_inputs.m` allows the user to provide program input without modifying analysis codes. The function is called in analysis codes to provide the shot numbers and reconstruction settings.

4. Run `DHI_recon_invert_all.m` (script included below), which performs the Fresnel transform reconstruction described in Sec. 3.3 and then conducts the Abel inversion process described in Sec. 3.7.2. The user needs to specify the axial location of the measurement as the `z_loc` variable in units of meters. The code stores the reconstructed line-integrated density and Abel inverted number density as images in `H:\Reconstructions\<shotnum>\inverted` for easy viewing. The code also uses function `MDS_DHI_put.m` to save data to ZaP-HD's DHIHD MDSplus data tree for easy recollection and future analysis. Fig. C.4 shows the DHIHD data tree, and its contents are detailed in Table C.1.

The daily analysis codes do not conduct the error analysis detailed in Sec. 3.7 because such analysis takes more computation time. The error analysis can be performed on selected shots by running `DISS_DHI_error.m`, which also reads shot numbers and reconstruction settings from `shotnumber_inputs.m`. The flow chart in Fig. C.5 shows the process involved in identifying the error in the Fresnel transform reconstruction for one density profile. According to the chart, the density profile on the lower side of the cross-section is Abel transformed to line-integrated density, which is converted to a phase shift with Eq. 2.10. That phase is interpolated, stacked into a 2D matrix, and added to a linearly varying function. Taking the cosine of the resulting sum generates a synthetic hologram of resolution comparable to the empirical hologram. The linearly-varying function causes evenly-spaced fringes, which are modulated by the phase shift corresponding to the line-integrated density. This synthetic hologram is then reconstructed by the Fresnel transform method. The line-integrated density from the reconstruction of the synthetic hologram is compared to the measured line-integrated density. The difference in these line-integrated densities is the $\sigma_{N_e}(r)$ of Eq. (3.31) described in the explanation of the error analysis in Sec. 3.7.1.
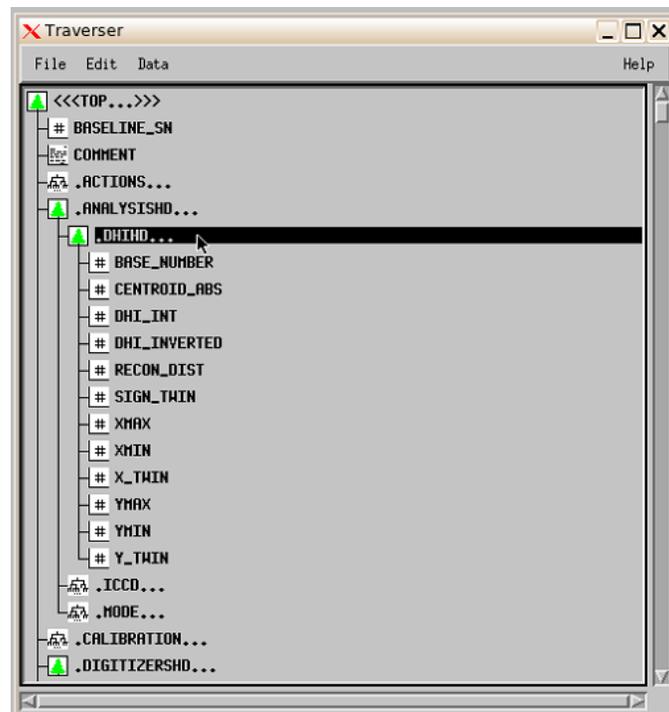
Figure C.4: The DHIHD data tree contains the reconstruction settings and reconstructed density data for each plasma hologram pulse.

Node Name	Data Type	Data Description
base_number	Scalar	Baseline shot number used the reconstruction
centroid_abs	Vector	Centroid locations in units of pixel number
dhi_int	2D Matrix	Line-integrated density
dhi_inverted	2D Matrix	Abel inverted number density
recon_dist	Scalar	Reconstruction distance
sign_twin	Scalar	Sign of the twin image (can account for 180 degree phase shift between the twin images)
xmax	Scalar	Coordinate of analyzed twin image
xmin	Scalar	Coordinate of analyzed twin image
x_twin	Vector	Horizontal axis of dhi_int and dhi_inverted data
ymax	Scalar	Coordinate of analyzed twin image
ymin	Scalar	Coordinate of analyzed twin image
y_twin	Vector	Vertical axis of dhi_int and dhi_inverted data

Table C.1: DHIHD tree contents

C.1 Main codes required for daily DHI analysis

shotnumber_inputs.m

```matlab
1  % shotnumber_inputs.m
2  % Author:  Michael P. Ross
3  % Date = Sept. 6, 2016
4  % Description:  This script allows for user control of the shotnumbers and
5  % reconstruction settings in other DHI analysis codes.  The subfunction
6  % shot_base_pair can be made to identify pairs of adjacent plasma
7  % (deformed) and baseline shots or adjacent baseline shots.
8
9  function [shots,d,xmin,xmax,ymin,ymax,sign_twin] = shotnumber_inputs(import,
       varargin)
10
11 % using varargin to accept input identifying if the user desires
12 % deformed—baseline or baseline—baseline pairs
13 switch(nargin),
14     case 0,
15         whichPair = 1; % if second input is not provided, the program seeks
16         %deformed—baseline pairs by default
17     case 1,
18         whichPair = 1; % if second input is not provided, the program seeks
19         %deformed—baseline pairs by default
20     case 2,
21         whichPair = varargin{1}; % a second input value of 1 tells the
22         %program to seek for deformed—baseline pairs, a value of 0 tells
23         %the program to seek for baseline—baseline pairs
24 end
```
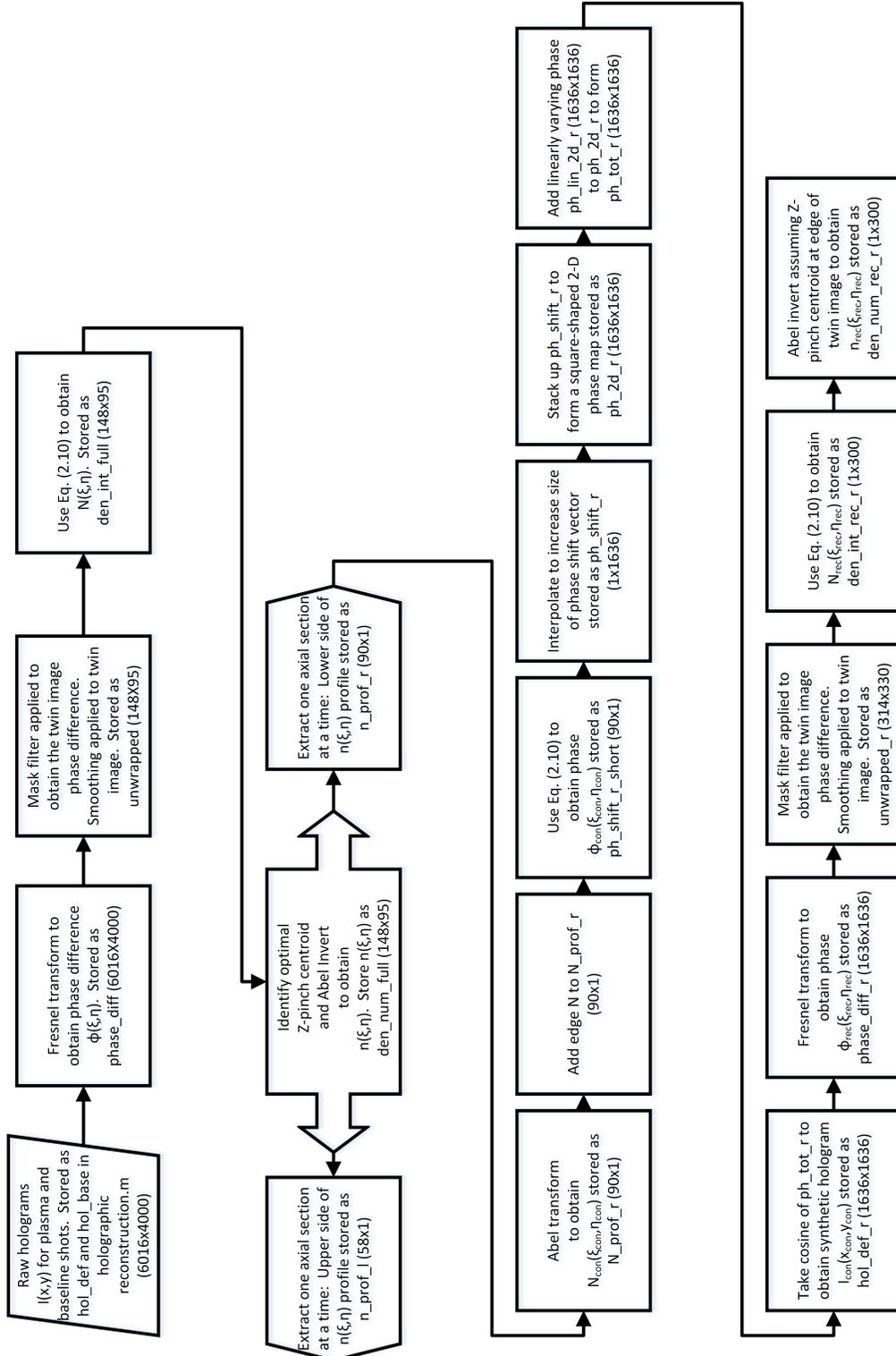
Figure C.5: Flow chart showing the error analysis procedure for a single density profile. The process involves using the measured density to create a synthetic hologram, which is then holographically reconstructed. The resulting line-integrated density profile from the reconstruction of the synthetic hologram is compared to the measured line-integrated density profile to obtain the error in the Fresnel transform reconstruction. The chart references variable names in `DISS_DHI_error.m`. For an example cross-section, sizes of the variables are included in parentheses to more clearly illustrate when interpolation occurs and how the data is handled throughout the analysis.

```matlab
switch(import) % this switch statement gives the user some flexibility to
    % toggle between different groups of shots for analysis.  Usually, case
    % 2 is used.
    case 1

        shots_tmp = shot_base_pair(shotnum,whichPair);
        d(1:size(shots_tmp,1)) = 0.5;
        xmin(1:size(shots_tmp,1)) = 0.0446;
        xmax(1:size(shots_tmp,1)) = 0.0555;
        ymin(1:size(shots_tmp,1)) = 0.0237;
        ymax(1:size(shots_tmp,1)) = 0.0429;
        sign_twin(1:size(shots_tmp,1)) = -1;
        shots = shots_tmp;

    case 2

        % RSI 2016 Paper shots for analysis:
        shots = [160524000+[21,20]];  % identify range of pulses (first
        % pulse must be a baseline
        shots_tmp = shot_base_pair(shots,whichPair);
        d = 0.5;
        xmin = 0.0446;
        xmax = 0.0555;
        ymin = 0.0237;
        ymax = 0.0429;
        sign_twin = -1;
        shots = shots_tmp;
```

```
53   end
```

DHI_basicRecon.m

```
1  % DHI_basicRecon.m
2  % Author:  Michael P. Ross
3  % Date = Sept. 6, 2016
4  % Description:  This code performs the Fresnel transform reconstruction to
5  % obtain the phase difference between specified plasma and vacuum
6  % holograms.  This code primarily allows the user to view the
7  % reconstruction plane to identify the bounds of the twin images for
8  % further analysis.  The code proceeds through 9 main sections:
9  %
10 % 1.) Declare reconstruction parameters/constants
11 % 2.) Input holograms from file
12 % 3.) Mask filter the hologram
13 % 4.) DC image suppression
14 % 5.) Apply windowing to the holograms
15 % 6.) Reference wave generation
16 % 7.) Fresnel transform reconstruction
17 % 8.) Compute the phase difference
18 % 9.) Plotting the reconstruction plane
19
20 tic; clear all; clc;
21 close all; drawnow;
22 format compact;
23
24 section = 0;
25 cross_sect = section;
26
27 shotnum_base_vec = [160817006]; % user specifies vacuum/baseline shot here
```

```matlab
for shotnum_def_it = [160817007] % user specifies plasma shot here
    close all, drawnow;
    close all, drawnow;

    ind_base_tmp = find((shotnum_def_it-shotnum_base_vec)>0,1,'last');
    shotnum_base_it = shotnum_base_vec(ind_base_tmp);

    %% 1.) Declare reconstruction parameters:
    % Significantly, the reconstruction
    % distance, d, only affects the resolution of the reconstructed
    % interference phase.  Maximize resolution by selecting the
    % reconstruction distance to maximize the size of the twin images while
    % still separating them from the DC term.


    status = sprintf('Initializing... \n')


    res = (3.85e-6);% [m] Pixel size of Nikon 3200D, 4.3e-6 for Canon T2i
    lambda = 532e-9;% [m] Nd:YAG wavelength, ruby is 694.3e-9 [m]
    d =.50; % [m] Reconstruction distance
    n_c = 2.312e27; % [m^-3] Critical plasma density

    %% 2.) Input holograms from file:
    % This section uses imread() to load MxN-sized uint8 datatype color
    % holograms into MATLAB.  Each MxN color hologram is stored in an MxNx3
    % array.  Each of the three MxN slices correspond to the intensity
    % distribution of each color in the the RGB color palette.  To consider
    % the total intensity at each pixel, this code converts the MxNx3 array
```

```matlab
56      % to an MxN grayscale array with rgb2gray().  The grayscale intensity
57      % value at a given pixel location amounts to a norm of the three RGB
58      % intensities at that pixel.  Finally, the code converts the uint8
59      % datatype to double to prepare the intensity information for
60      % mathematical manipulation.
61
62      %%% Starting with ZaP's shot number convention:
63      SN_def = num2str(shotnum_def_it);
64      SN_base = num2str(shotnum_base_it);
65
66      %%% Converting to Canon Camera shot number convention:
67      year_def = num2str(2000+str2num(SN_def(1:2)));
68      month_def = num2str(SN_def(3:4));
69      day_def = num2str(SN_def(5:6));
70
71      year_base = num2str(2000+str2num(SN_base(1:2)));
72      month_base = num2str(SN_base(3:4));
73      day_base = num2str(SN_base(5:6));
74
75      date_def = [year_def,'_', month_def,'_', day_def];
76      date_base = [year_base,'_',month_base,'_',day_base];
77      date_plot = [year_def, month_def, day_def];
78
79      shot_def = SN_def(7:end);
80      shot_base = SN_base(7:end);
81
82      % Specifying where the raw holograms are stored:
83      hol_def_rgb = imread(['H:\Raw Holograms\',date_def,'\',...
```

```matlab
        date_def, '_', shot_def,'.jpg']);
    hol_base_rgb = imread(['H:\Raw Holograms\',date_base,'\',...
        date_base, '_', shot_base,'.jpg']);

    % Converting from RGB to grayscale (rgb2gray is not a supported command
    % without the image processing toolbox):
    rgb_red = 0.3;
    rgb_green = 0.59;
    rgb_blue = 0.11;

    hol_def = double(hol_def_rgb(:,:,1).*rgb_red + hol_def_rgb(:,:,2).*
        rgb_green + hol_def_rgb(:,:,3).*rgb_blue)';
    hol_base = double(hol_base_rgb(:,:,1).*rgb_red + hol_base_rgb(:,:,2).*
        rgb_green + hol_base_rgb(:,:,3).*rgb_blue)';

%% 3.) Mask filter the hologram:
% This section applies a mask filter by selecting only a limited
% section of the grayscale holograms.  The mask filter can improve the
% quality of the reconstruction by cutting out unused parts of the
% camera sensor.

% xmin = 1200;
% xmax = 4200;
% ymin = 1000;
% ymax = 4000;
% hol_def = hol_def(ymin:ymax,xmin:xmax);
% hol_base = hol_base(ymin:ymax,xmin:xmax);
```

```matlab
110    % Determining the size of the holograms:
111    L = size(hol_def);
112    M = L(2);  % x—direction
113    N = L(1);  % y—direction
114
115    %% 4.) DC image suppression:
116    % This section subtracts the mean intensity of the hologram from the
117    % intensity at each pixel location.  In some cases, this can improve
118    % the reconstructed intensity.  For the purpose of reconstructing the
119    % phase, the benefit is minimal as long as the twin images are
120    % sufficiently separated from the DC term, so this section can be
121    % omitted to save computation time. Subtracting the mean intensity from
122    % the hologram serves to suppress the DC diffraction term by
123    % eliminating the DC (or zeroth) order term in the discrete Fourier
124    % series of the hologram. Our reconstruction relies on the discrete
125    % Fourier transform, so removing its DC term reduces the DC diffraction
126    % term, improving the reconstructed intensity.  Recall that the DC term
127    % of the Fourier series is merely the mean value of the function.
128
129    % [hol_def,hol_base] = DC_suppression(hol_def,hol_base,M,N);
130
131    %% 5.) Apply windowing to the hologram:
132    % Applying a window to the raw holograms before reconstruction
133    % can reduce Gibb's phenomena by smoothing out non—periodic boundary
134    % conditions.  This provides marginal noise reduction in the
135    % reconstructed interference phase distribution.  Two window functions
136    % are available here.
137
```

```
138    % Hamming window:
139    % [hol_def,hol_base] = hamming_window(hol_def,hol_base);
140    % Hyperbolic window:
141    % [hol_def,hol_base] = hyperbolic_window(hol_def,hol_base);
142
143    %% 6.) Reference wave generation:
144    % Because our hologram recording utilizes planar reference waves, we
145    % can model our reference beam as a plane wave.  If we use lenses to
146    % create a spherical reference beam during recording, modeling the
147    % reference wave will involve a complex exponential.
148
149    ref = 1;
150
151    %% 7.) Fresnel transform reconstruction:
152    % The Fresnel transform reconstruction method generates the electric
153    % field strength at reconstruction distance d for the deformed and
154    % baseline holograms.  The Fresnel method, which assumes parabolic
155    % wavelets as source functions, is an approximation of scalar
156    % diffraction theory applicable for sufficiently large reconstruction
157    % distances.
158
159    b_def = fresnel(hol_def,d,lambda,res,ref);
160    b_base = fresnel(hol_base,d,lambda,res,ref);
161
162    %% 8.) Compute the phase difference:
163    % Properties of complex numbers are applied to the complex wavefield to
164    % compute the phase difference.
165
```

```matlab
166     phase_diff = phase_diff_func(b_def,b_base);
167
168     %% 9.) Plotting the reconstruction plane:
169
170     fnt = 20;
171     xsize_fres = abs(d*lambda/M/res);
172     ysize_fres = abs(d*lambda/N/res);
173     x = 0:xsize_fres:(M-1)*xsize_fres;
174     y = 0:ysize_fres:(N-1)*ysize_fres;
175     x_plt = x - max(x)/2;
176     y_plt = y - max(y)/2;
177
178     figure(1); hold on;
179     fig1 = imagesc(x,y,phase_diff); axis image; colormap gray;
180     set(gca,'Ydir','normal');
181     title('Reconstructed Phase [rad]','fontsize',fnt);
182     ylabel('\xi [m]','fontsize',fnt);
183     xlabel('\eta [m]','fontsize',fnt);
184     set(gca,'fontsize',fnt);
185     colorbar;
186
187 end
```

DHI_recon_invert_all.m

```
 1  % DHI_recon_invert_all.m
 2  % Author:  Michael P. Ross
 3  % Date = Sept. 6, 2016
 4  % Description:  This code takes the shot numbers and reconstruction
 5  % settings specified in the shotnumber_inputs function and performs a
 6  % Fresnel transform reconstruction on the data.
 7  %
 8  % Then, it proceeds to Abel invert the line-integrated density data to
 9  % obtain number density.  The code follows the procedure described in
10  % Sec. 3.6.2 to minimize the difference in the resulting sides of the
11  % number density profile.
12  %
13  % The code saves some data as a .mat file for use in other analysis codes.
14  % It saves images of the reconstructed phase, line-integrated density, and
15  % number density to the holography network drive.  Finally, it uses the
16  % function MDS_DHI_put.m to store the density data alongside reconstruction
17  % settings in ZaP-HD's MDSplus data tree.
18
19  clear all; clc;
20  close all;
21
22  %% User inputs, file directories, and constants:
23
24  % Importing the desired shot numbers:
25  [shots,d,xmin,xmax,ymin,ymax,sign_twin] = shotnumber_inputs(2,1);
26  % Fraction along z axis for each cross-section:
27  cross_sect_frac = [.25 0.5 0.75];
```

```matlab
% Axial measurement location:
z_loc = 0.08; % [m]

% Creating a directory for .mat file and image storage:
date_ref = num2str(shots(1,1));
date = date_ref(1:6);
directory_save = ['H:\Reconstructions\',date,'\inverted'];
mkdir(['H:\Reconstructions\',date],'inverted');

% Declare constants and ZaP-HD plasma parameters:
e_0 = 8.85e-12; % Permitivity of free space
mu_0 = 1.257e-6; % Permeability of free space
k = 1.38e-23; % Boltzmann's constant in SI units
q = 1.6e-19; % electron charge [C]
c = 3e8; % speed of light [m/s]
mi = 1.67e-27; % proton mass [kg]
me = 9.12e-31; % electron mass [kg]
lambda = 532e-9; % laser wavelength [m]
R_electrode = 8*2.54/100;

%% 2.) Fresnel transform reconstruction and Abel inversion:
% Iterate through desired shots:
for shot_ind = 1:size(shots,1)
    % Close figures and clear data on each iteration for memory management:
    close all;
    clearvars -except h theta d_fringe step_sm Bw V ni ne Ti Te T r ...
        R_electrode lambda me mi c q k mu_0 e_0 z_loc cross_sect_frac ...
        shots d xmin xmax ymin ymax sign_twin shot_ind directory_save date
```

```matlab
    shotnum_base = shots(shot_ind,2);
    shotnum_def = shots(shot_ind,1);

%% Fresnel transform reconsruction:
[unwrapped,x_twin,y_twin,phase_diff,phase_x,phase_y] = ...
    holographic_reconstruction(shotnum_base,shotnum_def,xmin,...
    xmax,ymin,ymax,d);


% Plot and save the reconstructed phase:
fig999 = figure(999);
imagesc(phase_x,phase_y,phase_diff);
saveas(fig999,[directory_save,'\phase_map_',num2str(...
    shotnum_def),'_',num2str(shotnum_base),'POS.tif']);


% Define the indices for the selected cross sections:
cross_sect = round(cross_sect_frac*size(unwrapped,2));


% Converting the phase to the 2-D line-integrated density:
% Note that the sign of den_int_full here depends on the optical
% set up (e.g. the twin images can flip if the scene and reference
% beams flip orientation).
den_int_full = sign_twin*[unwrapped/((-q^2/(4*pi*c^2*me*e_0))...
    *lambda)]';
den_int_full = den_int_full - min(min(den_int_full));


% Reducing the size of x_twin and y_twin to match unwrapped
% (unwrapped is reduced in size because of boxcar smoothing):
```

```matlab
84       del_y = y_twin(2) − y_twin(1);

85       del_x = x_twin(2) − x_twin(1);

86       y_twin_red = [0:del_y:del_y*(size(den_int_full,2)−1)];

87       x_twin_red = [0:del_x:del_x*(size(den_int_full,1)−1)];


89       % Adjusting the zero value of x_twin and y_twin so the origin is

90       % centered.  Can adjust here for when the hologram is not centered at

91       % 0 impact param.

92       y_twin_red_adj = (y_twin_red − y_twin_red(end)/2);

93       x_twin_red_adj = x_twin_red − x_twin_red(end)/2+z_loc;


95       % Save .mat file with line−integrated data for further analysis:

96       save(['H:\Reconstructions\',date,'\Ne_',num2str(shotnum_def),...

97           '.mat'],'x_twin_red_adj','y_twin_red_adj','den_int_full');


99       % Identify number of cross sections:

100      num_of_cross_sect = size(unwrapped,2);


102      % Identify number of centroids:

103      num_of_centroids = 10;


105      % Identify number of n_edge values:

106      num_of_n_edge = 15;

107      n_edge_delta = 5e21;


109      %% Peform the Abel inversion:


111      % Iterate through cross sections:
```

```matlab
for k = 1:num_of_cross_sect

    % Identify the max Ne value and its index:
    den_int = den_int_full(k,:);
    [Ne_max(k),ind_Ne_max(k)] = max(den_int);

    % Initialize centroid_ind_tmp to enable determination of
    % centroid_abs (the centroid locations in absolute pixel-space):
    centroid_ind_tmp = ind_Ne_max(k)-num_of_centroids;

    % Reset the centroid_iterations if it was reduced to accomodate
    % centroids close to the bounds of the data:
    centroids_iterations = num_of_centroids;

    % Case statements to allow adjustments to the analysis for centroid
    % searches starting at or near the bounds of the data:
    quit2nextShot = 0; % for debugging
    % for centroids at the lower boundary:
    if centroid_ind_tmp <=0
        den_num_l{k} = NaN(size(unwrapped,1),1);%[];
        den_num_r{k} = NaN(size(unwrapped,1),1);
        centroid_abs(k) = 1;
        centroid(k) = 0;
    % for centroids at the upper boundary:
    elseif centroid_ind_tmp >= size(unwrapped,1)
        den_num_l{k} = NaN(size(unwrapped,1),1);
        den_num_r{k} = NaN(size(unwrapped,1),1);%[];
        centroid_abs(k) = size(unwrapped,1);
```

```matlab
                centroid(k) = 0;
            else

                % for centroids near (within 2*num_of_centroids of) the upper
                % boundary:
                if centroid_ind_tmp >= size(unwrapped,1)-2*num_of_centroids
                    centroids_iterations = 2*num_of_centroids-...
                        (centroid_ind_tmp-(size(unwrapped,1)-2*...
                        num_of_centroids));
                % for centroids near the lower boundary:
                else
                    centroids_iterations = 2*num_of_centroids;
                end

                % Iterate through centroids:
                for i = 1:centroids_iterations

                    % Selecting the left side of the Ne profile and flipping it
                    Ne_1d_left{k,i} = fliplr(den_int(1:centroid_ind_tmp));

                    % Selecting the right side of the Ne profile:
                    Ne_1d_right{k,i} = den_int(centroid_ind_tmp+1:end);

                    % Iterate the index to prepare the code to move to the next
                    % centroid value on the next loop iteration:
                    centroid_ind_track(k,i) = centroid_ind_tmp;
                    centroid_ind_tmp = centroid_ind_tmp + 1;
```

```matlab
                % Conductig the Abel inversion to compute the ne profile on
                % each side of the assumed centroid:
                ne_1d_left{k,i} = abel_invert(y_twin,[Ne_1d_left{k,i}-...
                    min(Ne_1d_left{k,i})]');
                ne_1d_right{k,i} = abel_invert(y_twin,[Ne_1d_right{k,i}-...
                    min(Ne_1d_right{k,i})]');

                % When the centroid does not divide the Ne profile in half,
                % the longer of the two sides must be truncated to match
                % the length of the shorter side.  The following case
                % statements conduct this truncation:
                len_left(k,i) = length(Ne_1d_left{k,i});
                len_right(k,i) = length(Ne_1d_right{k,i});

                if len_left(k,i)>len_right(k,i)
                    ne_1d_left_trunc{k,i} = ne_1d_left{k,i}(1:...
                        len_right(k,i));
                    ne_1d_right_trunc{k,i} = ne_1d_right{k,i};
                elseif len_left(k,i)<len_right(k,i)
                    ne_1d_left_trunc{k,i} = ne_1d_left{k,i};
                    ne_1d_right_trunc{k,i} = ne_1d_right{k,i}(1:...
                        len_left(k,i));
                else
                    ne_1d_left_trunc{k,i} = ne_1d_left{k,i};
                    ne_1d_right_trunc{k,i} = ne_1d_right{k,i};
                end

                % Identify the nominal n_edge_0 value as the density in the
```

```matlab
                % longer profile at the radius of the edge of the short
                % profile:
                if len_left(k,i)>len_right(k,i) && len_right(k,i)~=0
                    n_edge_0(k,i) = ne_1d_left_trunc{k,i}(len_right(k,i));
                elseif len_left(k,i)<len_right(k,i) && len_left(k,i)~=0
                    n_edge_0(k,i) = ne_1d_right_trunc{k,i}(len_left(k,i));
                else
                    n_edge_0(k,i) = 0;
                end

                % Initialize n_edge_tmp to enable determination of
                % centroid_abs (the centroid locations in absolute
                % pixel-space):
                n_edge_ind_tmp = -num_of_n_edge;

                % Iterate through n_edge values:
                for j = 1:2*num_of_n_edge
                    % populating list of all n_edge attempted:
                    n_edge_val(j) = n_edge_ind_tmp*n_edge_delta;

                    % Iterating through n_edge values for the shorter
                    % profile:
                    if len_left(k,i)>len_right(k,i)
                        ne_1d_left_compare{k,i,j} = ne_1d_left_trunc{k,i};
                        ne_1d_right_compare{k,i,j} = ...
                            ne_1d_right_trunc{k,i}+...
                            n_edge_delta*n_edge_ind_tmp;
                    elseif len_left(k,i)<len_right(k,i)
```

```matlab
                    ne_1d_left_compare{k,i,j} = ...
                        ne_1d_left_trunc{k,i}+...
                        n_edge_delta*n_edge_ind_tmp;
                    ne_1d_right_compare{k,i,j} = ...
                        ne_1d_right_trunc{k,i};
                else
                    if ne_1d_left_trunc{k,i}(end) > ...
                            ne_1d_right_trunc{k,i}(end)
                        ne_1d_left_compare{k,i,j} = ...
                            ne_1d_left_trunc{k,i}+...
                            n_edge_delta*n_edge_ind_tmp;
                        ne_1d_right_compare{k,i,j} = ...
                            ne_1d_right_trunc{k,i};
                    else
                        ne_1d_left_compare{k,i,j} = ...
                            ne_1d_left_trunc{k,i};
                        ne_1d_right_compare{k,i,j} = ...
                            ne_1d_right_trunc{k,i}+...
                            n_edge_delta*n_edge_ind_tmp;
                    end
                end

                % Iterate the index to prepare the code to move to the
                % next n_edge value on the next loop iteration:
                n_edge_ind_track(k,i,j) = n_edge_ind_tmp;
                n_edge_ind_tmp = n_edge_ind_tmp + 1;

                % Computing the L2 norm of the difference in the sides
```

```matlab
                    % of the ne profile:
                    dens_diff{k,i,j} = abs(ne_1d_left_compare{k,i,j}-...
                        ne_1d_right_compare{k,i,j});
                    norm_dens(k,i,j) = norm(dens_diff{k,i,j},2)/...
                        (length(dens_diff{k,i,j}));
                end

            % Changing all zero-valued elements in norm_dens to NaNs
            % (allows the code to ignore them when searching for the
            % minimum)
            ind_zeros = find(norm_dens(k,i,:)==0);
            norm_dens(k,i,ind_zeros) = NaN;

            % Find the minimum L2 norm value for each combination of
            % cross-section and centroid.  (n_edge_intermediate records
            % the index location of n_edge yielding minimum L2 norm)
            [norm_intermediate(k,i),n_edge_intermediate(k,i)] = ...
                min(norm_dens(k,i,:),[],3);
        end

        % Find the minimum L2 norm value for each cross-section.
        % (centroid records the relative index location of the centroid
        % location yielding minimum L2 norm)
        [norm_min_val(k),centroid(k)] = min(norm_intermediate(k,:)...
            ,[],2);
        n_edge(k) = n_edge_intermediate(k,centroid(k));

        % Assigning the final left and right number density profiles:
```

```matlab
            if centroid(k) == 0 % do not adjust for axial density variation
                %for non-inverted cross-sections

            elseif len_left(k,centroid(k))>len_right(k,centroid(k))
                den_num_l{k} = ne_1d_left{k,centroid(k)};
                den_num_r{k} = ne_1d_right{k,centroid(k)}+n_edge_delta*...
                    (n_edge(k)-num_of_n_edge);
                den_int_edge_axial(k) = den_int_full(k,1);

            elseif len_left(k,centroid(k))<len_right(k,centroid(k))
                den_num_l{k} = ne_1d_left{k,centroid(k)}+n_edge_delta*...
                    (n_edge(k)-num_of_n_edge);
                den_num_r{k} = ne_1d_right{k,centroid(k)};
                den_int_edge_axial(k) = den_int_full(k,end);

            else
                if ne_1d_left_trunc{k,i}(end) > ne_1d_right_trunc{k,i}(end)
                    den_num_l{k} = ne_1d_left_trunc{k,centroid(k)}+...
                        n_edge_delta*(n_edge(k)-num_of_n_edge);
                    den_num_r{k} = ne_1d_right_trunc{k,centroid(k)};
                    den_int_edge_axial(k) = den_int_full(k,end);

                else
                    den_num_l{k} = ne_1d_left_trunc{k,centroid(k)};
                    den_num_r{k} = ne_1d_right_trunc{k,centroid(k)}+...
                        n_edge_delta*(n_edge(k)-num_of_n_edge);
                    den_int_edge_axial(k) = den_int_full(k,end);
```

```matlab
            end
        end


        % Computing the centroid indices in absolute pixel coordinates:
        if centroid_ind_track(k,centroid(k)) == 0
            centroid_abs(k) = size(unwrapped,1);
        else
            centroid_abs(k) = centroid_ind_track(k,centroid(k));
        end
    end
end

if quit2nextShot == 0 % for debugging

    %% Compiling the inverted number density data to form the
    % den_num_full matrix:
    den_num_full = zeros(size(den_int_full));
    for k = 1:num_of_cross_sect
        if centroid_abs(k) == 1 || centroid_abs(k) == size(unwrapped,1)
            den_num_full(k,:) = zeros(size(unwrapped,1),1);
        else
            den_num_full(k,(1+centroid_abs(k)-length(den_num_l{k})):...
                centroid_abs(k)) = flipud(den_num_l{k});
            den_num_full(k,(1+centroid_abs(k)):(centroid_abs(k)+...
                length(den_num_r{k}))) = den_num_r{k};
        end
    end
```

```matlab
        %% Plotting the data:
        x_0 = x_twin_red_adj(1);
        y_0 = y_twin_red_adj(1);

        den_num_full = den_num_full';
        den_int_full = den_int_full';

        fnt = 24;

        % Plotting Ne (den_int_full):
        fig1 = figure(1);hold on;
        h11 = pcolor(x_twin_red_adj,y_twin_red_adj,den_int_full);
        set(h11,'edgecolor','none');
        colormap jet
        set(fig1,'position',[1290 520 560 420]);
        colorbar;
        xlim([x_twin_red_adj(1) x_twin_red_adj(end)]);
        ylim([y_twin_red_adj(1) y_twin_red_adj(end)]);
        title('Line-integrated electron density, N_e [m^{-2}]',...
            'fontsize',fnt);
        xlabel('Axial distance [m]','fontsize',fnt);
        ylabel('Impact parameter [m]','fontsize',fnt);
        set(gca,'fontsize',fnt);
        set(gca,'xtick',[0.145 0.15 0.155]);

        % Plotting number density not adjusted for axial variation:
        fig3 = figure(3);hold on;
        h31 = pcolor(x_twin_red_adj,y_twin_red_adj,den_num_full);
```

```matlab
        set(h31,'edgecolor','none');
        h32 = scatter(x_twin_red_adj,y_twin_red_adj(centroid_abs),'k','.');
        set(h32,'sizedata',1000);
        colormap jet
        set(fig3,'position',[1867         519         560         420]);
        colorbar;
        xlim([x_twin_red_adj(1) x_twin_red_adj(end)]);
        ylim([y_twin_red_adj(1) y_twin_red_adj(end)]);
        line([cross_sect(1)*del_x+x_0 cross_sect(1)*del_x+x_0],...
            [y_twin_red_adj(1) y_twin_red_adj(end)],'color','k');
        line([cross_sect(1)*del_x+x_0 cross_sect(1)*del_x+x_0],...
            [y_twin_red_adj(1) y_twin_red_adj(end)],'color','k',...
            'linewidth',3);
        if length(cross_sect)==3
            line([cross_sect(2)*del_x+x_0 cross_sect(2)*del_x+x_0],...
                [y_twin_red_adj(1) y_twin_red_adj(end)],'color','k',...
                'linewidth',3);%,'linestyle',':');
            line([cross_sect(3)*del_x+x_0 cross_sect(3)*del_x+x_0],...
                [y_twin_red_adj(1) y_twin_red_adj(end)],'color','k',...
                'linewidth',3);%,'linestyle','--');
        else
        end
        title('Electron number density, n_e [m^{-3}]','fontsize',fnt);
        xlabel('Axial distance [m]','fontsize',fnt);
        ylabel('Impact parameter [m]','fontsize',fnt);
        set(gca,'fontsize',fnt);
        set(gca,'xtick',[0.145 0.15 0.155]);
```

```matlab
        %% Adjusting number density to account for axial variation of phase
      if exist('centroid') % do not adjust for axial density variation
          % for non-inverted cross-sections

          for k = 1:num_of_cross_sect

              if centroid_abs(k) == 1
                  y_edge_l{k} = 0:del_y:del_y;
                  y_edge_r{k} = 0:del_y:size(unwrapped,1)-1;
                  y_count(k) = max(y_edge_l{k});


                  x_edge_l(k) = 2*sqrt(R_electrode^2-max(y_edge_l{k})^2);
                  x_edge_r(k) = 2*sqrt(R_electrode^2-max(y_edge_r{k})^2);

              elseif centroid_abs(k) == size(unwrapped,1)
                  y_edge_l{k} = 0:del_y:(size(unwrapped,1)-1)*del_y;
                  y_edge_r{k} = 0:del_y:del_y;
                  y_count(k) = max(y_edge_l{k});

                  x_edge_l(k) = 2*sqrt(R_electrode^2-max(y_edge_l{k})^2);
                  x_edge_r(k) = 2*sqrt(R_electrode^2-max(y_edge_r{k})^2);

              else
                  y_edge_l{k} = 0:del_y:(length(den_num_l{k})-1)*del_y;
                  y_edge_r{k} = 0:del_y:(length(den_num_r{k})-1)*del_y;

                  y_count(k) = max(y_edge_l{k});
                  x_edge_l(k) = 2*sqrt(R_electrode^2-max(y_edge_l{k})^2);
```

```matlab
            x_edge_r(k) = 2*sqrt(R_electrode^2-max(y_edge_r{k})^2);
        end

        if centroid(k) == 0 % do not adjust for axial density
            %variation for non-inverted cross-sections

        elseif len_left(k,centroid(k))>len_right(k,centroid(k))%%
            den_num_edge_axial_l(k) = den_int_edge_axial(k)/...
                x_edge_l(k);
            den_num_edge_axial_r(k) = 0;

            den_num_axial_l{k} = den_num_l{k} + ...
                den_num_edge_axial_l(k);
            den_num_axial_r{k} = den_num_r{k} + ...
                den_num_edge_axial_l(k);

        elseif len_left(k,centroid(k))<len_right(k,centroid(k))
            den_num_edge_axial_l(k) = 0;
            den_num_edge_axial_r(k) = den_int_edge_axial(k)/...
                x_edge_l(k);

            den_num_axial_l{k} = den_num_l{k} + ...
                den_num_edge_axial_r(k);
            den_num_axial_r{k} = den_num_r{k} + ...
                den_num_edge_axial_r(k);

        else
            den_num_edge_axial_l(k) = 0;
```

```matlab
                    den_num_edge_axial_r(k) = 0;

                    den_num_axial_l{k} = den_num_l{k};
                    den_num_axial_r{k} = den_num_r{k};
                end
            end

        % Compiling the adjusted number density into a single matrix:
        for k = 1:num_of_cross_sect

            if centroid(k) ==0
                den_num_full_axial(k,1:size(unwrapped,1)) = ...
                    zeros(size(unwrapped,1),1);
            else
                den_num_full_axial(k,(1+centroid_abs(k)-...
                    length(den_num_axial_l{k})):centroid_abs(k)) = ...
                    flipud(den_num_axial_l{k});
                den_num_full_axial(k,(1+centroid_abs(k)):...
                    (centroid_abs(k)+length(den_num_axial_r{k}))) = ...
                    den_num_axial_r{k};
            end
        end
        den_num_full_axial = den_num_full_axial';

        %% Plotting the number density adjusted for axial variation:
        fig33 = figure(33);hold on; fnt = 24;
        h31 = pcolor(x_twin_red_adj,y_twin_red_adj,den_num_full_axial);
        set(h31,'edgecolor','none');
```

```matlab
            h32 = scatter(x_twin_red_adj,y_twin_red_adj(centroid_abs),...
                'k','.');
            set(h32,'sizedata',1000);
            colormap jet
            set(fig33,'position',[1867 519 560 420]);
            colorbar;
            xlim([x_twin_red_adj(1) x_twin_red_adj(end)]);
            ylim([y_twin_red_adj(1) y_twin_red_adj(end)]);
            title('Electron number density, n_e [m^{-3}]','fontsize',fnt);
            xlabel('Axial distance [m]','fontsize',fnt);
            ylabel('Impact parameter [m]','fontsize',fnt);
            set(gca,'fontsize',fnt);
            set(gca,'xtick',[0.145 0.15 0.155]);
            legend(h32,'centroid');

            % Saving figures as images:
            if sign_twin > 0
                saveas(fig1,[directory_save,'\den_int_contour_',...
                    num2str(shotnum_def),'_',num2str(shotnum_base),...
                    'POS.tif']);
                saveas(fig33,[directory_save,'\den_num_contour_',...
                    num2str(shotnum_def),'_',num2str(shotnum_base),...
                    'POS.tif']);
            else
                saveas(fig1,[directory_save,'\den_int_contour_',...
                    num2str(shotnum_def),'_',num2str(shotnum_base),...
                    '.tif']);
                saveas(fig33,[directory_save,'\den_num_contour_',...
```

```matlab
                        num2str(shotnum_def),'_',num2str(shotnum_base),...
                        '.tif']);
            end

            for k = 1:num_of_cross_sect
                rad_l_tmp{k} = 0:del_y:(length(den_num_l{k})-1)*del_y;
                % del_y is in empirical reconstruction coords.
                rad_r_tmp{k} = 0:del_y:(length(den_num_r{k})-1)*del_y;
            end
            for k = 1:length(cross_sect)
                rad_l{k} = rad_l_tmp{cross_sect(k)};
                rad_r{k} = rad_r_tmp{cross_sect(k)};
            end

        else
        end

    else
    end

    %% Writing data to the ZaP-HD MDSplus data tree:
    MDS_DHI_put(shotnum_def,shotnum_base,den_int_full,den_num_full,...
        centroid_abs,d,xmin,xmax,ymin,ymax,sign_twin,...
        x_twin_red_adj,y_twin_red_adj)
end
```

C.2   Functions for DHI analysis

DC_suppression.m

```matlab
% DC_suppression.m
% Author:  Michael P. Ross
% Date = Sept. 6, 2016
% Description:  This code suppresses the zeroth order diffraction image by
% subtracting the mean intensity from each hologram.


function [hol_def,hol_base] = DC_suppression(hol_def,hol_base,M,N)

hol_def = hol_def - ones(N,M)*mean(mean(hol_def));
hol_base = hol_base - ones(N,M)*mean(mean(hol_base));

status = sprintf('DC diffraction image suppressed... \n')
```

hyperbolic_window.m

```matlab
% hyperbolic_window.m
% Author:  Michael P. Ross
% Date = Sept. 6, 2016
% Description:  This code performs applies a hyperbolic window function to
% the holograms to remove Gibbs phenomena in the resulting recontructions.

function [hol_def, hol_base] = hyperbolic_window(hol_def,hol_base)

L = size(hol_def);
M = L(2);  % x-direction
N = L(1);  % y-direction

param = 8;
x2 = linspace(-param*pi,param*pi,M+1); x = x2(1:M);
y2 = linspace(-param*pi,param*pi,N+1); y = y2(1:N);

for i = 1: length(hol_def(:,1))
    hol_def(i,:) = hol_def(i,:).*(tanh(x+(param-1)*pi)-tanh(x-(param-1)*pi))
        ;
    hol_base(i,:) = hol_base(i,:).*(tanh(x+(param-1)*pi)-tanh(x-(param-1)*pi
        ));
end

for j = 1: length(hol_base(1,:))
    hol_def(:,j) = hol_def(:,j).*(tanh(y+(param-1)*pi)-tanh(y-(param-1)*pi))
        ';
```

```
24      hol_base(:,j) = hol_base(:,j).*(tanh(y+(param−1)*pi)−tanh(y−(param−1)*pi
            ))';
25  end
```

holographic_reconstruction.m

```matlab
% holographic_reconstruction.m
% Author:  Michael P. Ross
% Date = Sept. 6, 2016
% Description:  This code performs the Fresnel transform reconstruction and
% computes the phase shift between specified plasma and vacuum holograms.
% It also extracts a twin image from the data and smooths and unwraps that
% twin image.

function [unwrapped,x_twin,y_twin,phase_diff,x,y] = ...
    holographic_reconstruction(shotnum_base,shotnum_def,xmin,xmax,ymin,...
    ymax,d,varargin)

% Constants:
res = (3.85e-6); % [m] Pixel size of Nikon 3200D 4.3e-6 for Canon Rebel T2i

% Starting with ZaP's shot number convention:
SN_def = num2str(shotnum_def);
SN_base = num2str(shotnum_base);

% Converting to Canon Camera shot number convention:
year_def = num2str(2000+str2num(SN_def(1:2)));
month_def = num2str(SN_def(3:4));
day_def = num2str(SN_def(5:6));

year_base = num2str(2000+str2num(SN_base(1:2)));
month_base = num2str(SN_base(3:4));
day_base = num2str(SN_base(5:6));
```

```matlab
28
29  date_def = [year_def,'_', month_def,'_', day_def];
30  date_base = [year_base,'_',month_base,'_',day_base];
31  date_plot = [year_def, month_def, day_def];
32
33  shot_def = SN_def(7:end);
34  shot_base = SN_base(7:end);
35
36  hol_def_rgb = imread(['H:\Raw Holograms\',date_def,'\',...
37      date_def, '_', shot_def,'.jpg']);
38  hol_base_rgb = imread(['H:\Raw Holograms\',date_base,'\',...
39      date_base, '_', shot_base,'.jpg']);
40
41  % Converting from RGB to grayscale (rgb2gray is not a supported command
42  % without the image processing toolbox):
43  rgb_red = 0.3;
44  rgb_green = 0.59;
45  rgb_blue = 0.11;
46
47  hol_def = double(hol_def_rgb(:,:,1).*rgb_red + hol_def_rgb(:,:,2).*...
48      rgb_green + hol_def_rgb(:,:,3).*rgb_blue)';
49  hol_base = double(hol_base_rgb(:,:,1).*rgb_red + hol_base_rgb(:,:,2).*...
50      rgb_green + hol_base_rgb(:,:,3).*rgb_blue)';
51
52  % If an eighth input = 1 is passed to the function, the hologram intensity
53  % values are truncated within the range hol_max_cut:hol_min_cut.
54  if nargin == 8
55      hol_contrast = varargin{1};
```

```
56
57        hol_max_cut = 100;
58        hol_min_cut = 70;
59
60        if hol_contrast == 1;
61            hol_def(find(hol_def>hol_max_cut)) = hol_max_cut;
62            hol_def(find(hol_def<hol_min_cut)) = hol_min_cut;
63        else
64        end
65    else
66    end
67
68    % Reconstruction:
69    [phase_diff,x,y,xsize_fres,ysize_fres] = DHI_rec(hol_base,hol_def,d,res);
70
71    M = size(hol_def,2);
72    N = size(hol_def,1);
73
74    x_plt = -max(x)/2:x(2)-x(1):max(x)/2;
75    y_plt = -max(y)/2:y(2)-y(1):max(y)/2;
76
77    % Extracting the twin image:
78
79    % Labeling the matrix indices:
80    x_ind_vec = 1:1:M;
81    y_ind_vec = 1:1:N;
82
83    % Interpolating to match a spatial coordinate values to the
```

```matlab
84  % nearest integer matrix indices:
85  x_min_ind = round(interp1(x,x_ind_vec,xmin));
86  x_max_ind = round(interp1(x,x_ind_vec,xmax));
87  y_min_ind = round(interp1(y,y_ind_vec,ymin));
88  y_max_ind = round(interp1(y,y_ind_vec,ymax));
89
90  % Defining the x,y spatial coordinate vectors for the extracted twin image:
91  x_twin = x(x_min_ind:x_max_ind);
92  x_twin = x_twin(1:10:end);
93  y_twin = y(y_min_ind:y_max_ind);
94  y_twin = y_twin(1:10:end);
95
96  twin_img = phase_diff(y_min_ind:y_max_ind,x_min_ind:x_max_ind);
97  twin_img = twin_img(1:10:end,1:10:end);
98
99  % Smoothing and unwrapping the twin image:
100 width = 8;
101 [unwrapped,phase_f,unsmoothed_unwrapped] = smooth_unwrap(twin_img,width);
```

DHI_rec.m

```matlab
1  % DHI_rec.m
2  % Author:  Michael P. Ross
3  % Date = Sept. 6, 2016
4  % Description:  This code performs the Fresnel transform reconstruction and
5  % computes the phase shift between specified plasma and vacuum holograms.
6
7  function [phase_diff,x,y,xsize_fres,ysize_fres] = DHI_rec(hol_base,...
8      hol_def,d,res)
9
10 %% Declare parameters:
11 lambda = 532e-9; % [m] Nd:YAG wavelength, 694.3e-9 [m] ruby wavelength
12 n_c = 2.312e27; % [m^-3] critical plasma density
13
14 L = size(hol_def);
15 M = L(2);  % x-direction
16 N = L(1);  % y-direction
17
18 ximg = linspace(0,res*M,M);
19 yimg = linspace(0,res*N,N);
20
21 %% Applying windowing to the holograms:
22 [hol_def,hol_base] = hyperbolic_window(hol_def,hol_base);
23 % [hol_def,hol_base] = DC_suppression(hol_def,hol_base,M,N);
24
25 %% Reconstruction with Fresnel method:
26 ref = 1;
27 b_def = fresnel(hol_def,d,lambda,res,ref);
```

```matlab
28  b_base = fresnel(hol_base,d,lambda,res,ref);
29
30  %% Computing the phase from the complex wavefield:
31  phase_diff = phase_diff_func(b_def,b_base);
32
33  %% Preparing axes necessary for plotting:
34  xsize_fres = abs(d*lambda/M/res);
35  ysize_fres = abs(d*lambda/N/res);
36  x = 0:xsize_fres:(M-1)*xsize_fres;
37  y = 0:ysize_fres:(N-1)*ysize_fres;
```

fresnel.m

```matlab
% fresnel.m
% Author:  Michael P. Ross
% Date = Sept. 6, 2016
% Description:  This code performs the Fresnel transform reconstruction
% and outputs the electric field strength as a matrix of complex numbers b.

function [b] = fresnel(hol,d,lambda,res,ref)

% Declaring pixel and sensor size in the hologram plane:
L = size(hol);
M = L(2);       % number of pixels along x-direction
N = L(1);       % number of pixels in y-direction
del_xi = res;  % pixel size in x-direction
del_eta = res; % pixel size in y-direction
chirp = ones(N,M);


% Computing the length scales in the reconstruction plane:
xsize_fres = abs(d*lambda/M/res);
ysize_fres = abs(d*lambda/N/res);
xfres = [-(M/2)*xsize_fres:xsize_fres:(M/2)*xsize_fres];
xfres = xfres(1:M);
yfres = ([-(N/2)*ysize_fres:ysize_fres:(N/2)*ysize_fres]);
yfres = yfres(1:N);


k = 2*pi/lambda;


% Generating the chirp function required by the Fresnel transform:
```

```matlab
28  status = sprintf('Generating chirp...')
29  for n = 0:N—1
30          for m = 0:M—1
31
32              % Chirp function:
33              chirp(n+1,m+1) = exp((1i*pi/(d*lambda))*(((n—N/2)^2*...
34                  del_eta^2)+((m—M/2)^2*del_xi^2)));
35
36              % Complex, constant phase factor:
37              % This factor is only required if we want a correctly scaled
38              % reconstructed intensity distribution.  It is not needed in
39              % computing the interference phase distribution.
40              % A(n+1,m+1) = (exp(1i*k*d)/(1i*lambda*d))*...
41              % exp((1i*pi/(d*lambda))*(xfres(m+1)^2+yfres(n+1)^2));
42
43          end
44  end
45
46  status = sprintf('done with chirp. \n')
47
48  % Set the complex factor to 1 when only reconstructing phase.
49  A = 1;
50
51  % Multiply the hologram intensity distribution with the reference beam:
52  hol_ref = hol*ref;
53
54  % Convolving the product of the hologram function and reference wave with
55  % the chirp function.
```

```
56  status = sprintf('Computing Fresnel transform...')
57  b = A.*ifftshift(ifft2(fftshift(hol_ref.*chirp)));
58  status = sprintf('done with Fresnel transform. \n')
```

phase_diff_func.m

```matlab
% phase_diff_func.m
% Author:  Michael P. Ross
% Date = Sept. 6, 2016
% Description:  This code computes the wrapped phase difference between
% plasma and vacuum holograms.

function [phase_diff] = phase_diff_func(b_def,b_base)

status = sprintf('Computing interference phase...')
phase_diff = atan2(imag((b_def).*conj((b_base))),real((b_def).*...
    conj((b_base))));
status = sprintf('done computing interference phase. \n')
```

fresnel.m

```matlab
1   % smooth_unwrap.m
2   % Author:  Michael P. Ross
3   % Date = Sept. 6, 2016
4   % Description:  This code smooths the extracted wrapped twin image and then
5   % unwraps the phase.  The function outputs smoothed and unsmoothed versions
6   % of the unwrapped phase.
7
8   function [unwrapped,phase_f,unsmoothed_unwrapped] = smooth_unwrap(...
9       twin_img,width)
10
11  % Transforming into cosine/sine space:
12  s = sin(twin_img);
13  c = cos(twin_img);
14
15  % Boxcar averaging (change the width parameter to change the size of the
16  % sliding boxcar window):
17  % width = 4;
18  sf = boxcar2(s,width);
19  cf = boxcar2(c,width);
20
21  % Inverting back to phase space:
22  phase_F = atan2(sf,cf);
23  phase_f = phase_F(2*width+1:end-(2*width+1),:);
24
25  % unwrapping the smoothed extracted twin image:
26  unwrapped = zeros(size(phase_f,1),size(phase_f,2));
27
```

```matlab
% unwrap rows
for i =1:size(phase_f,1)
    unwrapped(i,:) = unwrap(phase_f(i,:));
end
% unwrap columns
for j =1:size(phase_f,2)
    unwrapped(:,j) = unwrap(unwrapped(:,j));
end

unwrapped = unwrapped − max(unwrapped(:));

% unwrapping the unsmoothed extracted twin image:
unsmoothed_unwrapped = zeros(size(twin_img,1),size(twin_img,2));

% unwrap rows
for i =1:size(phase_f,1)
    unsmoothed_unwrapped(i,:) = unwrap(twin_img(i,:));
end
% unwrap columns
for j =1:size(phase_f,2)
    unsmoothed_unwrapped(:,j) = unwrap(unsmoothed_unwrapped(:,j));
end

unsmoothed_unwrapped = unsmoothed_unwrapped − max(unsmoothed_unwrapped(:));
```

MDS_DHI_put.m

```matlab
% MDS_DHI_put.m
% Author:  Michael P. Ross
% Date = Sept. 6, 2016
% Description:  This script stores the relevant DHI data to the dhihd tree.

function MDS_DHI_put(shotnum,base_number,den_int_full,den_num_full,...
    centroid_abs,recon_dist,xmin,xmax,ymin,ymax,sign_twin,x_twin,y_twin)

import MDSplus.*
tree_string = 'dhihd';
dhihdTree = Tree(tree_string,shotnum,'EDIT');

%% create the nodes in the DHIHD tree:
try
    dhihdTree.addNode('base_number','NUMERIC');
catch
end
try
    dhihdTree.addNode('dhi_int','NUMERIC');
catch
end
try
    dhihdTree.addNode('dhi_inverted','NUMERIC');
catch
end
try
    dhihdTree.addNode('centroid_abs','NUMERIC');
```

```
28  catch
29  end
30  try
31      dhihdTree.addNode('recon_dist','NUMERIC');
32  catch
33  end
34  try
35      dhihdTree.addNode('xmin','NUMERIC');
36      catch
37  end
38  try
39      dhihdTree.addNode('xmax','NUMERIC');
40      catch
41  end
42  try
43      dhihdTree.addNode('ymin','NUMERIC');
44      catch
45  end
46  try
47      dhihdTree.addNode('ymax','NUMERIC');
48      catch
49  end
50  try
51      dhihdTree.addNode('sign_twin','NUMERIC');
52      catch
53  end
54  try
55      dhihdTree.addNode('x_twin','NUMERIC');
```

```matlab
56        catch
57    end
58    try
59        dhihdTree.addNode('y_twin','NUMERIC');
60    catch
61    end
62
63    dhihdTree.write() % need to write the nodes to the tree before storing data
64
65    %% Storing data to the tree and creating tagnames:
66    current_node = dhihdTree.getNode('base_number');
67    current_node.putData(MDSarg(base_number));
68    try
69        current_node.addTag('base_number');
70    catch
71    end
72
73    current_node = dhihdTree.getNode('dhi_int');
74    current_node.putData(MDSarg(((den_int_full'))));
75    try
76        current_node.addTag('dhi_int');
77    catch
78    end
79
80    current_node = dhihdTree.getNode('dhi_inverted');
81    current_node.putData(MDSarg(((den_num_full'))));
82    try
83        current_node.addTag('dhi_inverted');
```

```
84   catch
85   end
86
87   current_node = dhihdTree.getNode('centroid_abs');
88   current_node.putData(MDSarg(centroid_abs));
89   try
90       current_node.addTag('centroid_abs');
91   catch
92   end
93
94   current_node = dhihdTree.getNode('recon_dist');
95   current_node.putData(MDSarg(recon_dist));
96   try
97       current_node.addTag('recon_dist');
98   catch
99   end
100
101  current_node = dhihdTree.getNode('xmin');
102  current_node.putData(MDSarg(xmin));
103  try
104      current_node.addTag('xmin');
105  catch
106  end
107
108  current_node = dhihdTree.getNode('xmax');
109  current_node.putData(MDSarg(xmax));
110  try
111      current_node.addTag('xmax');
```

```
112  catch
113  end
114
115  current_node = dhihdTree.getNode('ymin');
116  current_node.putData(MDSarg(ymin));
117  try
118      current_node.addTag('ymin');
119  catch
120  end
121
122  current_node = dhihdTree.getNode('ymax');
123  current_node.putData(MDSarg(ymax));
124  try
125      current_node.addTag('ymax');
126  catch
127  end
128
129  current_node = dhihdTree.getNode('sign_twin');
130  current_node.putData(MDSarg(sign_twin));
131  try
132      current_node.addTag('sign_twin');
133  catch
134  end
135
136  current_node = dhihdTree.getNode('x_twin');
137  current_node.putData(MDSarg((x_twin)));
138  try
139      current_node.addTag('x_twin');
```

```
140  catch
141  end
142
143  current_node = dhihdTree.getNode('y_twin');
144  current_node.putData(MDSarg((y_twin)));
145  try
146      current_node.addTag('y_twin');
147  catch
148  end
149
150  dhihdTree.write()
151  dhihdTree.close()
```

Appendix D

STRUCTURAL ANALYSIS OF ZAP-HD ENDPLATES AND OUTER ELECTRODE

This appendix explains the structural analysis employed in designing ZaP-HD's interchangeable endwalls. Installation of an endwall to the end of the outer electrode enables ZaP-HD to form on-axis Z-pinches with axially-uniform high current densities by providing an on-axis current connection point. Because ZaP-HD aims to drive plasma currents up to 500 kA, the induced mangetic pressure can impulsively load the endwall with tens-of-thousands of pounds of force over a 100 μs duration.

Two endwalls are analyzed. A single hole design closely replicates an endwall from the original ZaP experiment. This design (see Fig. D.1) includes a central hole to allow on-axis plasma to flow through without stagnating. While this central hole does help reduce stagnation near machine axis, velocity profile observations from ZaP indicate stagnation still occurs off axis. A flow shear reversal occurs where, although the fastest plasma velocities are initially at large radii, they eventually slow so that the fastest velocities are located on-axis. A spoked endwall design (see Fig. D.2) is an attempt to alleviate this flow stagnation.

The analysis identifies worst case and best case loading scenarios and then identifies how much plasma current the endwalls could survive for each case. The worst case scenario occurs when the Z-pinch attachment to the endwall is completely off-center allowing nearly all magnetic pressure, plasma pressure, and plasma momentum to push against the endwall. The best case occurs when the plasma's attachment is well centered allowing much of the pressure to simply push plasma through the hole at the center of the endwall. If ZaP-HD forms repeatable, on-axis pinches, the plasma current may be increased beyond the highest survivable current for the worst case loading.
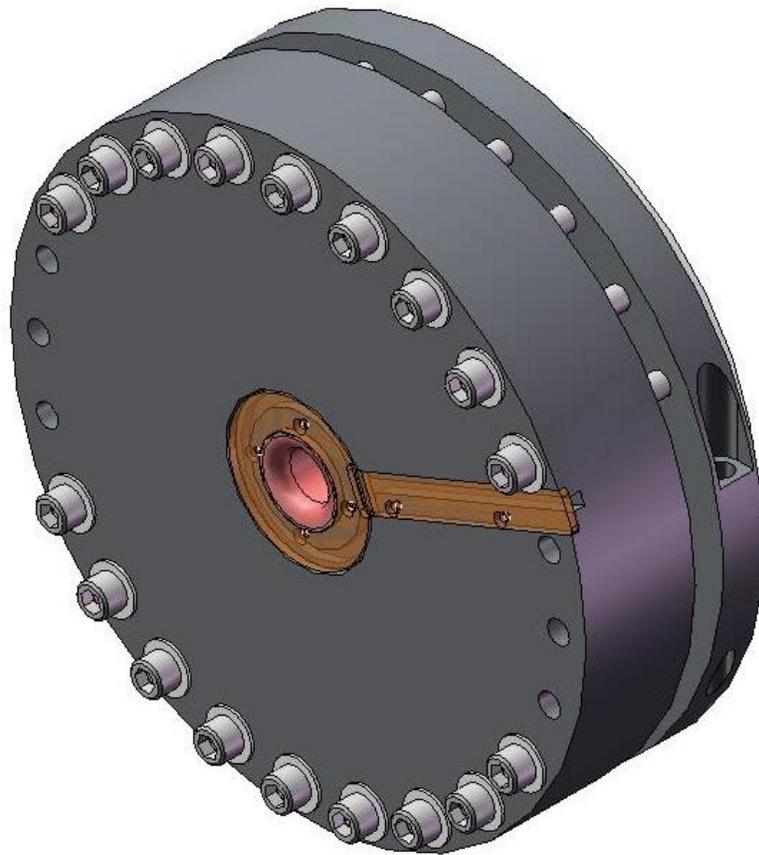
Figure D.1: The single hole endwall design closely matches an endwall used on the orignal ZaP experiment. This view shows the endwall bolted to the downstream split ring on the outer electrode. Red surfaces indicate Tungsten spray, and the orange plates are shields covering a Rogowski coil used to measure the current flow through the central hole.
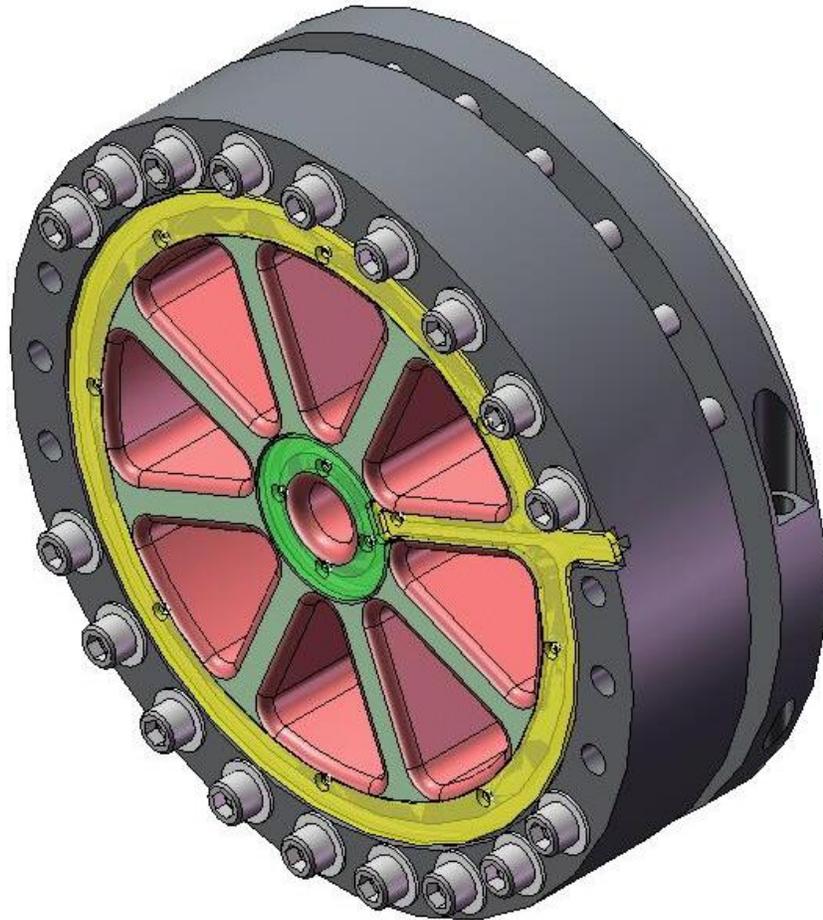
Figure D.2: The spoked endwall design aims to alleviate flow stagnation. This view shows the endwall bolted to the downstream split ring on the outer electrode. Red surfaces indicate Tungsten spray, and the green and yellow plates are shields covering two Rogowski coils used to measure the current flow through the central hole and through all holes respectively.

D.1   Estimating the force on the endwall

Computing the cumulative force on the endwall requires theoretically predicting the state of the ZaP-HD plasma. Adiabatic scaling relations are used to find the Z-pinch's density, temperature, and diameter at an elevated plasma current. Applying these estimated plasma parameters to Ampere's law and ideal MHD force balance allows the determination of magnetic field and pressure profiles. Integrating the pressure over the entire plasma-facing endwall surface computes the worst case load, while integrating the pressure over the plasma-facing surface excluding the central hole computes the best case. Conducting this analysis for a range of elevated plasma currents generates plots of endwall loading versus plasma current for each case. These plots are compared to a series of ANSYS simulations to select the proper endwall geometry.

D.1.1   Scaling the Z-pinch from ZaP to ZaP-HD

The plasma parameters density, temperature, and pinch diameter are required to solve for pressure profiles to integrate, but these parameters change with increased plasma current. ZaP-HD's main goal is to scale up plasma current, I, while maintaining constant linear density, N. ZaP-HD's parameters can be estimated for a range of plasma currents using the adiabatic scaling relations (Eq. 1.7,1.8,1.9). Here, the subscripts correspond to two different states. The initial state represents ZaP's parameters: $n_1 = 6 \times 10^{22}$ $[m^{-3}]$, $T_1 = 20$ $[eV]$, $a_1 = 1$ $[cm]$, and $I_1 = 50$ $[kA]$. The second state represents ZaP-HD at a given current, I_2. Knowing the plasma parameters at a given current enables the determination of endwall loading for that current.

D.1.2   Control volume analysis

Finding the cumulative endwall loading reduces to integrating pressure over the plasma-facing endwall surface. This method arises from a control volume analysis of force balance in the region near the ZaP-HD outer electrode endwall. Integrating the ideal MHD momentum

equation (Eq. D.1) within a control volume yields the expression for net force on the volume (Eq. D.2).

$$\frac{\partial}{\partial t}\rho\vec{v} + \nabla \cdot \tilde{T} = 0 \tag{D.1}$$

$$\vec{F}_{net} = \int -\nabla \cdot \tilde{T} dV = -\oint d\vec{S} \cdot \tilde{T} \tag{D.2}$$

Here, ρ is the plasma mass density, $\vec{v}$ is the flow velocity, and $\tilde{T}$ is Maxwell's stress tensor (Eq. D.3). In the stress tensor, P is isotropic pressure. $\tilde{I}$ is an identity tensor.

$$\tilde{T} = \rho\vec{v}\vec{v} + \left[P + \frac{B^2}{2\mu_0}\right]\tilde{I} - \vec{B}\vec{B} \tag{D.3}$$

A control volume is chosen surrounding the endwall as shown in Fig D.3. The integration of Eq. D.2 is split into three parts corresponding to each surface of the control volume.

$$\vec{F}_{net} = -\int_1 d\vec{S}_z \cdot \tilde{T} - \int_2 d\vec{S}_z \cdot \tilde{T} - \int_3 d\vec{S}_r \cdot \tilde{T} \tag{D.4}$$

1. **Surface 1** lies beyond the downstream side of the endwall. This analysis assumes this surface experiences no plasma pressure and all magnetic field components on the surface are zero, which is reasonable considering no major currents penetrate the surface.

2. **Surface 2** experiences plasma pressure as it resides in the region containing the Z-pinch. It also experiences significant azimuthal magnetic field. The analysis assumes this surface does not see any radial or axial fields.

3. **Surface 3** is outside the outer electrode (the current return path), so it does not experience any fields or plasma pressure.

In summary, only surface 2 contributes to the net force on the control volume. Its surface integral can be written as in Eq. D.5, which amounts to integrating pressure over the endwall's plasma-facing surface.
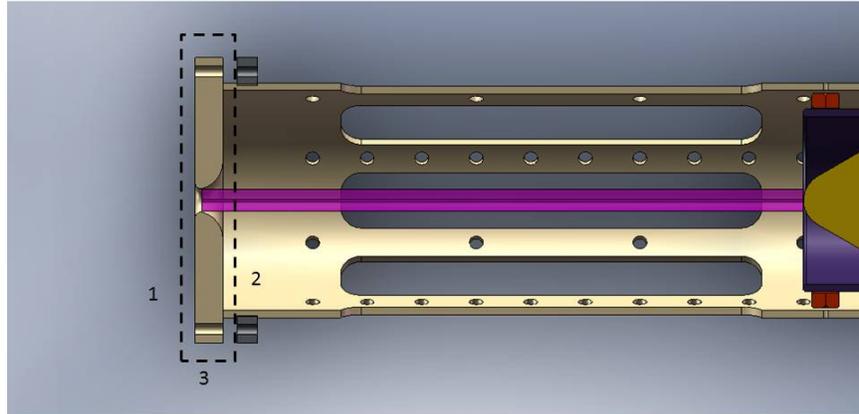
Figure D.3: A cylindrical control volume encompassing the endwall is used to solve for the net force on the endwall in the worst case.

$$\vec{F}_{net} = -\hat{z} \int \left[\frac{B_\theta^2}{2\mu_0} + P + \rho v_z^2 \right] 2\pi r dr \qquad (D.5)$$

D.1.3   ZaP-HD pressure profiles

Computing a pressure profile requires assuming a current distribution to obtain a magnetic field profile from Ampere's law. Assuming two different current distributions, a skin current and a uniform current, reveals the sensitivity of the endwall load to current distribution.

Eqs. (D.6) and (D.7) express the pressure profiles for a skin current and uniform current respectively. Each pressure profile is the sum of magnetic pressure, static plasma pressure, and kinetic plasma pressure. For the skin current, $B(r) = 0$ within the pinch radius and $B(r) = \mu_0 I/2\pi r$ outside the pinch. For the uniform current, $B(r) = \mu_0 jr/2$ inside the pinch and $B(r) = \mu_0 I/2\pi r$ outside. The plasma density, n, and temperature, T, are assumed uniform, m_p is the mass of a proton, and v_z is the bulk plasma velocity assumed to be a
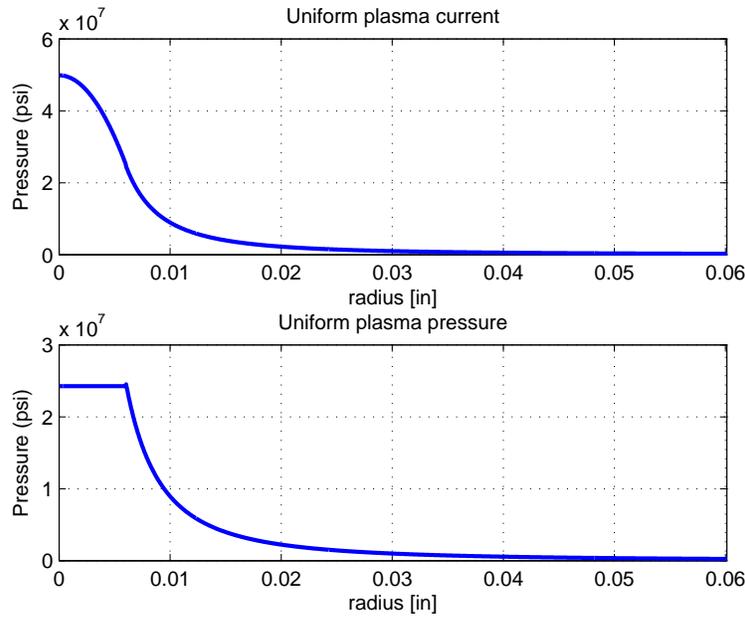
Figure D.4: Pressure profiles for a 500 kA plasma current. The top plot shows the pressure for a uniform plasma current while the bottom plot shows the pressure for a skin current. The profiles are identical beyond the radius of the plasma (0.005").

uniform 100 km/s within the pinch. These pressure profiles are plotted in Fig. D.4 for a 500 kA plasma current.

$$P(r) = \frac{B(r)^2}{2\mu_0} + 2nkT + m_p n v_z^2 \tag{D.6}$$

$$P(r) = \frac{B(r)^2}{2\mu_0} + \frac{\mu_0 j^2 d^2}{4} + m_p n v_z^2 \tag{D.7}$$

D.1.4   Integrating to find the applied force

Worst case loading

In the worst case, all of the plasma pressure pushes on the endwall. This loading is computed by integrating the pressure profiles over all of surface 2 from the control volume analysis.
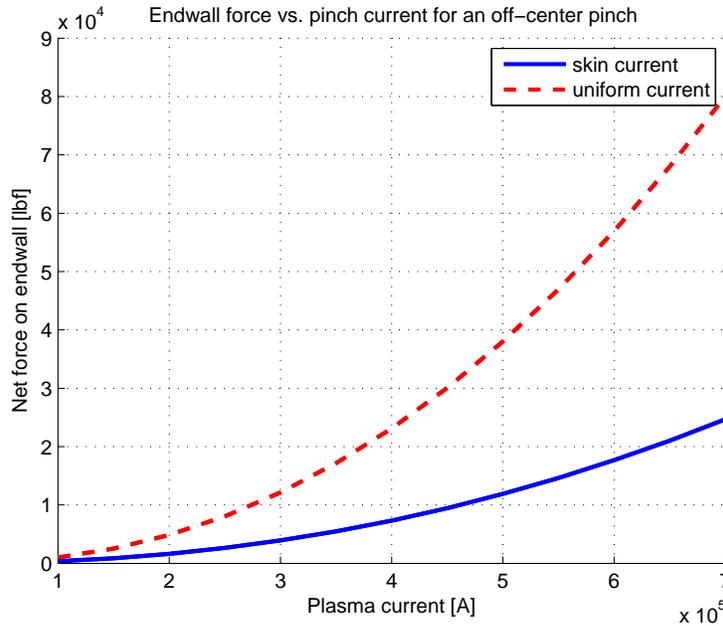
Figure D.5: For off-axis pinches (the worst case loading scenario), the choice of current profile significantly alters the scaling relation between load and current. The uniform current profile scales to much higher endwall loads for a given current than does the skin current profile.

The integrations for skin and uniform currents analytically reduce to Eqs. (D.8) and (D.9) respectively. Note that here d is the pinch radius, and D is the radius of the outer electrode.

$$F_{skin} = \frac{\mu_0 j^2 \pi}{4} d^4 \ln \frac{D}{d} + 2nkT\pi d^2 + m_p n v_z^2 \pi d^2 \tag{D.8}$$

$$F_{uniform} = \frac{\mu_0 j^2 \pi}{16} d^4 + \frac{\mu_0 j^2 \pi}{4} d^4 \ln \frac{D}{d} + \frac{\pi \mu_0 j^2}{4} d^4 + m_p n v_z^2 \pi d^2 \tag{D.9}$$

Plotting these forces for a range of plasma currents yielded Fig. D.5, which shows the choice of current distribution has a significant effect on the estimated load.
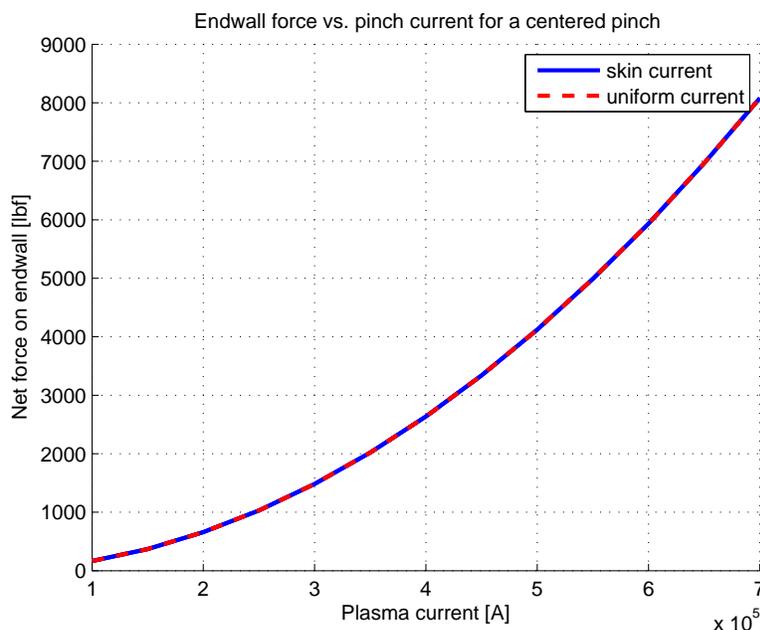
Figure D.6: For on-axis pinches (the best case loading scenario), the current profile does not affect the scaling between load and current. This lack of sensitivity is expected because the pressure profiles for the current profiles are identical beyond the radius of the pinch.

Best case loading

In the best case, the Z-pinch is centered on machine axis, so the largest plasma pressure does not impinge upon the endwall. In this case, the pressure profiles were numerically integrated over surface 2 excluding the area of the center hole. Because the pressure profiles at radii beyond the pinch radius are identical, the scaling of applied force is the same for both current distributions as shown in Fig. D.6.

D.2 Transient structural analysis in ANSYS

Knowing the expected endwall the loading, the structural analysis proceeds to determine how the endwall assemblies react to such forces, and many transient structural simulations are computed with ANSYS to optimize the endwalls' geometries. These simulations solve for the time evolution of von Mises stresses in various portions of the geometry based on

prescribed loading and boundary conditions. Relying on the distortion-energy theory for ductile materials [75], the analysis aimed to find a geometry that would keep the von Mises stresses below the yield strength of 304 stainless steel by a reasonable safety margin.

D.2.1   ANSYS model set up

The ANSYS model is prepared to maximize simulation speed, minimize user input between simulations, and maximize realism.

To reduce the size of the problem, the simulation applies symmetry boundary conditions to a quarter of each endwall. Also, the use of a relatively coarse mesh is enabled by applying the approximate pressure profile shown in Fig. D.7 (a) normal to the endwall's plasma-facing surface. Appreciable resolution of the pressure profile would require significant mesh refinement at the expense of computational efficiency. Instead of a finely resolved profile, a uniform pressure is applied to an annular area of the endwall beyond the radius of the center hole. This area and pressure are chosen such that the total applied force matched the theoretically estimated load for the plasma current under consideration. The applied force is ramped up and down linearly as shown in Fig. D.7 (b) over the course of 80 μs to approximate the timescale of ZaP-HD's current waveform.

To minimize the required user input, endwall geometries are imported into ANSYS directly as .SLDASM files. Importing the geometries from this file format allows relatively easy modifications: geometric changes made in SolidWorks can be refreshed into ANSYS. Unfortunately, some updates to the SolidWorks geometries do break contacts previously defined between the parts in ANSYS. These broken contacts sometimes need to be redefined.

Much of the realism in the model comes from selecting the proper contacts between assembled parts. The various contacts applied are listed below.

- **Split ring to endwall:** The downstream split ring is designed to clamp into the groove at the end of the outer electrode. During initial ANSYS simulations, the split ring surfaces were bonded to the electrode groove, but this led to unrealistic bending

caused by the split ring pulling radially away from the electrode's outer surface. The final simulations are conducted with the split ring surfaces frictionally contacted to the groove, which allow the ring to detach from but not penetrate the outer electrode. Unless otherwise noted, all frictional contacts utilize a friction coefficient of 0.5 to represent the steel-on-steel interfaces. This change reduces stresses while making the structural dynamics qualitatively more realistic.

- **Outer electrode to endwall:** The end of the outer electrode is designed to fit into a circular groove machined in the endwall. The ID and OD of the outer electrode are no separation contacted with their respective sides of the groove. Also, the end of the outer electrode is frictionally contacted with the base of the groove in the endwall. In this case, the frictional contact is used simply to prevent part interpenetration, so the frictional coefficient for this contact is set to 0.002 to ease simulation convergence. These contacts between the outer electrode and the endwall allow the two parts to separate as axial pressure is applied to the system, but they also prevent the parts from intersecting.

- **Bolts to assembly:** Multiple contact types are applied to the bolts. The bolt heads are frictionally contacted to washers, which are frictionally contacted to the endwall. This allows the bolt heads and washer to slip and move relative to one another and relative to the endwall. The bodies of the bolts are no separation contacted with their endwall through holes to prevent any penetration of the bolts into the endwall. Note that a frictional contact was tried to achieve the same purpose, but it led to practically identical results. The bolt threads are bonded to their split ring holes.

To improve the realism of the simulation, pre-tension is applied to the bolts. The magnitude of the pre-tension was estimated by estimating a likely bolt torque and then relating the torque to bolt tension with Eq. D.10. Here, K = 0.18 is a friction coefficient for a lubricated bolt and d is the bolt diameter. The applied bolt torque was estimated to be 25 ft-lbs based
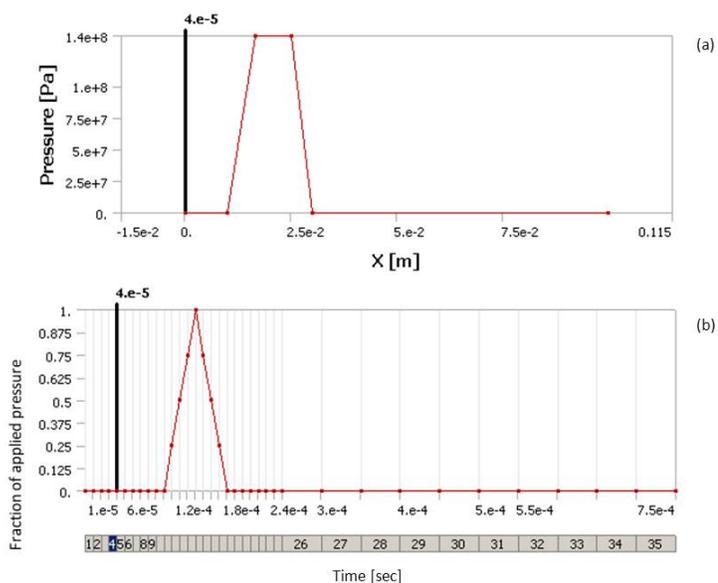
Figure D.7: (a) shows the spatial distribution of applied axial pressure on the plasma-facing endwall surface. The pressure and annular area to which it is applied are selected to match the expected cumulative applied load. Here, X is the radial component of a coordinate system centered on machine axis. (b) shows the time evolution of the applied pressure. The simulation is instructed to apply the specified fractions of the profile in (a) at each time point. The linear ramp up starts well after the simulation's start to ensure the transient behavior of the bolt pre-tension does not affect the results.

on physical experience (ie: how much force does it feel like we apply when we tighten the endwall bolts on ZaP). Increasing bolt pre-tension increased stresses in all the parts in the simulations.

$$F = \frac{T}{Kd} \tag{D.10}$$

The pre-tension is applied as a load during the first time step of the simulation and then is locked at all subsequent time steps. When applying pre-tension, ANSYS splits the bolts along a user-defined plane. The split allows ANSYS to create two new elements on which to apply external forces. After these forces are applied, the position of the two new elements must be locked together to avoid the bolt halves from flying apart. Even though the load is only defined for the first time step, it is applied as a constant throughout the rest of the simulation. In transient simulations, it does take a finite amount of time for the pre-tension to propagate through the length of the bolts. In these simulations on such short time scales, the pre-tension actually takes a few time steps to fully disperse. This leads to spikes in the bolt von Mises stresses early in time, which leads to overestimated stresses in the electrode and split ring. This was found by initiating the applied pressure profile later in time (after the pre-tension became steady) and comparing to simulations ran with the plasma pressure profile initiated before the pre-tension stabilized. This explains why the stresses in Figs D.8 and D.9 are lower than in Figs D.10 and D.11.

Finally, the upstream side of the outer electrode section was set to a fixed boundary condition.

D.2.2   ANSYS results

The time dependent solutions show the endwall assemblies ring in response to the impulsive applied pressure. Each simulation proceeds just long enough in time to verify the vibrations are damped, which ensures we observed the maximum resulting stresses. Iterations on the endwall geometries progressed based on the computed stresses given in space and time.

ANSYS tracks the time evolution of von Mises stresses in four different regions within the geometry: the electrode, endwall, split ring, and bolts. Fig. D.8 shows how the single hole endwall takes the initial load and transfers it to the bolts, which then pull on the split ring and electrode. Stresses prior to 100 μ s result from bolt pre-tension. The endwall feels the impulsive pressure first, at 100 μ s, and its maximum stress coincides with the peak in the applied pressure around 150 μ s. One-hundred μ s after the endwall stress maximizes, the bolt stress peaks, suggesting a propagation speed around 1200 m/s, which is on the same order of the sound speed in 304 stainless steel. Fifty μ s after the peak bolt stress, the electrode and split ring stresses peak simultaneously, which corresponds to a 1500 m/s progagation speed. Here, the stresses in all components except the bolts remain below the material's yield strength. High strength bolts can be purchased to handle stresses higher than the yield strength. Fig. D.9 shows the same temporal evolution occurs for the spoked endwall, but larger stresses in the spoked endwall offset lower stresses in the electrode and split ring.

A parametric study varying endwall thickness and applied force identified endwalls 1.75 inch thick could withstand loading from 450 kA plasma currents. First, an adequate thickness was found by running many simulations at different endwall thicknesses for a plasma current of 500 kA. Simulations with a 1.75 inch thickness produced stresses slightly above 304 SS's yield strength for both the single hole and spoked endwalls. Increasing the thickness further was deemed impractical, so this thickness was held constant in the remaining analysis to hone in on exactly how much current the endwalls could handle.

The rest of the study varied applied force while holding endwall thickness at 1.75 inch, which revealed more precisely the maximum plasma current the endwalls could withstand. For instance, Fig. D.10 shows the stresses in a 1.75 inch thick single hole endwall, electrode, and split ring increase linearly with the applied load. The electrode limits the strength of the entire assembly as its maximum stress exceeds the yield strength at the lowest applied load. That applied load ($\approx$ 35000 lbf) corresponds to a plasma current of 475 kA for a skin current according to Fig. D.5. This indicates for a worst case plasma pulse, the single hole
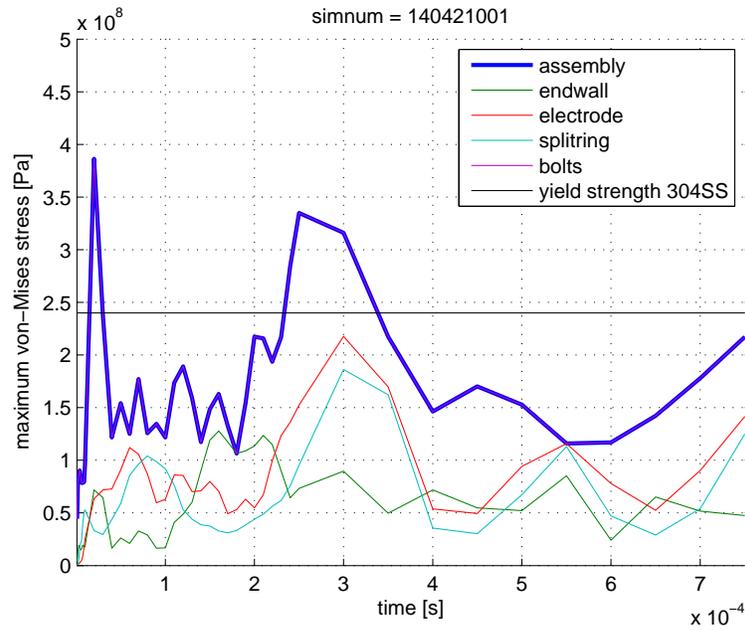
Figure D.8: The max von Mises stresses in each component of the single hole endwall assembly exhibit damped oscillations in time. Stresses before 100 μs are caused by bolt pre-tension.
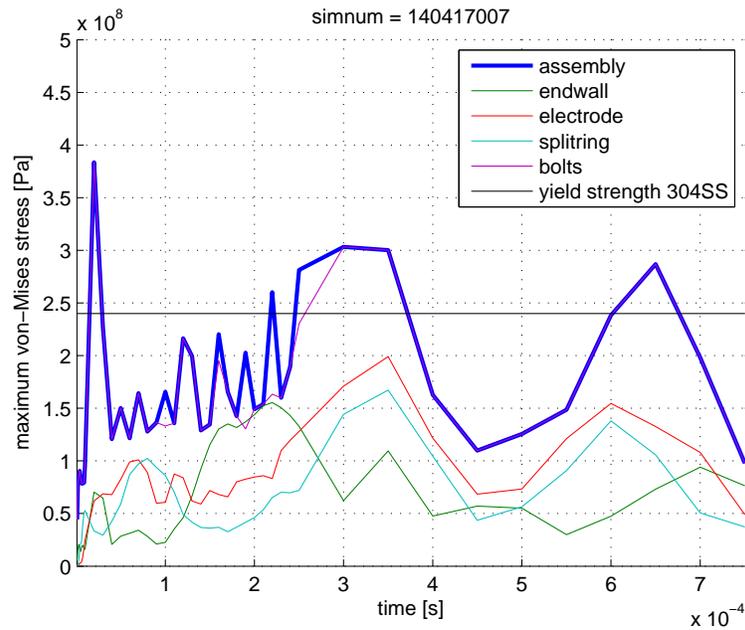
Figure D.9: The max von Mises stresses in each component of the spoked endwall assembly exhibit damped oscillations in time.
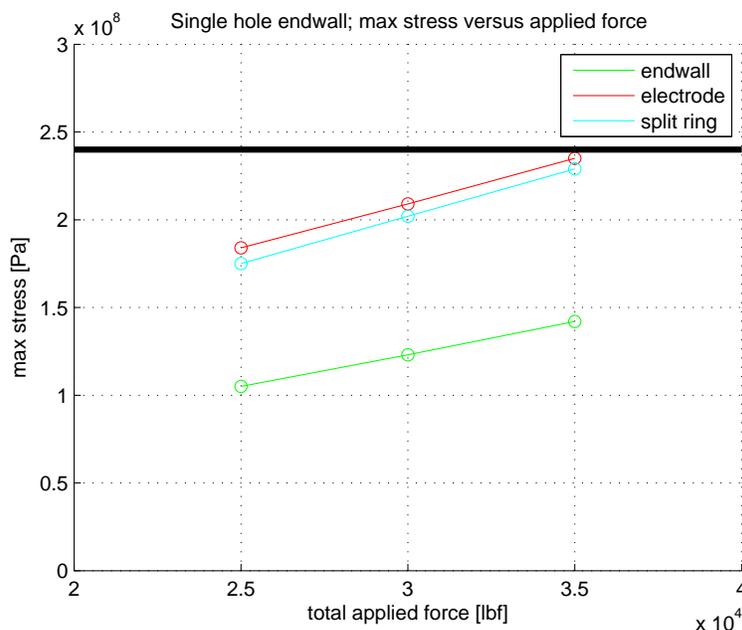
Figure D.10: For the single hole endwall, the maximum von-Mises stresses in the endwall, electrode, and split ring each scale linearly with applied load. The horizontal black line indicates the yield strength of 304 SS. This plot indicates the electrode limits the resilience of the assembly, as its max stress exceeds the yield strength at the highest applied load.

endwall can survive a plasma current of 475 kA. Comparing the 35000 lbf applied load to Fig. D.6 reveals that in the best case, ZaP-HD can run at currents in excess of 750 kA. Thus, if operators can ensure well-behaved, on-axis plasmas, the single hole endwall assembly can survive virtually any amount of current the ZaP-HD power supply can provide.

For a 1.75 inch thick spoked endwall, the same considerations apply to Fig. D.11. The electrode limits the strength of the entire assembly as it yields at an applied load around 31500 lbf. In the worst case, the spoked endwall could handle currents up to 450 kA, and in the best case it could handle any current the power supply can deliver.

ANSYS also solves for the stresses at all points in space. Knowing precisely where the stresses peaked in each part drove modifications to the simulations and to the part geometries. In many early simulations, max stresses occurred in strange places, which prompted
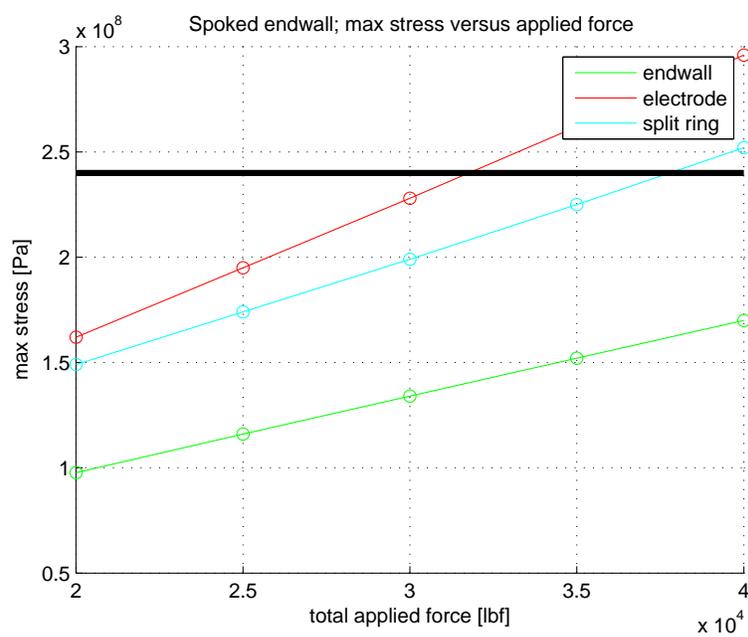
Figure D.11: For the spoked endwall, the maximum von-Mises stresses in the endwall, electrode, and split ring also each scale linearly with applied load. Again, the horizontal black line indicates the yield strength of 304 SS. The electrode limits the resilience of the spoked assembly, as its max stress exceeds the yield strength at the lowest applied load.
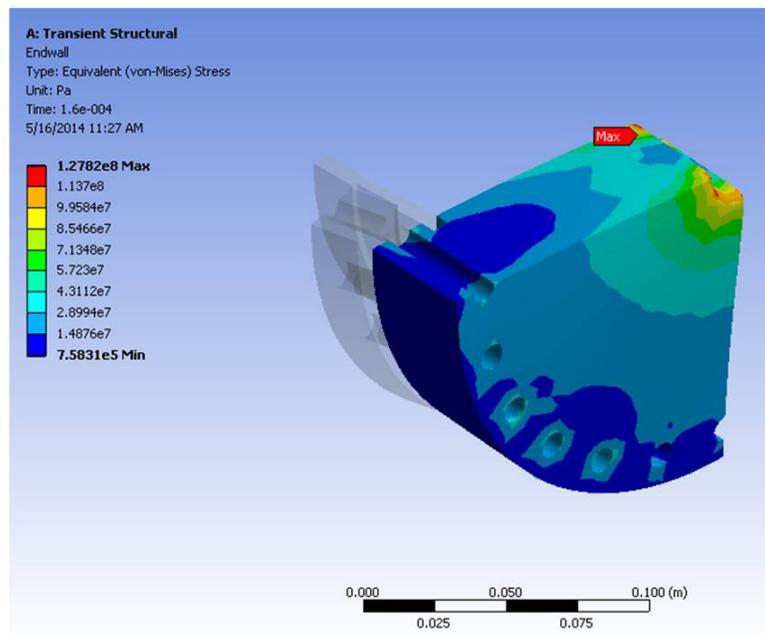
Figure D.12: For the single hole endwall, the von Mises stresses in the endwall at the instant of maximum stress.

changes to the contacts between parts to improve the model's realism. Later, changes to part geometries (ie: changing endwall thicknesses or enlarging radii) were made to minimize stresses. Figs. D.12-D.15 show the distributions of von Mises stress in the final design of the single hole endwall at the time instants when the maximum stresses are observed. Figs. D.16 - D.19 show the distributions for the final spoked endwall. Note that in both the single hole and spoked designs, the maximum stresses occur in the electrode's split ring groove.

D.2.3 Structural analysis of ZaP-HD outer electrode

Structural analysis of the endwalls reveals the electrode's split ring groove yields before any other part. However, this analysis models only a short section of the electrode, so a global analysis of its integrity is required to comprehensively evaluate its strength.

To simplify the simulation, the model solely considers the electrode's geometry instead of examining an assembly of parts. Details like threaded holes and interferometry ports are
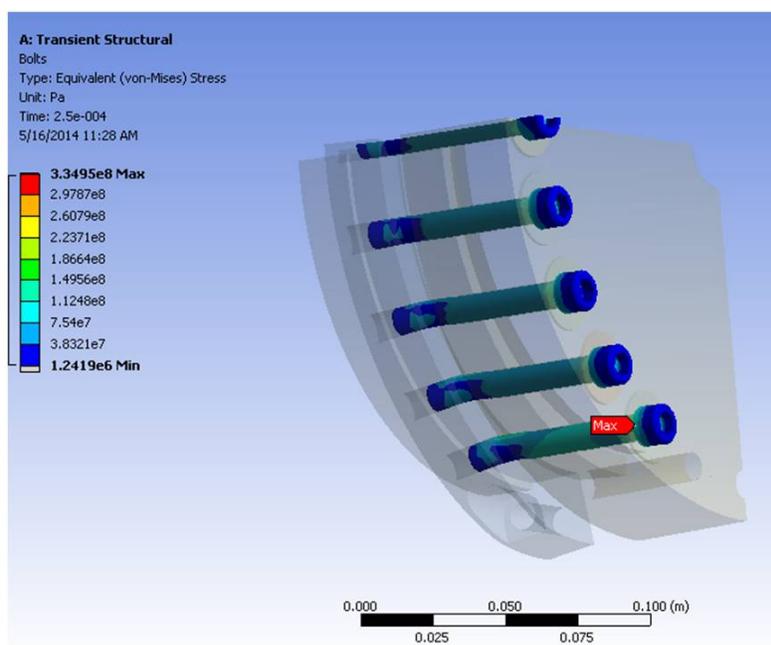
Figure D.13: For the single hole endwall, the von Mises stresses in the bolts at the instant of maximum stress.
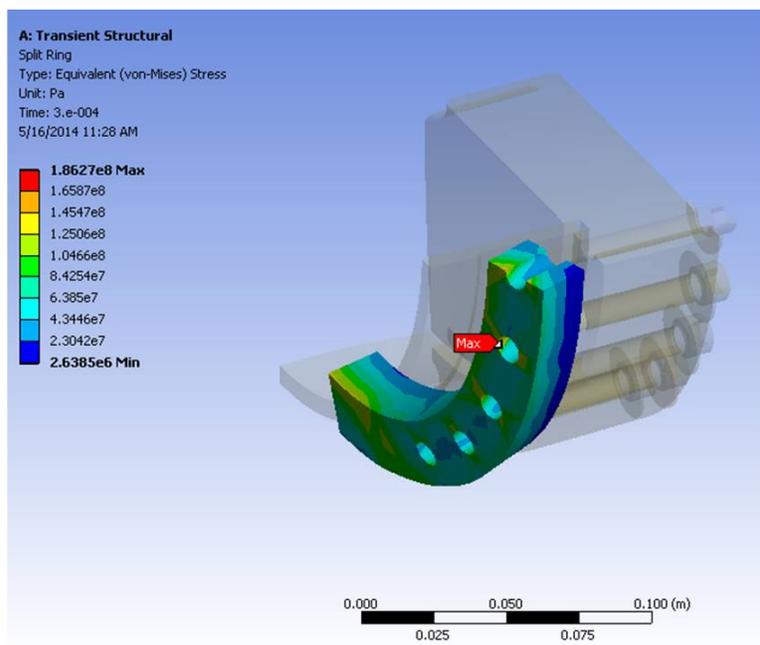
Figure D.14: For the single hole endwall, the von Mises stresses in the electrode at the instant of maximum stress.
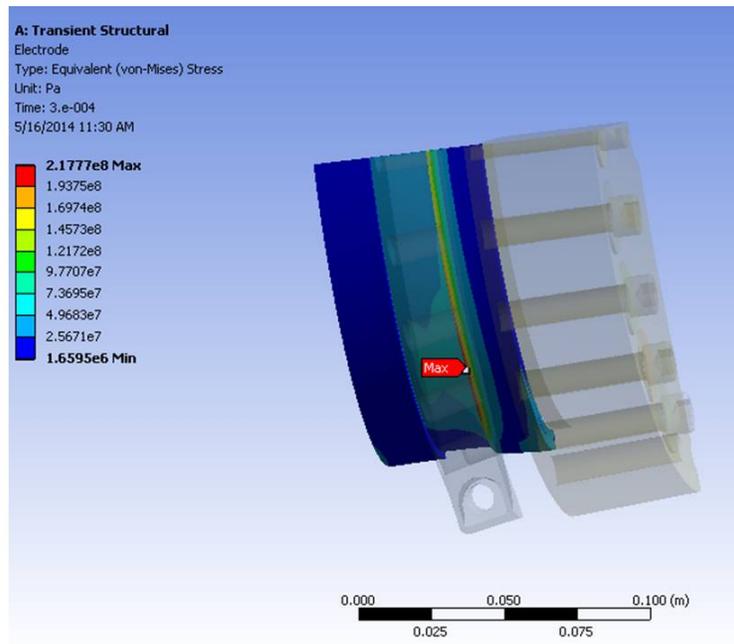
Figure D.15: For the single hole endwall, the von Mises stresses in the split ring at the instant of maximum stress.
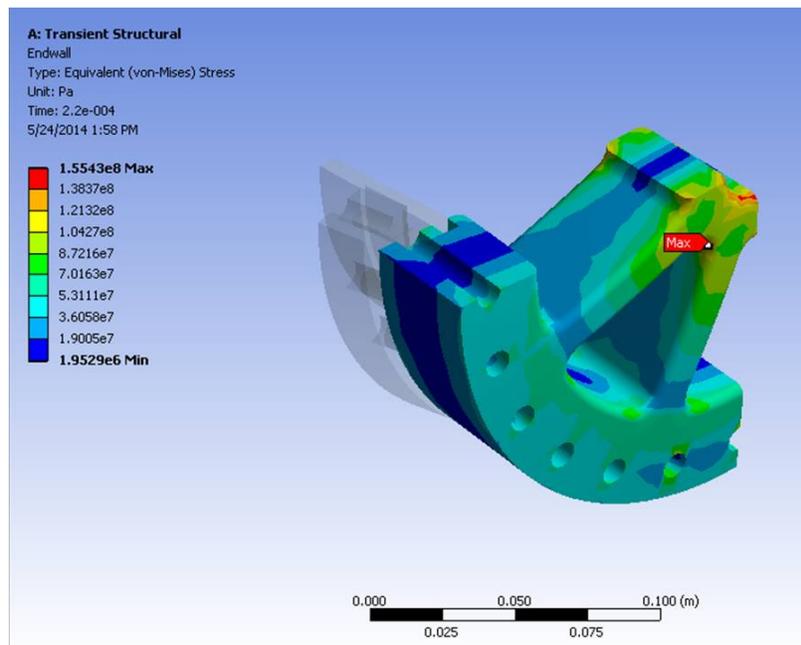
Figure D.16: For the spoked endwall, the von Mises stresses in the endwall at the instant of maximum stress.
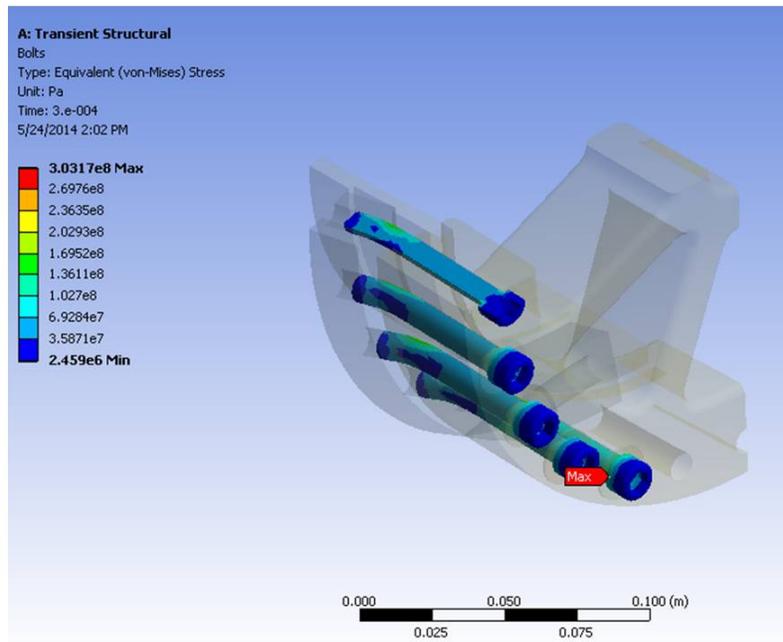
Figure D.17: For the spoked endwall, the von Mises stresses in the bolts at the instant of maximum stress.
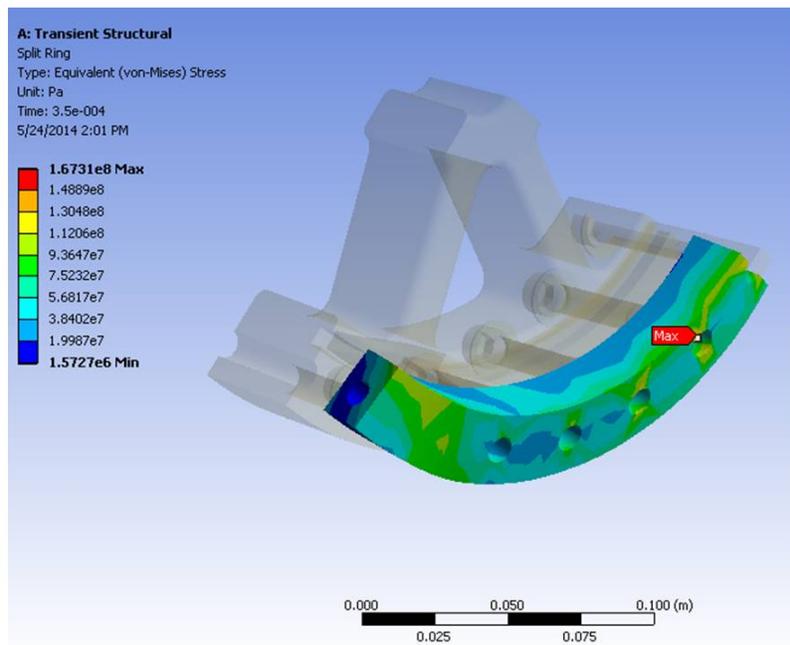
Figure D.18: For the spoked endwall, the von Mises stresses in the split ring at the instant of maximum stress.
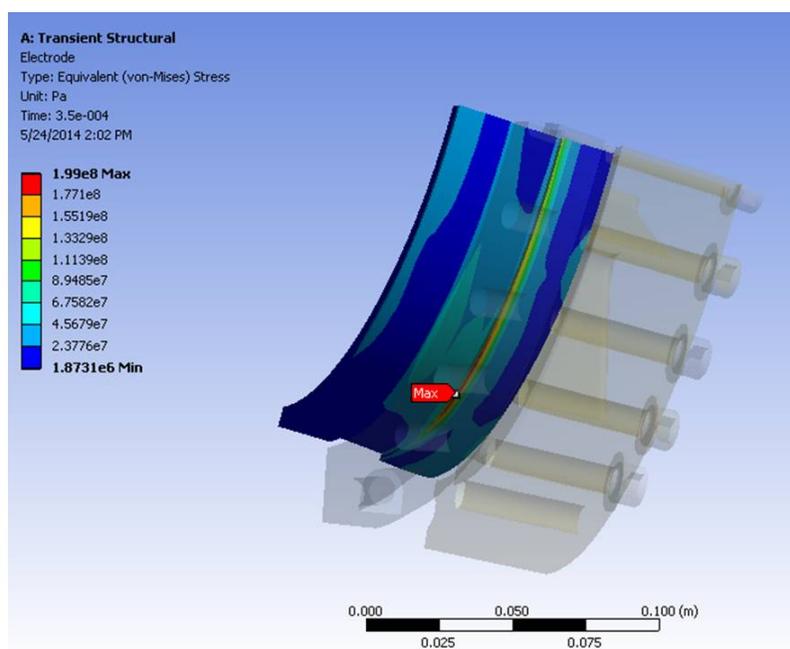
Figure D.19: For the spoked endwall, the von Mises stresses in the electrode at the instant of maximum stress.

removed, but all magnetic probe holes are included because of their significant size relative to the electrode rods. The model applies a radially outward, uniform pressure to the inner diameter of the electrode equal to the magnetic pressure induced by the plasma current at that radius. Unlike the endwall simulations where the axial force reaches the electrode indirectly through the bolts and split ring, here the 35,000 lbf axial load is applied as a uniform pressure directly to the downstream end of the electrode. Both loads are linearly ramped up and down in time as in the endwall simulations.

The results show significant stresses initiate at the downstream end of the electrode and then propagate at 4000 m/s upstream until they reflect off of the upstream end. After this reflection, a complicated superposition of stresses proceeds. The max von Mises stress oscillates erratically throughout the simulation, but it remains below the 304 SS yield strength by a 1.7 safety margin. The maximum stresses occur in the rods around the magnetic probe holes. The significant stresses seen previously in the split ring groove do not occur here
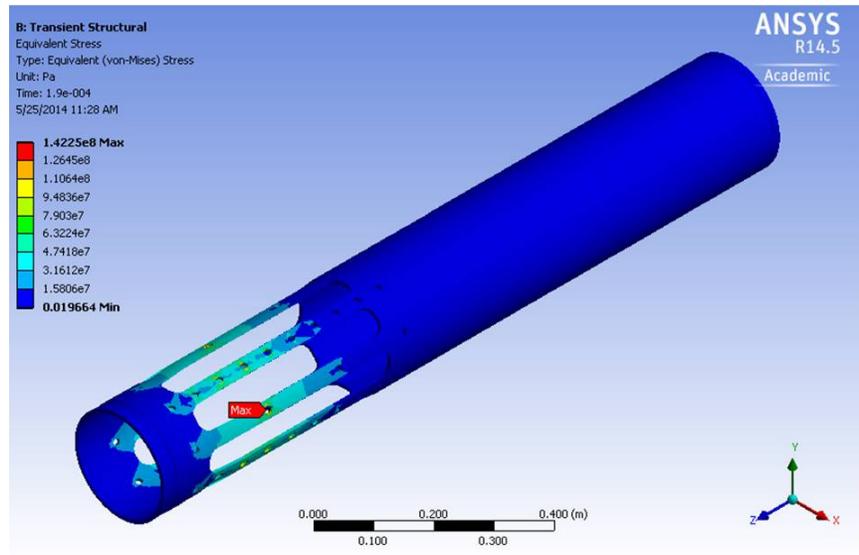
Figure D.20: In the outer electrode, the maximum stresses occur in the rods around the magnetic field probes. This solution results from linearly ramping up and down a uniform radial magnetic pressure as well as a 35,000 lbf axial load applied as a uniform pressure on the downstream end of the electrode. The maximum von Mises stresses remain below the material yield strength by a healthy safety margin of 1.7.

because this model applies the axial force to the end of the electrode instead of the groove. This analysis indicates the outer electrode will withstand the worst case load of a 475 kA Z-pinch.

VITA

Michael P. Ross was born in Altus, Oklahoma in 1988. The son of Air Force officers, he developed a healthy affinity for airplanes, helicopters, and spacecraft as his family moved from base to base across the country. In 2006, he graduated from Grand Junction High School in the beautiful city of Grand Junction, Colorado. During college, he pursued his interest in aerospace, working internships at a precision machine shop and conducting student research in solar photovoltaics and active flow control aerodynamics. He earned a Bachelor of Science in Aerospace Engineering from University of Arizona in 2010. Later that year, he joined the ZaP research group at University of Washington eager to learn about space propulsion. He earned a Doctor of Philosophy from the William E. Boeing Department of Aeronautics & Astronautics at the University of Washington in 2016.